Molecular Structure, Stability and Crystallisation of Isethionate Ester Surfactants

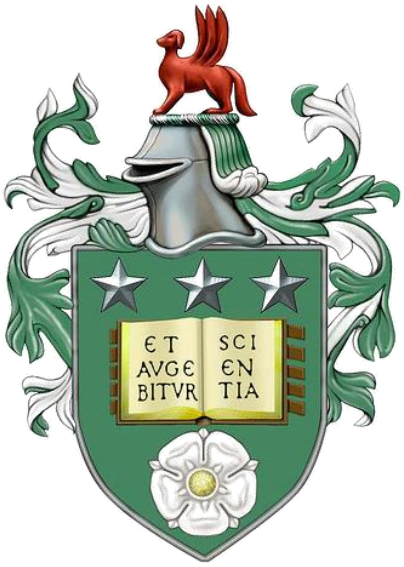

Mohammed Ismail Jeraal

Submitted in accordance with the requirements for the degree of Doctor of Philosophy

School of Chemical and Process Engineering

University of Leeds

October 2019

The candidate confirms that the work submitted is his own, except where work which has formed part of jointly-authored publications has been included. The contribution of the candidate and the other authors to this work has been explicitly indicated below. The candidate confirms that appropriate credit has been given within the thesis where reference has been made to the work of others.

- Chapter 4 of the thesis was published as a jointly-authored journal article in *ACS Sustainable Chemistry and Engineering* as follows:

  M. I. Jeraal, K. J. Roberts, I. McRobbie and D. Harbottle, 'Process-Focused Synthesis, Crystallization, and Physicochemical Characterization of Sodium Lauroyl Isethionate', *ACS Sustainable Chemistry & Engineering*, 2018, **6**, 2667-2675.

- Chapter 5 of the thesis was published as a jointly-authored journal article in *Industrial & Engineering Chemistry Research* as follows:

  M. I. Jeraal, K. J. Roberts, I. McRobbie and D. Harbottle, 'Assessment of the Thermal Degradation of Sodium Lauroyl Isethionate Using Predictive Isoconversional Kinetics and a Temperature-Resolved Analysis of Evolved Gases', *Industrial & Engineering Chemistry Research*, 2019, **58**, 8112-8122.

In regard to both publications, Mohammed I. Jeraal conducted all experiments, performed all data analysis and wrote all sections of the manuscript. Project supervision, manuscript editing and proofreading was performed by Kevin J. Roberts, Ian McRobbie and David Harbottle.

Acknowledgments

I would first like to send my sincerest thanks to my primary supervisors, travel companions and mentors David Harbottle and Kevin Roberts. Their perfect balance of guidance, support and academic freedom yielded an engaging and thoroughly enjoyable research experience over last few years. I also thank my supervisor Michael Rappolt for his technical insight and helpful discussions on small angle X-ray scattering.

My gratitude is extended to Innospec Ltd for their financial and technical support of the project. My wholehearted thanks go to Ian McRobbie whose project supervision and industrial insight were truly invaluable to the project. I also acknowledge the EPSRC Centre for Doctoral Training in Complex Particulate Products and Processes at the University of Leeds for the provision of funding, access to research facilities and support with continuing professional development.

I would additionally like to thank Tim Dunn, Chris Tassone and Cindy Patty at the Stanford Synchrotron Radiation Lightsource for access to facilities and technical support during the high-resolution SAXS experiments. At the University of Leeds, I would also like to thank Martin Huscroft, Simon Barrett, Mary Bayana, Ben Douglas, Adrian Cunliffe and Karine Alves-Thorne for analytical support.

Shout-out to everyone in Engineering G29 (formerly Chemistry 4.15): Paul, Guilherme, Yefeng, Jess, Toby, Charlotte, Jamie, Josh, Matt, Julio, Joe and Alex. Additional thanks to James Goode, Tom Turner and Xue Tang for helping me nagivate the more perilous parts of the project. My heartfelt, sincere appreciation lastly goes to Abdulrahman Ajina for his camaraderie, level-headed advice and inexhaustible encouragement for the duration of my PhD.

I would finally like to dedicate this thesis to my family who selflessly supported me through the years I spent pursuing this degree.

Abstract

An absence of fundamental research into the chemistry, structure and properties of isethionate ester surfactants has resulted in notable shortcomings in the manufacture of modern personal care products. Through a detailed characterisation of molecular structure under both ambient and elevated temperatures this research aimed to develop the foundations upon which a holistic understanding of the isethionate ester system could be achieved.

Sodium lauroyl isethionate (SLI) was selected as a representative model surfactant, after it was revealed to be the most abundant constituent in a commercial isethionate ester blend. SLI was synthesized through a bespoke single step process free from ancillary solvents, catalysts and chlorinated agents. The material was isolated to reproducible purity levels of 98% via three recrystallisations in methanol, whilst a turbidimetric solubility analysis generated process parameters for the controlled scale-up of this crystallisation process. The resulting physicochemical analysis revealed a critical micellar concentration (CMC) of 5.4 mM and a plateau surface tension of 38 mN/m at 20°C. Both values were lower than the previously reported values for SLI in water. Dynamic vapour sorption studies demonstrated a reversible 2.3% mass gain when exposed to sustained humidity of 87%, suggesting possible formation of a hemi-hydrated structure.

A kinetic analysis of the thermal degradation of SLI indicated that mass loss was 28 times higher in air than nitrogen. Validated predictive models suggest that reaction temperatures could be increased to 250°C for an increased reaction rate, before significant increases in degradation were observed over typical synthetic timescales. An evolved gas analysis revealed risk of carbon dioxide, carbon disulfide, sulfur dioxide, water vapour and VOC evolutions at elevated temperatures. The predictive isoconversional models indicated that rapid structural measurements were necessary to thermal degradation, risk of gas evolution and structural anomalies resulting from thermal degradation.

The crystal structure of SLI was determined through a combination of powder X-ray diffraction and molecular modelling techniques. The crystal lattice was found to exhibit a monoclinic unit cell with P 21/c space group, with molecules in a trans-trans tilted lamellar bilayer conformation, similar to the anhydrous structure of sodium dodecyl sulfate (SDS). A characterisation of the intermolecular interactions revealed that coulombic interactions between sulfonate and sodium ions constituted over 80% of the total lattice energy.

Due to reduced structural order and greater phase complexity at elevated temperatures, the temperature dependent analysis of SLI was conducted using a combination of synchrotron-derived small angle X-ray scattering (SAXS), molecular mechanics and density functional theory. Between 40 and 150°C, the predominant lamellar crystalline phase exhibited an increase in scattering intensity, where the measured increase in lamellar spacing (0.1 nm) correlated to the structural changes previously reported for the annealing of sodium laurate. Above 150°C, the appearance of additional phases decreased the scattering intensity in the primary phase until isotropic melting was observed at >220°C, as confirmed via DSC. When compared with previously reported phases of traditional soaps, both 'crystalline' and 'lamellar' phases were observed. Evidence of the hemi-hydrated phase measured via DVS was also found at lower temperatures. Molecular mechanics calculations led to a predicted crystal structure based upon the measured lattice spacing. Both the anhydrous and hydrated structures of SLI correlated very well with previously published trends in lamellar tilt angle and headgroup size in dodecyl-chained, sulfur-based anionic surfactants.

Contents

List of Figures

List of Tables

Chapter 1: Introduction

Synopsis: *This chapter provides a general introduction to traditional soap manufacture and how the need for synthetic detergents arose from the issues exhibited by orthodox carboxylate soaps. This is followed by a review of the literature concerning the manufacture of sodium cocoyl isethionate; the primary species of interest in this project. Finally, an overview of the limitations of synthetic detergent manufacture lead to the proposed research question. The section is concluded with the aims and objectives of the research, information on how the project was managed, as well as a structural framework through which the remainder of the thesis is presented.*

1.1. Research Context

1.1.1. Introduction to Soap Manufacture

Soap is the oldest known skin cleanser and has been in existence for thousands of years.[1] It is a popular form of surface active agent or 'surfactant' which lowers the surface tension between two liquids due to its *amphiphilic* nature (originating from the Greek words, *ampha* (both) and *philic* (love)). A lipid-soluble hydrophobic tail and water soluble headgroup cause soap to preferentially bind at interfaces and aggregate to form complex structures in solution.

Saponification is the process by which triglycerides are esterified under a strong alkali base to form three molecules of the corresponding sodium carboxylate 'soap' and a molecule of glycerol, as displayed below.[2]

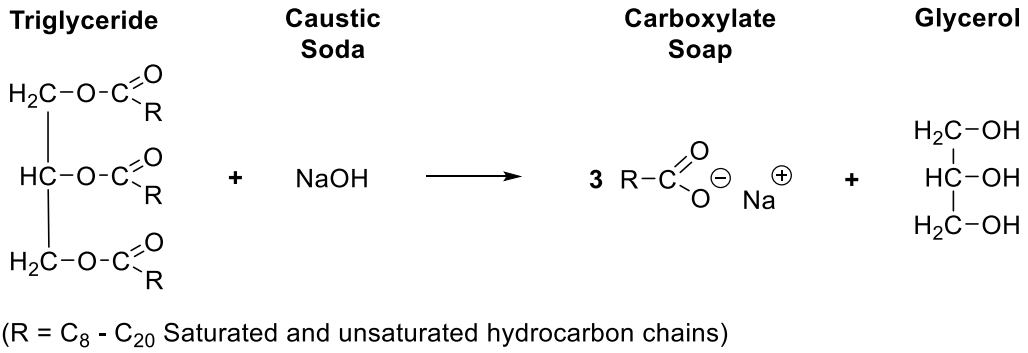

Figure 1.1. Soap manufacture by saponification of natural fats (triglycerides). Reaction is typically executed in water via the Kettle Process, where reagents are boiled within a single reaction vessel. Upon completion, the immiscible soap is left to separate from the aqueous glycerol, which is subsequently drained away. The R group is dependent on the composition of fats present in the feedstock blend.[2]

A blend of triglycerides is typically utilised by soap manufacturers to optimise the performance of the resulting soap bar. Nut oils, such as coconut oil and palm kernel oil, are predominantly composed of shorter chained triglycerides (such as C12) and consequently display a higher aqueous solubility and a higher lather than their longer chained counterparts.[3] Tallow and palm oil, consisting of C16/C18 chains are blended in

combination to improve lather stability and increase hardness in the end product.[4] Intense agitation is required to start the reaction due to poor miscibility between the triglycerides and aqueous base. Following initiation, the soap product helps emulsify the two reagents, thus increasing the rate of reaction via autocatalysis.[5]

Upon completion, brine is blended into the aqueous phase to aid phase separation between the soap and glycerine. On an industrial scale, triglycerides are often hydrolysed with water prior to base-catalysed saponification, as illustrated in Figure 1.2.[6] This significantly improves glycerol recovery and negates the need for subsequent brining. The hydrolysis is achieved by treating the triglycerides with high pressure steam prior to saponification. Because the fatty acids are more volatile than the corresponding carboxylate soaps, they can be easily distilled from glycerol, significantly improving recovery levels over traditional saponification.

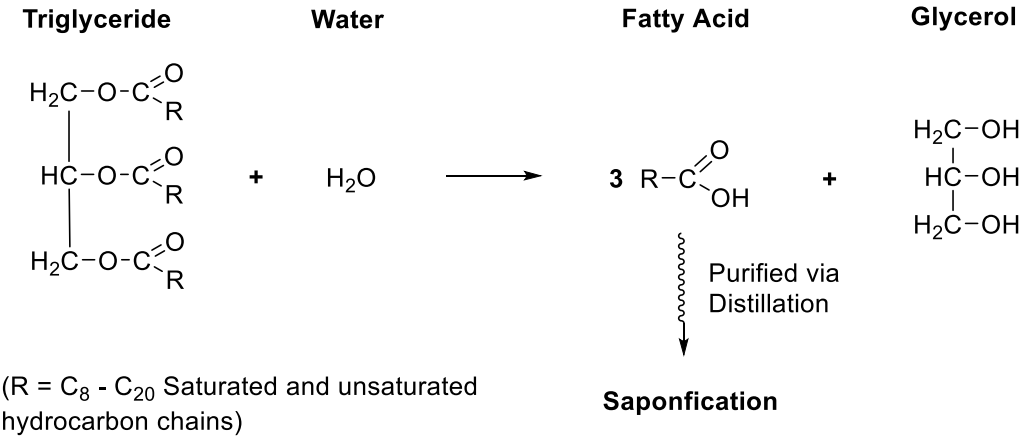

Figure 1.2: Hydrolysis of triglycerides prior to base catalysed saponification. The R group is dependent on the composition of fats present in the feedstock blend.[7]

Both methods of saponification and the resulting soap bar product, however, exhibit two major disadvantages. When in contact with water, traditional carboxylate soaps are prone to hydrolysis, much like the triglycerides depicted in Figure 1.2.

Traditional soaps are also impacted by mineral ions, present in the water in which they are utilised. In the UK, water is regarded 'hard' when its calcium concentration exceeds 100 mg/l.[8] Beyond these levels, calcium and magnesium ions hinder the performance of carboxylate soaps, as depicted in Figure 1.3.[7]

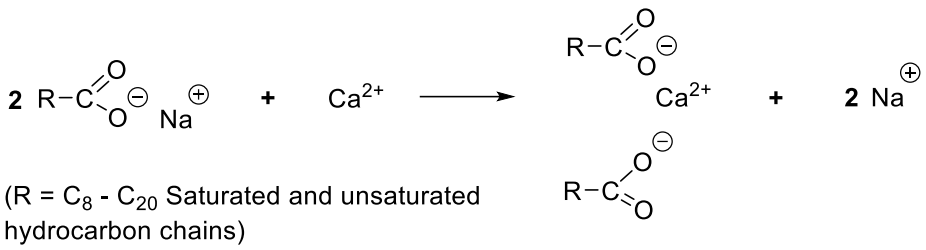

Figure 1.3: Inhibition of carboxylate soaps by Ca^{2+} ions present in hard water. An identical reaction occurs with the Mg^{2+} ions in hard water.[7]

Since the resulting calcium minerals salts are of lower amphiphilicity than the carboxylate soaps, surface activity is significantly reduced thus resulting in a reduction in detergency and lathering performance. The minerals salts are also insoluble in water and therefore precipitate as unsightly solid deposits, which are difficult to remove from bathroom surfaces.[7] Dermatological studies indicate that the same phenomenon also occurs on the skin surface at a microscale during product use.

1.1.2. Synthetic Detergents

In the 1930s, demand for a general detergent able to withstand the activity reduction and acidity of hard water, led to the development of the 'taurate' synthetic detergent.[9] The cosmetics industry soon discovered the superior detergency and foaming of synthetic surfactants when compared with traditional soap bars. This resulted in the development of 'isethionate' based synthetic detergent soap bars, the most famous of which is Dove, created by Unilever in 1955.[10] Despite a shift in consumer trends towards liquid based products such as shower gels and liquid cleaners, soap bars are still purchased by 72% of US consumers on a regular basis and the US soap bar industry alone is estimated to be worth over £1.7 billion (2013).[11] Sodium cocoyl isethionate (SCI) is the primary surfactant in Dove soap and most common synthetic soap bars.

Synthetic detergents (or syndets) were first commercially manufactured in 1932. The textiles and laundry industry approached IG Farben, a German chemical conglomerate, to create a surfactant able to sustain its detergency when used with hard water.[9] Their acid chloride synthesis of acyl taurates in Figure 1.4 is one the earliest published examples of synthetic detergents.[12] The product is chemically very similar to the isethionate class of surfactant

typically utilised in cosmetic soap bars and demonstrates many of the advantages that synthetic detergents exhibit over traditional soaps.[9]

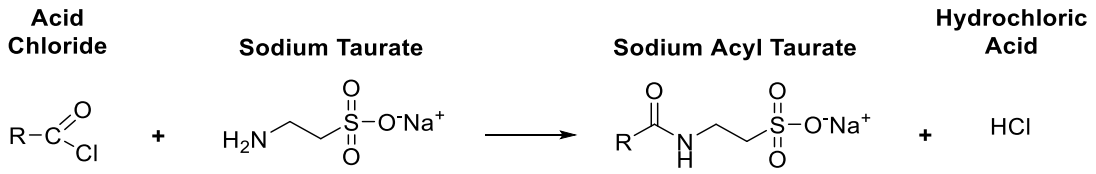

Figure 1.4: Taurate based synthetic detergents synthesised via the acylation of taurine. This surfactant was developed for the textiles industry and eventually led to the development of sodium cocoyl isethionate (SCI).[12]

It was proposed that the increased molecular stability resulting from the amide, inhibited the ability for the sodium salt to be displaced by Ca^{2+}/Mg^{2+} ions present in hard water. The lathering and detergency performance was therefore unaffected by water quality and because the alkali earth ions remain in aqueous solution, there was no formation of mineral deposit with prolonged use of the product. In the case of saponified soaps, a stoichiometric quantity was often lost to mineral ions in hard water, thus increasing the quantity and cost expended to the end consumer.[12] Within the textiles industry, this performance and economic advantage in hard water has meant that global sales synthetic detergents now vastly outstrip those of saponified products by over 9:1. There were however, many disadvantages to the acid chloride synthesis developed by IG Farben. Due to the required phosphorous trichloride, the acid chloride precursor synthesis was significantly more hazardous and costly than the hydrolysis of coconut oil later adopted by the cosmetics industry. During the surfactant synthesis, the released chloride reacted with both sodium and water in the system. While HCl could be azeotropically distilled with water, the sodium chloride was more challenging to remove and significantly increased the hygroscopic nature of any resulting soap product.[13]

The direct condensation of coconut oil derived fatty acids to yield isethionate-based surfactants addressed many of these issues, thus resulting in the commercial success of synthetic cosmetic detergents. The absence of chlorinated agents was deemed particularly advantageous. Upon commercial deployment, the soap industry thus developed the direct condensation synthesis of synthetic detergents (Figure 1.5). It forwent the need for toxic acid chlorides and instead utilised the fatty acid precursors derived from the traditional triglyceride

hydrolysis reaction (Figure 1.2). The direct condensation reaction is a Fischer esterification between an acid and alcohol.

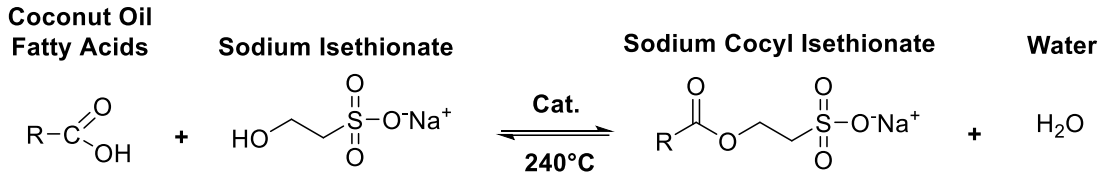

Figure 1.5: Synthesis of SCI via direct condensation of coconut oil derived fatty acids. Fatty acids are derived through the hydrolysis of pure coconut oil. A range of acid, soap and metal catalysts can be utilised. The condensation reaction can be similarly executed with sodium taurate to yield taurate based synthetic detergents. [7]

In order to drive the reaction to produce the desired ester, any water produced during the reaction must therefore be distilled away' in accordance with Le Chatalier's principle, to minimise the rate of the ester hydrolysis.[14] A commercial manufacturer of SCI, reported the melting point of pure sodium cocoyl isethionate as >220°C.[15] The temperature was therefore necessary to maintain a stirrable liquid phase during manufacture.

1.1.3. Sodium Cocoyl Isethionate (SCI) Manufacture

Due to the highly industrial nature of this project, much of the existing research into the manufacture of sodium cocoyl isethionate has resulted from commercial interest and was therefore published in patent literature.

The most comprehensive overview of the industrial synthesis is perhaps located in a patent filed by the Lever Brothers (now Unilever) in 1969.[16] The reaction was identical to the direct condensation isethionate synthesis described in Figure 1.5. The novelty of this particular example arose from the ability to continuously supply the reaction vessel with raw material, resulting in a semi-continuous manufacturing process. A further review of more recent patent literature indicates that while there has been innovation with regard to the raw materials and reaction conditions utilised in isethionate syntheses, the fundamental manufacturing process has changed little since this patent was published in 1960s. A schematic of the synthetic detergent reaction system is depicted in Figure 1.6 overleaf.[16]

The key features of the reaction system (Figure 1.6) are outlined below. The information was derived from a series of patents published by Holland *et al.*, [16] Lemaire *et al.* [17] and Holt *et al.* [18]. Numbers in brackets correspond to labels in Figure 1.6.

The reaction is initiated by feeding coconut derived fatty acids (10), sodium isethionate (12) and a catalyst (14) into a jacketed, agitated reactor (16).

- While the reaction can be executed at stoichiometric quantity of reagent, a molar ratio of 1:1.3 of isethionate to fatty acid is recommended. An excess of fatty acid is preferred to isethionate because it is easily removed by distillation following complete esterification of sodium isethionate.

- The esterification is executed at 260°C. At this temperature, any water produced during the reaction is vaporised and distilled away via a connecting pipe (38) into a condenser (40). The water is removed to maintain the thermodynamic driving force required to drive the reaction to complete conversion.

- The water distilled from the reaction forms an azeotropic mixture with the lighter coconut fatty acids in the reactor. Because an excess of fatty acid must be maintained in the reactor to maximise the conversion of sodium isethionate, a liquid-liquid phase separation is executed at the separator (48). The volatile fatty acids are stored in vessel (52) and subsequently recirculated back into the reactor via a pump (53).

- A stream of nitrogen (36) is circulated directly through the reactor to maintain an inert atmosphere. The flow of gas assists in driving water vapour out the reactor, thus minimising hydrolysis of the isethionate ester product. The presence of oxygen also induces the formation of a deep-brown organic impurity which discolours the product. Any discolouration often renders the isethionate unsuitable for use in cosmetic applications, where appearance of the product is paramount to customer adoption.

- The abundance of surfactant in the reactor (16), coupled with the refluxing water-fatty acid azeotrope results in significant foaming. This is reduced by continuous, vigorous stirring to shear gas-liquid interfaces which also minimises hot spots within the reactor.

- Upon completion of the reaction, the product is pumped into the stripper (60) to vacuum distill lighter, volatile fatty acids into a storage vessel (80). The formulation is blended with heavier fatty acids (62) resulting in an SCI active concentration of 70-85 wt%, depending on the desired properties of the product.[16]

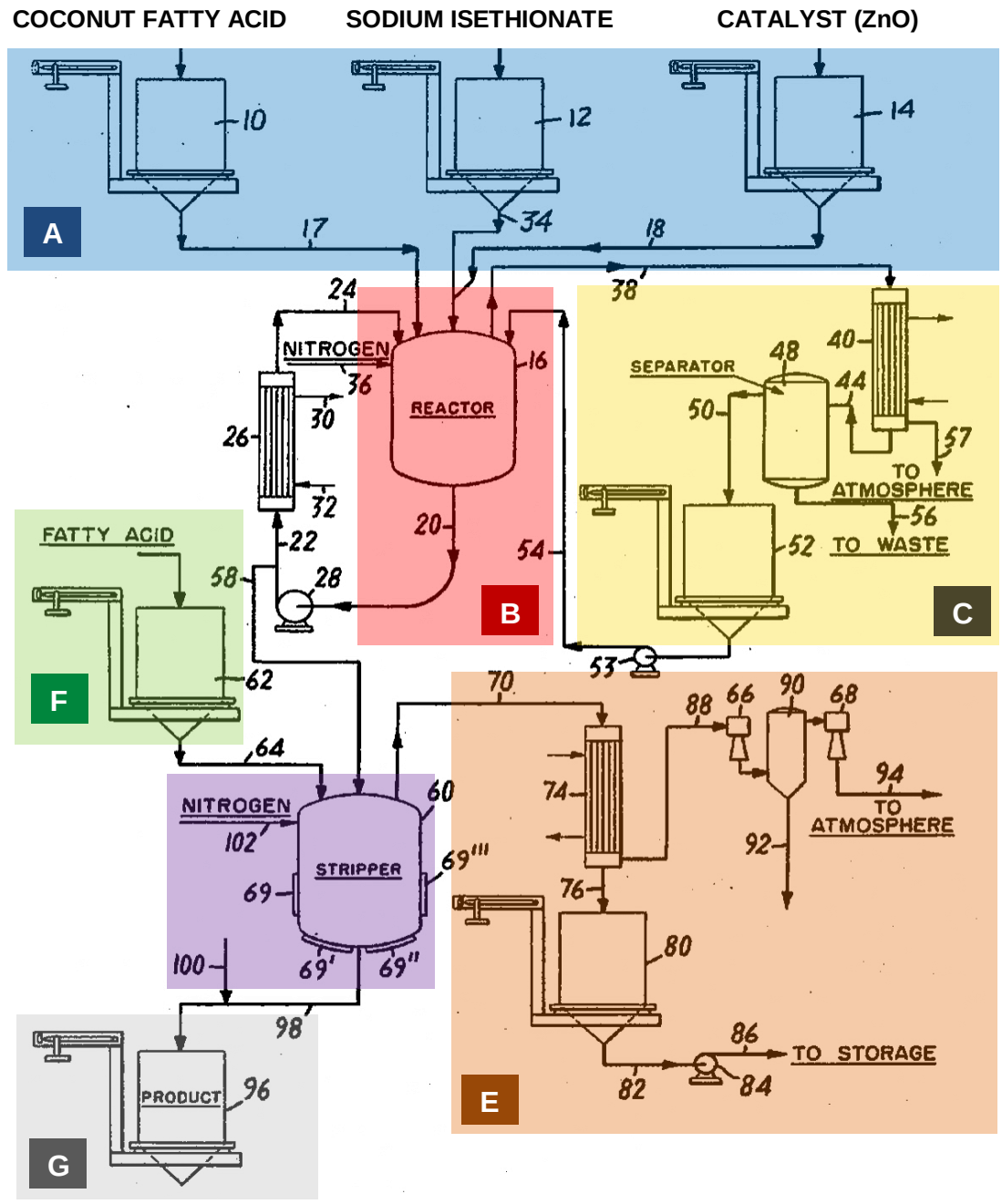

Reagent pumps (A) feed raw materials into a **batch reactor (B)** which is heated to 260°C**.** Distilled water is removed from reaction while volatile fatty acids are fed back into the **batch reactor** via a **biphasic separator (C).** Following completion of the reaction, the crude mixture is pumped into a **stripping vessel (D)** to distill away any volatile **unreacted fatty acid (E)**. **Additional fatty acid (F)** is blended in prior to **product collection (G).**

Figure 1.6: Industrial process for the continuous production of sodium cocoyl isethionate. Coconut derived fatty acids (10), sodium isethionate (12) and catalyst (14) are fed into reactor (16) and heated to 260°C. Upon completion, the product is diverted into a stripper (60) for purification before collection at vessel (96). Adapted from Holland et al. [16]

1.1.4. Process Optimisation of Traditional Soap Manufacture

Traditional soaps were extensively studied throughout the 20th century to determine the influence of process parameters on the phased behaviour of solid formulations. Fundamental studies have investigated the correlation between manufacturing conditions and molecular structure for a range of alkyl carboxylates including sodium soaps,[19, 20] potassium soaps [21, 22] and choline soaps.[23] This understanding of the principles of surfactant behaviour permits the manipulation of crystal structure within the soap to produce specific phase combinations with desirable performance characteristics.[24]

In traditional soaps, structure-performance models have been developed to link the surfactant formulation process to the user experience. Simple 'macro' models assess the impact of compositional changes on the hardness of a soap. A combination of temperature, alkyl chain length, unreacted fatty acid content and dissociated sodium levels together build an assessment of solid content from which properties can be predicted.[25] More complex models utilise changes in molecular structure as the soap is crystallised to model critical performance criteria such as texture, hardness and solubility. Upon crystallisation of a liquid melt, carboxylate soaps are reported to first exhibit a metastable solid phase. Unlike the stable crystalline phases of pure soap systems characterised by XRD, these transient phases exhibit poorer solubility and lathering due to their reduced structural order.[25, 26] Similar to macro models, manipulation of temperature, fatty acid content and chain length distribution are then used to predict key performance characteristics. Unlike the macro model, however, molecular models base these predictions on changes in phase, polymorphic form and crystallite size based on temperature and chemical composition of the surfactant mixture.

1.1.5. Challenges with Modern Synthetic Detergent Manufacture

Despite the widespread utilisation of sodium acyl isethionates in both solid and liquid personal care formulations,[27] there is a complete absence of analogous research into their chemistry, structure and properties. The patent literature cited in the previous sub-section demonstrates how the development of current isethionate ester manufacturing processes was conducted through successive cycles of iterative empirical improvement.[16-18] An absence of physicochemical understanding to support the isethionate manufacturing process has resulted in notable shortcomings in modern personal care formulation.

The rigidity of commercial operating windows has increased the challenges associated with acquiring surfactants within a desired performance specification. The formation of unknown impurities has been a frequently documented issue in the synthesis of synthetic detergents.[28] Previous patents had advised the addition of hydrogen peroxide to improve the colour of manufactured products.[29] However, the impurities can also produce unpleasant odours which bleaching alone cannot overcome. Several manufacturers including Unilever[30] and Colgate-Palmolive[31] have reported the issue of phase separation in the manufacture of syndet bars. Since the product inception in the 1960s, until as recently as 2009,[32] patents have been periodically published describing process modifications which seek to address the issue. Although the industrialists have proposed theories for the possible causes of phase separation, an absence of fundamental research into the melt crystallisation process means that all of these hypotheses are unconfirmed. The challenges associated with the production of isethionate esters within desirable performance specifications has reduced the number of companies capable of manufacturing a product within desirable specifications concerning product appearance, odour, performance and physical properties. Traditional soaps and other sulfate based surfactants are produced by numerous organisations as a commodity chemical. SCI as a standalone surfactant, however, is only reported available from Innospec, Clariant and Rhodia as of 2016.[33] The report further discusses how the composition of SCI, as well as the formulation of Dove, is relatively unchanged since their respective inceptions decades ago.

1.2. Research Question

Olsen's three-link chain model (Figure 1.7) proposes that an understanding of how process conditions, material structure, material properties and product performance successively influence each other '*encompass the central paradigm of materials science and engineering*'.[34] Thomas and Allen further confirm that the relationships between these four factors form the cornerstones of interdisciplinary materials research.[35] The first link specifically concerning structural characterisation was identified by both Olsen[34] and Thomas and Allen[35] as the most influential component in the development and optimisation of materials technologies.

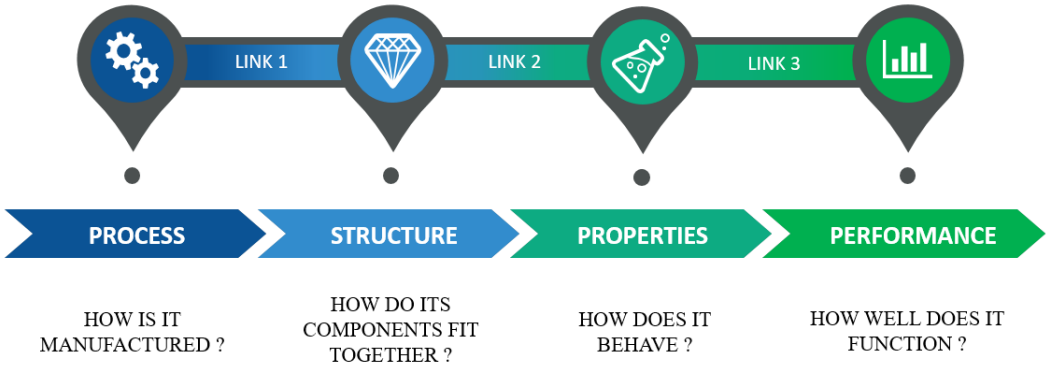

Figure 1.7: Olsen's three link chain model for the design of performance-focused materials from fundamental scientific principles. Created using information from Olsen.[34]

The process optimisation models of traditional soaps (in the previous section) were derived from a knowledge of how process conditions influence structure, as well as how structure then successively influences performance-critical product properties. When compared with the iterative processes of incremental, empirical improvement used for the current process optimisation of isethionate esters, they demonstrate how syndet based products and processes could be designed with desirable performance characteristics, directly from fundamental scientific principles. It is therefore proposed that a similar understanding of surfactant behaviour in isethionate esters could be used to help address some of the manufacturing issues associated with acquiring syndet products within marketable specifications. To begin this process, the specific aim of this project is to address the crucial first link in the holistic materials characterisation of isethionate esters:

"How do process parameters influence structure, phase behaviour and crystallisation in the manufacture of isethionate ester surfactants?"

1.3. Research Objectives

1) Synthesise and purify a model surfactant to represent SCI at the laboratory scale.

   Sodium cocoyl isethionate (SCI) is commercially synthesised from hydrogenated coconut oil to produce a blend of surfactants of varying chain length.[36] Since the pure constituent isethionate esters are not commercially available, a compositional

analysis will be performed to identify the most abundant species in the commercial surfactant system. A synthesis and purification procedure will then be designed to provide a means for obtaining a sufficiently pure and reproducible surfactant species upon which a fundamental materials characterisation study can be based.

2) Conduct a holistic physicochemical characterisation of the model surfactant system.

   Due to the absence of fundamental literature on isethionate ester surfactants, a physicochemical characterisation will be conducted to confirm the identity of the model surfactant, whilst also providing an understanding of key physical properties prior to further analysis. Information specifically related to the thermal stability of the surfactant will help identify whether any manufacturing issues are thermally induced, whilst simultaneously providing operating windows in which *in-situ* structural studies could be conducted.

3) Obtain an atomistic crystal structure of the model surfactant system.

   In-depth structural analyses have been identified as the key to understanding the behaviour of functional materials. Prior to an *in-situ* analysis of surfactant structure under commercial manufacturing conditions, the atomistic crystal structure will be used to obtain an assessment of the most stable structure under ambient conditions. A quantitative synthonic and energetic analysis will be conducted to help identify and understand why the surfactant has manifested itself in the observed structural form. The assessment will also provide a benchmark for the ideal isethionate surfactant structure, whilst assisting the characterisation of non-ideal, transient structures observed in subsequent dynamic studies.

4) Perform an *in-situ* dynamic, structural analysis of the model surfactant system under commercial manufacturing conditions.

   Given the rich and varied phase behaviour identified through existing structure-performance studies of traditional soaps, an *in-situ* structural analysis will be executed over the commercial operating range to observe how the structure of the model detergent changes with temperature. The structural information from this study is anticipated to develop the aforementioned link between process and structure, on which future structure-performance models of isethionate ester surfactants are expected to be based.

1.4. Project Management

The project was primarily supervised by Dr David Harbottle and co-supervised by Professor Kevin Roberts at the School of Chemical and Process Engineering at the University of Leeds. Professor Michael Rappolt, of the School of Food Science and Nutrition at the University of Leeds, was also a member of the supervisory team and was consulted for guidance on X-ray scattering techniques. Dr Ian McRobbie of Innospec Ltd was an external supervisor providing both industrial and technical expertise with respect to soap manufacturing processes. The project was funded both by Innospec and the EPRSC, through the Centre for Doctoral Training in Complex Particulate Products and Processes.

1.5. Report Structure

The next chapter consists of an overview of the fundamental science underpinning much of the surfactant crystallisation process research. The following chapter provides a background on the key experimental and computational techniques utilised in this study. The four succeeding chapters then address each of the four research objectives in respective succession. Due to the absence of a common scientific methodology between results chapters, a dedicated introduction, review of relevant literature and experimental section is provided with each individual chapter. The thesis concludes with a summary of findings from the project, their significance to the proposed research question, as well as propositions for further work based on current observations. A schematic illustrating a route map through which the thesis will progress is provided in Figure 1.8.

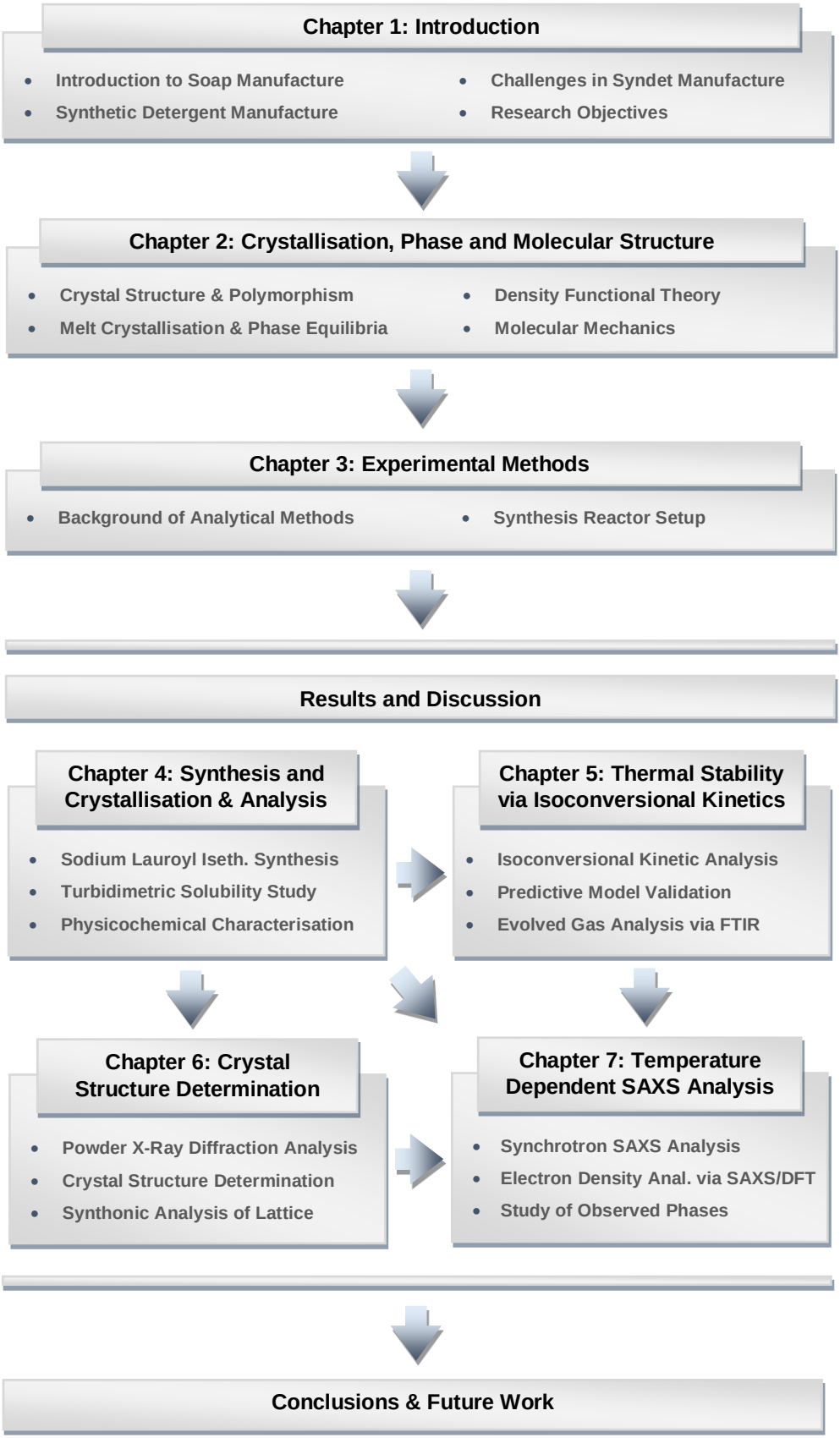

Figure 1.8: Schematic depicting a route map of the thesis chapter structure.

Chapter 2: Crystallisation, Phase and Molecular Structure

Synopsis: *This chapter begins by reviewing the structural forms in which a crystalline species can exist within the solid state. An overview of polymorphism then discusses how thermodynamics influence the solid state structure by which a crystal is formed. The succeeding overview of melt crystallisation compares the methods by which solid surfactants can be isolated from a liquid melt, whilst providing the terms and concepts by which multi-phasic systems can be characterised. The chapter is concluded with a brief introduction to the molecular modelling techniques utilised in this study.*

2.1. Crystal Structure

Solid, liquid and gas are three of the four major states of matter in which a material can exist. A 'crystal' is any solid species whose atoms, or molecules, are arranged in a regular pattern which extends in three dimensions.[37] Often, the repeating atoms or molecules are replaced by hypothetical 'lattice points' with each point existing in identical surroundings in space. The term 'unit cell' is then used to describe the smallest group of atoms from which a systematic three dimensional 'lattice' can be constructed, without loss of translational symmetry. Any unit cell can be characterised by three spatial dimensions (a, b and c) and three angular dimensions (α, β and γ).[38] These principles are illustrated in Figure 2.1.[39]

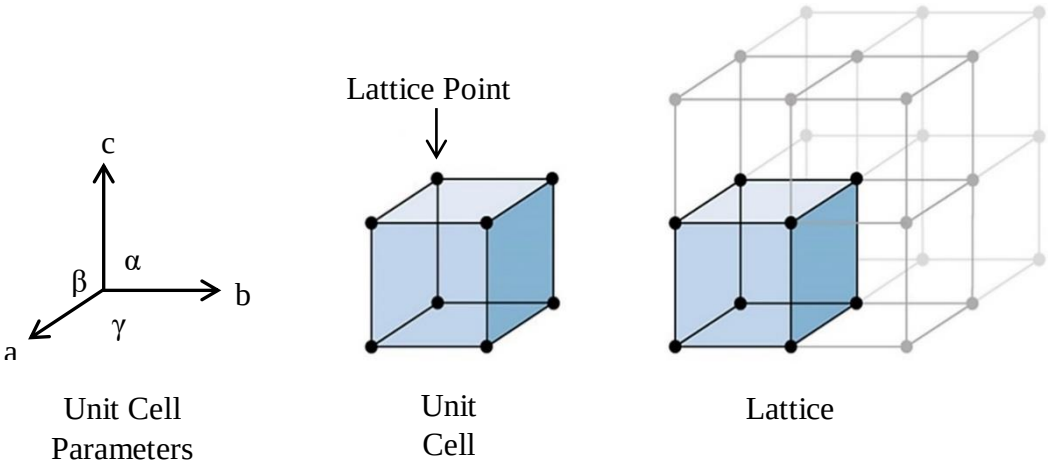

Figure 2.1: Diagram of the nomenclature and dimensions used to characterise crystalline solid structures. Angle α is designated to lie opposite vector a, etc. Unit cells are allocated such that a ≤ b and that all angles are as close to 90° as possible.[39]

Unit cells can be classified into one of seven crystal systems, the categorisation of which is dependent on the unit cell parameters and the minimal rotation symmetry exhibited by the resulting structure.[37] (See Table 2.1)

Table 2.1: Seven crystal systems classified of unit cell and essential rotational symmetry. Table created using Mullin.[38]

Crystal System	**Unit Cell Parameters**	**Essential Symmetry**
Triclinic	None	None
Monoclinic	$\alpha = \gamma = 90°$	1 x two-fold rotation
Orthorhombic	$\alpha = \beta = \gamma = 90°$	3 x two-fold rotation
Tetragonal	$a = b$; $\alpha = \beta = \gamma = 90°$	1 x four-fold rotation
Rhombohedral	$a = b = c$; $\alpha = \beta = \gamma \neq 90°$	1 x three-fold rotation
Hexagonal	$a = b$; $\alpha = \beta = 90°$; $\gamma = 120°$	1 x six-fold rotation
Cubic	$a = b = c$; $\alpha = \beta = \gamma = 90°$	4 x three-fold rotation

In order to maintain angles as close to 90° as possible, thus maximising symmetry exhibited by the unit cell, additional lattice points can be incorporated into the face, body or base of the structure. Bravais therefore expanded the seven crystal system into 14 fundamental 'Bravais' lattices structures.[40] (See Figure 2.2).

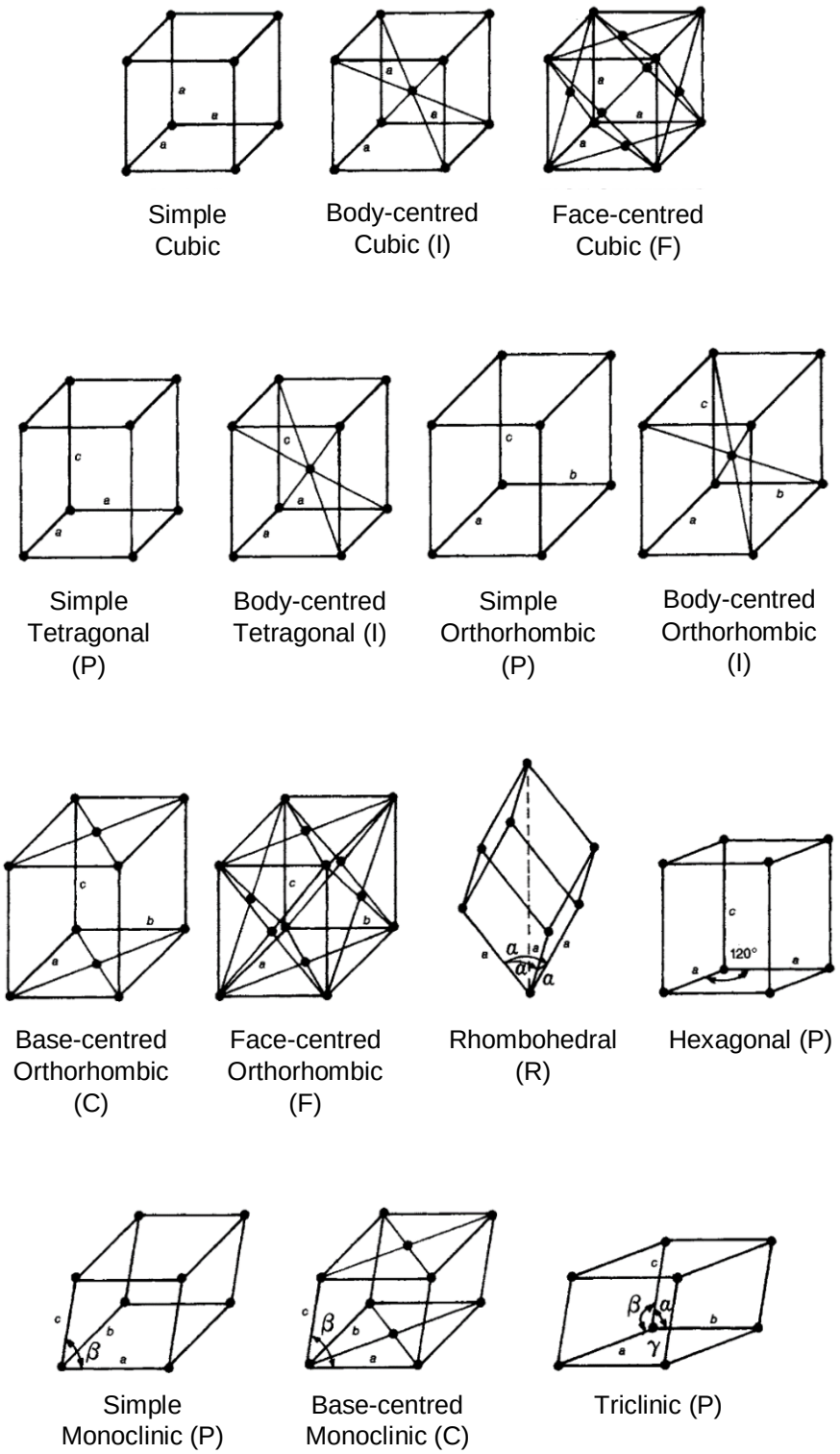

Figure 2.2. 14 Fundamental Bravais lattices. P = Primitive (no additional lattice points), F = face centred, I = body centred, C = base centred and R = rhombohedral structures. Adapted from Myerson.[37]

Within the 14 lattices, there are 32 point groups through which the lattice points can be rotated and reflected whilst maintaining structure. These symmetries influence the optical properties inherent to the crystal.[41] Translation within the unit cell, in combination with rotations and reflections, results in the screw axis and glide plane symmetries. Screw axes combine rotational and translational motion while glide planes integrate both reflection and translation. These additional symmetries, when combined with the 32 point groups, result in a total of 230 space groups which encompass all possible crystallographic symmetries.[41]

2.2. Miller Indices

The two dimensional planes intersecting a crystal lattice can be described in terms of the degree to which they intercept the three crystallographic axes introduced in Figure 2.1.[38] The plane is numerically represented by three integers (*hkl*), with reciprocal values assigned according to the frequency of interception in the a, b and c axes.

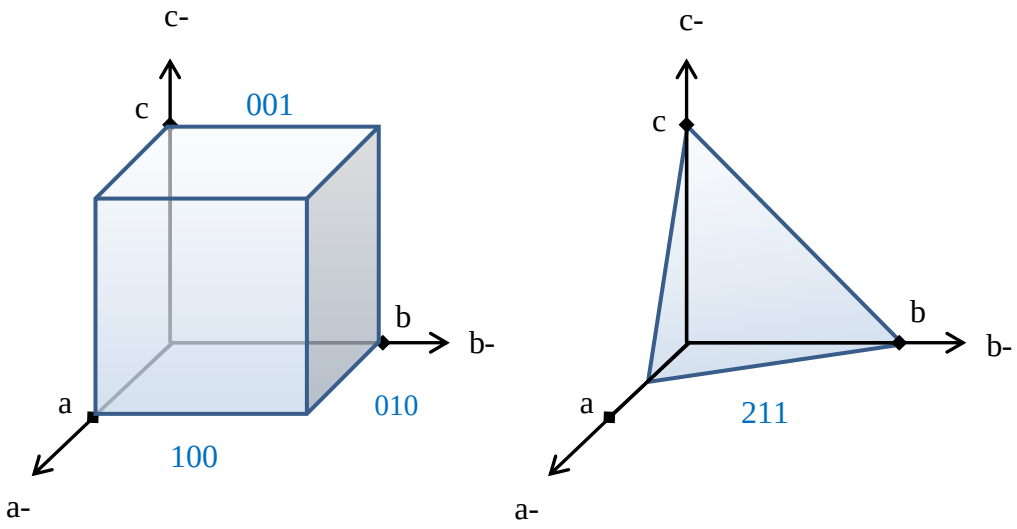

Figure 2.3: Examples of 2D planes and their corresponding Miller indices. Each integer in the index corresponds to one of the crystallographic axes. Its value pertains to the reciprocal of the intersection point. The 211 plane (right), for example, intersects the unit cell at 0.5 (a-axis), 1.0 (b-axis) and 1.0 (c-axis). Created using information from Tiley.[41]

As expected, planes parallel to any given axis result in a value of zero with respect to the corresponding integer. Because the faces on a crystal lie parallel to the crystallographic lattice planes, they are also characterised through the Miller Index system. Figure 2.3 displays examples of both parallel and intersecting 2D planes characterised by the Miller index notation.[41] In addition to the identification of crystallographic faces, 2D planes and the systematic spacing between them is also used to determine the unit cell parameters via the diffraction of X-ray radiation from the lattice structure.[39]

2.3. Polymorphism

Substances of identical chemical composition with a varying spatial arrangement of molecules are deemed to exhibit 'polymorphism'.[42] The term typically refers to a change in the molecular arrangement within the crystalline lattice, however, the phenomenon could also arise from a variation in molecular conformation.[38] While the chemical properties of polymorphs are identical, there is often a variation in the observable physical behaviour. Measurable changes in properties resulting from polymorphic changes including melting point, density, optical activity, heat capacity and thermal conductivity.[37] A common example of polymorphism influencing performance is that of the antiviral drug Ritonavir, where an unexpected change in crystal structure resulted in a significant reduction in solubility and bioavailability when compared with the desired polymorphic form.[43] Polymorphic selectivity can be achieved through the temperature, pressure and the solvent environment in which the crystal is obtained. The solvent can additionally incorporate itself into the lattice structure of the crystallising lattice where the resulting polymorph is referred to as a 'solvate' (or a 'hydrate' if the crystallising medium is water).[42]

The process parameters dictating the structural form of a crystalline lattice, often require precise control to obtain the desired polymorph. Because polymorphs can readily transform from one to another through modification of process parameters, some additional control of parameters is required to ensure an undesired transition does not occur once the desired polymorph has been isolated. 'Ostwald's Step Rule' dictates that "the state which is initially obtained is not the most stable state but the least stable state that is closest to the original in terms of free energy change."[37] According to Ostwald, the solid form which a crystal lattice first adopts, is likely to be an 'metastable' state after which a more stable polymorph form will be adopted.

Thermodynamically driven processes, such as crystallisation, can be driven by enthalpy ($\Delta H < 0$) or entropy ($\Delta S > 0$).[44] The unifying balance between these driving forces quantifying the spontaneity of a given thermodynamic process, at a given temperature (T), is known as the Gibbs free energy (ΔG). Figure 2.4 shows how polymorphic stability is consequently thermodynamically dependent on the Gibbs free energy, which itself is dependent on enthalpy, entropy and temperature.[44]

While less stable forms exist initially due to favourable kinetics, the most stable polymorphs exhibit the lowest free energy. Less stable forms of a chemical species are therefore energetically driven to form most stable structures. Such transitions are, however, can be subject to kinetic barriers. A highly kinetic induction can also result in the formation of a non-crystalline or 'amorphous' phase prior to the observation of a stable crystalline phase. This phenomenon is most prevalent in molecules of high molecular weight with a predominantly organic structure.[38]

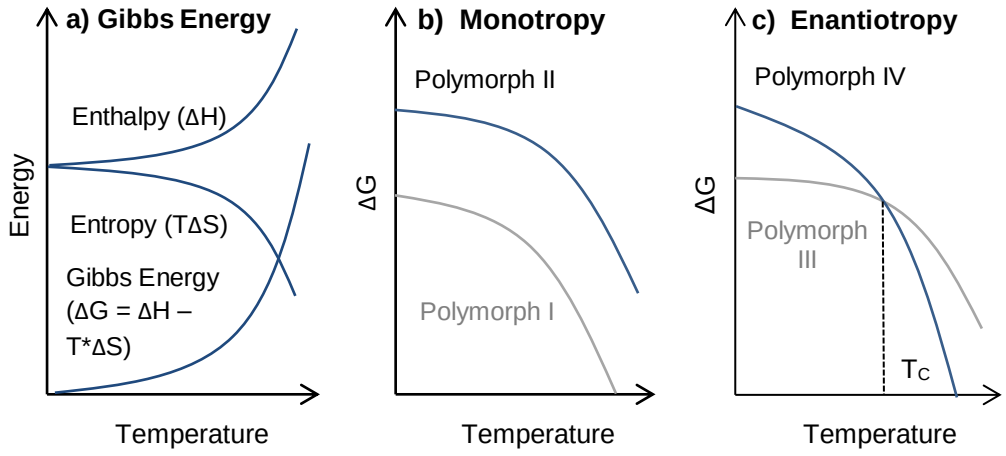

Figure 2.4: Comparison of temperature dependent enantiomeric and monotropic crystal systems. a) Temperature dependence of change in Gibbs free energy (ΔG), enthalpy (ΔH) and entropy (ΔS) for a given transformation. b) Monomeric Polymorphs I and II. c) Enantiomeric Polymorphs III and IV. Polymorph I consistently maintains a lower Gibbs free energy than II and remains the most stable form across the given temperature range; the system is therefore considered monotropic. Polymorph III (c) is the most stable structure prior to Tc. Beyond this temperature, however, Polymorph IV displays the lower Gibbs energy thus making it the more stable polymorph. This transition in (c) is indicative of enantiomeric crystal. Created using Beckmann.[42]

The absolute stability of a particular polymorph is governed by the extent of attractive intermolecular interactions such as van der Waal's, electrostatic and hydrogen bonding. More stable polymorphs with a higher degree of intermolecular interactions expectedly exhibit a higher melting point than their less stable counterparts. In cases where the most stable polymorph is unaffected by temperature, the corresponding species is deemed to be 'monotropic'. Other species can display a temperature dependent shift in the polymorph which exhibits the highest stability. Such species are described as being 'enantiotropic'.

2.4. Melt Crystallisation

'Melt' is a term most accurately used to describe a pure molten solid.[42] In crystallisation, however, the term is more commonly utilised to refer to any homogeneous mixtures of liquids that typically assume the solid form at ambient pressure and temperature.[38] Where crystalline solids exhibit long range order in the form of a lattice structure, the corresponding liquids only display short range order. The complementary increase in entropy minimises the free energy of the melt phase allowing it to take precedence over the crystal phase beyond the melting point of the crystalline system.[45]

Like the solution crystallisation process, melt crystallization is a method of separating and purifying substances via the selective solidification of a desired species, from a liquid mixture of compounds. In a binary mixture, the resulting phases in a melt crystallisation are determined by the temperature of the system and the relative concentrations of the two species, as is the case with a solution crystallisation.[37] In addition to the dominant phase at room temperature, Ulrich proposed that the distinction between the two crystallisation processes arises from the underlying mechanism of phase separation. In solution, the crystallisation is dictated by the mass transfer of the solvating species. However, if the transition is limited by heat transfer then the process can be considered a melt crystallisation.[46] The dominating mechanism is alleged to influence the rate of crystal growth, with melt processes typically exhibiting faster growth rates (~10^{-5} m/s) than that of solvent mediated crystallisations (10^{-7} - 10^{-9} m/s).[46] Assuming equivalent rates of nucleation, higher relative rates of crystal growth would lead to larger crystals.

2.5. Solid Layer and Suspension Melt Crystallisation

Melt crystallisations can be categorised into one of two types of process: solid layer melt crystallisation and suspension melt crystallisation.[47] A solid layer crystallisation (or progressive freezing process) crystallises a liquid melt perpendicular to cooled surface. The process can be executed in batch or continuous flow depending on whether the liquid melt is static or dynamic. Solidification is induced by temperature differential between the liquid melt and the cool solid surface with which it maintains contact.[48] Suspension crystallisation relies on the nucleation of solid suspended crystals in a cooling liquid melt. The driving force for crystal growth in this instance is the temperature differential between the surface of the solid crystal and liquid phase.[46]

Cooling of a melt can sometimes be assisted with solvent evaporation or addition of refrigerant to increase rate of nucleation. As with solution crystallisation, the process is typically executed in an agitated batch vessel. The driven agitator often extends to the wall of the reactor to limit the build-up of solid material, thus improving heat transfer into the vessel.[42] Some key distinctions between two melt crystallisation techniques are outlined in Table 2.2.

*Table 2.2: Comparison of solid layer and suspension melt crystallisation techniques. Based on a typical industrial process, as described by Ulrich et al.[48]. *Tc = Pure melting temperature. § = % of initial mass.*

Crystallisation Parameter	**Solid Layer Melt Cryst.**	**Suspension Melt Cryst.**
Temperature	Above Tc*	Below Tc*
Heat transfer medium	Crystalline layer	Liquid melt
Growth rate	Fast (10^{-5} - 10^{-7} m/s)	Fast (10^{-7} - 10^{-8} m/s)
Crystallising area	10-100 m^2 per m^3	~1000 m^2 per m^3
Solid crystallising mass	50-75% §	30-40% §
Transported material	Liquid only	Solid – liquid suspensions
Transport apparatus	Pumps only	Agitated batch crystalliser
Product separation	Easy (draining)	Filtration or centrifugation

Suspension crystallisation exhibits close to isothermal conditions since the heat of fusion resulting from the crystallisation is absorbed by the melt.[48] The consequently slow rate of crystal growth, coupled with a larger surface area on which crystallisation can be executed, allows for purity in excess of 99% to be achieved.[46] As the crude product is a solid-liquid slurry, however, the technique is limited by the additional unit operations required to transport and purify the multi-phase product. The viscosity and settling velocities must be taken into consideration when designing a process to avoid complications with a build-up of solid material.[42]

2.6. Phase Equilibria

A 'phase diagram' is a visual representation of the chemical species existing within a system at thermodynamic equilibrium. In a melt crystallisation process, it provides quantitative information regarding the degree of separation attainable through the manipulation of thermodynamic parameters such a pressure (p) and temperature (T).[49] Although enthalpy and entropy are also examples of intensive thermodynamic variables; p and T are often selected in preference due to the simplicity with which they can be experimentally controlled and measured.[50]

The term 'phase' is used to describe any homogeneous region of a phase diagram, with the term 'heterogeneous' referring to any region consisting or two or more phases in simultaneous equilibrium.[50] Liquids completely miscible in each other are considered to be of a single phase under this nomenclature. The 'components' of a system are the fundamental independent species required to characterise the chemical composition of all phases within a given phase diagram.[38]

2.7. The Phase Rule

Between the years of 1874 and 1878, Willard Gibbs published his proposition of the 'phase rule' upon which the fundamentals of phase equilibria have been formed.[51]

$$F = C - P + 2$$

Figure 2.5. Phase rule for chemical species within a heterogeneous system. F = Number of degrees of freedoms (independent thermodynamic variables), C = number of fundamental chemical components, P = total number of phases at equilibrium. Theory is applicable to any chemical system consisting or two or more phases at equilibrium. First proposed by J. W. Gibbs.[51]

Figure 2.5 states that the largest number of independent thermodynamic parameters that can be varied whilst preserving the total number of phases existing at equilibrium is determined by the number of chemical components and the total number of phases within a given system as shown. While a full thermodynamic justification of the theory is included in the original research,[51] a more accessible summary is available from Atkins *et al*. [44] The phase rule can be illustrated using the classical pressure-temperature phase diagram of pure water. A schematic is depicted in Figure 2.6.

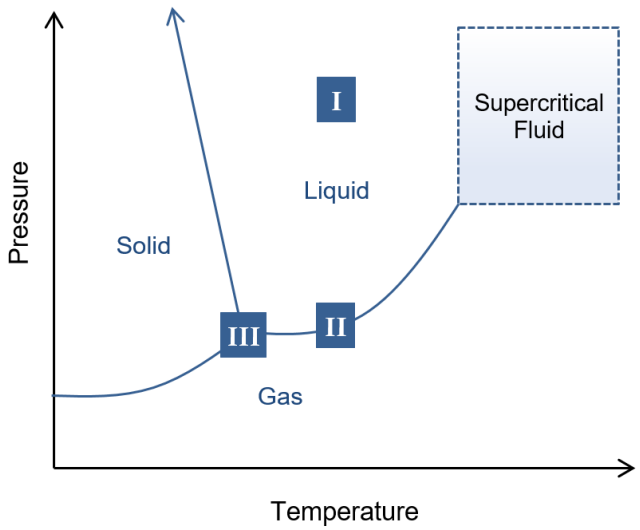

Figure 2.6. Schematic of a single-component pressure-temperature phase diagram of pure water. Regions where one, two and three phases exist in equilibrium are represented by the labels I, II and III respectively. Concepts concerning the phase rule are explained in the adjoining text. Diagram created using information from Adkins.[50]

At point I (Figure 2.6), a single homogeneous liquid phase exists at equilibrium. According to the Gibbs' phase rule, two thermodynamic parameters (both p and T) may be changed independent without affecting the total number of phases in the system. If the conditions are altered such that both liquid and gaseous water exist at equilibrium (point II, Figure 2.6), then the rule states that only one independent variable may be changed to retain both phases at equilibrium. At equilibrium, a change in temperature, for example, would necessitate a change in pressure to preserve both phases, thus indicating that the variables are no longer independent. Where three phases exist in equilibrium (point III, Figure 2.6), no change in thermodynamic parameters would permit the preservation of all three phases. Such conditions are considered to exhibit zero degrees of thermodynamic freedom.

2.8. Molecular Modelling Methods

A brief, accessible introduction to the molecular modelling techniques used in this study are provided in the following section. The sub-sections on quantum mechanical theory, Hartree-Fock theory and density functional theory were written using texts from Koch and Holthausen,[52] Hanson *et. al.*,[53] Baseden and Tye,[54] Thijssen,[55] and Atkins and Friedman.[56] Whilst key studies have been cited where relevant, the final two texts can be consulted in addition to the original sources for a more in-depth, mathematical description of the corresponding phenomena.

2.8.1. The Schrödinger Equation

In theoretical physics, the state of a quantum mechanical system at any spatial position can be described by the time-independent Schrödinger equation[57] and the corresponding wavefunction (ψ). Its general form is provided below:

$$\hat{H}\psi = E\psi \qquad (1)$$

The Hamiltonian operator ($\hat{H}$) can take on various forms depending on the type of the system being characterised and the number of dimensions under consideration. If the wavefunction (ψ) is iterated until the energy (E) is minimised, then the resulting wavefunction corresponds to the ground state on the corresponding system and in the case of a molecule, the state in which it is most likely to exist.

2.8.2. The Born-Oppenheimer Approximation

In a molecular system consisting of nuclei and electronic components, the electrons and nuclei experience a mutual attractive force due to their opposing charges. The mass of a nucleus is over 1000x higher than that of an electron and its acceleration as a result of these forces is consequently significantly lower ($F = ma$). The Born-Oppenheimer approximation[58] therefore postulates that while the electronic wavefunction is dependent on the position of a nucleus, nuclear motion can be negated when describing the electronic states in a molecular system.

Using the Born-Oppenheimer approximation to parameterise the terms corresponding to nucleus-nucleus interactions, the Hamiltonian operator encompassing a molecular system consisting of nuclei and electrons can be written as follows, where $\hat{T}$ is the kinetic energy of the nucleus and $\hat{V}_{ne} + \hat{V}_{ee}$ are the respective potentials corresponding to nuclear-electron and electron-electron interactions.

$$\hat{H}_{elec}\psi_{elec} = \hat{T} + \hat{V}_{ne} + \hat{V}_{ee} \tag{2}$$

The operator $\hat{H}_{elec}$ can be used to determine to determine E_{Elec} through ψ_{elec} using the Schrödinger equation. As E_{Nuc} has now been parameterised into constants through the Born-Oppenheimer approximation, the total energy of a molecular system can be described as follows.

$$E_{Tot} = E_{Elec} + E_{Nuc} \tag{3}$$

The focus is consequently now on finding a solution for the electronic portion of the equation. In a system consisting of more than one electron, the electron-electron interaction term in Eq. (2) is simultaneously dependent on the co-ordinates of all electrons. The impossibility in obtaining a wavefunction to characterise this many-body system precludes an exact solution of the Schrödinger equation.

2.8.3. The Hartree-Fock Method

One way to address the many-body issue is to separate the multi-body wavefunctions of electrons into a product of single electron wavefunctions as follows:

$$\psi(x_1, x_2, .. x_n) = \psi_1(x_1), \psi_2(x_2), .. \psi_n(x_n) \quad (4)$$

In this form, the Hartree-Fock (HF) approximation[59, 60] assumes that electrons are uncorrelated so that the many-electron wavefunction can be expressed as the matrix displayed in Eq. (5). Known as the Slater determinant,[61] ψ_x corresponds to the wavefunction of a specific electron while its corresponding variable *x* contains the spatial and spin co-ordinates of the respective electron.

$$\psi_{HF}(x_1, x_2, .. x_n) = \frac{1}{\sqrt{n!}} \begin{vmatrix} \psi_1(x_1) & \psi_2(x_1) & \cdots & \psi_n(x_1) \\ \psi_1(x_2) & \psi_2(x_2) & \cdots & \psi_n(x_2) \\ \vdots & \vdots & \ddots & \vdots \\ \psi_1(x_n) & \psi_2(x_n) & \cdots & \psi_n(x_n) \end{vmatrix} \quad (5)$$

In the HF method, the electron-electron interaction term ($\hat{V}_{ee}$ in Eq. (2)) is replaced by the Hartree Potential. The term proposes that the interaction between individual electrons can be approximated by the Coulomb potential of the system (U_r), where each electron interacts with the average electrostatic field resulting from all other electrons in the system. This potential can be calculated from the electronic charge distribution of the system using the Hartree equations.[62]

An exchange interaction in the HF method accounts for the Pauli Exclusion Principle,[63] which states that two or more electrons cannot simultaneously occupy the same quantum state. However, the Hartree-Fock method does not account for the mutual coulombic repulsion between electrons resulting from electrons of parallel spin, or its correlated influence on electronic motion. The exchange interaction also exhibits a slow decay with respect to distance which significantly increases computational cost when many-bodied systems are considered.

2.8.4. Density Functional Theory

In 1927, Thomas [64] and Fermi [65] demonstrated how the difficulties associated with electronic wavefunction, Slater determinant and most importantly, correlation terms, can be overcome by using a holistic representation of electron density to describe a many-electron system. Progressive approximations, most notably by Hohnberg, Kohn

and Sham,[66, 67] ultimately led to the inception of modern Density Functional Theory (DFT) where:

> *(Function):* Uses a number as an input to produce a number as an output.
> *[Functional]:* Uses a function as an input to produce a number as an output.
> *[Density functional]:* Uses the electron density, which itself is function of position co-ordinate (r) to output the energy of a molecular system.

Hohnberg, Kohn and Sham proposed that the total electronic energy and other physical characteristics of a many-electron system can be calculated in terms of the electron density $n(r)$ using a single functional $E_{Tot}[n(r)]$. The individual energy terms, which constitute the universal functional, are displayed in Eq. (6). Positive terms are coloured *green* while negative terms are coloured *red*.

$$E_{Tot}[n(r)] = E_T[n(r)] + E_v[n(r)] + E_J[n(r)] + E_X[n(r)] + E_C[n(r)] \quad (6)$$

$E_{Tot}[n(r)]$	$E_T[n(r)]$	$E_v[n(r)]$	$E_J[n(r)]$	$E_X[n(r)]$	$E_C[n(r)]$
Total Energy Electronic	**Kinetic E.** Electronic	**Potential E.** Elec-Nuc Attraction	**Potential E.** Elec-Elec Repulsion	**Exchange E.** Electronic	**Correlation E.** Electronic

While its intended purpose from HF theory is unchanged, the E_X exchange term in DFT does not correspond directly with the exchange interaction in the Hartree-Fock method. E_C is also a new term to account for the repulsive correlative motion exhibited by electrons in a parallel spin state. This phenomenon was unaccounted for in previous Hartree-Fock approximations. Both E_X and E_C were introduced to supplement the repulsive electron-electron energies quantified through E_J.

In Eq. (6), E_T (kinetic energy of an electron) and E_V (potential energy between an electron and nucleus) can be obtained directly from algebraic expressions.[55] To evaluate E_J, the Hartree-Potential can be integrated with respect to the electron density in the system $[n(r)]$. The remaining exchange (E_X) and correlation (E_C) functionals are approximated using single exchange-correlation functionals (E_{XC}) to provide a representative combination of the local potential corresponding to each electron. Whilst the term functional has been defined in a

general sense, many texts and computer programs also use the term *functional* to specifically to refer to the exchange-correlation functional $[E_{XC}]$. The development and refinement of approximations for $[E_{XC}]$ is a vast and expanding field of research, with the suitability of various options being dependent on the chemistry of the molecular system in question. The B3LYP[68] functional uses 3 parameters to combine the Hartree-Fock exchange functional with the existing LYP correlation functional to quantify dynamic electron correlation. With over 80000 citations on the aforementioned paper, B3LYP is reportedly a popular functional with applications pertaining to a range of organic systems.[69]

With the Hamiltonian energy expression ($\widehat{H}_{elec}$) now addressed through DFT, the electronic wavefunction (ψ_{elec}) defining the spatial co-ordinates and states of a system can be represented by molecular orbitals. A simple example is a single Gaussian Type Orbital (GTO), which can be represented by an integrable algebraic function. In practice, most modern computational programmes integrate linear combinations of orbitals with additional polarisation functions to provide a more representative spatial characterisation of the electron shells in a molecular system. The set of functions used to generate these molecular orbitals are known as *basis sets.* Like the exchange-correlation functional described previously, the suitability of a specific *basis set* is often dependent on the molecular system under analysis. A popular example is Pople's[70] 6-31G basis set where the core orbital consists of 6 contracted GTOs, while the valence orbital is represented by one contracted set of three GTOs, augmented by a final single GTO.

In the energy optimisation of a chemical system, a user-generated molecular model of the system is used to define an initial representation of the electron density. Typically, the Hartree-Potential and the electron density $[n(r)]$ are interdependent where knowledge of one is required to define the other. With algebraic expressions available for both, the two phenomena can be iterated through to minimise the global energy, thus producing an electronic representation of the desired molecular system in the ground state.

2.8.5. Molecular Mechanics

The Hartree-Fock method and DFT use the Schrödinger equation and quantum mechanical theory as the fundamental basis for modelling molecular systems.

Molecular mechanics conversely use classical mechanics to achieve the same goal.[69] While quantum mechanical theory states that electronic charge is not localised to specific atoms, molecular mechanics functions under the approximation that each atom is a particle with a designated radius and atomic charge.[71] Molecules are then considered to be individual atoms linked through mechanical springs at a distance equivalent to the equilibrium bond length.[72] Early examples by Kettering *et al.* apply the approximations to chemical systems,[73] with later studies developing computational methods to minimise the energy of a molecular system based on bond characteristics and non-bonding interactions.[74]

The total energy of the molecular system is calculated in terms of these bonded covalent interactions (*blue*) and non-covalent interactions (*orange*) as shown in Eq. (7). The labels below each term correspond to the key physical characteristic determining the respective energy.

$$E_{Total} = E_{Bond} + E_{Bending} + E_{Torsion} + E_{vDW} + E_{Coulombic} \quad (7)$$

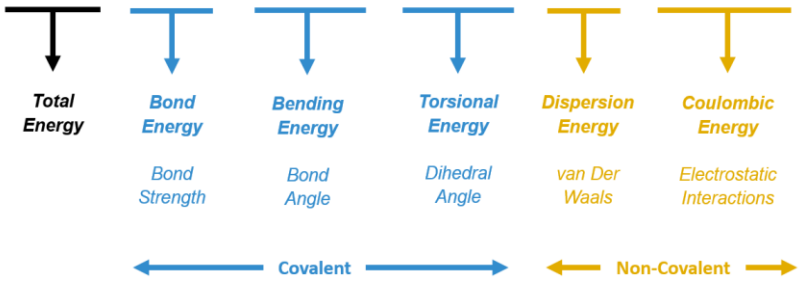

In molecular mechanics, the term *forcefield* is typically used to refer to the set of functions used to calculate the total energy of the system.[69] As with *basis sets* and *functionals* in DFT, forcefield selection is dependent on the specific system under consideration. Both DFT and molecular mechanics are extremely useful for the characterisation of organic materials, with computational energy minimisations being utilised to assist in the prediction of crystal structures,[75] visualisation of particle morphologies[76] and detailed energetic characterisation of crystalline phases.[77]

Chapter 3: Experimental Background

Synopsis: *This chapter contains the background science pertaining to the experimental methods utilised in the succeeding results sections. The specific experimental details and mathematical methods pertaining to each study are provided in the corresponding sub-section of the relevant results chapter.*

3.1. Gas Chromatography

Given the general trends of increased boiling temperature within the homologous series' of long chain lipids, gas chromatography is useful for distinguishing between fatty acids of varying alkyl chain length.[78] In gas chromatography, a mixture of analytes in solution is transported through a coated capillary 'column' by an inert carrier gas (H_2, He or N_2).[79, 80] Liquid samples are typically injected into a heated chamber in which they rapidly vaporise. The gaseous samples are then propelled through the capillary by means of the carrier gas. Separation of analytes can be achieved by manipulating varying degrees of chemical interaction with the column, as well as differences in vaporisation temperatures within the mixture of analytes.[81] Following separation, the end of the column is connected to a range of detector types in order to detect and quantify species of interest.[79] In this study, the hydrolysed coconut oil commonly used to synthesise SCI was separated to identify and quantify its constituents using a combined gas chromatography-mass spectrometer (GC-MS) instrument.[82] A schematic is provided in Figure 3.1.

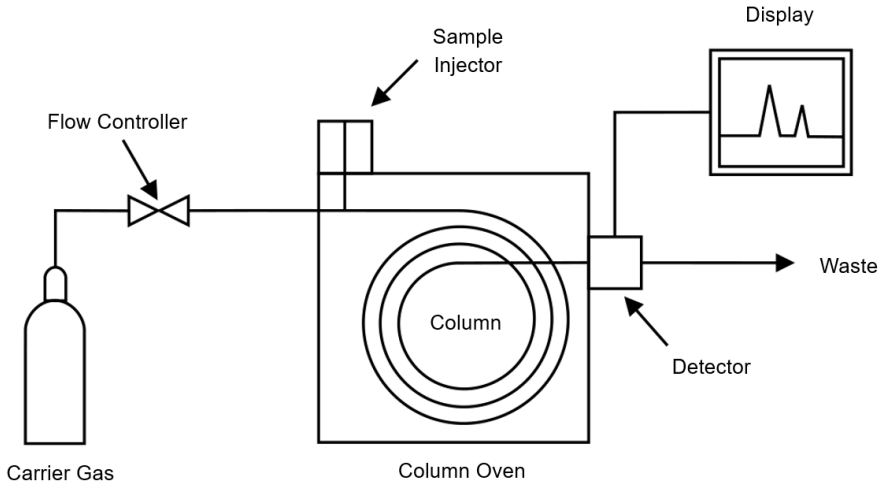

Figure 3.1. Schematic of a simple gas chromatography instrument. Edited using Harris et al.[80]

Previous chromatographic analyses of fatty acids indicate that the carboxylic acid functional group can adsorb onto a variety of Gas Chromatography (GC) columns,[83] resulting in peak tailing and long retention times.[84] While researchers have produced high resolution

chromatograms of free fatty acids through the use of selectively acidified polyethylene glycol stationary phases,[85] the standard AOCS method of fatty acid analysis recommends methylation with GC-MS analysis of the corresponding fatty acid methyl esters (FAMEs).[86]

3.2. Surfactant Synthesis Reactor Development

The chemical synthesis of sodium lauroyl isethionate (SLI) via the zinc catalysed esterification of lauric acid (LA) and sodium isethionate (SI) is depicted in Figure 3.2.

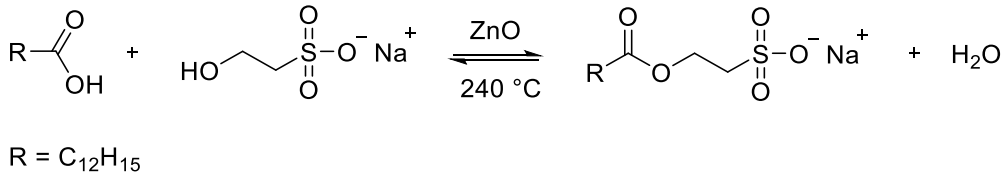

Figure 3.2: Esterification of lauric acid with sodium isethionate to form sodium lauroyl isethionate. Reaction is commercially executed with a blend of linear, saturated fatty acids between C8 and C18.[7]

The laboratory scale process used to synthesise isethionate esters in this project has been derived from the continuous industrial synthesis of SCI, patented by Unilever in 1969.[16] A description of the manufacturing process together with a schematic of the corresponding reactor is provided in Section 1.1.3, Figure 1.6. Both the water vapour and distilled fatty acids are typically evolved from the reaction once the mixture is heated.[87] An organic-aqueous separator was therefore implemented in the industrial synthesis of SCI to allow removal of both the water of reagent dilution and the water of reaction (Figure 1.6, Part C). The chemical reaction is in dynamic equilibrium so any water present in the system must be removed to maintain a thermodynamic driving force in favour of the desired product (Figure 3.2).[7] In the industrial process, volatile fatty acids are conversely recycled back into the reactor following distillation to maximise the conversion of sodium isethionate.[87] When the commercial blend of surfactants were manufactured, the recycle ensured that the lipid composition of the product matches that of the starting material.[36] In the laboratory scale system, this separation was achieved using a Dean-Stark (DS) receiver where the position of the organic-aqueous interface, was regulated via a stopcock. Lauric acid has a low density

relative to the aqueous phase,[78] which makes the DS apparatus ideal for simulating the industrial recirculation.

Cahn *et al.* have reported that the SCI reaction mass is highly prone to oxidation in the presence of air.[87] The resulting impurities influence both the whiteness and odour of the crude product. An inert atmosphere was therefore created in the laboratory reactor via a constant stream of nitrogen bubbled directly into the reaction mixture. The reagents were also purged with nitrogen before the reaction was heated to further minimise product degradation.

During the post-reaction fatty acid distillation, Walele *et al.*[36] recommended that the pressure be reduced incrementally from approximately 800 mbar to 50 mbar, but guidance was not provided on how this is best achieved. During trial laboratory scale reactions, it was observed that excessive reduction of pressure did indeed result in severe foaming of the reaction mass. Standard vacuum controllers, such as those commonly associated with rotary evaporation systems, regulate vacuum levels by systematically bleeding air into the reaction system. The introduction of air into this reaction, however, would compromise the inert atmosphere and increase product degradation. The pressure was therefore controlled by regulating the flow of nitrogen into the system under absolute vacuum, as depicted in Figure 3.3.

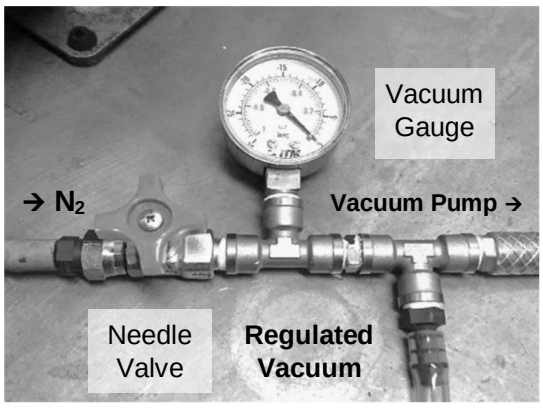

Figure 3.3: Three way valve to regulate vacuum within the detergent synthesis apparatus via N_2 valve.

Due to the lack of active heating within the distillation glassware, any reaction mass carried through to the distillation pathway posed a significant risk of reactor blockage. The melting point of the desired product is reportedly in excess of 200 °C.[15] Although the vacuum was

regulated to minimise the unintended loss of reaction mass, the distillation pathway was lagged with an insulating ceramic fibre rope and gently heated with a hot air gun throughout the fatty acid distillation process to minimise the risk of flow hindrance.

3.3. Titrative Purity Analysis

Titration techniques for the quantification of anionic surfactants were developed and implemented prior to the inception of isethionate ester detergents.[88] The current PhD study utilises a biphasic titration in which the endpoint is observed by an equalling in colour intensity between two immiscible liquid phases.[89]

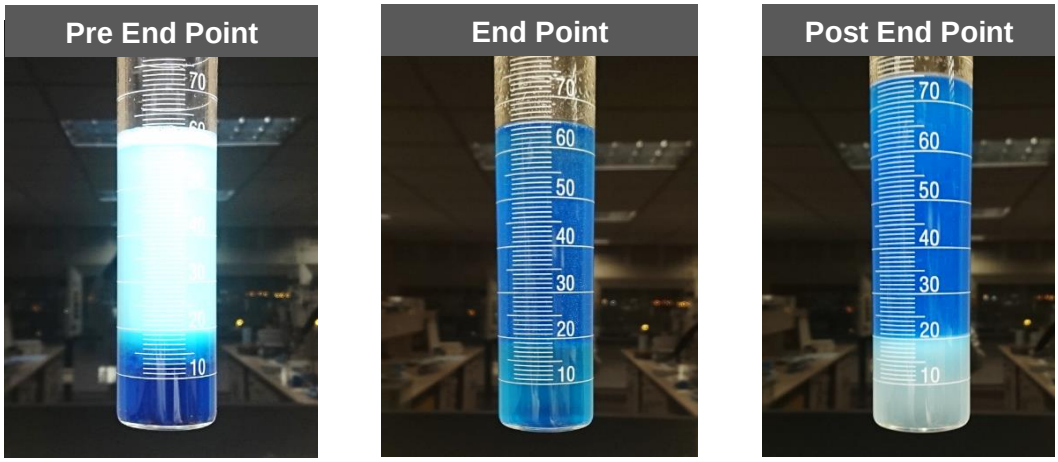

Figure 3.4: Anionic activity titration with Hyamine 1622 solution and methylene blue indicator. Endpoint is indicated by an equal intensity of blue in the organic and aqueous phases.

The technique was first reported by Epton in 1947[90] and has since formed the basis for many standard analytical methods.[91] The endpoint of the titration in this study was indicated by an equal intensity of methylene blue in a biphasic DCM-water mixture, as depicted in Figure 3.4. The underlying chemistry is explained in Figure 3.5.

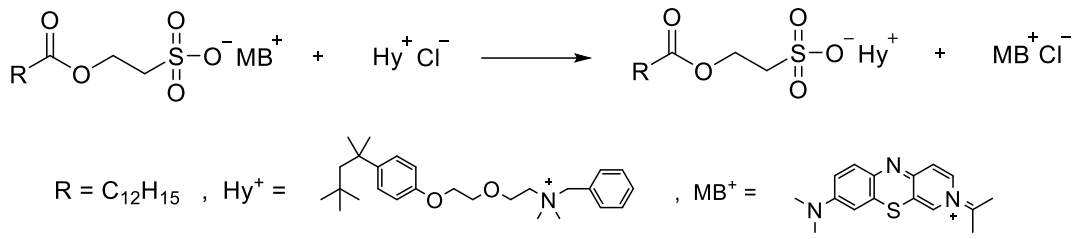

Figure 3.5: Biphasic titration of SLI with Hyamine (Hy^+) to quantify surfactant levels. The isethionate species and methylene blue indicator (MB^+) initially form a complex which is preferentially soluble in the organic phase. Addition of the stronger cationic titrant (Hy^+) results in the formation of a more favourable soap complex, thus releasing an aliquot of blue indicator into the aqueous phase. The end point is reached when a stoichiometric quantity of Hyamine has been added.

The accuracy of the endpoint relies on the precision with which solutions are prepared.[92] Although in this instance, the cationic titrant was standardised by the chemical supplier and used as received. Its concentration can be verified by standardisation against sodium dodecyl sulphate, which itself can be standardised against 1 M sulfuric acid. Details of these procedures have been published by Longman.[89]

3.4. Differential Scanning Calorimetry

Through the breaking and formation of thermodynamically favoured intermolecular interactions, endothermic and exothermic energy changes result from melting and crystallisation processes respectively. Calorimetry is a method by which such phase transitions can be detected by measuring the flow of heat into and out of a material.[93]

Differential Scanning Calorimetry (DSC) is a common form of calorimetry in which the energy required to heat a sample is measured against a reference as a function of temperature. The differential between the sample and reference can be quantified in one of two ways: power compensation or heat flow.[94] The two methods are depicted in Figure 3.6.

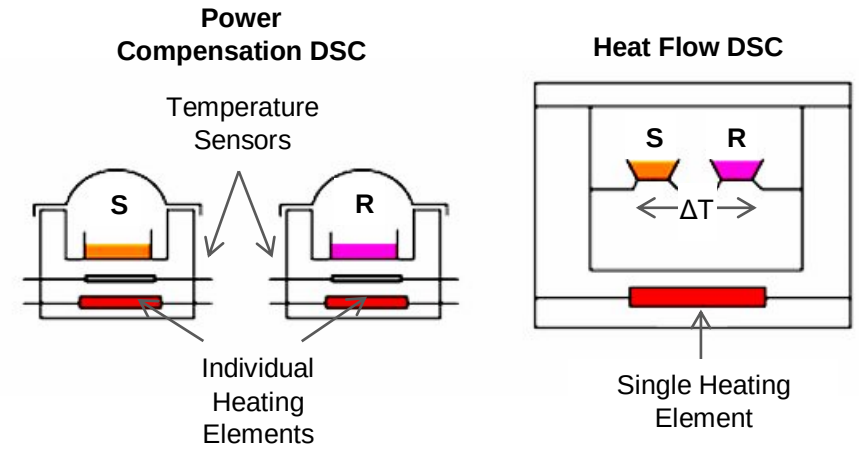

Figure 3.6 Comparison of power compensation and heat flow differential scanning calorimeters (DSC). Sample (S) is heated within a crucible typically constructed from aluminium, alumina or platinum. An empty reference crucible (R) is subjected to the same temperature profile.[93]

A power compensation DSC (left, Figure 3.6) contains two heating elements and two thermocouples. Upon thermal analysis, the temperature of the sample is continuously adjusted to match that of the reference. Any differential in the energy required to do so is indicative of a phase transition. In a heat flow DSC (left, Figure 3.6), both crucibles are instead heated via a single heating element. The heat flow resulting from a phase transition is contrastedly detected by a temperature differential between the two crucibles.[94]

The interpretation of the resulting thermal curve is independent of the instrument format. Both systems report no change between the sample and reference crucibles in the absence of a thermal event.[95] In the event of an endothermic transition (such as the melting of a solid species), a power compensation DSC would report a decrease in the thermal energy required to heat the reference crucible, with respect to the sample. A heat flow DSC would conversely detect the event as a decrease in the sample temperature, with respect to the reference. Consequently, an endothermic transition always corresponds to an inverted peak signal, irrespective of the instrument type. Figure 3.7, displaying the thermal curve obtained from melting of myristic acid, demonstrates how phase transformation characteristics are measured. Analogous methodologies are utilised for the measurement of crystallisation processes.

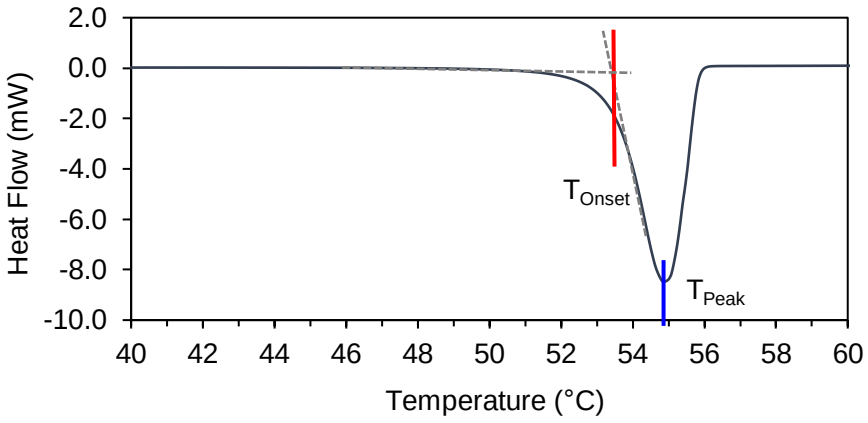

Figure 3.7: Example of melting transition recorded via a differential scanning calorimeter (DSC). Obtained by heating a sample of myristic acid using a Mettler Toledo DSC 1 power compensation calorimeter. T_{Onset} = Onset of solid melting (red) was obtained through tangential extrapolation as shown. T_{Peak} = Peak melting temperature (blue) was measured as the temperature at which peak enthalpy change is detected.

3.5. Thermogravimetric Analysis

Thermogravimetric Analysis (TGA) is an analytical method in which the mass of a substance is measured as it is exposed to a controlled atmosphere or temperature over a defined time period.[96] A TGA instrument consists of a sample holder placed within a temperature controlled chamber where the sample pan in a TGA is supported by a precision balance. Many instruments also contain temperature sensors permitting the simultaneous collection of DSC data (Section 3.4).[94] A purge gas is often directed over the sample to control the sample environment. Standard thermal analyses typically employ inert gases such as nitrogen and argon, whilst oxidative studies utilise air or nitrogen. The gases evolved from the analysis can be characterised using a variety of analytical methods to provide additional chemical information on the degradation by-products.[97] Mass spectrometers (MS)[98] and infrared spectrometers (IR)[99] are commonly utilised in this application. When complex mixtures of gases are simultaneously produced, a gas chromatography instrument can be introduced to separate evolved gases prior to spectroscopic analysis. In this study, a TGA instrument was connected directly to an IR spectrometer for the *in-situ* analysis of evolved gases (see Section 3.6)

3.6. Infrared Spectroscopy of Evolved Gases

Infrared spectroscopy (IR) functions on the fundamental basis that organic molecules are in a state of continuous vibrational and rotational motion.[100] If a material is exposed to infrared radiation of a frequency that is equal to the frequency of a molecular vibration, then the radiation is quantifiably absorbed and converted into vibrational energy.[101]

The selection rules of IR state that a vibrational transitional within a molecule is allowed and therefore 'IR active', only if a change in dipole moment results from the corresponding vibration.[102] Homonuclear diatomic species therefore cannot be observed via IR due to the absence of an excitation-induced dipole moment. Heteronuclear species such as CO_2, in contrast, are observable despite the lack of a dipole moment at equilibrium due to an asymmetric displacement of the centre of charge in the molecule. Non-linear molecules containing *n* number of atoms exhibit 3 *n* – 6 degrees of vibrational freedom. There six normal vibrational modes that can be exhibited via polyatomic molecule, all of which are represented in Figure 3.8 by the CH_2 group in an alkyl chain:

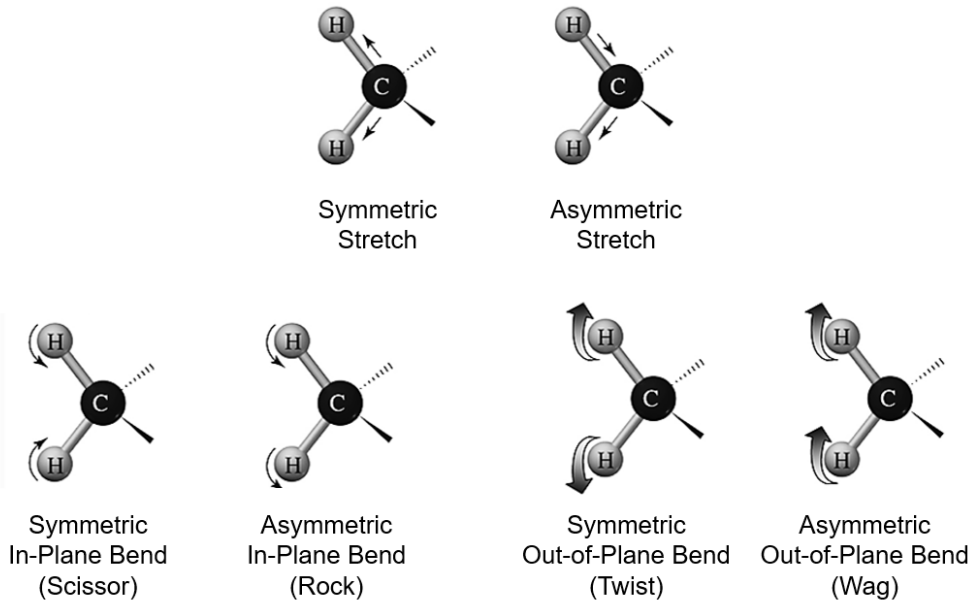

Figure 3.8. IR active vibrational modes of CH_2. Bending motions can also be termed as deformation motions. [103]

The 'middle' IR region at wavenumbers between ~500 and 4000 cm^{-1} is reportedly the most useful form of infrared spectroscopy in the analysis of lipid molecules.[78] Modern infrared spectrometers operate through means of an interferometer, as depicted in Figure 3.9. [104]

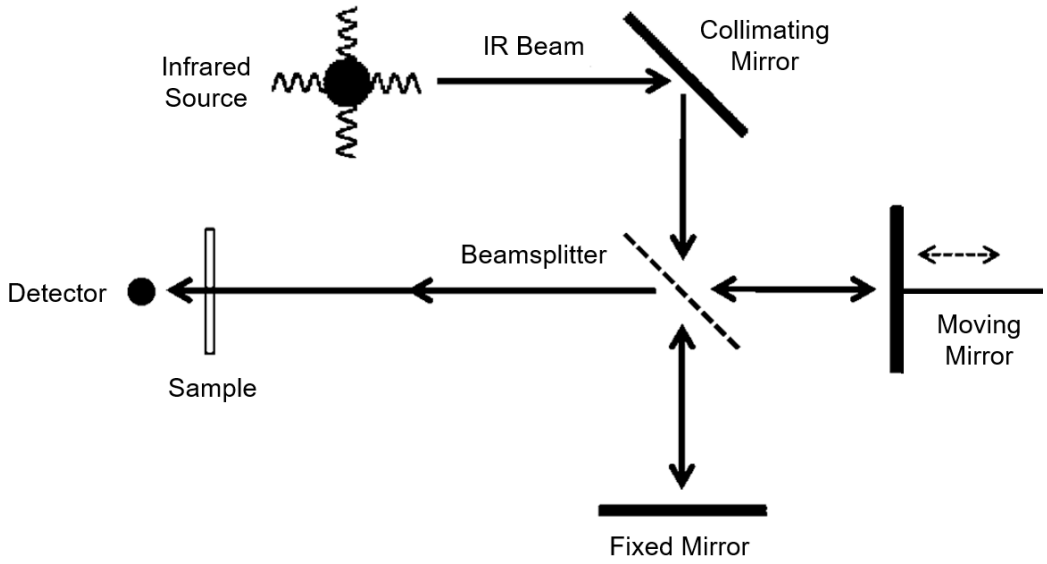

Figure 3.9. Schematic of the interferometer in a modern Fourier-transformed infrared (FTIR) spectrometer. Reproduced from Smith et al.[104]

Infrared radiation from a black body source is directed into a beamsplitter, which creates two optical beams from the incoming IR radiation. The optical beams travel through the designated paths depicted in Figure 3.9, before reconverging at the beamsplitter. While one beam has travelled a fixed distance, the path length of the second beam is dependent the position of the moving mirror. The signal exiting the beamsplitter is referred to as 'interferogram' as it is a combination of the interference between the two signals.[105] Through adjustment of the moving mirror, the interferogram permits the measurement of all IR frequencies in a single measurement, thus significantly reducing analysis times. A Fourier-transformation is subsequently utilised to convert the interferogram into an FTIR spectrum depicting the absorbance of the sample at wavenumbers between ~500 and 4000 cm^{-1}. [104] A background sample is typically collected to avoid characteristic signals water or CO_2 in the atmosphere from impeding the analysis.[106]

When approximated as a vibrating spring, a diatomic molecular bond can be described by Hooke's Law (Eq. (8)): [104]

$$\bar{\upsilon} = \frac{1}{2\pi c}\sqrt{\frac{k}{\mu}} \quad (8)$$

Where:

$$\mu = \frac{m_1 m_2}{m_1 + m_2} \quad (9)$$

Here, $\bar{\upsilon}$ is wavenumber (cm^{-1}), c is the speed of light (cm/s) and μ is the reduced mass where m_1 and m_2 are the atomic masses of each atom in the diatomic bond. k corresponds to the bond force constant (N/cm) which is an indication of bond strength.

In the analysis of solvated liquid samples, changes in intermolecular forces between polar and non-polar solvents can influence localised changes in the force constant.[106] Gas-phase molecules can be considered as existing in an extremely diluted, non-polar environment; where both solvent-sample and sample-sample intermolecular interactions would be negligible. As vapour phase molecules are predominantly present in the monomeric state, compared with the dimeric and polymeric states observed in more condensed states, there are significant decreases in hydrogen-bonding levels.[107] Frequencies of both O-H and C=O absorption bands in the vapour state specifically exhibit notable changes in frequency when compared with solid and liquid samples.

3.7. X-Ray Diffraction

The wavelength of X-ray radiation (~10^{-10} m) is of the same order of magnitude as the interatomic distance observed in most organic and inorganic materials.[108] When incoming X-ray radiation interacts with the electrons in an atomic array, it is scattered in a similar manner to the way that visible light interacts with objects at a larger scale.[109] The extent to which electrons are scattered is dependent on the number of electrons in the atoms. This amplitude can be used to distinguish atoms by element, particularly when there is a large discrepancy in atomic mass between neighbouring atoms. [108]

In general, if the difference in path length between in-phase X-rays is equivalent to the wavelength of the incoming X-ray radiation (or a common multiple), then the intensity of the resulting wave is greatly increased through constructive interference. All scattered X-ray radiation resulting from this constructive interference is diffracted at a single angle equal to that of the incoming radiation.[110] Figure 3.10 is a 2D representation of an ordered array of atoms, in a hypothetical 3D lattice, to display how these principles can be used to measure interatomic distances in crystalline materials.

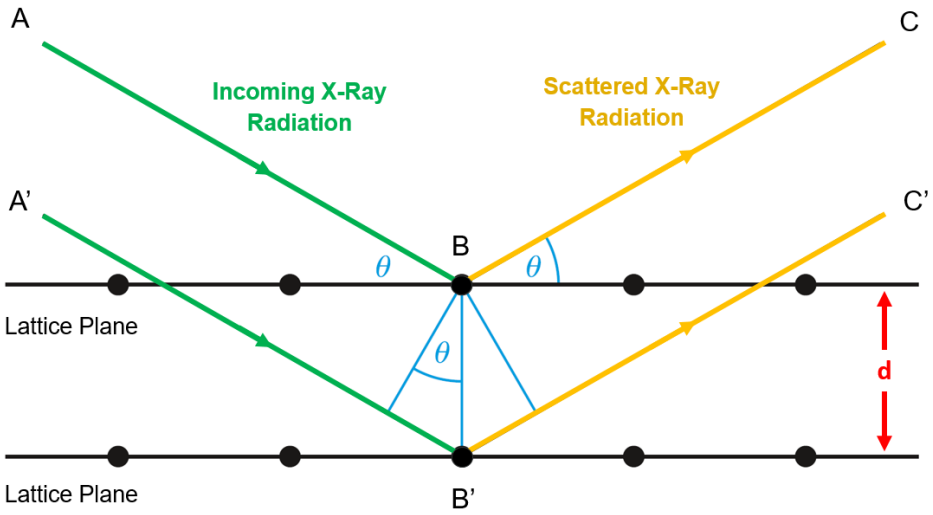

Figure 3.10. Bragg diffraction of X-ray radiation in adjacent crystallographic planes.[108]

In the displayed example, the difference in path length (d) between ABC and A'B'C' is equal to the integer multiple of the incoming X-ray radiation (λ), resulting in a diffracted beam where the angle of incidence from the incoming radiation is equal to the angle of reflection of the scattered radiation. These principles can be summarised by the Bragg Law. [111]

$$n\lambda = 2d \sin\theta \qquad (10)$$

Where θ is the angle of incidence of the incoming X-ray radiation, λ is the wavelength of the incoming X-ray radiation, n is the integer 'order' of the diffraction (n = 1, 2,

3,..) and *d* is the interplanar lattice spacing. By varying the angle of incidence and observing the points at which constructive interference is observed, a representation of interatomic distances within the lattice can be obtained.

In the analysis of other lipids and long chain hydrocarbons, large numbers of randomly orientated microcrystals are simultaneously analysed via powder X-ray diffraction (PXRD).[112] A typical powder X-ray diffractometer typically consists of an X-ray source, a stage on which the powdered sample is mounted, a goniometer through which angles are adjusted and an X-ray detector. The PANanalytical X'Pert Diffractometer utilised in this project exhibits a Bragg-Brentano geometry (Figure 3.11). The sample stage remained stationary whilst the goniometer simultaneously rotated the X-ray source and detector to measure the X-ray diffraction at angles between 2 and 50° (2θ). The wavelength from the Cu-kα source was fixed at 0.154 nm to ensure that crystallographic planes produced just a single set of diffraction signals.

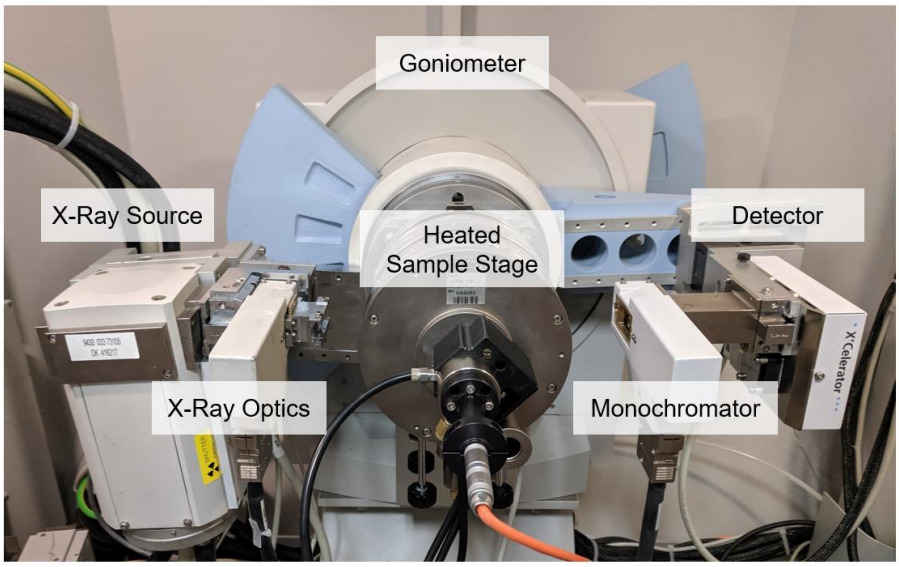

Figure 3.11. PANalytical X'Pert Powder X-ray Diffractometer exhibiting a Bragg-Brentano geometry.

3.8. Small Angle X-Ray Scattering

In complex multi-component lipid systems, increased levels of disorder often result in semi-crystalline or liquid crystalline phases exhibiting *quasi*-Bragg diffraction.[113] Whilst there is

reduced scattering from atomistic intermolecular interactions between alkyl chains, the 00*l* reflections originating from planes of liquid crystal structures can still be observed by small angle X-ray scattering (SAXS).[78] The components of a SAXS instrument are similar to that of a powder X-ray diffractometer. An X-ray source directs a beam of radiation onto a powdered or liquid sample, after which the scattering is measured by a detector.[114] Unlike the PXRD setup, the SAXS systems in this study utilise a 2D detector setup which simultaneously captures scattering at all angles, without the need for goniometer to rotate the X-ray source, sample stage or detector.[115] (Figure 3.12)

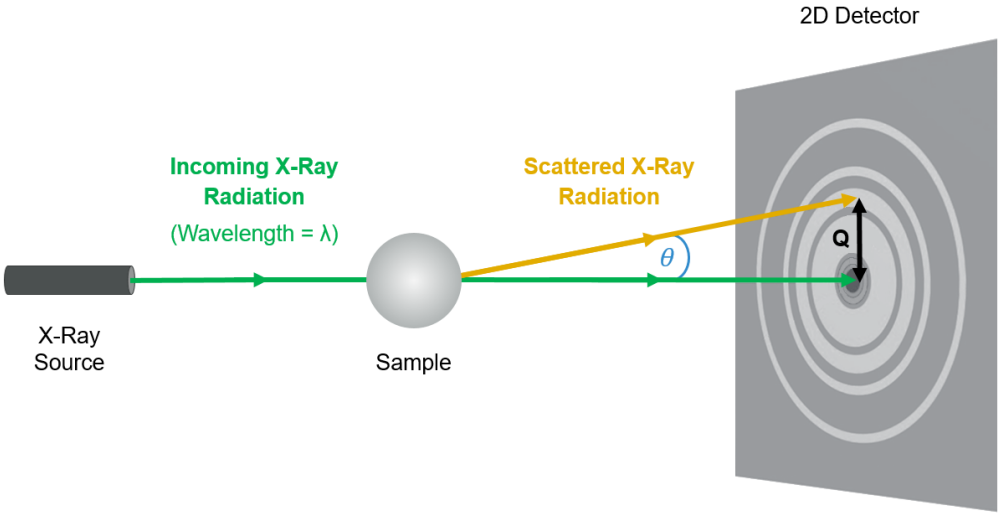

Figure 3.12. Schematic of a small angle X-ray scattering (SAXS) instrument featuring a 2D detector in transmission mode. The diagram shows how scattering length (Q) in a SAXS instrument relates to Bragg angle (θ) in a powder diffractometer. Varying the distance between the sample and detector varies the scattering length (Q) detected by the instrument. Created using Londono et al. [115]

Instead of the Bragg scattering angle (θ), the SAXS instrument measures the scattering length (Q). [114] The *d* spacing (Eq. (Bragg)) can be obtained from the scattering length using Eq. (11) to permit the measurement of lattice spacing in the absence of atomistic ordering in the crystalline phase.[113] In SAXS, the order of diffraction is more commonly denoted by *h* rather than *n*.

$$Q = \frac{2\pi h}{d} \tag{11}$$

Powdered samples, isotropic liquids and dispersed samples exhibiting a random molecular orientation in the sample produce a scattering pattern of radial uniformity. When texture in the scattering pattern is observed, structural information relating the particle morphology can be inferred. The degree and intensity of anisotropy can be used to measure the extent of preferred orientation. As observed in single crystal X-ray diffraction, a single particle orientated specifically to the incident beam produces intense spots pertaining to the individual Bragg reflections in the material.

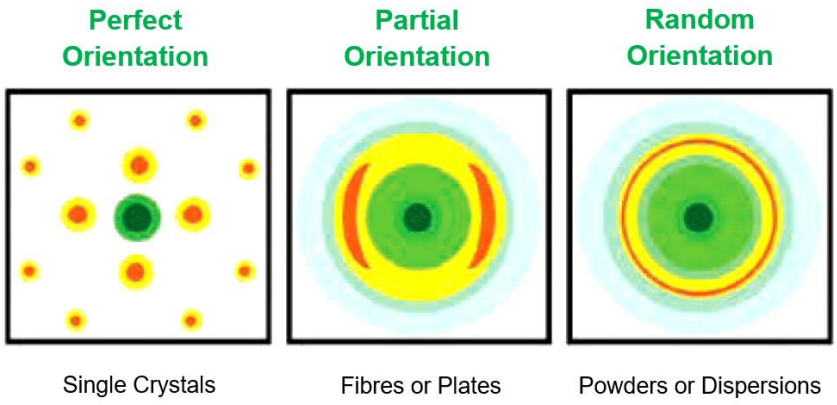

Figure 3.13. X-Ray scattering from a 2D SAXS instrument of a single crystal (left), randomly orientated powder (right) and materials displaying preferred orientation (cenre).[114]

SAXS is often used to probe special dimensions of larger systems such as proteins, nanomaterials and biological membranes.[116] By increasing the sample-to-detector distance, the scattering length (Q) can be used to probe distances of several nanometres. In such systems, broader, characteristic shapes in the scattering curve can be used to distinguish between spheres, plates, rods and discs in the sample nanostructure.[114] In the current study, however, SAXS will primarily be used as an extension to PXRD, to observe Bragg reflections that are produced at *d* spacings just beyond those that observable using a typical laboratory diffractometer.

Chapter 4: Process Focused Synthesis, Crystallisation and Physicochemical Characterisation of SLI

Synopsis: *The results chapter describes how sodium lauroyl isethionate (SLI) was selected as a model isethionate ester surfactant from the analysis of commercial materials. Following a bespoke synthesis of SLI, a turbidimetric solubility analysis was conducted to identify conditions through which it could be reproducibly purified. A physicochemical characterisation was finally executed to verify the chemical identity of the surfactant, whilst simultaneously revealing key physical properties underpinning its performance in personal care formulations. In relation to the proposed research question, this chapter specifically developed the means of acquiring a reproducible model detergent for a detailed structural characterisation.*

4.1. Introduction

Personal care products such as soap bars, shampoos and liquid cleansers contain surfactants to remove grease and sebaceous oils from the skin. Repeated exposure to surfactants is known to cause skin irritation,[117] dryness,[118] tightness[119] and damage to the stratum corneum.[120] These effects are reported with the use of both traditional carboxylate soaps and synthetic surfactants such as sodium dodecyl sulfate (SDS).[121-125] Sodium cocoyl isethionate (SCI) is a milder surfactant also prevalent in personal care formulations.[9] Its lower charge density, larger polar head group and high activity at neutral pH improves its compatibility with the skin, thus reducing the negative effects experienced by the consumer.[124] Studies have demonstrated reduced irritation,[124] dryness[126] and binding to the stratum corneum,[127] compared with soaps and alkyl sulphates. In the presence of hard water, traditionally saponified carboxylate soaps exhibit a loss in surface activity as the sodium counter-ion is displaced by magnesium and calcium ions.[128] A larger quantity of product is often utilised by consumers in order to compensate for the consequent loss in detergency and lather.[7] The poor aqueous solubility of the inactive alkali earth salts also results in the precipitation of solid 'scum' on bathroom surfaces.[129] SCI is conversely stable in the presence of alkali earth metals and does not form any deposits or display significant loss of lather volume in the presence of hard water.[7, 28]

The molecular structure of SCI is shown in Figure 4.1. On a commercial scale SCI is manufactured through the functionalisation of hydrolysed coconut oil.[128] Once hydrolyzed, the coconut oil consists of a blend of linear, saturated carboxylic acids ranging between octanoic (C8) and octadecanoic acid (C18). Sodium derivatives are most prevalent within surface active isethionates; although protic[130] and ammonium[131] isethionates have also been prepared for pharmaceutical applications.

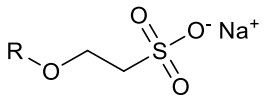

Figure 4.1. Molecular structure of the isethionate functional group. For sodium cocoyl isethionate (SCI), R = linear, saturated carboxylic acid chain between octanoyl- (C8) and octadecanoyl- (C18).

A compositional analysis of coconut oil indicates that the dodecanyl (C12), tetradecanyl (C14) and octadecanyl (C18) chain lengths are the most abundant with concentrations of 47.7%, 19.9% and 10.3% respectively.[132] Although this chain length distribution is representative of commercial SCI, there is a natural disparity between batches due to the compositional variation in the raw material.[7] Because of this variation, previous studies on SCI have focused on the most abundant isethionate derivatives existing in the natural surfactant blend.

Bistline et al. prepared a series of even numbered, consecutive isethionates ranging from sodium dodecanoyl isethionate (C12) to sodium octadecanoyl isethionate (C18) via a two-step catalytic process.[133] The corresponding linear, saturated carboxylic acids were first esterified using propyne under zinc catalysis to form the equivalent isopropenyl esters. These derivatives were then mixed with sodium isethionate and heated to 200°C in the presence of a p-Toluenesulfonic acid catalyst to create the desired acyl isethionate.[133] Hikota also prepared sodium decanoyl isethionate (C10) and sodium dodecanoyl isethionate (C12) as part of a larger investigation into ester-based surfactants.[134] Carboxylic acids were reacted with thionyl chloride to form the corresponding acyl chlorides. Following a reduced pressure distillation, the acyl chlorides were reacted with sodium isethionate at 90°C to yield the acyl isethionate surfactants. Both studies utilised a two-step synthesis route and while Hikota's reaction temperature was lower, the chlorinated reagents were significantly more hazardous than those utilised by Bistline *et al.*[133] In the aforementioned studies, both authors repeatedly recrystallised the sample in alcoholic solvent to purify the crude product. A recent review of acyl isethionates,[33] reports that commercially synthesized SCI typically ranges in crude purity from 78 to 85% and the product is not purified prior to application in personal care formulations.[128]

In the current study, sodium lauroyl isethionate (SLI), the most abundant constituent in the natural SCI blend, has been synthesised via the single-step esterification of lauric acid and sodium isethionate. Our reaction exhibits numerous environmental advantages over previous studies reporting the synthesis of SLI including a reduced number of reaction steps, an increased atom economy and complete removal of ancillary solvent, catalyst and chlorinated species from the synthesis.

Following synthesis, the crude SLI was successively recrystallised in methanol with accompanying purity analyses at each stage. A polythermal solubility turbidimetric analysis was subsequently completed to determine the optimum crystallisation parameters for the scalable purification of SLI. There is a notable lack of published literature concerning the fundamental properties and characteristics of sodium acyl isethionates. The resultant purified surfactant was therefore subjected to a detailed physicochemical characterisation and analysis which included melting, decomposition, vapor sorption and surface tension measurements. The fundamental data reported in the study provides a much needed insight into how the physicochemical properties influence the commercial scale manufacture, performance and synthesis of acyl isethionate surfactants from biorenewable sources.

4.2. Experimental

4.2.1. Materials

4.2.1.1. GC-MS Analysis of Fatty Acid Components

Hydrolysed coconut oil was provided by Innospec Ltd. Sulphuric acid ACS reagent (95-98%), was obtained from Sigma-Aldrich. Methanol ACS analytical reagent (99.8%), was obtained from VWR.

4.2.1.2. Synthesis and Purification of SLI

Lauric acid (99%, Acros Organics) and sodium isethionate (98%, Acros Organics) were obtained from Fisher Scientific. Methanol (99.8%) was obtained from VWR. Materials were used as supplied with no further purification.

4.2.1.3. Cationic titration for surfactant activity.

Methylene Blue powder (96%) was obtained from Alfa Aesar. Anhydrous sodium sulfate (99%) was obtained from Fisher Scientific. Sulphuric acid ACS reagent (95-98%), was obtained from Sigma-Aldrich. Dichloromethane ACS analytical reagent (99.9%), was obtained from VWR. Hyamine 1622 cationic titrant was standardized to 0.004 M by the manufacturer (Vickers Labs).

4.2.2. GC-MS Analysis of Fatty Acid Components

4.2.2.1. Preparation of fatty acid methyl esters (FAMEs) from fatty acids

400 µl sulphuric acid in 20 ml methanol (2% w/v) was added to 5.0 g of hydrolyzed coconut oil in a 50 ml RB flask. The mixture was magnetically stirred at 450 rpm and heated under reflux at 50°C for three hours. 50 ml of aqueous sodium chloride solution (5% w/v) was added to a 250 ml separating funnel. Upon completion of the reaction, the fatty acid mixture was also poured into the separating funnel. Methyl esters were extracted into 3 × 50 ml of hexane.

4.2.2.2. FAME Analysis via Gas Chromatography - Mass Spectrometry (GC-MS)

GC-MS analysis was executed via a Perkin Elmer Clarus 560S single quadrupole GC/MS system, equipped with a Perkin Elmer Elite-5 MS capillary column (250 µm diameter × 30 m length, 0.25 µm film thickness). Following injection, the sample was ionized via electron impact with an MS solvent delay of 4 mins. Oven temperature was increased from 60°C to 200°C at 10°C/min, held for 10 mins then increased to 270°C at 10°C/min and held for 5 mins. Helium carrier gas was supplied at 1 ml/min. A response factor was obtained from the methyl decanoate internal standard and applied to the species of interest to obtain a chain length distribution.

4.2.3. Synthesis of SLI

120.8 g of lauric acid, 0.25 g of zinc oxide and 111.2 g sodium isethionate solution (57% w/v in water) were placed in a 500 ml three neck round bottom flask and magnetically stirred at 600 rpm. The reaction vessel was equipped with a temperature probe and a 6" stainless steel sparge needle, as depicted in Figure 4.2. Under a continuous stream of nitrogen, the stirred reaction flask was heated to 150 °C and maintained for 90 minutes to remove the

aqueous isethionate diluent. Upon complete distillation, the reaction temperature was increased to 240°C and maintained for four hours. Any azeotropically distilled lauric acid was returned to the reaction mixture via a 10 ml Dean-Stark (DS) receiver. The water of reaction, along with any biphasic interfacial material, was retained within the DS and collected in a 100 ml measuring cylinder.

When accumulation of water had ceased, the Dean-Stark apparatus was removed and replaced with a vertical still head coupled with a 250 ml three neck receiving flask. Magnetic stirring, nitrogen flow and 240°C reaction temperature were maintained during the equipment exchange and atmospheric exposure was minimised via intermediary use of glass stoppers.

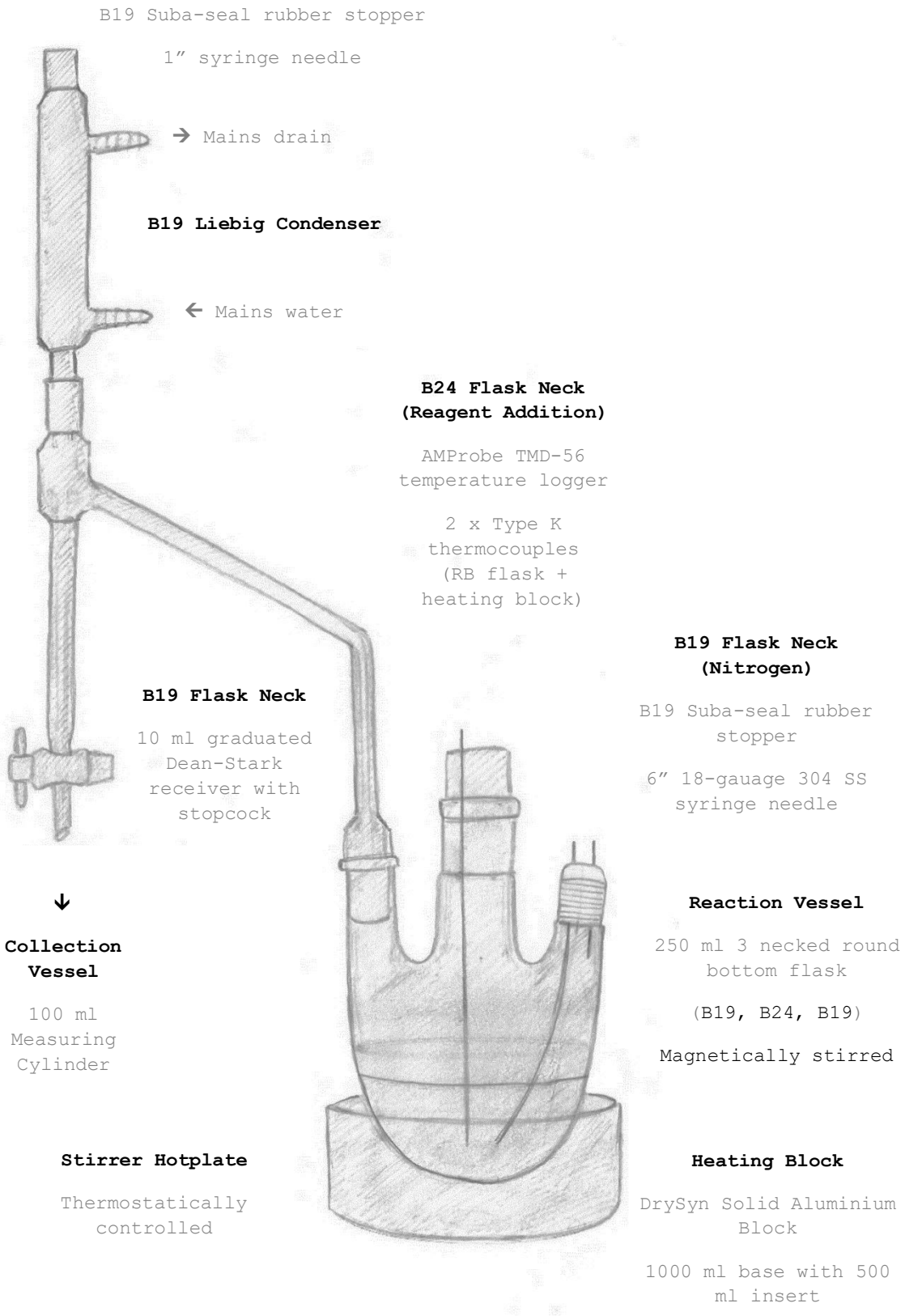

Figure 4.2. Schematic of SLI synthesis setup during esterification.

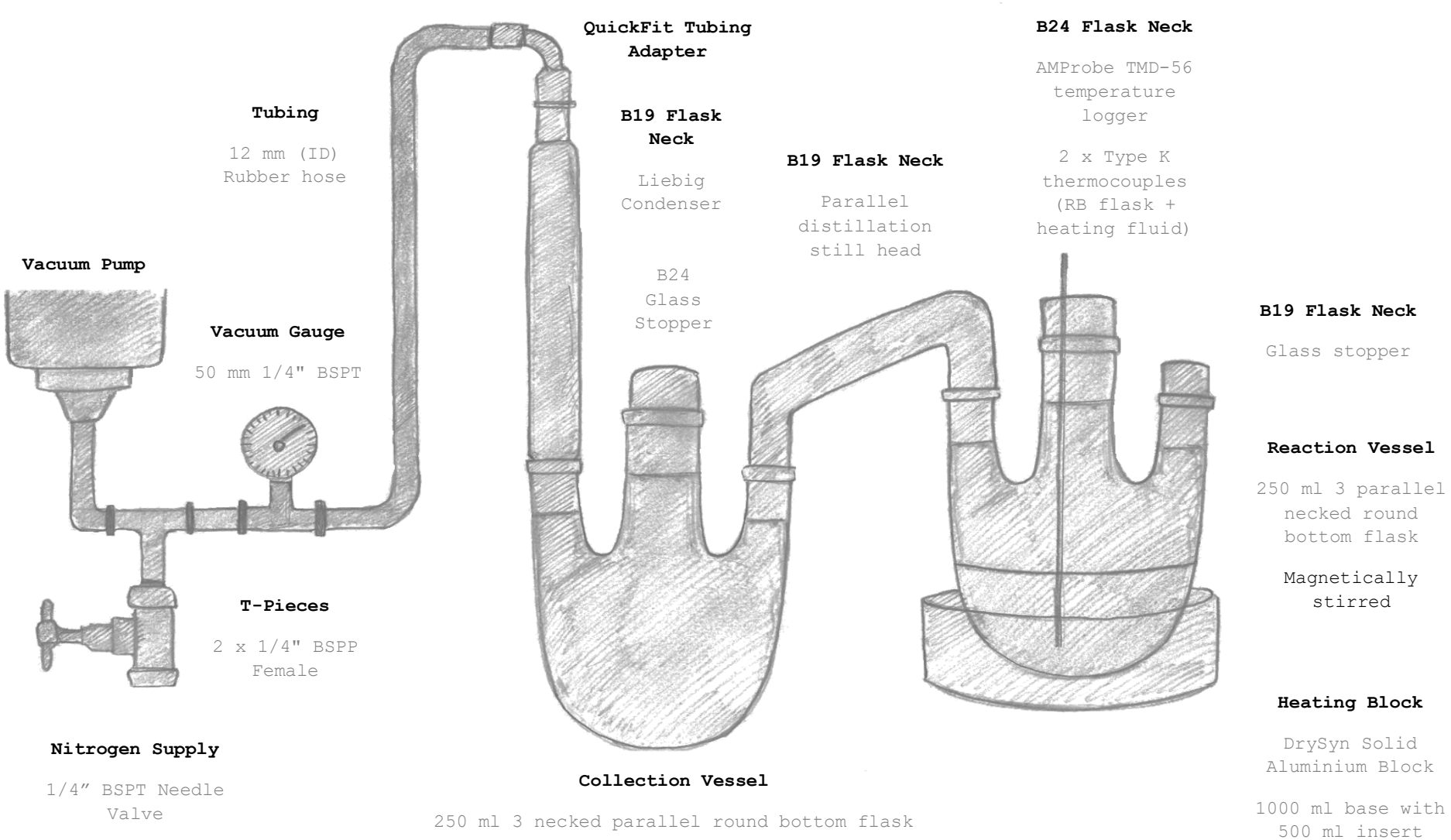

Figure 4.3. Schematic of Sodium Lauroyl Isethionate synthesis setup during the fatty acid distillation.

A condenser was fitted to receiving flask and a vacuum of 200 mbar was first applied to collect any unreacted lauric acid. The pressure was then gradually decreased to 50 mbar with care taken to minimise foaming of the surfactant product. The pressure was controlled by a needle valve regulating the ratio of nitrogen flow into the reactor against the vacuum produced from an Edwards E2M2 High Vacuum Pump (Figure 3.3). After 60 minutes, the molten reaction mixture was poured onto a borosilicate glass tray and precipitated at room temperature.

4.2.4. Anionic Activity Analysis

A methylene blue indicator solution was prepared by adding 0.03 g of methylene blue powder and 50 g of anhydrous sodium sulfate to a 1000 ml volumetric flask and dissolving in 500 ml water. 12 g sulphuric acid was added dropwise and the solution was diluted to the mark. 0.2004 g of crude reaction material was dissolved in water and diluted in a 100 ml volumetric flask. 10 ml of solution was transferred to a 100 ml stoppered measuring cylinder via volumetric pipette. 20 ml of dichloromethane and 25 ml of methylene blue indicator solution were added and the cylinder was shaken. The biphasic mixture was titrated with Hyamine 1622 (0.004 M) until the two phases reach the same intensity of blue. An industry standard cationic titration method was subsequently employed to gauge conversion levels within the crude reaction product.[90] Eq. (12) was used to quantify the anionic surfactant levels in the crude mixture, relative to that of a pure surfactant solution.

$$\text{Anionic Surfactant (\%)} = \frac{V \times M \times MW \times 10}{C} \qquad (12)$$

In Eq. 1, V = volume of Hyamine titre (ml) , M = molarity of Hyamine solution (mol/dm^3), MW = molecular mass of surfactant (g/mol) and C = concentration of sample solution (g/dm^3). Volumetrically adjusted from equation published by Turney *et al*.[92]

4.2.5. FTIR Analysis of SLI

Solid samples of crude and purified SLI were analyzed using a Thermo Scientific Nicolet iS-10 FTIR Spectrometer. An ATR sampling accessory was used to measure transmittance between 500 and 4000 cm^{-1}.

4.2.6. NMR Analysis of SLI

50 mg of sample was dissolved in 2 mL of d-DMSO using a Fisherbrand vortex mixer. 1H NMR analysis was executed using a Bruker Avance III 500 MHz spectrometer. Norrell XR-55 high precision NMR tubes were utilized throughout. Chemical shift, integration and multiplicity in the resulting signals were measured using the MestreNova software package. Assignments were compared against NMR simulations generated by the PerkinElmer ChemNMR software package.

4.2.7. LC-MS Analysis of SLI

25 mg of crude and purified SLI were each dissolved in 5 mL methanol using a Fisherbrand vortex mixer. The resulting solution was analyzed via a combined liquid chromatography-mass spectrometry system (LC-MS). Samples were injected into and separated using a Dionex UltiMate 3000 Rapid Separation UHPLC System. Material was eluted through a C18 column by a binary solvent mixture consisting of acetonitrile (MeCN) and water. The linear gradient elution method varied the concentration of MeCN from 5% to 95% over 60 secs. Compounds were then detected by diverting the separated species through a Bruker Amazon Speed mass spectrometer. Sample was ionized via electrospray ionization with quantification of both positive and negative ion via the ion trap detection system.

4.2.8. Recrystallisation of SLI

The crude SLI was purified by repeat recrystallisation in methanol. SLI was mixed with 100 mL of methanol and heated to 60°C in a round bottom flask with a condenser. The mixture was stirred at 300 rpm with the solvent incrementally added until the SLI had completely dissolved. Any insoluble particles observed in solution were hot filtered through a stemless funnel. Solutions were then cooled overnight at 0.5°C/min. The resulting crystals were isolated via Buchner filtration and dried in a vacuum desiccator prior to further purification steps. Cationic benzethionium chloride titrations were completed at each purification step, as previously described. After five

recrystallisations, SLI was obtained in the form of white powder. The purified material was used for the subsequent physicochemical analysis. NMR, FTIR and LC-MS data of the crude and purified SLI is provided.

4.2.9. Thermal Analysis of SLI

4.2.9.1. Thermogravimetry

Samples of lauric acid, crude SLI and purified SLI were analysed using a Mettler Toledo TGA/DSC 1 Thermogravimetric Analyser. 2-5 mg of each sample was weighed to the nearest 0.1 µg using a Mettler Toledo UMX2 Ultra-Microbalance and placed in a 70 µL alumina crucible. Samples were heated from 25°C to 500°C at 10°C/min under N_2 flow of 50 mL/min. Sample mass was measured every second to the nearest 0.01 µg to identify any temperature-induced phase transitions. The analysis was used to determine the presence of ancillary species of the crude and purified samples of SLI.

4.2.9.2. Differential scanning calorimetry

Samples of crude SLI and purified SLI were analysed using a Mettler Toledo DSC 1. 2-5 mg of each sample was weighed and deposited in hermetically sealed 40 µL aluminium crucibles. Samples were heated from 25°C to 150°C at 50°C/min under N_2 flow of 50 mL/min. After 10 min at 150°C, the temperature was raised by 1°C/min to 250°C. Following a further 10 min, the temperature profile was reversed and the temperature reduced to 25°C at 1°C/min. Prior to analysis, the instrument was calibrated against certified reference materials of zinc and indium obtained from Mettler Toledo. Enthalpy of fusion (ΔH_{Fus}) and melting temperature (T_m) were obtained from the area and the peak maximum temperature observed from the primary melting peak.

4.2.10. Dynamic Vapor Sorption Analysis of SLI

The water vapor sorption of purified SLI was measured using the DVS Advantage (Surface Measurement Systems, UK). Approximately 10 mg of sample was added to an aluminium crucible and placed into a thermostatically controlled chamber at 25°C. Samples were then dried under a flow of dry N_2 at 50 mL/min until the sample mass had stabilised to the nearest 0.1 µg over a period of 5 min. Relative humidity (RH)

was subsequently varied between 0 and 90%, at 10% increments. Target humidity levels were maintained until the sample mass had stabilized and the sample mass, humidity and temperature were continuously recorded at 60 s intervals. The data provides information on the storage stability of SLI with respect to changing humidity levels at room temperature.

4.2.11. Solubility Analysis of SLI

Solutions of SLI in methanol were prepared at concentrations between 20 g/L and 35 g/L, at 5 g/L increments. Purified SLI was accurately weighed using an analytical balance (to the nearest 0.1 mg) and diluted with 5 mL methanol. The resulting solutions were heated to 40°C and stirred at 300 rpm to ensure complete dissolution. Micropipettes were then used to transfer 1 mL of each solution into 1.5 mL capped glass vials. Four vials were filled at each concentration, thus 16 samples were considered for further analysis. The solutions were analysed using the Technobis Crystal16 parallel crystalliser. The crystalliser provides independent temperature control of four blocks, with each block consisting of four glass vials. Samples were subjected to five heating and cooling cycles between -10 to 50°C, with each solution concentration undergoing rates of 3, 2, 1 and 0.5 °C/min. Vials were individually magnetically stirred at 700 rpm and solubility was determined using the integrated turbidity detectors. T_{Diss} (clear point) was identified as the temperature when the measured transmission equalled 100% during heating, while T_{Cryst} (cloud point) was identified as the temperature when the transmission first dropped below 95% upon cooling. Sample vials were continuously flushed with N_2 to avoid external surface condensation at low temperatures. Equilibrium solubility parameters at each concentration (T_{Diss} and T_{Cryst}) were obtained by plotting the respective values against heating rate and extrapolating to 0°C/min. The experimental solubility was then compared with the ideal solubility through a van't Hoff analysis.

Praustnitz *et al.*[135] stated that, assuming a negligible contribution from the heat capacity (C_p), the molar solubility (χ) in an ideal system was obtained from eq. (2) using the enthalpy of fusion (ΔH_{Fus}) and melting temperature (T_m) measured via DSC:

$$\ln(\chi) = \frac{\Delta H_{Fus}}{R}\left[\frac{1}{T} - \frac{1}{T_m}\right] \quad (13)$$

The enthalpy and entropy of dissolution (ΔH_{Diss} and ΔS_{Diss} respectively) were then calculated from the ideal and experimental solubility data using Eq. (14). These values quantify the enthalpy change when one mole of solute is dissolved into an infinite quantity of saturated solution.

$$\ln(\chi) = -\frac{\Delta H_{Diss}}{RT} + \frac{\Delta S_{Diss}}{R} \quad (14)$$

The activity co-efficient (γ) was then used to quantify the experimental deviation from ideality, in accordance with Eq. (15), where χ and χ_{Ideal} are the experimental and ideal molar solubilities.

$$\gamma = \frac{\chi_{Ideal}}{\chi} \quad (15)$$

Further details on the experimental method and subsequent analysis can be found in previous publications.[136] [137]

4.2.12. Surface Tension Measurements of Aqueous SLI Solutions

Solutions of SLI in water were prepared at concentrations between 0.01 mM and 10 mM as described previously. A single droplet was generated at the tip of a blunt-end 22 gauge needle with a 1 mL Hamilton 1001 LT threaded syringe. Surface tension was measured using a Theta tensiometer (Biolin Scientific) in the pendant drop mode. A period of 10 min (frame rate capture, 1 fps) was allocated to stabilize the droplet and ensure accurate measurement of the surface tension. Edge detection was applied to the images and the droplet shape was fitted to the Young-Laplace equation using the Attension Theta software. The equilibrium surface tension was determined by averaging the last 30 images of the 10 min period, with three experimental repeats at each concentration. The needles were replaced between samples and the syringes were rinsed with deionised water and oven dried before reuse. All sample preparation and measurements were obtained at room temperature, 20°C. Surface tension of the air-water interface was measured to be 72.7 ± 0.1 mN/m.

4.3. Results and Discussion

A compositional analysis of a commercial hydrolysed coconut oil blend, typically used to synthesize SCI, is displayed in Figure 4.4. The fatty acid mixture was derivatized to form the corresponding fatty acid methyl esters (FAMEs) to avoid peak tailing and long retention times. The resulting GC-MS chromatogram correlates with the review literature,[132] indicating that the dodecanyl (C12), tetradecanyl (C14) and octadecanyl (C18) are the most abundant chain lengths with concentrations of 43.9%, 20.0% and 10.9%, respectively. Due to the abundance of the dodecyl chain length in the commercial feedstock, the lauryl (C12) homologue of SCI, sodium lauroyl isethionate (SLI), was selected as a model isethionate ester surfactant for this study.

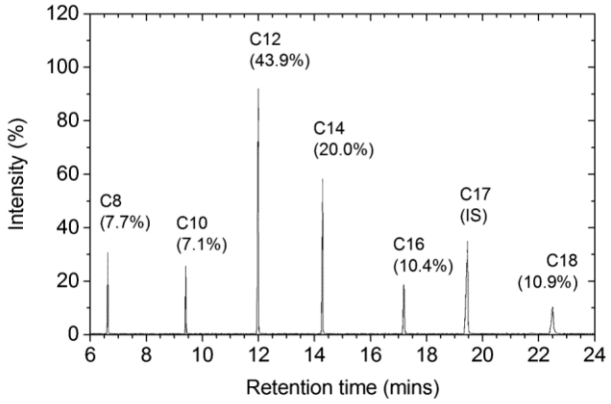

Figure 4.4. Gas chromatogram depicting the chain length distribution of carboxylic acids within the coconut derived fatty acid blend used to commercially synthesize sodium cocoyl isethionate. IS = Internal standard. Analysed as FAMEs via GC-MS.

4.3.1. Synthesis and Purification of SLI

Sodium lauryl isethionate (SLI) was synthesised via a single-step esterification of lauric acid and sodium isethionate with the use of additional solvents or catalysts. During the commercial synthesis of similar amide-based surfactants, a continuous recycle of distilled volatile carboxylic acids has been incorporated to maintain the acid excess necessary to drive the acylation.[138] In the synthesis of isethionates from biorenewable sources, the recycle of volatile components ensured that the desired chain length distribution of the feed material was maintained in the product. The distillation of fatty acids also means these raw materials can be reutilised in future syntheses with minimal change to the physical properties of the resulting product.

In the current study, SLI was obtained at a crude purity of 83% (via cationic titration) following a vacuum distillation. This purity is comparable to analogous materials produced via alternative synthesis routes which include catalysts and solvents, where the highest reported purity was 85%.[33] Successive cooling crystallisations in methanol at 0.5°C/min led to a 15% increase in purity following three purification cycles, after which no significant improvement was observed (Figure 4.5).

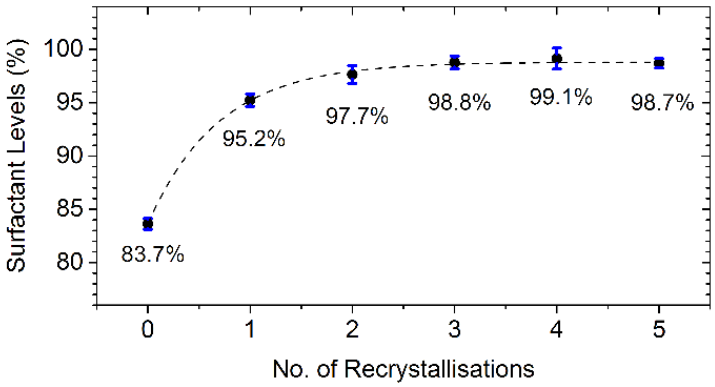

Figure 4.5. Purification profile of the SLI product. Repeat cooling crystallisations were conducted from 60°C to 20°C at 0.5°C/min. Surfactant levels were measured at each stage via cationic titration with benzethonium chloride. Data was fitted to an exponential association function. Errors bars obtained from repeat titrations.

As alkaline potentiometric pH titrations fail to distinguish between the surfactant and residual acid,[139] the industry standard method of cationic titration with benzethonium chloride solution was used for determining surfactant levels. However, this method has been reported to display an error of ~1%, as observed in the current study. [139] Possible attributable phenomena include operator error, the sparing solubility of organic complexes in the aqueous phase, and trace inorganic impurities in the methylene-blue solution.[89] Although newer titrants such as dialkylmethylimidazolium chloride (TEGO®trant) address some of these discrepancies,[140] an LC-MS analysis was additionally utilised in the current study to confirm that a purity of 98% had been achieved after three purification steps. Chemical structure was further verified by NMR.

4.3.2. FTIR Analysis of SLI

An FTIR analysis of SLI was carried out in an effort to characterize the impurities separated from the crude reaction mixture during the purification process. The spectra obtained from crude and purified samples of SLI are depicted in Figure 4.6. Absorptions of interest were assigned to their respective bonds and compared against literature values (see Table 4.1).

Table 4.1. Characteristic peaks observed via FTIR analysis of sodium lauroyl isethionate. Tabulated absorptions were obtained from reference analytical data.[141]

Spectrum	**Measured** $\tilde{\nu}_{max}$ (cm^{-1})	**Assignment**	**Tabulated** $\tilde{\nu}_{max}$ (cm^{-1}) [141]
Crude only	1718.3	Aliphatic C=O (Carboxylic Acid) Stretch	1700-1725 (strong)
Crude & Pure	1731.8	Aliphatic C=O (Ester) Stretch	1730-1750 (strong)
Crude only	2400-3300	O-H (Carboxylic Acid) Stretch	2500-3300 (broad)

Compared to the purified sample, the crude spectrum displays evidence of the residual lauric acid from broad O-H stretch observed between 2400 and 3300 cm^{-1}. The lauric acid also produces an additional C=O acid stretch in the crude sample at 1718 cm^{-1}. The strong absorption appears to be characteristic of the C=O ester stretch in SLI.

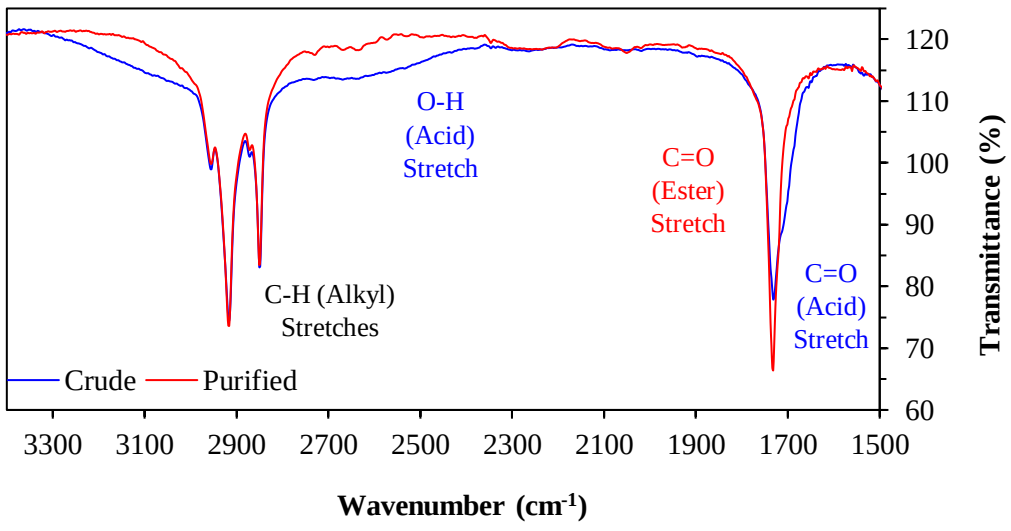

Figure 4.6. FTIR spectra of crude and purified samples of sodium lauroyl isethionate. Obtained using a Thermo Scientific Nicolet iS-10 FTIR Spectrometer.

4.3.3. NMR Analysis of SLI

The purified SLI was characterized by ^{1}H NMR spectroscopy to confirm that the ~98% surfactant levels measured via titration and LC-MS were indeed attributable to sodium lauroyl isethionate. The resulting NMR spectra and assignments are displayed in Figure 4.7 and Table 4.2.

Table 4.2. ^{1}H NMR signals observed from the analysis of purified SLI in d-DMSO with a 500 MHz NMR spectrometer. Chemical shift, integration and multiplicity were measured using the experimental spectrum using the MestreNova software package. Simulated shifts were generated by the PerkinElmer ChemNMR software. Tabulated shifts were obtained from structural libraries published by Pretsch et al.[141] Molecular assignments correspond to the model displayed in Figure 4.7.

Peak	**Chemical Shift (δ)**	Simulated Shift (δ)	Tabulated Shift (δ)[141]	Assignment	**Int.**	Expected No of H's	**Multi.**	Molecular Assignment
A	**0.87**	0.88	0.86	-C**H$_3$**	**2.00**	2	**Triplet**	(a)
B	**1.28**	1.26-1.33	1.31	-C**H$_2$**-	**16.08**	16	**-**	(b)
C	**1.51**	1.66	1.61	-C**H$_2$**-CH$_2$-COOR	**1.97**	2	**Triplet**	(c)
D	**2.26**	2.32	2.31	R-C**H$_2$**-COO-R	**1.99**	2	**Triplet**	(d)
E	**2.52**	-	2.50	DMSO	**-**	-	**Quintet**	-
F	**2.75**	2.75	2.94	-C**H$_2$**-SO$_2$	**2.01**	2	**-**	(f)
G	**3.33**	-	3.31	DMSO (D_2O)	**-**	-	**Singlet**	-
H	**4.20**	4.52	4.12	R-COO-C**H$_2$**	**1.99**	2	**-**	(h)

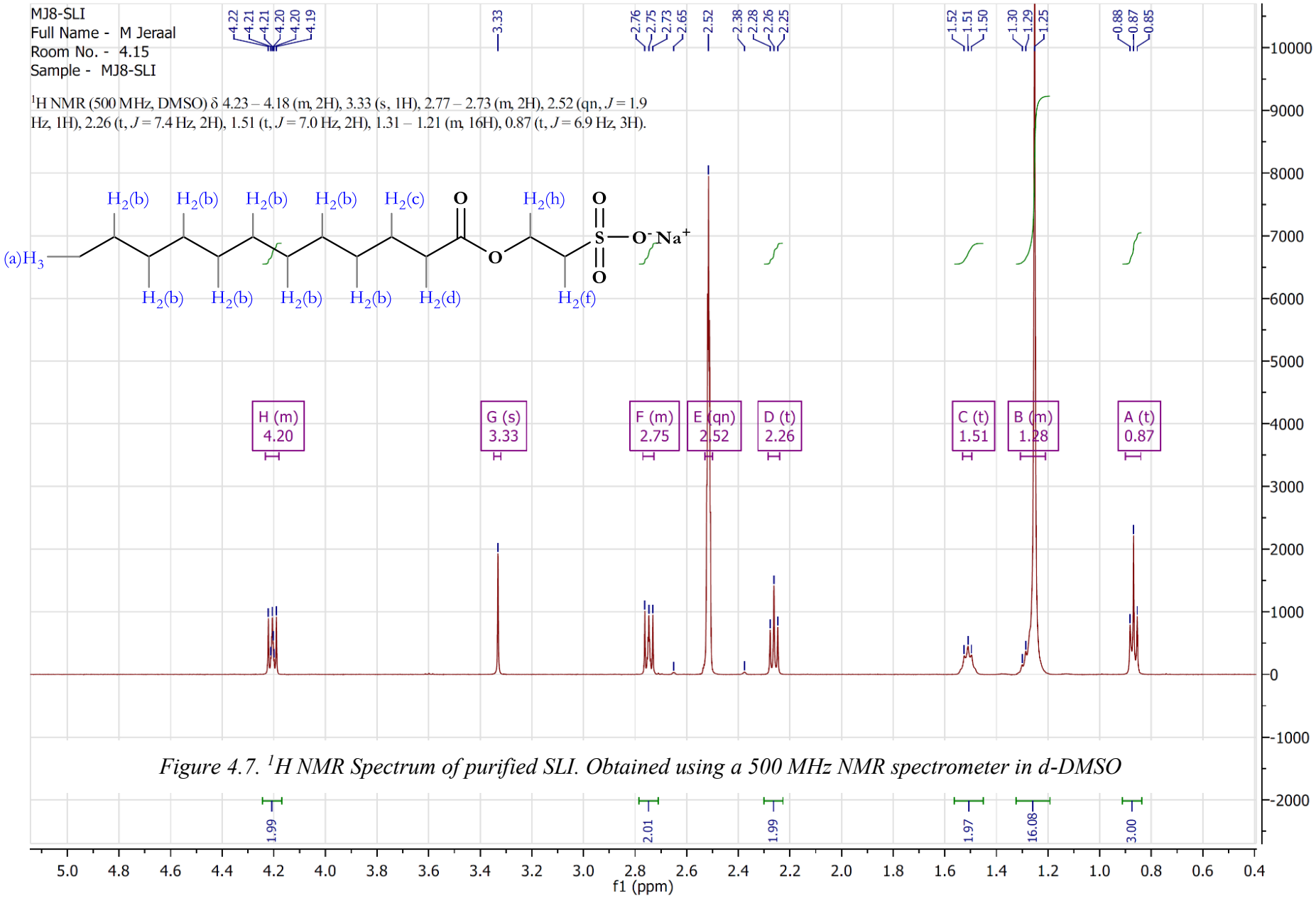

Figure 4.7. [1]H NMR Spectrum of purified SLI. Obtained using a 500 MHz NMR spectrometer in d-DMSO

4.3.4. LC-MS Analysis of SLI

In order to verify the structure assigned via NMR, a final LC-MS of the purified SLI sample was performed. The resulting chromatogram is displayed in Figure 4.8 indicates that the sample is now predominantly composed of a single chemical species.

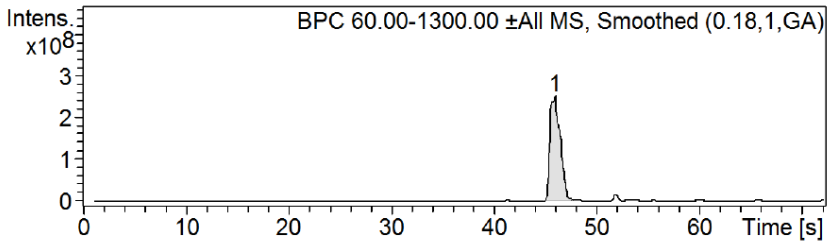

Figure 4.8. LC-MS chromatogram of purified SLI. Peak areas correspond to both positive and negative ions detected by the spectrometer. Obtained using a Dionex UltiMate 3000 UHPLC system equipped with a Bruker Amazon Speed mass spectrometer

The raw mass spectra generated from compound 1 (Figure 4.10) show how all the significant mass fragments detected by the mass spectrometer can be attributed to the desired SLI product.

Figure 4.9. Mass spectrometry peaks arising from LC-MS analysis of pure SLI. Quoted masses are the exact masses resulting from the most common isotopes of the corresponding elements, as provided by NIST.[142] M = 330.15 g/mol.

Spectrum	Peak (m/z)	Assignment	Theoretical m/z
+MS	331.22	$[M+H]^+$	331.16
+MS	639.11	$[2M+2H-Na]^+$	639.34
+MS	661.31	$[2M+H]^+$	661.30
+MS	683.34	$[2M+Na]^+$	683.28
-MS	307.22	$[M-Na^+]^-$	307.16
-MS	615.28	$[2M-2Na^+ + H^+]^-$	615.32
-MS	637.42	$[2M-Na^+]^-$	637.31

Upon closer inspection of the purified SLI chromatogram (Figure 4.8), an additional peak can be seen at a retention time of 52 s. An LC-MS analysis of pure lauric acid also produced a strong peak at 52 s using the same analytical method. When coupled with the other analytical information presented in this study, this data suggests that the ~2% of unaccounted mass is residual lauric acid.

Purified SLI – Positive ion (+MS) Mass Spectrum.

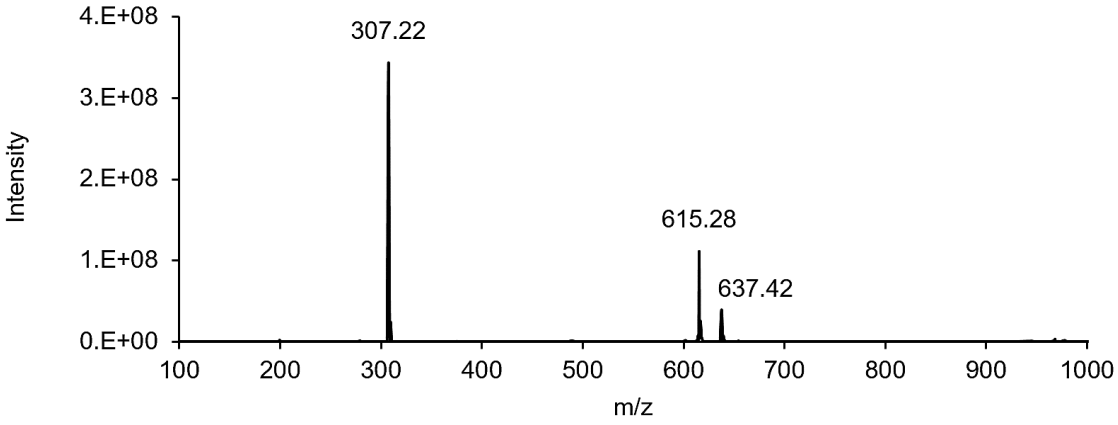

Purified SLI – Negative ion (-MS) Mass Spectrum.

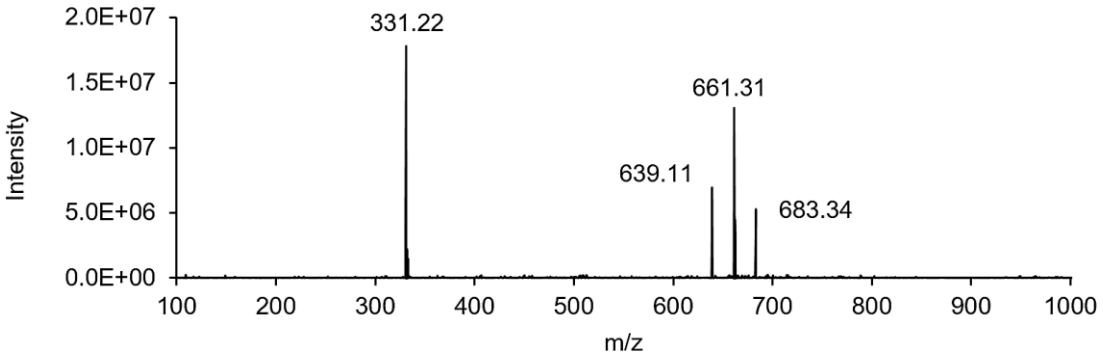

Figure 4.10. Positive-ion (top) and Negative-ion (bottom) mass spectrum of the main species (1) detected via the LC-MS analysis of purified SLI. See Figure 4.8 for the corresponding chromatogram. Thermal Analysis of SLI

Thermogravimetric analysis of the crude and purified samples (Figure 4.11) confirms that the main impurity within the crude SLI was residual lauric acid, which was removed to undetectable quantities in the purified sample. The absence of a measurable mass loss below

300°C in the purified SLI indicates that the anhydrous form of the surfactant was obtained and the subsequent storage of the purified SLI at an ambient humidity of ~60% for several weeks resulted in no significant moisture uptake. From an average of three measurements, the decomposition onset temperature of purified SLI was determined to be 331 ± 1°C. Consequently, there is minimal risk of thermal decomposition (and formation of SO_2 and SO_3) at the proposed reaction temperature of 240°C.

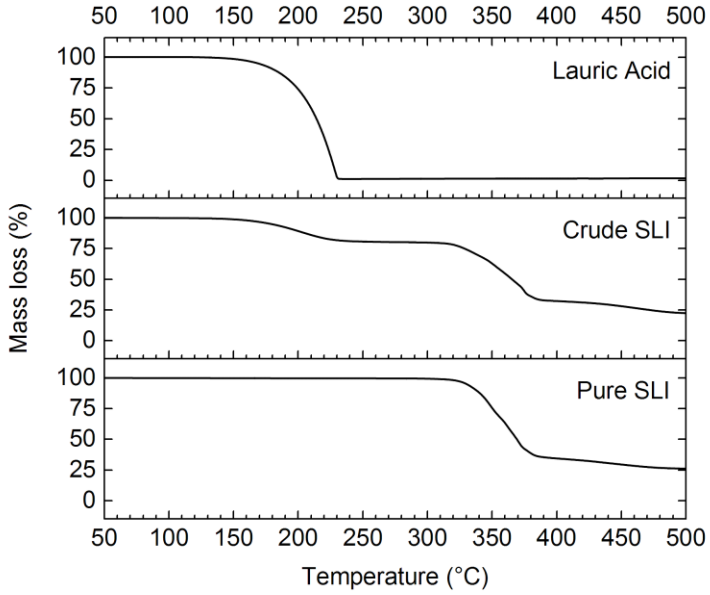

Figure 4.11. TGA profiles of lauric acid, crude and purified SLI at a heating rate of 10°C/min. Mass loss was normalised as a percentage of the initial sample mass. TGA was used to identify the presence of moisture at 100°C; impurities between 150 and 230°C; and the decomposition profile of SLI at temperatures beyond 300°C.

Differential scanning calorimetry (DSC) of the purified SLI (98% purity) produced a peak melting temperature of 225.2°C with a melting range of 224-226°C, see Figure 4.12. The previously reported melting range for SLI was 214-216°C, but no quantified purity was specified.[133] The crude SLI (melting temperature of 214.2°C) displayed some correlation with the previously reported values, thus suggesting that an improved purity could be the cause of the disparity with previous data through freezing point depression. The peak broadening observed in the crude SLI are suspected to result from combinations of the lauric acid and sodium isethionate pre-cursors.

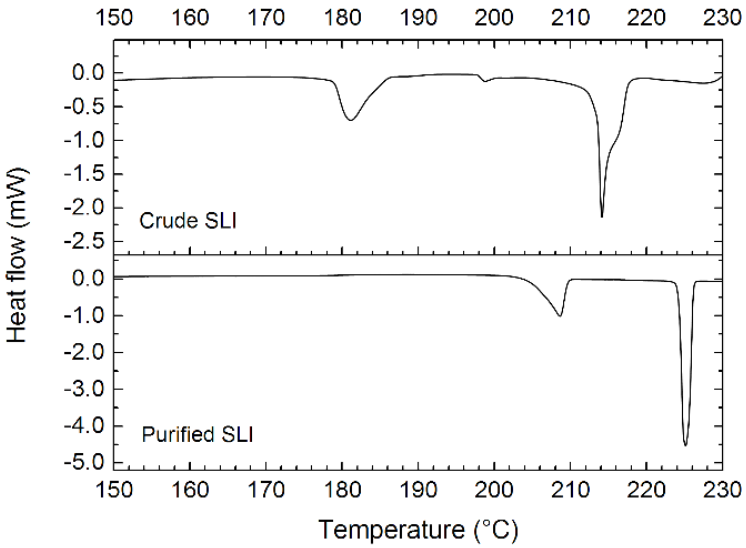

Figure 4.12. DSC analysis of crude reaction SLI and purified SLI. Samples were heated to 150°C at 50°C/min and then heated to 250°C at 1°C/min. Crude and purified SLI exhibited peak melting temperatures of 214.2°C and 225.2°C, respectively.

Measuring five independent SLI samples, the corresponding melting enthalpy (ΔH_{Fus}) was found to be 162 ± 2 kJ/mol. The transition at ~210°C in the purified SLI and ~180°C in the crude SLI are believed to be thermotropic phase transitions. These are widely reported to exist in anionic surfactant systems in the absence of water.[143-145]

4.3.5. Dynamic Vapor Sorption Analysis of SLI

An isothermal DVS analysis was conducted at 25°C to better understand moisture uptake during the commercial storage of isethionate ester surfactants. Although Karl-Fischer titration is the most common method of determining bulk moisture content in anionic surfactants,[139] the DVS method can provide sorption kinetics and thermodynamic data over a range of humidity levels.[146, 147] Prior to measurement, sample drying under N_2 flow showed a total mass loss of 0.01%. While alkyl sulfates are known to readily exist in hydrate form,[148-150] the lack of significant moisture loss observed during TGA and DVS analyses suggests that the anhydrous form of SLI was obtained using the current synthesis method. At 40% R_H, the sample mass had increased by 0.2%, suggesting relative stability of the sample during storage at or below 40% R_H. At 87% R_H, the mass gain was 2.35% which confirms the surfactant to be "slightly hygroscopic" according to Callahan *et al.*[151] and the European Pharmacopoeia.[152] There are three primary sorption mechanisms by which materials

take up moisture: i) surface adsorption, ii) bulk adsorption and iii) liquefaction by surface dissolution.[153] On reducing the R_H to 0%, the sample mass returned to its original value with an insignificant discrepancy of 0.005%. Since the sorption process is reversible, liquefaction is unlikely to be the predominant mechanism. With a 2.35% mass increase at 87% R_H, the surfactant could have formed a hemihydrate, which would yield a theoretical mass increase of 2.7%. Further analysis would be required to confirm both the structure and mechanism pertaining to the proposed transition. The hysteresis shown in Figure 4.13 does however indicate that any moisture uptake during storage at higher humidity can be significantly reduced if the sample is later exposed to a humidity level below 20%. This irreversibility is common in the sorption analysis of solid-gas systems.[154] While the hysteresis is significantly reduced below 20% RH, hysteresis is observed to some extent across the entire humidity range. Everett suggests that this behaviour results from a sorption mechanism that is independent of solid surface area,[155] thus supporting the postulation of a molecular hemihydrate species at elevated humidity levels.

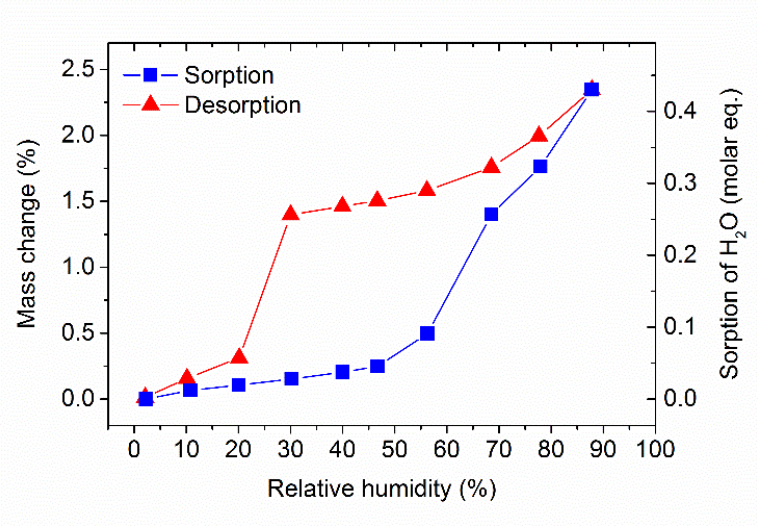

Figure 4.13. Dynamic vapor sorption analysis of purified SLI. The technique determines hygroscopicity by adjusting humidity levels and measuring the resulting sample mass. SLI was exposed to relative humidity levels between 0 and 90%, resulting in both sorption and desorption isotherms at a thermostatically controlled temperature of 25°C. Left axis shows mass increase relative to the initial mass of SLI (%). Right axis displays this increase as the molar sorption of water, relative to one mole of SLI.

4.3.6. Crystallisability of SLI

A polythermal solubility analysis was conducted to define the optimal crystallisation parameters for the commercial purification of isethionate surfactants. This approach was utilised in the current study as there was no prior solubility data for the SLI sample. Alcoholic solvents were considered as the purification solvent for SLI after a recent study revealed them to exhibit a high solubility for lauric acid, which the TGA data indicated to be the primary impurity in the crude product. Methanol was specifically selected as it exhibits a higher solubility for lauric acid than ethanol,[156] isopropanol[157] and n-butanol[157] at 20°C.

Preliminary solubility studies yielded very high ambient solubility in water, while ethanol exhibited a significantly lower solubility than methanol at elevated temperatures. Although methanol exhibits a higher toxicity than these substances, the preliminary data indicates that their adoption would be detrimental to both throughput and recoverable yields of SLI. Methanol was selected in preference to maximize the corresponding commercial value of the purification process.

Figure 4.14a shows the turbidimetric data for purified SLI in methanol during a heating and cooling cycle, highlighting well-defined crystallisation and dissolution on-set points as a function of temperature. The TGA, NMR and LC-MS analyses of the recrystallised SLI confirmed that the resulting precipitate was free from significant solvent and impurity levels. The metastable zone width (MSZW) as a function of cooling rate, displayed in Figure 4.14b, shows how equilibrium crystallisation and dissolution temperatures (T_{Cryst} and T_{Diss}) were explained. The MSZWs, as well as T_{Cryst} and T_{Diss}, were collated at each concentration to form the solubility curve of SLI in methanol (Figure 4.14c).

The metastable zone denotes conditions where the system is beyond the solubility limit; and nucleation can be induced through seeding, surface coarseness or the presence of foreign particulates.[46] Spontaneous nucleation in a binary homogenous system is kinetically precluded until the system reaches the limit of the metastable zone (Figure 4.14c).[158] The minimal dependence of the MSZW on the cooling rate at 20 g/L (Figure 4.14b) is reflected for all solution concentrations. This phenomenon indicates the crystallisation and dissolution kinetics are not rate limiting to their respective phase transition processes.[137] With decreasing temperature the system

exhibits an increasing MSZW. Knowledge of these changes to MSZW are important to controlling the commercial crystallisation processes and thus ensuring a reproducible crystal size, morphology and purity between batches.[46] The implementation of *in-situ* process analytical techniques could be used to maintain process conditions within the metastable zone at high temperatures, where the MSZW is smaller.[159]

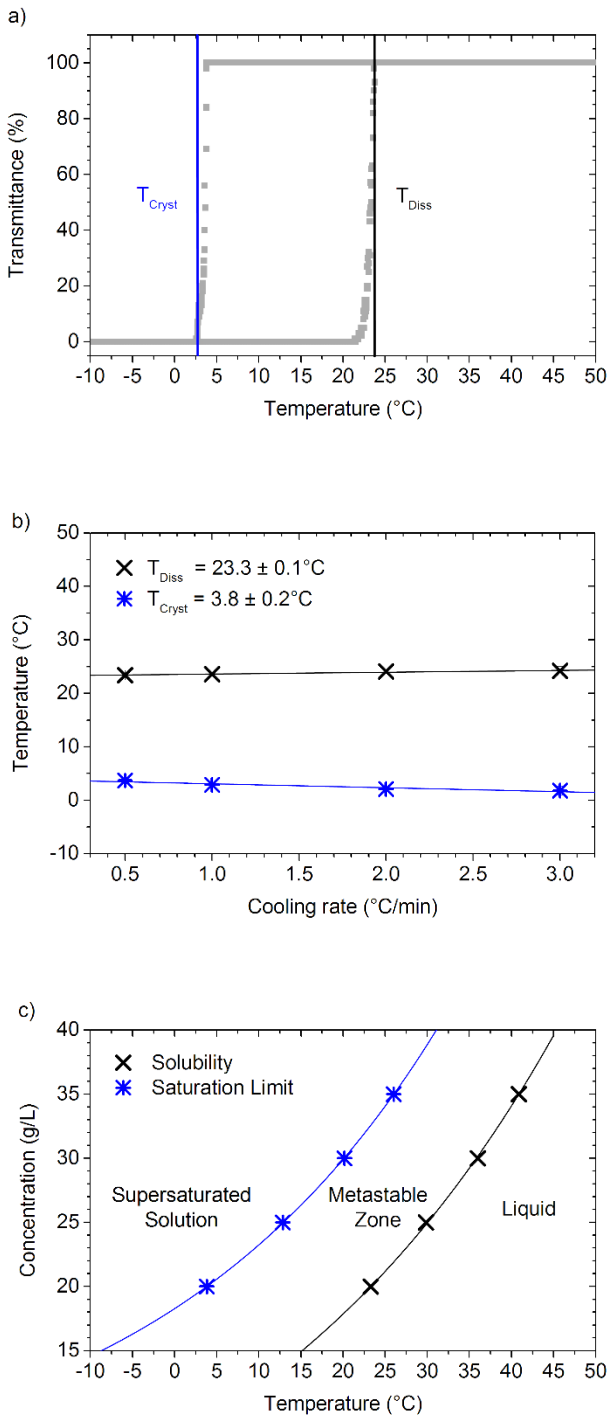

Figure 4.14. Polythermal turbidimetric solubility analysis of purified SLI in methanol between -10°C and 50°C at 700 rpm. a) Reaction profile of light transmission (%) vs. temperature (°C) depicting the extraction of crystallisation (T_{Cryst}) and dissolution (T_{Diss}) temperatures from Crystal16 system at 20 g/L. b) Change in T_{Cryst} and T_{Diss} with varying cooling rates at 20 g/L. Extrapolation to 0°C/min provides equilibrium values of T_{Cryst} and T_{Diss}. Legend displays equilibrium transition temperatures with the linear regression error.

c) Solubility curve of purified SLI in methanol plotted from equilibrium transition temperatures (T_{Cryst} and T_{Diss}) at all studied concentrations. Crystallisation and dissolution events were measured at concentrations of 20, 25, 30 and 35 g/L, each at temperature ramps of 3, 2, 1 and 0.5°C/min. See Figure S9 and S10 in the ESI for tubidimetric profiles and solubility data of all concentrations and cooling rates

4.3.7. Solubility Analysis of SLI

Through a van't Hoff analysis, the experimental solubility data can be compared with the ideal solubility of SLI, in a solvent-free environment, to determine the influence of the solvent on the crystallisation behavior. Both ideal and experimental Hoff analyses of SLI are shown in Figure 4.15.

This large deviation from ideality, when compared to other organic systems analysed using the same methodology,[137] suggests that the solvent-solute system exhibits a strong preference for solute-solute interactions. When the data is compared with a conductivity-based solubility analysis of SDS, the solubility of SLI in methanol at 50°C is approximately ~30% of the measured SDS solubility.[160] With respect to theoretical yields, a cooling crystallisation from -10°C to 50°C is predicted to recover more SLI than SDS, with predicted yields of 79% and ~71% respectively. The values of ΔH_{Diss} and ΔS_{Diss} for SLI indicate that the phase transition is strongly dependent on the enthalpy, see Table 1. The thermodynamic parameters for the dissolution of SDS in methanol are $\Delta H_{Diss} = 22.3$ kJ mol^{-1} and $\Delta S_{Diss} = 54.3$ J mol^{-1}.[160] Despite analogous dodecyl alkyl chains, the additional ethyl-ester group in the isethionate species creates a difference in chain length between SDS and SLI. This structural disparity and consequent hydrophilicity may contribute to the higher absolute solubility exhibited by SDS in a methanolic environment.

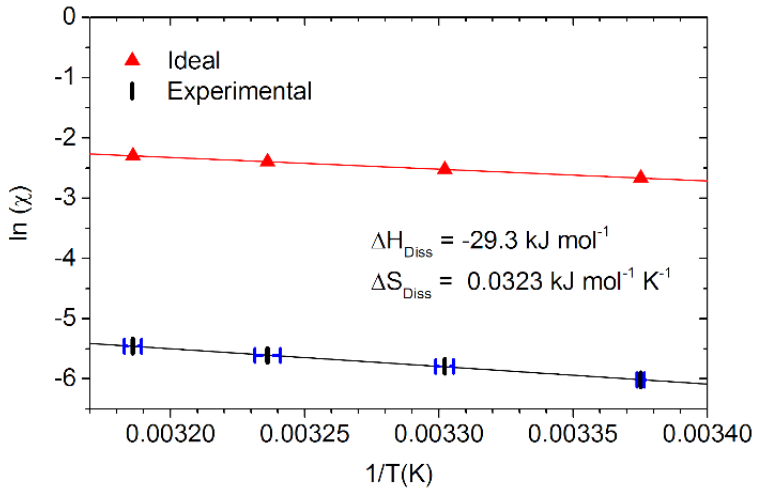

Figure 4.15. van't Hoff plot of polythermal solubility analysis of purified SLI in methanol between -10°C and 50°C. χ = mole fraction of SLI in methanol. Ideal solubility was calculated from the melting enthalpy (ΔH_{Fus}) and temperature (T_{Fus}) obtained via DSC.

The temperature-dependent activity coefficient (γ) for the crystallisation of SLI in methanol was finally calculated to quantify the deviation from ideality induced by the methanolic solvent environment. Turner *et al.* describe how this value is obtained by dividing the ideal solubility derived from the van't Hoff analysis, with the experimental solubilities measured via the polythermal solubility analysis.[137]

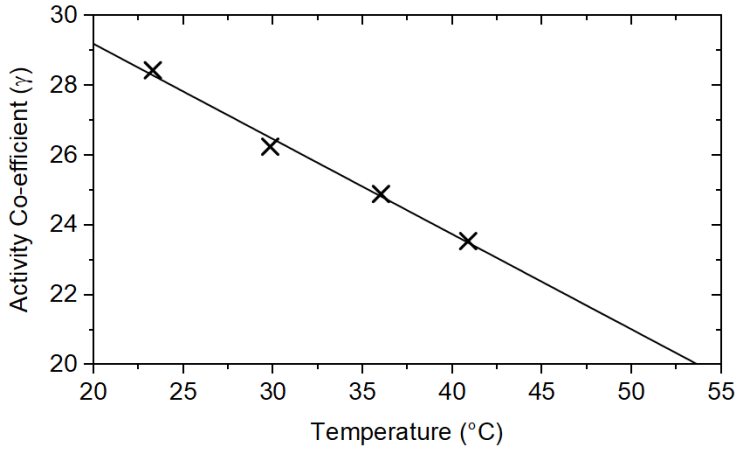

Temperature dependent activity co-efficient quantifying the deviation from ideality of the experimental solubility of SLI in methanol when compared with the ideal van't Hoff solubility.

4.3.8. Surface Tension Measurements of Aqueous SLI Solutions

The CMC of SLI at 20ºC was found to be 5.36 mM with a lower plateau surface tension of 37.9 mN/m, see Fig. 9. Bistline et al. reported a slightly higher CMC (6.4 mM) and plateau surface tension (46.6 mN/m) for SLI synthesized by the two-step process.[133] The lower surface tension in the current study suggests a higher wettability in aqueous environments, while a lower CMC confirms that a lower surfactant concentration was required to reach peak wetting performance. It is worth noting that the method used to determine the CMC and surface tensions was different from that reported by Bistline et al.[133]. However, the observed improvement in performance is more likely to result from an improved sample purity, as the CMC of alkyl sulfate surfactants is very susceptible to error from surface active impurities.[161] Foreign species can cause the surface tension to fluctuate and drop, below the CMC limit before stabilising at the actual micellar concentration. The absence of such fluctuation provides evidence that such impurities were not present in the current sample.

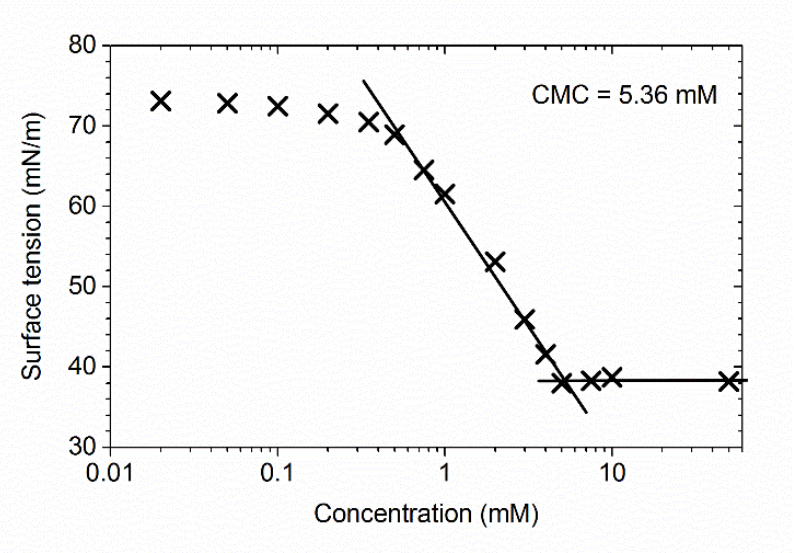

Figure 4.16. Surface tension as a function of the SLI concentration in water. The surface tension was determined by pendant drop analysis at 20°C. Equilibrium surface tension values were obtained by fitting the droplet shape to the Young-Laplace equation. Reported values are an average of 30 consecutive images (1 fps).

Recent studies have shown that SDS exhibits a CMC of 8.0 mM at 20°C,[162] with a corresponding plateau surface tension of 33 mN/m at pH 7.[163] The plateau surface

tension beyond the CMC for SLI (38 mN/m) is therefore higher than that measured for SDS (33 mN/m) at 20°C. The CMC, however, for SLI is higher than that for SDS at equivalent conditions. Hence, the proposed crystallisation process and resultant higher sample purity could therefore be critical to obtaining surface tension levels exhibited by SDS whilst maintaining the increased mildness offered by isethionate ester surfactants.

In summary, the thermodynamic and physicochemical properties determined from the characterization of SLI are provided in Table 1, along with the corresponding literature values for its alkyl sulfate analogue, sodium dodecyl sulfate (SDS).

Table 4.3. Thermodynamic and physicochemical properties of purified SLI (current study) and SDS (literature values).

	T_m (°C)	Solubility** (g/L)	ΔH_{Diss}** (kJ mol^{-1})	ΔS_{Diss}** (kJ mol^{-1})	Activity** coeff. (γ)	CMC* (mM)	Surf. tension at CMC* (mN/m)
SLI	225	17.9	29.3	0.0322	29.1	5.4	37.9
SDS	206 [164]	79.1 [160]	22.3† [160]	0.0543† [160]	*n/a*	8.0 [162]	33‡ [163]

* Measured at 20°C. ‡ pH 7 † Parameters obtained by processing the cited raw data using methodologies described in the current study.** Measured in MeOH.

4.4. Conclusions

Sodium lauroyl isethionate (SLI), the most abundant derivative of sodium cocoyl isethionate (SCI), was directly synthesised at the 500 mL scale without the use of solvent or catalytic species. The direct esterification of lauric acid reduced the number of reaction steps and eliminated the risk of HCl production which resulted from previous acyl chloride based reactions.[134] When compared with current published syntheses of SLI, the ancillary solvent-free route was to found to have the potential to increase process output, reduce material costs and remove the time and energy required for an industrial scale solvent recovery. While catalytic routes had previously been proposed for this type of reaction,[33] their use had led to an undesired phase separation in the resulting product at concentrations above 0.2 w/w%.[87] The reaction times, temperatures and yields in the current study were also similar to previous

catalytic routes.[33] The new process therefore eliminated the handling and recovery of catalytic materials without significant detriment to process efficiency.

The proposed recrystallisation of crude SLI resulted in a purity level of 98% after three successive recrystallisations in methanol. Following a recent review of commercially available surfactants,[33] this is considered by the authors to be the highest published purity of a sodium acyl isethionate surfactant. The use of crystallisation over chromatographic techniques meant that the purification could be scaled to industrial quantities and the solubility analysis of the purified surfactant provided process conditions through which this could be achieved. Although this study utilized a cooling crystallisation, the data was also deemed applicable to evaporative processes.[165] While the estimated throughput was lower than an analogous purification of SDS, SLI displayed higher yields at equivalent temperatures which was prospectively more important given its higher market value.

An aqueous surface activity analysis of the purified SLI yielded a surface tension much closer to the performance of SDS than previously reported samples of SLI. Given the widely acknowledged mildness of isethionate ester surfactants compared to traditional soaps and synthetic surfactants such as sodium dodecyl sulfate (SDS), the increased performance achieved through purification could be utilised in high value personal care formulations where harsher surfactants may be undesirable. High purity isethionates could also be used to create analytical standards, thus permitting the adoption of spectroscopic techniques to evaluate commercial surfactant synthesis. Reductions in time, labour and chemical use could be achieved when compared with the successive titration techniques currently used to detect and quantify surfactants in the personal care industry.

Chapter 5: Assessment of the Thermal Degradation of SLI Using Predictive Isoconversional Kinetics and Analysis of Evolved Gases

Synopsis: *This results chapter describes a detailed characterisation of the thermal degradation of SLI in both inert and oxidative environments. Predicted rates of isothermal degradation for a range of process conditions were determined using isoconversional kinetic methods. The gases evolved from the degradation of sodium lauroyl isethionate were then identified via TGA-FTIR. When coupled together, the two studies could be applied to minimise the evolution of undesirable or hazardous gases in isethionate manufacturing processes. In relation to the proposed research question, this chapter specifically identified the operating windows in which a detailed structural characterisation could be conducted.*

5.1. Introduction

Surfactants are the primary ingredients in most personal care formulations. They are present in shampoos, liquid cleansers and soap bars to reduce the surface tension of water and aid in the solubilisation of lipidic, sebaceous residues on the skin.[91] Due to its mildness, sodium lauroyl isethionate (SLI) is becoming an increasingly popular surfactant in such applications.[9] When compared with traditional counterparts such as alkyl carboxylates and sodium dodecyl sulfate (SDS), studies into SLI have demonstrated reduced irritation,[124] dryness [126] and adhesion to the stratum corneum[127] in personal care applications. SLI is also comparatively more stable in the presence of hard water by exhibiting no deposit formation or significant loss in lathering abilities in the present of alkali earth metals.[128]

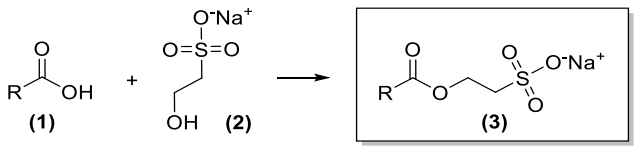

Figure 5.1. Reaction of lauric acid (1) with sodium isethionate (2) to form the dodecyl-chained (C12) sodium lauroyl isethionate (SLI) (3).[166] In this example, R= $C_{11}H_{25}$. A mixture of chemical homologues of alkyl chain length ranging between C8 and C18 can also be formed from the respective mixture of carboxylic acids. The resulting blend of surfactants is known as sodium cocoyl isethionate (SCI).[166]

SLI can be synthesised via the esterification of lauric acid with sodium isethionate,[166] as shown in Figure 5.1. In the study corresponding to the Figure 5.1, the materials were reacted at a temperature of 240°C for 4 hrs.[166] Patent literature relating to the commercial synthesis of SLI, as well as its homologues, report similar process temperatures of >200°C and analogous reaction times of 4-6 hrs.[16, 36, 87] In some instances, temperatures as high as 260°C for prolonged periods have been reported.[18, 167] A patent by Login *et al.* reported that the molten isethionate reaction mixture was

prone to thermal degradation at reaction temperatures in excess of 220°C.[168] In addition to reducing surfactant activity levels and consequent product efficiency, degradation was also reported to significantly harm the appearance and odour of the resulting product.[169] Whilst this work recommended an oxygen-free atmosphere to minimise process-induced degradation, no information pertaining to the quantitative stability of isethionate esters was provided.

While previous research regarding the thermal behaviour of isethionates has been limited, there have been studies on the stability and degradation characteristics of other alkyl surfactants, such as SDS. The initiation of thermal degradation in SDS was reported as 380°C,[170] indicating its comparatively higher stability with respect to SLI.[168] A pyrolysis-gas-chromatography analysis of SDS by Liddicoet *et al.* identified the degradation products following prolonged exposure to 650°C under an inert atmosphere.[171] It revealed large quantities of primary alcohol, coupled with traces of dodecyl vinyl chains. While both SDS and SLI consist of analogous lauryl alkyl chains, differences between the chemistry of their respective sulfate and sulfonate groups, coupled with the additional acid-ester group present in SLI might suggest an influence on its resulting material stability and associated evolved gas composition.

For the characterisation of thermal degradation processes, kinetic methods are typically applied to quantify the rates at which the underpinning chemical and physical processes occur.[172] These rates allow the evaluation of the corresponding energetic parameters; the correct identification of which permits the prediction of material stability.[173] In contrast to isothermal techniques where degradation is measured at multiple fixed temperatures, nonisothermal (or polythermal) isoconversional methods rely on multiple linear heating experiments to obtain the necessary data for kinetic model development.[174] While isothermal degradation techniques do exhibit some advantages, such as the ease of induction time measurement, their nonisothermal counterparts are becoming the recommended methodology for the kinetic analysis of thermally stimulated processes.[175, 176] With isothermal methods, it can be challenging to cover a representative range of temperatures within the measurable degradation zone. Slow degradation rates at lower temperatures can be time-consuming to measure to completion, while isothermal degradation at higher temperatures can be difficult to specifically identify if mass loss occurs whilst the sample is reaching the desired

isotherm.[175] Absolute isothermal analyses can often be difficult to achieve due to this inevitable period of equilibration, particularly when a sample is exposed to elevated temperatures.[174] While differential methods can be applied to help alleviate such discrepancies,[175] nonisothermal analyses can experimentally avoid these shortcomings, whilst simultaneously allowing the fast acquisition of degradation data across a broad range of temperatures.[172]

In this study, the thermal stability of SLI under the temperatures experienced during representative manufacturing conditions was evaluated. Thermogravimetric analysis (TGA), coupled with isoconversional kinetic modelling, was used to assess the thermal degradation of SLI in N_2 and air environments. Measurement under inert conditions was used to simulate degradation under the representative manufacturing conditions, whilst the analogous measurements in an oxidative environment were used to determine the influence of air ingress into the process system. Differential and integral isoconversional methods were used to independently quantify critical energetic parameters. These factors were then applied to predict the isothermal degradation of SLI, as a function of temperature, to determine the most suitable process conditions for minimising degradation. Following the kinetic overview, TGA-FTIR was used to obtain a real-time analysis of the gaseous evolutions resulting from the degradation process.

5.2. Isoconversional Kinetic Theory for Thermal Analysis

5.2.1. Introduction to Isoconversional Kinetic Methods

Thermogravimetric analysis (TGA) and differential scanning calorimetry (DSC) are commonly used to derive the data required to characterise thermal degradation processes using isoconversional kinetic methods.[172] Although TGA will be the focus of the current study, the techniques described can also be applied to data obtained from infrared spectroscopy,[177] mass spectrometry[178] and rheometry.[179] For the isoconversional kinetic analysis of TGA data, it is common for the experimentally obtained mass losses to be converted to a normalised, dimensionless, temperature-dependent mass loss (α) where $0 < \alpha < 1$.[176] In the context of thermal decomposition kinetics derived via TGA, α is commonly referred to as the 'degree of degradation'.[175]

In this study, Eq. (16) shows how α was obtained from the initial sample mass before heating ($m_{Init.}$), the final sample mass after heating ($m_{Fin.}$) and the observed sample mass ($m_{Curr.}$) at a given temperature.

$$\alpha = \frac{m_{Init.} - m_{Curr.}}{m_{Init.} - m_{Fin.}} \tag{16}$$

Nonisothermal (or polythermal) isoconversional degradation kinetics are fundamentally derived from the Arrhenius equation Eq. (17).

$$k\,(T) = A\,exp\left(-\frac{E_a}{R \cdot T}\right) \tag{17}$$

k(T) is the Arrhenius rate constant, A the Arrhenius pre-exponential factor, R the universal gas constant (8.314 J mol^{-1} K^{-1}), E_a the activation energy (J mol^{-1}) and T the absolute temperature in Kelvin. Vyazovkin states that the rate of thermally stimulated processes are dependent on the reaction model *f(α)* and temperature-dependent rate constant *k(T)*, as shown in Eq. (18).[176]

$$\left(\frac{d\alpha}{dt}\right) = k(T) \cdot\ f(\alpha) \tag{18}$$

Some forms of the equation include an additional pressure-dependent variable *h(P)*. However, in the case of thermal degradation kinetics, this is assumed insignificant and neglected in most cases.[175] Combining Eq. (17) and (18) yields the general rate equation Eq. (19) for the nonisothermal kinetic analysis of thermally stimulated degradation processes.

$$\left(\frac{d\alpha}{dt}\right)_{\beta} = A\,exp\left(-\frac{E_a}{R \cdot T}\right)\,f(\alpha) \tag{19}$$

The rate ($d\alpha/dt$) is a function of heating rate (β), which corresponds to a constant linear heating rate where $\beta = dT/dt$. The reaction model *f(α)* is dependent on, and consequently indicative of, the thermal degradation mechanism.[180] For conventional isothermal analyses, the type of mechanism can be determined by identifying the relationship between *f(α)* and α. When fitting experimental data to such models,

however, similarity between fits can complicate the identification of a single reaction model.[172] Criado *et al.* have previously demonstrated how the same predicted TGA curve can be generated from three different reaction models.[181] The model fitting approach can also be overly simplistic with respect to more complex systems, which can exhibit one mechanism at the start of the degradation process, then transition into another at higher degradation temperatures. Eq. (3) additionally shows how it can be numerically challenging to mathematically separate and distinguish between $k(T)$ and $f(\alpha)$, thus further increasing the difficulty in obtaining a single reaction model.

Isoconversional kinetics conversely forgo the fitting of a reaction model $f(\alpha)$, as well as the calculation of a single pre-exponential factor A. This approach is based on the fundamental assumption that a single form of Eq. (4) is only applicable to a single degree of degradation (α).[172, 182] This temperature dependence on the Arrhenius parameters is proposed on the basis that solid-state thermal decomposition is typically a complex, interdependent multi-step chemical process. The multitude of constituent, concurrent physical processes include the diffusion, sorption, and sublimation of different species in multiple phases.[183] Any single activation energy value therefore used to represent a process of corresponding complexity, is inherently composed of the individual activation energies related to its constituent physical and chemical processes. Since the relative contributions of these individual processes to the overall degradation rate changes with respect to temperature, any effective activation energy (E_a) determined for the holistic characterisation of thermal degradation process is consequently a function of temperature and the degree of degradation (α). Through multi-rate degradation experiments, values of the temperature-dependent effective activation energy can be obtained following differential or integral treatment of Eq. (19). Through the parametrisation of $f(\alpha)$ and the Arrhenius factor A, predictions of process degradation rates and material lifetimes can be reliably achieved. Compared with traditional isothermal kinetic analyses, nonisothermal isoconversional methods therefore permit the holistic kinetic analysis of complex thermally stimulated processes, without any prior knowledge of the degradation mechanism(s). The concept of variable activation energy, its basis in complex multiple-step processes, as well as its broader application in the characterisation of thermal stability, polymerisation, crystallisation and phase transitions are described in the literature.[172] In order to obtain a more comprehensive analysis of the thermal degradation characteristics of

organic materials.[31-32] both isoconversional and model-fitting techniques can be applied in tandem, with research comparing both approaches when studying analogous chemical systems.[33]

5.2.2. Calculation of Activation Energies

Both differential and integral approaches were separately used to calculate the effective activation energy (E_a). The Friedman method is a common differential method for the isoconversional analysis of thermal degradation processes.[184, 185] It is derived by taking the natural log of Eq. (19), as shown in Eq. (20).

$$ln\left(\frac{d\alpha}{dt}\right)_{\alpha} = ln[A(\alpha) \cdot f(\alpha)] - \frac{E_a(\alpha)}{R \cdot T(\alpha)} \quad (20)$$

In addition to the rate ($d\alpha/dT$) and reaction model $f(\alpha)$, the activation energy (E_a), pre-exponential factor (A) and temperature (T) are also considered to be dependent on the degree of degradation (α). Where applicable, the respective variables will be denoted as $E_a(\alpha)$, $A(\alpha)$ and $T(\alpha)$ to reflect this. Due to the direct differential treatment of Eq. (4) utilised by the Friedman method, the resulting experimental rate data can be susceptible to background noise.[174, 186] While data smoothing techniques prior to isoconversional analysis can be applied to reduce the error in extracted activation energies,[124] these issues can be avoided by employing an integral solution to the general rate equation for thermal degradation.

At multiple heating rates, Eq. (19) can be rearranged and integrated to form Eq. (21).

$$\int_0^{\alpha} \frac{d\alpha}{f(\alpha)} = \frac{A}{\beta}\int_0^{T} exp\left(-\frac{E_a(\alpha)}{R \cdot T(\alpha)}\right) dT \quad (21)$$

The left hand side of Eq. (6) is commonly abbreviated to $g(\alpha)$. Through orthodox model-based kinetic analyses, $g(\alpha)$ could be characterised by integrating the corresponding mechanistic reaction model $f(\alpha)$. The temperature integral on the right hand side, however, results in an incomplete gamma function which is insolvable in its closed form.[187, 188] A range of mathematical approximations to this integral,

however, have permitted the development of integral isoconversional methods for the kinetic analyses of thermal processes.[189] The Flynn-Ozawa-Wall (FWO) method is an early and popular integral application of the isoconversional technique,[190] utilising Doyle's approximation for the temperature integral.[188] A more accurate method proposed by Kissinger-Akahira-Sunose (KAS),[191] is an isoconversional development of a previous method for thermal analysis which originally assumed a constant activation energy.[192] KAS is related to the Coats and Redfern method,[193] as both approaches use the Murray approximation to the temperature integral.[180, 194] Through this approximation, Eqs. (19) and (20) can be combined to form Eq. (22), which depicts the KAS method for the integral analysis of thermal processes.

$$ln\left(\frac{\beta}{T(\alpha)^2}\right)_\alpha = -ln\left[\frac{E_a(\alpha)}{R \cdot T(\alpha)} \cdot \int_0^\alpha \frac{d\alpha}{f(\alpha)}\right] - \frac{E_a(\alpha)}{R \cdot T(\alpha)} \qquad (22)$$

Variations of Eq. (22) include integral isoconversional methods by Starink[195] and Lyon,[196] which adopt a similar application to the KAS method. Recently, more advanced mathematical approaches by Vyazovkin[197, 198] have further produced exact integral solutions without numerical approximation. These methods can reliably predict both isothermal and nonisothermal levels of degradation in the absence of a reaction model *f(α)* and Arrhenius factor (*A*).[172] For ease of application and comparison, however, the current study focused on the KAS method for the integral acquisition of activation energy values.

5.2.3. Prediction of Isothermal Degradation

By rearranging and integrating Eq. (19), the time-dependent isothermal degradation at a specified temperature (T_0) can be predicted. Eq (23) derived by Friedman describes the corresponding execution in the current study.[184, 199]

$$t_\alpha = \int_0^\alpha \frac{exp\left(\frac{E_a(\alpha)}{R \cdot T_0}\right)}{[A(\alpha) \cdot f(\alpha)]}\, d\alpha \qquad (23)$$

The values of the integral with respect to α are calculated using the Friedman-derived activation energies. Values for $A(\alpha) \cdot f(\alpha)$ can be obtained from the y-intercepts of the fitted lines used to obtain the corresponding activation energies. The resulting integral can then be plotted against α and iteratively integrated at increments of $\Delta\alpha = 0.01$ to obtain t_α at the given isothermal temperature (T_0).

5.3. Experimental

5.3.1. Thermogravimetric Analysis (TGA) of SLI

Sodium lauroyl isethionate was prepared and isolated to 98% purity in accordance with the methods described previously.[166] Samples of SLI were analysed using a Mettler Toledo TGA/DSC 1 Thermogravimetric Analyser. 3-4 mg of material was weighed to the nearest 0.1 µg using a Mettler Toledo UMX2 Ultra-Microbalance and placed in a 100 µL aluminium crucible with pierced lid. Individual samples were heated from 30°C to 550°C at rates of 5, 10, 20 and 50°C/min. Sample mass measurements were collected every second to the nearest 0.01 µg. Separate samples were analysed in air and in N_2 atmospheres to permit the development of individual degradation models for the thermo-oxidative and thermal degradation of SLI. Gas flow was maintained at 50 mL/min throughout all analyses.

5.3.2. Data Processing and Isoconversional Kinetic Analysis

For all TGA derived nonisothermal degradation data, the mass loss (g) was converted to a degree of degradation (α) using Eq. (1). Individual sets of Friedman-derived activation energies for $0 < \alpha < 1$ were then calculated for the thermal degradation of SLI in both air and N_2. From the normalised TGA data, the rate ($d\alpha/dT$) was obtained for each run using Eq. (1). $ln(d\alpha/dT)$ was plotted against $1/T$ as a function of the degree of degradation (α) and the one-dimensional gradient in the z-plane was extracted at 0.01 increments of α. These gradient values were subsequently converted to the corresponding activation energies using the gas constant, in accordance with Eq. (5). Analogous activation energy values were concurrently determined via the Kissinger-Akahira-Sunose (KAS) method using Eq. (7), where $ln(\beta/T(\alpha))$ vs. $1/T$ was plotted as a function α at the experimental heating rates.

The isothermal degradation of SLI in both air and N_2 was calculated by the Friedman method using Eq. (8) and the Friedman-derived activation energies. Degradation was predicted at 10°C intervals between 220 and 280°C, and the predicted degradation at 5 hrs was considered to determine the influence of changing synthesis temperatures on degradation levels at the recommended reaction time.[166] To validate the isothermal predictions, samples of SLI were heated from 30°C to 240°C at 50°C/min and held at 240°C for 5 hrs, in accordance with the published synthesis conditions.[166]

5.3.3. Quantitative Evolved Gas Analysis via TGA-FTIR Spectroscopy

A Mettler Toledo TGA/DSC 1 Thermogravimetric Analyser was connected to a Thermo Scientific Nicolet iS-10 FTIR Spectrometer using a Thermo Scientific Nicolet TGA-IR module. The TGA-FTIR system consisted of a 5 ft glass-lined stainless steel transfer line (1/8" OD). Both the cell and transfer line were heated to 180°C to minimise condensation. Samples of SLI were heated via TGA from 30°C to 550°C at 10°C/min. SLI was separately analysed in both air and N_2 at respective flow rates of 50 mL/min. Prior to heating, the TGA gas was purged for 30 mins for the acquisition of a representative background FTIR spectrum. Sample spectra were then measured at 36 s intervals, via 36 consecutive scans between 500 and 4000 cm^{-1}, for the duration of the heat cycle. Species of interest were identified using the Nicolet FT-IR Vapor Phase Spectral Library from Thermo Scientific. The five most abundant species in each sample were then quantified via their respective characteristic bands using the Chemigram function in the Thermo Scientific OMNIC Series package.

5.4. Results and Discussion

5.4.1. Thermogravimetric Analysis (TGA) of SLI

The selected temperatures and heating rates for the TGA analysis of SLI were representative of the conditions utilised for previous isoconversional studies on chemically similar organic esters.[200, 201] Figure 5.2 depicts the DTG data of the resulting experiments.

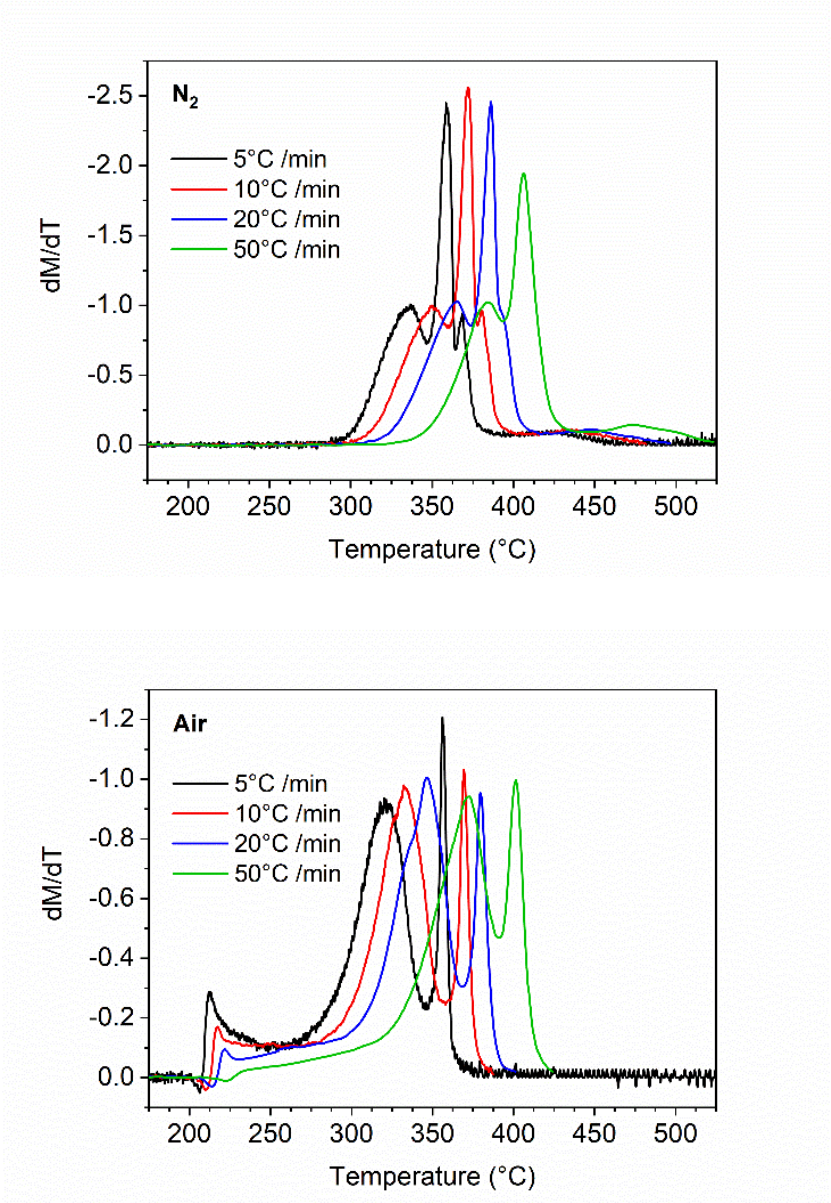

Figure 5.2. Differential DTG data for the degradation of SLI in N_2 (top) and air (bottom) at heating rates of 5, 10, 20 and 50°C/min. For dM/dT, M = mass loss (%) and T = temperature (°C).

SLI was found to exhibit three distinct degradation zones in air, while the inert system (N_2) displayed an additional fourth zone during the latter stages of the studied temperature range. After the final degradation zone, a period of thermal stability ($dM/dT \approx 0$) was observed at all heating rates in both air and N_2. Coupled with the reproducible thermal behaviour across different heating rates, this provided a robust window in which the data could be normalised and processed for isoconversional analysis. Mass loss (%) data was normalised in terms of the degree of degradation (α)

where the end of the final degradation zone was designated as $\alpha = 1$. Example data is shown in Figure 5.3. Onset temperatures of specific degradation zones, as well as the endset temperatures utilised for mass normalisation are provided in Table 5.1. In this context, the terms onset and endset correspond to temperatures at which degradation processes commence and conclude respectively.

Table 5.1. Tabulated values of onset temperatures for each degradation step identified in the thermal decomposition of SLI. Temperatures were measured via tangential extrapolation as described in Section 1.1. 'Endset' refers to the endset temperature of the final degradation zone. Only three degradation zones were observed in air so onset temperatures for step 4 are not provided.

Degrad. Step Onset	**N_2 Transition Temp. (°C)**				**Air Transition Temp. (°C)**			
	5°C /min	10°C /min	20°C /min	50°C /min	5°C /min	10°C /min	20°C /min	50°C /min
1	300.4	311.8	325.6	348.4	206.5	210.2	213.7	222.3
2	346.6	359.7	373.6	393.6	288.4	302.7	311.5	329.8
3	366.6	377.8	391.6	*	345.6	356.2	368.6	391.0
4	376.5	390.0	403.6	424.4	-	-	-	-
Endset	464.4	477.7	496.0	522.6	362.4	376.8	386.0	416.0

**Accurate onset measurement could not be obtained at 50°C/min.*

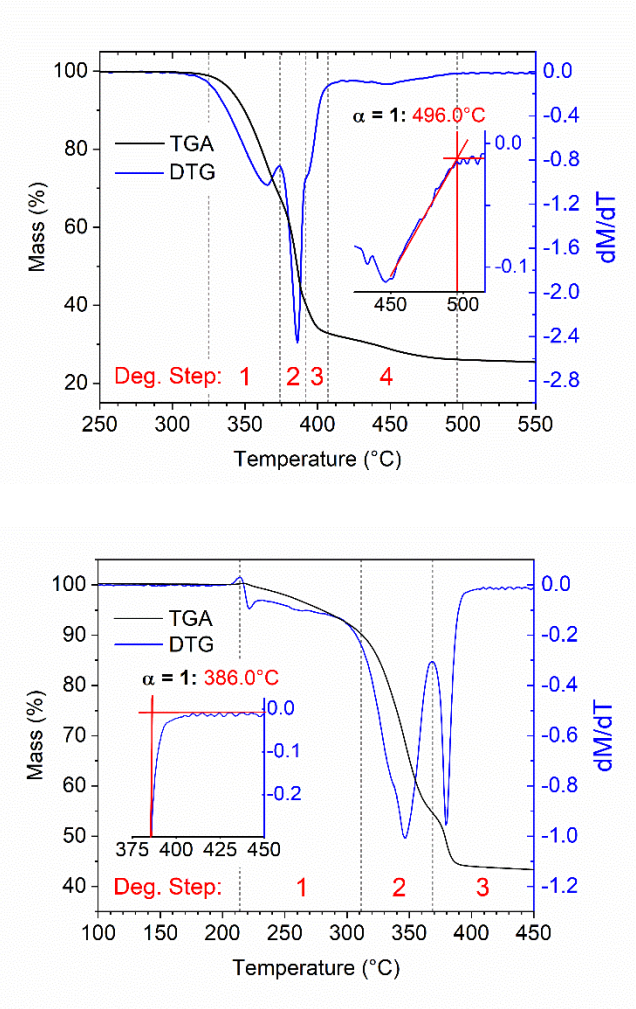

Figure 5.3. Identification of final mass (m_{fin}) from experimental TGA data. The data depicts decomposition of SLI in N_2 (top) and air (bottom) at 20°C/min. Black lines represent mass loss (%), while blue lines and axes show the corresponding differential DTG data. Inset shows an extract of the primary DTG data, showing greater detail in the y-axis. Onset, peak and endset temperatures for each degradation step were obtained via the tangential extraction of DTG data, as shown in the inset figure. Red numbers and dashed lines correspond to the degradation steps identified for the decomposition of SLI. In N_2, the final mass (m_{fin}) was designated as the sample mass at the endset temperature of degradation step 4, which corresponded to 496.0°C. In N_2, the final mass (m_{fin}) was designated as the sample mass at the endset temperature of degradation step 3, which corresponded to 386.0°C.

A high temperature degradation study of SDS reported a residual mass of 35 wt% following pyrolysis at 700°C in N_2.[202] Although the maximum temperatures in the current study were 550°C, post-analysis of the crucibles showed similar black residues

to those described in the SDS study, with comparable mass losses. The degradation onset in N_2 was found to be 348°C at 50°C/min and lower than that of SDS, where the decomposition temperature was reported to be 380°C.[170] The synthesised SLI displayed a strong dependence on heating rate, with a much lower decomposition onset of 300°C observed at 5°C/min (N_2). In air, there was less variation in degradation onset temperature with values between 206 and 222°C at the experimental heating rates of 5 to 50°C/min respectively. The melting point of SLI was reported as 225°C when heated at 1°C/min.[166] The commencement of degradation was not considered to be significantly influenced by melting, as mass loss was observed below this temperature at all experimental heating rates.

Due to the kinetics of the process, the absolute residual mass (wt%) at $\alpha = 1$ changes as a function of the heating rate (β). In order to obtain the mass (wt%) at $\alpha = 1$ which is independent of β, the masses derived in Section 1.1 were plotted as a function of the heating rate, then extrapolated back to 0°C/min. This extrapolated methodology for acquiring kinetic-independent parameters is commonly utilised in thermally stimulated processes[203] such as DSC[204] and crystallisation[136], in instances where a linear dependence on heating rate is exhibited. The resulting plots for the thermal degradation of SLI in air and N_2 are shown in Figure 5.4.

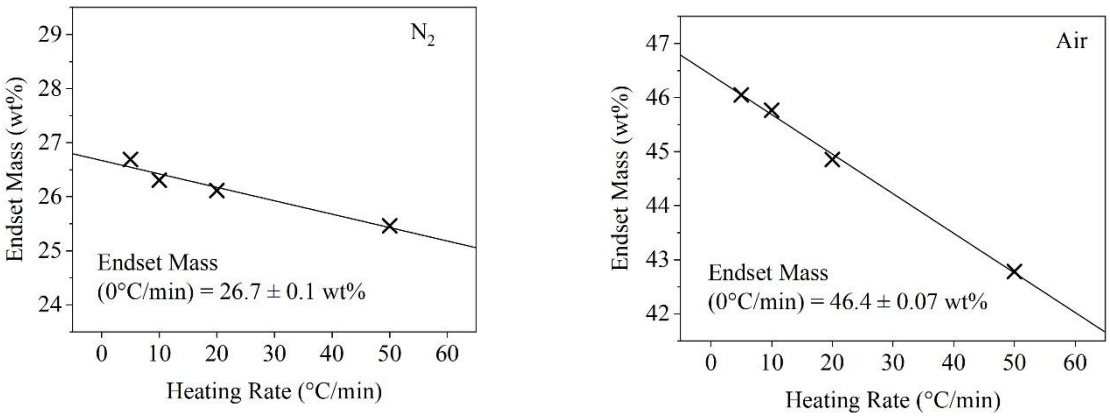

Figure 5.4. Extrapolation of endset temperatures ($\alpha = 1$) at different heating rates to determine the equilibrium residual mass at 0°C/min. Each point corresponds to the tangential endset temperatures identified in N_2 and air respectively. The quoted errors correspond to the error of the intercepts of the respective fitted lines.

The difference between degradation in air and N_2 correlates with Vyazokin's postulation that thermo-oxidative degradation typically occurs at approximately 100°C below the analogous process in an inert atmosphere.[205] Prior to degradation onsets, the observed SLI mass loss before 180°C in air and 280°C in N_2 was less than 0.2 wt%, indicating a minimal presence of retained water in SLI under ambient conditions.

5.4.2. Isoconversional Kinetic Analysis

Differential Friedman and integral KAS models were used to obtain the change in E_a as a function of the degree of degradation (α) in both air and N_2. An example plot of the gradients used to determine the activation energies via the Friedman method is shown in Figure 5.5.

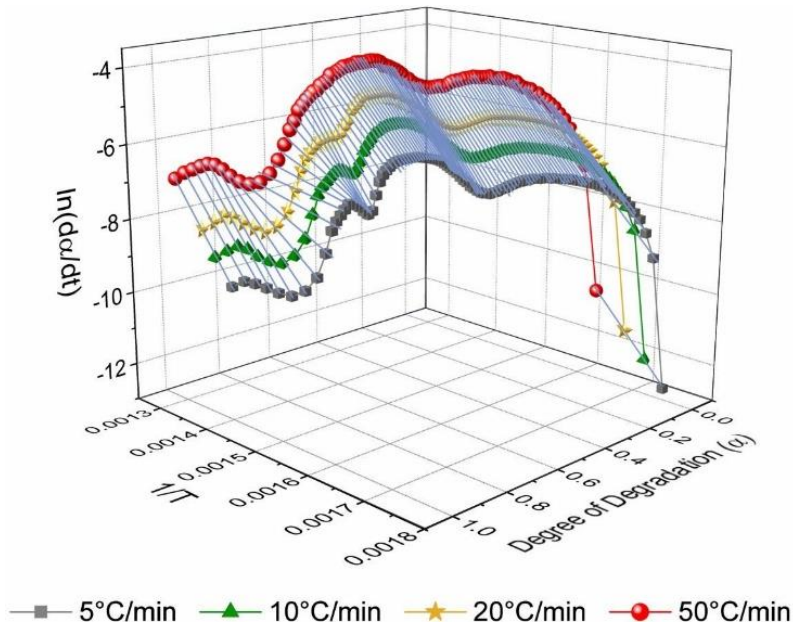

Figure 5.5. Activation energies obtained via the Friedman differential method of isoconversional kinetic analysis. The data depicts ln(dα/dT) vs. 1/T vs. α for the degradation of SLI in N_2 at heating rates of 5, 10, 20 and 50°C/min. Gradients in the z-plane (blue lines) correspond to the activation energy at the given degree of degradation (α), see Eq. (5)

The corresponding activation energies obtained by both isoconversional methods, in air and N_2, are displayed in Figure 5.6.

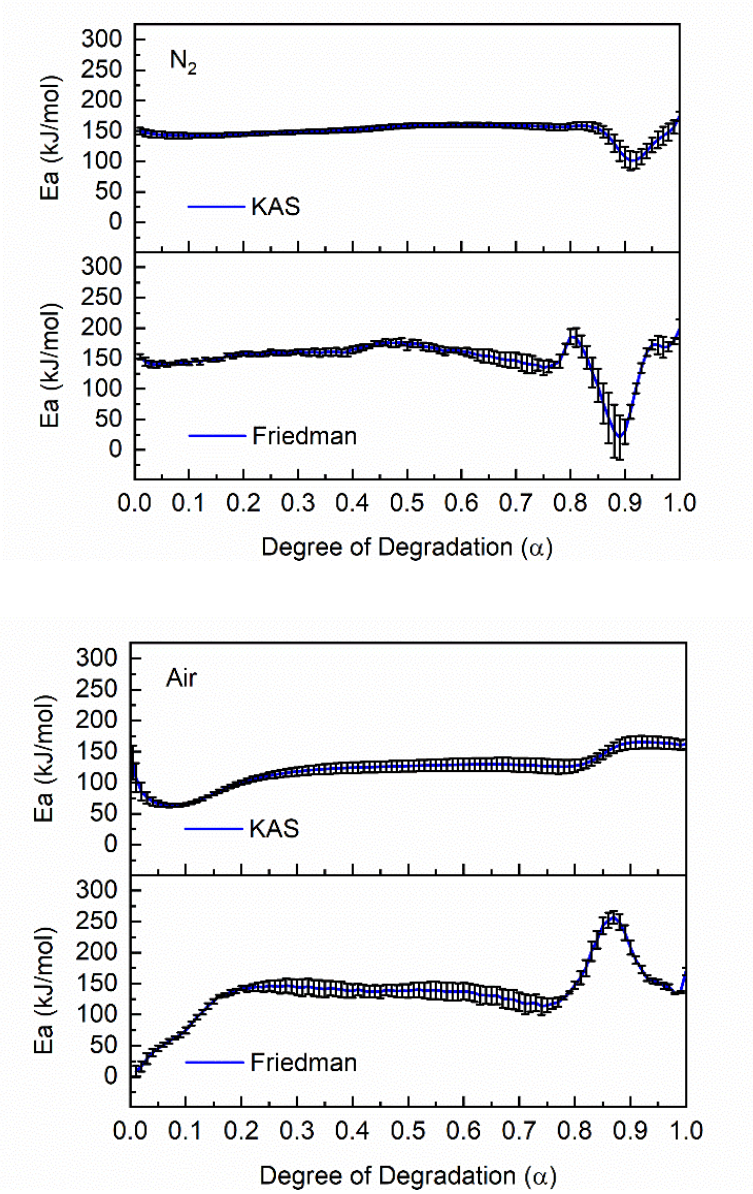

Figure 5.6. Change in activation energy for the thermal and thermo-oxidative degradation of SLI in N_2 (top) and air (bottom). Values were obtained using the Friedman and KAS isoconversional kinetic models. Error bars correspond to the error in the respective regression fits used to calculate energies. Activation energy values are provided in Tables A.1 to A.4 in the Appendix.

In N_2, environmental changes in E_a were found to approximately coincide with the different degradation zones, see Table 5.1 for tangential onset data. The activation energies between $\alpha = 0$ and 1 from the Friedman and KAS models were found to correlate well with each other, with average values of 150.1 and 149.1 kJ/mol

respectively. Biofuels exhibit some chemical similarity to SLI, with a common presence of alkyl chains, as well as a prevalence of C-C, C-O and C=O bonds. The triglyceride systems exhibited similar average Friedman values of 124 kJ/mol[200] and 167 kJ/mol[206] respectively. The reported degradation onsets of ~300°C for these species were also similar to those observed in the current study and much higher than the corresponding methyl esters where decomposition commenced between 100 and 150°C.[200, 206] This may suggest that the additional electron density donated by the isethionate group, when compared to a methyl group, stabilises the ester bond similar to the glycerol group and fatty acid chains in the triglyceride system, thus resulting in a greater thermal stability in an inert atmosphere.

In the oxidative air environment, average activation energy values between $\alpha = 0$ and 1 were calculated to be 135.6 and 120.8 kJ/mol using the Friedman and KAS models respectively. A drop in the activation energy compared to the inert process expectedly results in lower degradation onset temperatures.[207] It is worth noting that while activation energy values provide an insight into thermal decomposition behaviour, the degradation rate is also dependent on the pre-exponential factor *A*. Whilst Friedman values of $ln\,[A(\alpha)\cdot f(\alpha)]$ have been calculated, the physical meaning of *A* has been reported to be inconclusive in the context of isoconversional kinetics .[208, 209]

In both the N_2 and air environments, Figure 5.6 shows how the data obtained by the Friedman method appears noisier than the data obtained by KAS. As the former method directly differentiates the general rate equation, it typically produces a greater fluctuation in calculated E_a values.[210] While data smoothing filters are common,[211] they were not utilised as the majority of R^2 values relating to Friedman E_a values were greater than 0.98 and therefore deemed reliable, see Tables A.1 to A.4 in the Appendix. Although the R^2 values obtained using KAS exhibit more instances greater than 0.99, the approximations inherent to this integral method can introduce a systematic error into any obtained kinetic parameters.[172] The KAS model has also been shown to exhibit poorer predictive capabilities over an analogous Friedman model.[212]. For these reasons, the Friedman method was preferred and utilised to predict the isothermal degradation of SLI.

5.4.3. Predicted Isothermal Degradation

The experimentally-derived Friedman isoconversional degradation parameters and their corresponding models were used to determine the effect of changing process conditions on the degradation of SLI. A published synthesis of SLI reports an esterification temperature of 240°C, with a total process time of 5 hrs.[213] Predicted degradation isotherms were therefore produced at deviated temperatures between 220 and 280°C, see Figure 5.7.

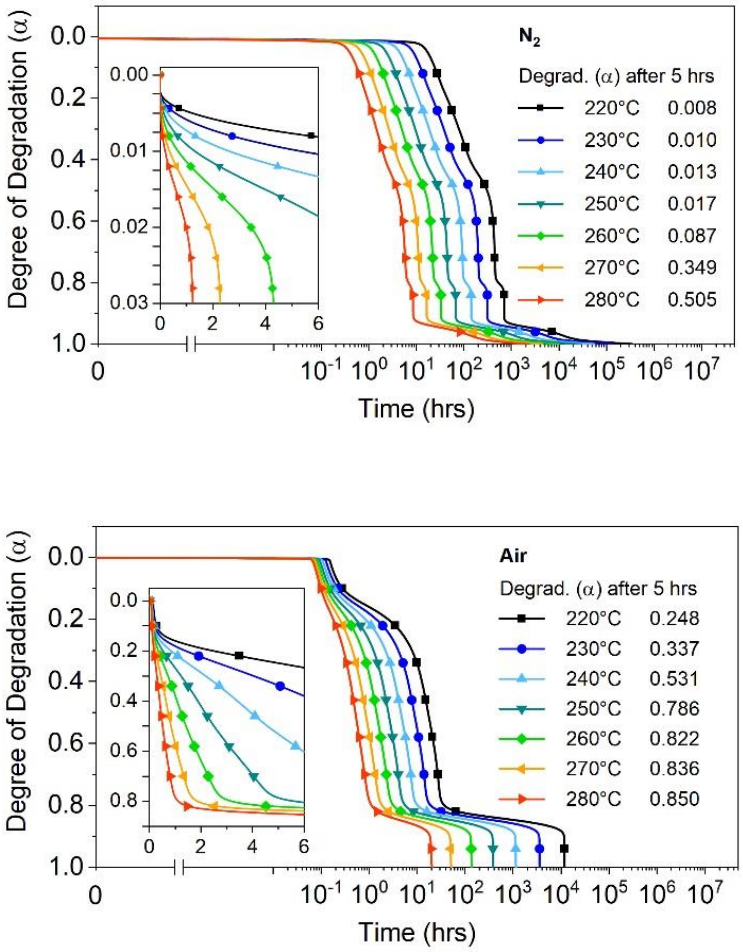

Figure 5.7. Predicted isothermal degradation of SLI in N_2 (top) and air (bottom) from exposure to sustained temperatures between 220 and 280°C. Inset shows the initial stages of degradation over a shorter timescale, where the inset x-axis represents time (hrs) on a linear rather than a log scale accordingly. Degree of degradation (α) was obtained from the respective Friedman activation energies using Eq. (8). Legend displays predicted degradation (α) after 5 hrs of isothermal exposure.

In the N_2 system, the degradation after 5 hrs at 240°C was found to be 0.013 (α), which equates to 1.0 wt% of the total SLI mass in physical terms. The degradation levels at 220°C and 230°C were 0.008 and 0.010 respectively. The esterification rate during the manufacture of SLI is reported to drop significantly when the reaction temperature is lowered below 230°C.[36] Decreasing the process temperature therefore may not decrease the process-induced thermal degradation, since the increase in reaction times required for an equivalent level of esterification, may offset the observed improvements in stability. At 260°C, there is a 530% increase in the degradation level over 5 hrs compared to 240°C, which increases to > 2800% at 270°C. In N_2, the ideal parameters for optimising the reaction rate whilst minimising decomposition therefore resides between 240 and 250°C.

In air, degradation levels at equivalent temperatures were found to be significantly higher than those observed in the N_2 environment. At 240°C, the predicted degradation after 5 hrs ($\alpha = 0.531$) equated to 28.5 wt% of mass loss. While a reduced operating temperature of 220°C is predicted to significantly decrease degradation to a mass loss of 13.3 wt%, these degradation levels would still be substantially higher than those for the inert system. Catalytic isethionate synthesis routes can be operated at temperatures as low as 200°C,[33] but an analysis of the degradation data indicates that mass loss is still predicted to be 9.5 wt%, over 5 hrs, at this lower temperature. Based on these observations, it becomes clear that any process involving the high temperature esterification of SLI should be operated within a rigidly controlled inert atmosphere in order to minimise yield loss to thermal degradation.

Whilst long-chain organic molecules similar to SLI have previously been studied by isoconversional methods,[200, 201, 206] the predicted isotherms were nevertheless compared with experimental isotherms to verify the applicability of the Friedman model to this particular system. SLI was heated to 240°C for 5 hrs to simulate published synthesis conditions and the mass was observed via TGA.[166] The resulting plots of mass loss in both air and N_2 atmospheres, together with their nonisothermally derived predictions, are shown in Figure 5.8.

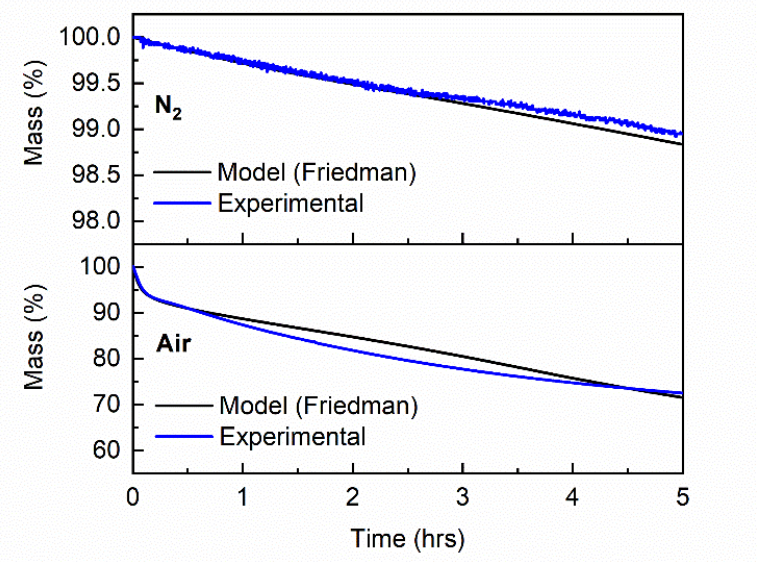

Figure 5.8. Experimental isothermal TGA plots of SLI in N_2 (top) and air (bottom) compared with the predicted model isotherms. Samples were heated to 240°C for 5 hrs to simulate the synthesis conditions for SLI.[166] Model isotherms were generated from nonisothermally derived Friedman models.

After 5 hrs at 240°C the measured degradation in air was substantially higher than N_2 with respective mass loss values of 28.9 wt% and 1.1 wt%. While the experimental data showed good agreement to the predicted data, deviations around 2.5 hrs in air and 4 hrs in N_2 were respectively observed. The associated differences between the observed and experimental mass losses were 3.0 wt% and 0.1 wt% in air and N_2 respectively. The underestimation in air could have resulted from increasing inaccuracies in the corresponding isoconversional model. The R2 values associated with the derivation of the corresponding activation energies are provided in Table A.3 in the Appendix. While values were predominantly greater than 0.99 in the early stages of the degradation process, a decrease to 0.98 is observed beyond $\alpha = 0.20$. The resulting increase in error for the Friedman-derived activation energies in air is also presented in Figure 4. While this error has manifested itself as a minor deviation in mass over the timescales presented in Figure 5.8, a greater error in the Ea values is observed at higher degrees of degradation ($\alpha > 0.75$), particularly in the inert system. As this could significantly impact the predictive capability of these models, their application at greater levels of degradation ($\alpha > 0.75$) is not recommended.

5.4.4. TGA-FTIR Analysis of SLI

Data from the TGA-FTIR analysis, conducted to identify the volatile products released from the decomposition of SLI, is shown in Figure 5.9.

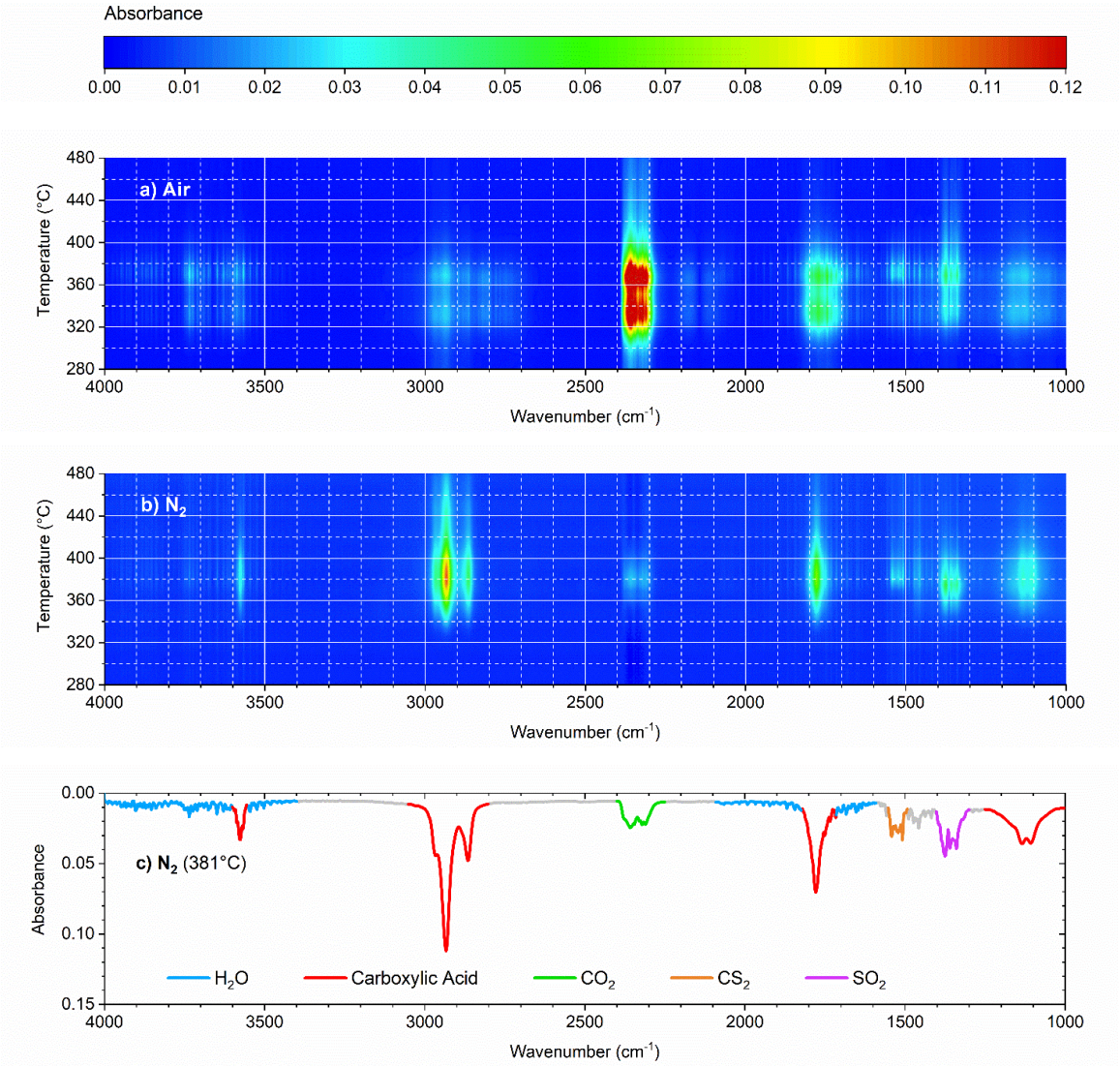

Figure 5.9. Colourmaps depicting the evolved gases measured via TGA-FTIR during the thermal degradation of SLI in a) air and b) N_2. Colour scale corresponds to the FTIR absorbance of evolved species at the corresponding temperature and wavenumber. Samples were heated from 30 to 550°C at 10°C/min. c) Single FTIR spectrum of the evolved gases in N_2 at 381°C. Legend depicts the five most abundant species.

The maximum total absorbance was measured at 381°C in N_2 and 369°C in air. At these temperatures all significant absorption bands were detected and the resulting single FTIR spectra were therefore considered to be representative of the gases produced in each system. A small time delay was expected between gas evolution in the TGA furnace and subsequent detection via the FTIR spectrometer. Given the combined volume of the furnace, transfer line and spectrometer cell, this delay is not considered to exceed the FTIR measurement interval at the experimental purge gas flow rate. Through comparison with library spectra, the five most spectroscopically abundant species from the thermal degradation of SLI were identified, as shown in Figure 5.9c. The temperature-dependent data (Figure 5.9a and 7b) showed that while the relative amounts of each gas differed with a change in degradation atmosphere, both the N_2 and air systems exhibited the same five gaseous species in highest quantity. The literature values used to identify and confirm these gaseous species are provided in Table 1. The specific vibrations corresponding to each band were determined where possible.

Table 5.2. Literature values for FTIR peaks characteristic of materials identified via the evolved gas analysis of SLI.

Material	Vibrational Mode	Bond	Wavenumber* (cm^{-1})
SO_2	Asymmetric Stretch (v_3)	O=S=O	1320-1395 [214]
CS_2	Asymmetric Stretch (v_3)	S=C=S	1523 [215]
CO_2	Asymmetric Stretch (v_3)	O=C=O	2349 [216]
H_2O	Asymmetric Stretch (v_3)	O-H-O	3755 [216]
	Symmetric Stretch (v_1)	O-H-O	3651 [216]
	Symmetric Bend (v_2)	O-H-O	1595 [216]
Lauric Acid [103]	Carboxylic Acid Stretch	C=O	1777 [107]
	Alkyl Stretches+	C-H	2840-2975 [217]
	Carboxylic Acid Stretch	O-H	3575 [107]
	Skeletal Stretch	C-C	1040-1175 [103]

* Where single values are provided the wavenumber corresponds to a peak value quoted in the literature. + See Hill *et al.* for detailed saturated acid peak assignments.[217]

From Table 5.2, the single bands attributed to sulfur dioxide (SO_2), carbon disulfide (CS_2), carbon dioxide (CO_2) and water vapour (H_2O) were distinctive, characteristic and easily attributable to the respective species. Carboxylic acids are common products in both the oxidative and inert thermal degradation of alkyl esters; formed via hydrolysis and intramolecular rearrangement.[218, 219] As the experimental FTIR peaks displayed very strong correlation with vapour spectra of acid homologues,[220] the remaining peaks in Figure 5.9c have been attributed to linear saturated carboxylic acids. Contrary to the dimeric condensed phase of carboxylic acids, vapour species typically exist in the monomeric form. This results in significant shifts to the IR stretching frequencies of C=O and O-H, which otherwise contribute to hydrogen bonding interactions.[107] The observed C=O (1777 cm^{-1}) and O-H (3576 cm^{-1}) bands were characteristic of vapour phase carboxylic acids and correlate very well with their respective literature peak widths and wavenumber values of 1777 and 3575 cm^{-1}.[107, 220] Analogous thermal degradation studies of similar lipids also report evolutions of alcohols, esters and aldehydes.[200, 201, 221] Primary, secondary and tertiary alcohol stretches typically occur between 3640 and 3670 cm^{-1} in the vapour phase.[107] Despite the large quantities of alcohol detected in the pyrolysis of SDS,[171] there is no significant evidence of this for SLI in air or N_2. Using the Beer-Lambert law, the intensity ratio measured between C=O and O-H in the displayed spectrum was found to be similar to that of a reference carboxylic acid spectrum.[107] However, a slight excess in C=O absorbance is consistent with the presence of additional carbonyl species such as aldehydes and ketones.

Quantitative Analysis of Evolved Gases

To quantify gas evolution as a function of degradation, the change in absorbance for each of the characteristic bands (identified in Figure 5.9c) were plotted as a function of temperature. While carboxylic acids were identified as the primary carbonyl constituent, decomposition within the alkyl chains was also likely to result from oxidative combustion, resulting in the evolution of independent alkyl fragments.[206, 222] The alkyl and carbonyl bands were therefore integrated individually to determine the relative quantities of each functional group. The resulting temperature-dependent absorptions in both air and N_2 atmospheres are shown in Figure 5.10.

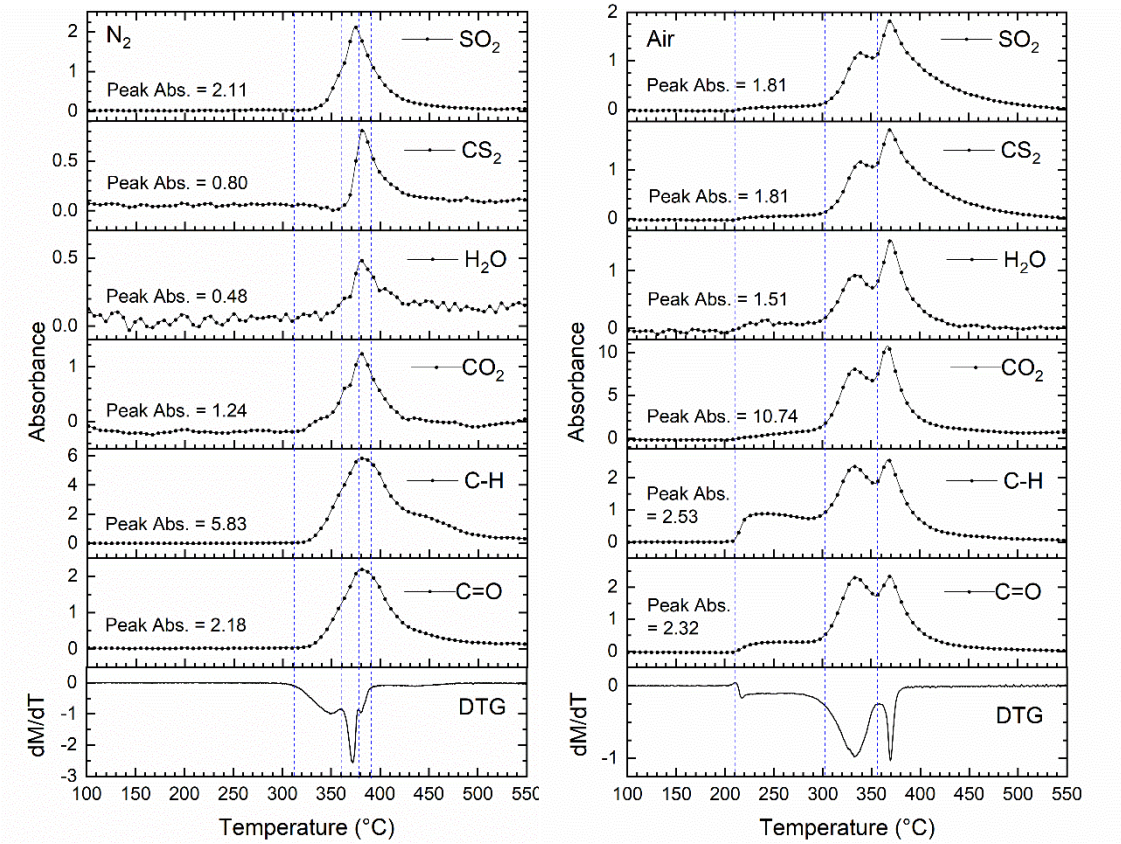

Figure 5.10. Absorbance of the characteristic FTIR bands of the evolved gas during the thermal decomposition of SLI in N_2 (left) and air (right). SLI samples were heated to 550°C at 10°C/min. Dashed lines represent the onset of degradation zones 1, 2, 3 and 4 (where applicable) as measured via TGA. The corresponding TGA data at 10°C/min is also provided. All measured transition temperatures are shown in full in Table 5.1

In both air and N_2, the temperatures at which changes in absorption occur, coincide with the degradation zones identified via the differential TGA analysis (Figure 5.2). See Table 5.1 for further data. Due to the inherent interdependencies between radical reactions, the measured species in each environment display comparable maxima with broadly similar evolution trends with respect to temperature. These shared temperature-dependent inclinations across gaseous species correspond with previous studies pertaining to similar methods and molecules.[201, 221, 223]

The significant evolutions of alkyl species, carboxylic acids, CO_2 and water vapour correspond with the gases produced from the thermal degradation of other long chain organic molecules.[200, 206, 221, 224] A decompositional study of SDS reported that the

surfactant degraded to form primary alkenes, with characteristic C=C vinyl stretches and general olefinic stretch reported to occur at 1640 cm^{-1} and 1580 cm^{-1} respectively.[103] In the current study, the experimental spectra displayed very limited activity in these regions to confirm any substantial formation of volatile alkenes in the inert thermal degradation of SLI (Figure 5.9a). The observed evolutions of SO_2 correspond with those reported for the thermal decomposition of alkyl sulfonated surfactants,[225] as well as SDS.[202] CS_2 is a less commonly reported degradation product of organic species. However, its presence in this study was confirmed by comparison with reference spectra and literature values of characteristic bands.[215] Significant increases in CO_2 and water vapour absorption were observed in air when compared to the inert system. In reported evolved gas studies of long-chain organic materials, similar increases have been proposed to result from oxidative combustion, particularly at the temperatures corresponding to the second and third degradation zones observed in the oxidative study of SLI (Figure 5.10).[221, 226] However, due to the highly complex, interdependent nature of the radical reactions pertaining to all evolved gases observed in this study, further time-resolved analyses would be required to confirm the specific mechanisms most relevant to the thermal degradation of isethionate surfactants.

5.5. Conclusions

The thermal degradation of sodium lauroyl isethionate (SLI) was measured using TGA and analysed via isoconversional kinetic methods. Dynamic experiments resulted in degradation onset temperatures of 300°C and 208°C in air and N_2 respectively; both of which were lower than the 380°C reported for sodium dodecyl sulfate.[170] Differential Friedman-derived activation energies were used to predict isothermal degradation levels under typical isethionate manufacturing conditions. Thoroughly inert synthesis conditions are recommended for isethionate production, after experimentally-verified data indicated that SLI degradation levels were 28 times higher in air than N_2 at published synthesis temperatures of 240°C.[166] Previous patent literature reported elevated SLI decomposition at temperatures higher than 220°C.[168] From the results in the current study, isethionate synthesis temperatures could be increased to 250°C under strictly inert manufacturing conditions, given that significant increases in degradation levels were not predicted until 260°C. Gradual heating of the

reaction vessel would be advocated to avoid exceeding desired temperatures, thus maximising product activity levels,[168] colour[36] and odour[169] by minimising degradation. Despite the current focus on a high temperature catalyst-free manufacturing process, the versatility of the obtained Friedman models permit the prediction of degradation resulting from any dynamic or isothermal temperature exposure,[186] thus extending their applicability to alternative processes pertaining to SLI manufacture. Even with increasing applications of isoconversional kinetics in the thermal analysis of biorenewable organic fuels,[200, 201] the methods were seldom utilised in the study of ionic surfactant systems. The correlation between predicted and measured degradation in this study supports their utilisation in the analysis of more complex organic systems, where metallic associations lead to greater complexity in atomic composition, polarity and columbic interactions.

A real-time TGA-FTIR analysis was conducted to identify and quantify the gases produced through the thermal degradation of SLI. The analysis revealed evolutions of carbon dioxide, carbon disulfide, sulfur dioxide, water vapour and organic fragments. In addition to improving product properties, managing degradation levels through the temperature-dependent presence of characteristic FTIR bands, would also reduce the risk of the observed toxic, pungent sulfurous emissions.[227] Walele *et al.* reported that activity levels of commercial isethionate esters vary between 78 and 85%,[36] which correlates with previous reviews of isethionate ester manufacture.[33] In order to determine if the upper limits on this range result from limited product stability, future work could utilise the models generated in this study to correlate product activity levels with decomposition of SLI. By associating activity levels with desired levels of product performance, the resulting material lifetimes could be used to optimise SLI manufacturing processes for acceptable levels of thermal degradation.

Chapter 6: Crystal Structure of SLI via Powder X-Ray Diffraction and Molecular Modelling Techniques

Synopsis: *This results chapter describes how the atomistic crystal structure of SLI was obtained using a combination of powder X-ray diffraction and molecular modelling techniques. A quantitative synthonic and energetic analysis was carried out to help identify and understand the thermodynamic driving forces behind the observed structural form. In relation to the proposed research question, this chapter provides a benchmark for the isethionate surfactant structure under ambient conditions, for the subsequent characterisation of structures observed under varying process conditions.*

6.1. Introduction

Surfactants are the primary ingredient in many personal care formulations. They are present in shampoos, liquid cleansers and soap bars to reduce the surface tension of water and aid in the solubilisation of lipidic, sebaceous residues on the skin.[91] Due to its mildness, sodium lauroyl isethionate (SLI) is becoming an increasingly popular surfactant in such formulated personal care products.[9] When compared with traditional counterparts such as alkyl carboxylates and sodium dodecyl sulfate (SDS), studies into SLI have demonstrated reduced irritation,[124] dryness[126] and adhesion to the stratum corneum in personal care applications.[127] It is also comparatively more stable in the presence of hard water by exhibiting no deposit formation or significant loss in lathering abilities in the present of alkali earth metals.[128] SLI is commercially synthesised via the esterification of lauric acid with sodium isethionate,[166] as shown in Figure 6.1.

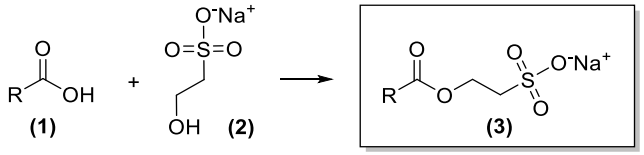

Figure 6.1: Reaction of lauric acid (1) with sodium isethionate (2) to form the dodecyl-chained (C12) sodium lauroyl isethionate (SLI) (3).[166] In this example, R= $C_{11}H_{25}$. A mixture of chemical homologues of alkyl chain length ranging between C8 and C18 can also be formed from the respective mixture of carboxylic acids. The resulting blend of surfactants is known as sodium cocoyl isethionate (SCI).[27]

Despite widespread application in both solid and liquid cleansing products, there is a notable lack of knowledge pertaining to the structure of SLI and its influence on product performance. While the specific influence of the crystal structure on the physical properties of synthetic surfactants has not been considered, the varying polymorphism exhibited by carboxylate soaps has long been known to influence the aqueous solubility, dissolution rate, lathering abilities, colour and physical hardness.[228, 229] The carboxylic acids used to

synthesise isethionate esters exhibit a complex polymorphic behaviour dependent on the alkyl chain length, purity, crystallisation rate, solvent and temperature. Lauric acid, specifically utilised in the synthesis of SLI, has at least four known polymorphs in the single-component state. The unit cell parameters for the C, A and A_{Super} forms are displayed in shown in Table 6.1.

Table 6.1. Lattice parameters for published crystal structures of lauric acid. a, b and c correspond to lengths of crystallographic axes (Å) in the unit cell, whilst α, β, and γ refer to the respective angles (°). Data corresponds to single crystal X-ray diffraction and powder X-ray diffraction, labelled (*).

Form	**Unit Cell Type**	**Space Group**	***a*** (Å)	***b*** (Å)	***c*** (Å)	***α*** (°)	***β*** (°)	**γ** (°)
C [230]	Monoclinic	P 21/c	27.563	4.963	9.527	90	98.01	90
C [231]*	Monoclinic	P 21/c	27.542	4.953	9.604	90	97.28	90
A [232]	Triclinic	P -1	18.00	21.54	5.41	96.48	90.42	111.02
A_1 [233]	Triclinic	P -1	7.450	5.400	17.470	96.88	113.13	81.12
A_{Super} [234]	Triclinic	P -1	5.415	25.964	35.183	69.82	113.14	121.15

The C-form of monoclinic cell type and P21/c symmetry is the most stable polymorph at room temperature. The crystalline bilayer structure is stabilised by hydrogen bonding between terminal carboxyl groups, with alkyl chains exhibiting a tilt angle of 35° perpendicular to the b-c crystallographic plane.[230] While the A-forms are also stable at room temperature and can be crystallised from various solvent combinations, they irreversibly recrystallise into the C-form upon heating. This is reported to occur prior to melting via a solid-solid transition.[235] Unlike the C-form, where all adjacent molecules are arranged in parallel rows, the A-form displays an antiparallel arrangement between groups of molecules resulting in asymmetrical bilayer structures. Visual depictions of the C, A_1, and A_{Super} forms of lauric acid are provided in Figure 6.2.

.

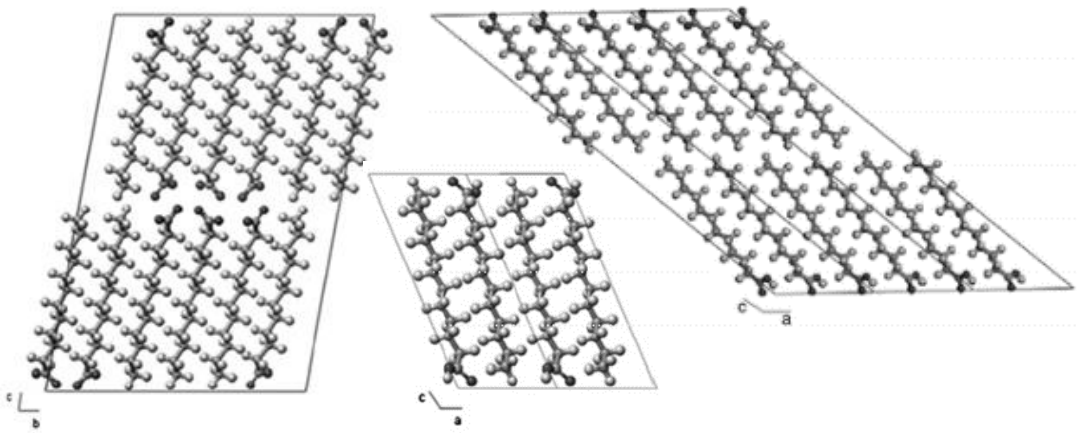

Figure 6.2: Polymorphs of lauric acid in the A_{Super} form (left), A_1 form (centre) and C form (right). The depictions display one, two and three unit cells in their respective polymorphic forms. Adapted from Moreno et al.[235]

Like SLI, sodium dodecyl sulfate (SDS) is a dodecyl-chained sulfate surfactant used in personal care formulations. Its solid phase crystalline structure in the anhydrous phase resembles that of a C-form carboxylic acid, with a monoclinic unit cell, P21/c space group and a tilted lamellar bilayer arrangement.[236] While multiple polymorphs have not been confirmed for alkyl sulfates, SDS exhibits a change in crystalline structure with respect to varying degrees of hydration as shown in Table 6.2. Increasing levels of hydration results in a concurrent contraction of the longest axis in the unit cell, caused by a reported increase in lamellar tilt angle. Given minimal changes in the perpendicular axis length, the crystal density also increases with hydration. Unlike the A-forms of lauric acid structure, all hydrates are structured in symmetrical, parallel tilted bilayers. The lamellar tilt in alkyl sulfates results from a disparity in width between the sulfate head groups and alkyl chain, where the latter is tilted to increase lateral packing efficiency within the unit cell.[150] Increased hydration results only in an increased tilt angle to reduce the unit cell dimensions, with no observed interdigitation between alkyl chains of adjacent layers within the lamellar phase.[237]

Table 6.2: Lattice parameters for published crystal structures of sodium dodecyl sulfate (SDS) and its varying hydrates. a, b and c correspond to lengths of crystallographic axes (Å) in the unit cell, whilst α, β, and γ refer to the respective angles (°). Measurements marked (*) were obtained via powder X-ray diffraction, where remaining studies utilised single crystal X-ray diffraction.

Form	**Unit Cell Type**	**Space Group**	***a*** (Å)	***b*** (Å)	***c*** (Å)	***α*** (°)	***β*** (°)	**γ** (°)
SDS (Anhy.) [236]*	Mono.	P 21/c	38.915	4.709	8.198	90	93.29	90
SDS.1/8 H_2O [238]	Mono.	C 2/c	78.693	10.220	16.410	90	98.28	90
SDS.1/2 H_2O [149]	Mono.	C 2	9.847	5.248	30.798	90	91.29	90
SDS.H_2O [150]	Tri.	P -1	10.423	5.662	28.913	86.70	93.44	89.55

In the current study, the crystal structure of sodium lauroyl isethionate (SLI) is determined via powder X-ray diffraction. Powder diffraction is becoming an increasingly common alternative to single crystal diffraction, particularly when there are difficulties associated with the crystallisation of a single crystal of suitable size and quality.[239] In addition to numerous other lipoid organic molecules,[112] polymorphic and hydrated structures of SDS [236] and lauric acid [231] have been solved via powder diffraction as a result of these challenges. Despite a variety of published indexing and search methodologies related to the crystal structure solution of molecular solids,[240] three primary steps are common to all methods pertaining to powder diffraction data.[241] An experimental powder pattern is first indexed to derive the unit cell type, lattice dimensions, and space group symmetry. A structure solution process based on molecular mechanics then searches for an atomistic representation of the unit cell, of suitable concurrence with respect to the experimental powder pattern. The corresponding structure is subsequently refined and characterised via peak profiling techniques. [242, 243] With a representative atomistic crystal structure determined, the system can be characterised via molecular modelling tools to understand the intermolecular interactions underpinning the molecular lattice and its macromolecular properties.[244, 245] Through this systematic deconvolution of the lattice energy, an understanding of crystallographic chemistry can be achieved.[246, 247]

Following a synthonic analysis, comparative analyses with existing crystal systems will be used to determine if the observed structure of SLI reflects the trends in hydration levels, lamellar spacing and tilt angle exhibited by other dodecyl chained surfactants such as SDS.

6.2. Experimental

6.2.1. Powder X-ray Diffraction Analysis of SLI

Sodium lauroyl isethionate (SLI) was prepared and isolated to 98% purity following methods described previously.[166] SLI was crystallised from methanol at 1°C/min as described and analysed within 24 h following isolation. Samples were analysed using a Phillips (PANalytical) X'Pert Pro (MPD) Modular Powder Diffractometer, equipped with an X'celerator position sensitive detector (PSD) in Bragg Brentano geometry. Powered samples were exposed to Cu-Kα radiation (λ = 0.154 nm, 40 keV, 40 mA), with a 20 μm Ni filter for Kβ radiation. Analysis was conducted between 2 and 40° (2θ) with an angular resolution of 0.033° and a sample exposure time of 11 hrs. The resulting powder diffraction pattern was processed using the PANalytical Highscore Plus program where the background was subtracted and exported for further analysis.

6.2.2. Indexing and Refinement of Unit Cell

The XRD pattern was indexed using the Powder Indexing module in the Materials Studio 17.1 (BIOVIA) molecular simulation package. With a low amplitude cut-off of 1 %, 35 peaks were detected using the peak search function. The resulting peak positions were auto-indexed using the DICVOL, ITO and X-Cell programs. Based on the available metrics and previously published literature structures (Table 6.2), searches were programmed to test for cubic, hexagonal, tetragonal, orthorhombic, monoclinic and triclinic cells. Successful unit cells produced from the DICVOL and X-Cell searches were refined using the Pawley method. Peaks were fitted to a Pseudo-Voigt function and optimised with respect to zero-point line shift, the U, V and W FWHM parameters, as well as the NA and NB profile parameters. (Note that the refinement of Pseudo-Voigt peak parameters provides the peak parameters subsequently used for the trial structure search. Only peak intensities and positions are specifically used for unit cell and space group determination). Given the proposed monoclinic unit cell type, the *a*-axis, *b*-axis, *c*-axis and *β*-angle of the indexed cells were optimised through 25 refinement cycles, with 75 evaluations per cycle per degree of freedom.

An automated space determination was lastly executed to determine the unit cell symmetry from systematic absences in the observed indexed reflections.

6.2.3. Trial Molecular Structure

A monomeric vapour phase structure of SLI was created using the Avogadro 1.2 molecular visualisation tool and optimised through molecular mechanics using the MMF95 force field. Structures were further refined using a density functional theory (DFT) based geometry optimisation using the ORCA 4.0 quantum chemistry program. Calculations were executed using the def2-TZVP basis set combined with the B3LYP-D3 functional. All calculations successfully completed within a convergence criteria of 1×10^{-8} a.u. and 125 iterations.

The DFT-derived molecular model of SLI was introduced into the Pawley-derived unit cell and optimised with respect to the experimental powder pattern using the Powder Solve module in Materials Studio. Trial molecular structures were generated using the Monte-Carlo based Parallel Tempering method aiming to maximise agreement between the experimental pattern and a simulated pattern derived from the Pawley-refined peak parameters. Free molecular components, torsional angles and bonding characteristics of functional groups were set as variable degrees of freedom. Due to the confirmed plate-like morphology of the SLI crystalline state, a March-Dollase preferred orientation correction was applied and simultaneously optimised with respect to the *a, b, c* and *R0* parameters. To improve the chemical viability of highly correlating structures and avoid unexpected contact between molecular fragments, a closed contact penalty was applied within 50% of the predicted van der Waals radius of each molecular constituent. Following 10 cycles of optimisation of 500000 steps each, the structure of lowest R_{wp} was refined via Rietveld methods.

6.2.4. Automated Rietveld Refinement and Structure Selection

Two individual Rietveld refinements were executed on the trial structure of lowest R_{wp}. The first optimisation involved an automated atomistic Rietveld refinement of the Pawley-refined Pseudo-Voight peak parameters. Unit cell parameters were fixed and single molecules were defined as motion groups with rotational and translational freedom. The zero-point line shift, the U, V and W FWHM parameters, as well as the NA and NB profile parameters were optimised to maximise correlation between simulated and experimental powder patterns. The second optimisation was executed

with the target of the minimising potential energy of the resulting molecular lattice through variation of the same peak parameters. Energy calculation and geometry optimisation of the molecule within the Pawley-refined unit cell was executed using the COMPASS II forcefield and its respective calculated charges. Like the Pawley refinement, Rietveld refinement was executed through 25 optimisation cycles, with 75 evaluations per cycle per degree of freedom

Bond lengths, angles and torsions were calculated using Materials Studio to characterise the two systems. To identify the influence of differing molecular conformations on the potential energy of the system, the DFT-derived monomeric structure was designated as a control structure and its C-O-C-C ester bond was varied between 0° and 360° in 1° increments. The resulting influence on potential energy was individually measured using the Drieding and COMPASS II molecular forcefields, coupled with their respective calculated charges.

6.2.5. Lattice Energy and Synthon Analysis

Partial atomic-charges of the R_{wp}-optimised lattice structure of SLI were first calculated through a quantum mechanical DFT calculation using the Gaussian 09 computational chemistry package. ESP charges were obtained using a Def2-TVZP basis set, coupled with a dispersion corrected B3LYP-D3 hybrid functional to complement the previous DFT calculations. The lattice energy was then calculated using HABIT98 combined with the Drieding forcefield. Energy convergence was confirmed through the construction of a radial network of 9 unit cells, with subsequent energy calculation at 5 Å intervals, between 0 and 100 Å. The synthons contributing the greatest absolute and non-columbic contributions to the overall lattice energy were calculated and subsequently visualised using the Mercury molecular visualisation tool from the Cambridge Crystallographic Data Centre (CCDC).

6.2.6. Lamellar Bilayer Structure of SLI

The proposed structure of SLI, as well as the published structure of SDS in its varying states of hydration, were characterised as follows. Lamellar layers were measured as the longest axis (*c*) of the corresponding unit cell (Å), divided by the number of lateral molecules parallel to the *c*-axis.[236] The headgroup area, as defined by Coiro *et al.*,[150] corresponds to *a * b / 2*, where *a* and *b* correspond to lengths of the axes perpendicular

to the longest *c*-axis. Headgroup volume per surfactant system was measured as the van der Waals radius of the headgroup atoms in an asymmetric unit, divided by the total number of surfactant molecules within the asymmetric unit. In the studied dodecyl-chained surfactants, the chain was defined as all the carbon and hydrogen atoms constituting the dodecyl alkyl chain, while all other atoms in the asymmetric unit were considered part of the headgroup. Lamellar tilt angles were measured as the angle between the primary axis of the dodecyl chain in a surfactant molecule and the perpendicular 00*l* Miller plane at the base of its headgroup, subtracted from 90°.

6.3. Results and Discussion

Following the synthesis and purification of SLI, colourless crystals of a plate-like morphology were obtained. Recrystallisation experiments were attempted in pursuit of material suitable for a single crystal X-ray diffraction analysis. Despite multiple approaches in a range of solvents, the spontaneous nature of the nucleation and plate-like morphology of the resulting crystals rendered it challenging to acquire a crystal of suitable length in all dimensions. The highly amphiphilic nature of the molecule, coupled with the formation of liquid crystal phases, further rendered some aqueous solvents combination and otherwise useful crystallisation methods, such as solvent layering, unsuitable for the studied system. The materials derived from the synthesis and purification was therefore analysed by X-ray powder diffraction to obtain the desired structural information.

6.3.1. Indexing and Refinement of Unit Cell

The resulting pattern was indexed using the DICVOL, ITO and X-Cell programs. Following a Pawley refinement, the DICVOL derived unit cell produced the lowest R_{wp} (weighted-profile) value after the proposed unit cell was compared with the experimental pattern. (Figure 6.3)

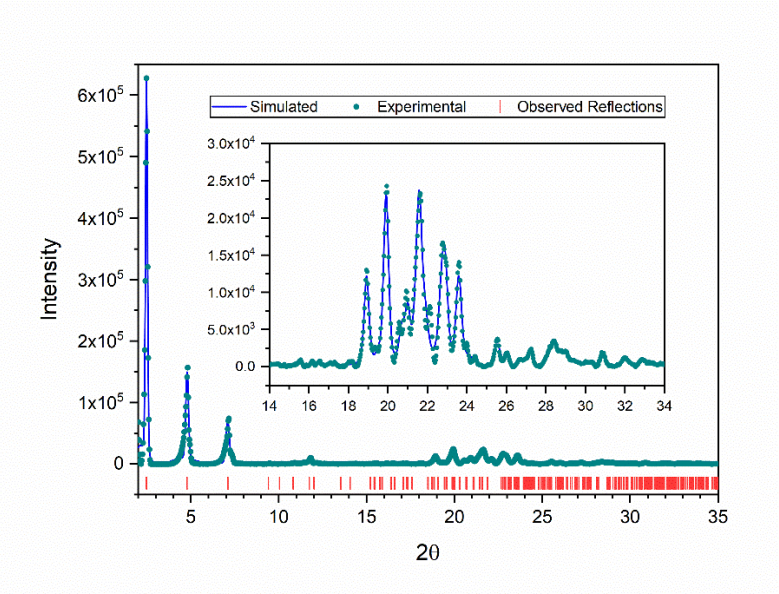

Figure 6.3. Powder diffraction pattern of sodium lauroyl isethionate. Diffraction angles (2θ) correspond to a Cu K-alpha wavelength of 1.5406 Å. Inset is an extract of the same data, displaying greater detail at higher diffraction angles. The unit cell parameters were determined using the DICVOL auto-indexing program. Following Pawley refinement, the experimental pattern (green points) exhibited an R_{wp} value of 8.85% against the simulated pattern (blue line). Red vertical lines denote observed reflections in the experimental and simulated patterns.

The obtained monoclinic unit cell type and dimensions correspond well with the anhydrous structure of SDS.[236] Other long chain surfactants, such as sodium palmitate, also exhibit monoclinic cells with one axis of a significantly larger length to accommodate their respective alkyl chains.[248] A refinement of the DICVOL derived unit cell parameters produced an R_{wp} value of 8.85%, where the R is a weighted squared sum of the difference in intensities, between the experimental and simulated patterns. For each iteration in the refinement process, the modified Pawley algorithm used to refine the unit cell parameters adopted a two-step optimisation procedure, first optimising peak intensities against the background, before the peak shape, zero-point and cell parameters were fitted. This two-step process was iterated until convergence with R_{wp} had been achieved. R_{wp} values of <10% are typically considered suitable for further analysis.[249] While agreement between backgrounds and artefacts can reduce perceived R_{wp} values without any improvement in the

structure, a background-subtracted R_{wp} value of 8.93% indicates that these ancillary features had a negligible contribution to the goodness of fit. In addition to these quantitative confidence metrics, there was also a visual agreement between the experimental powder pattern and a simulated pattern corresponding to the refined unit cell parameters (Figure 6.3). The P21/c space group also corresponded with comparative molecules from literature.[236] The inherent 2_1 screw axis to this space group is likely attributable to a symmetrical tilted bilayer structure typical of amphiphilic surfactant molecules in the solid phase. As with anhydrous SDS, which exhibits the same symmetry, the unit cell of SLI consists of one molecule of surfactant in the asymmetric unit, with four molecules in the unit cell.

Table 6.3: Experimental unit cell parameters of SLI compared with published values for sodium dodecyl sulfate. Both sets of measurements were obtained via powder X-ray diffraction.

	Unit Cell Type	**Space Group**	*a* (Å)	*b* (Å)	*c* (Å)	*α* (°)	*β* (°)	γ (°)	**Unit Cell Vol (Å^3)**
SLI	Mono.	P21/c	38.40	9.17	7.60	90	95.09	90	2666
SDS [236]	Mono.	P21/c	38.92	4.71	8.20	90	93.29	90	1500

6.3.2. Trial Molecular Structure Search

Molecular structures of SLI within the Pawley refined unit cell were generated and optimised via the parallel tempering (PT) system. PT is an alternative to the simulated annealing technique which similarly utilises a Monte Carlo (MC) approach. A single degree of freedom is adjusted with a single iteration, with evaluations based on the global energy within the system. A high initial energy overcomes any necessary thermodynamic barriers, while the progressive reduction in temperature ultimately yields the theoretical global minimum. Alternatively, PT explores several structures at a multitude of increasing and decreasing temperatures. While a similar MC approach is adopted with respect to initial structures, the simultaneous exploration of high and low temperature states, concurrently explores the optimisation space whilst refining any detected local minima. The parallel nature of the methodology can increase simulation times over simulated annealing but reduces the likelihood of the premature termination at a local global minimum.

Whilst initial optimisation runs produced lamellar bilayer structures characteristic of previous long chain anionic surfactants,[236] tilt angles of > 60° and a high degree of interdigitation in carbon chains resulted in a significant number of atoms with an unexpectedly close spatial proximity. In addition to the unfavourable molecular conformations, R_{wp} values in excess of 30% further indicated a poor correlation between generated structures and the experimental powder pattern.

To overcome the conformational issues and concurrently reduce the global energy of the system, a close contact penalty function was applied to generate more energetically favourable structures. The plate-like morphology observed through the single crystal growth experiments suggested that the sample was also susceptible to preferred orientation. The amplitude of low-angle 00*l* reflections relative to higher-angle peaks provides further experiment evidence of this. A March-Dollase (MD) preferred orientation correction was therefore applied to subsequent searches for trial structures. Given that preferred orientation was most likely prevalent in the c-axis, an initial value of 0 was applied to the MD equation to account for the plate-like morphology. The corresponding values pertaining to the *a* and *b*-axes were assigned values of 1, assuming random orientation along these crystallographic planes. The algorithm was then set to optimise these values as part of the structure search to negate any influence of preferred orientation on the ability to reach a global energy minimum, whilst simultaneously maximising the correlation between trial structures and the experimental powder pattern.

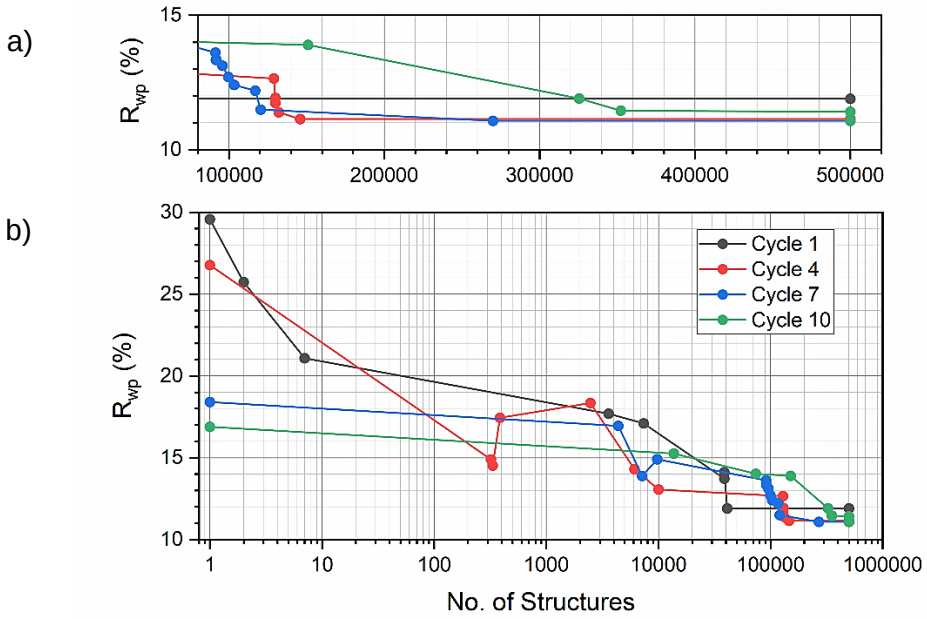

Figure 6.4: Optimisation of R_{wp} (%) as a function of step number during the computational structure search for sodium lauroyl isethionate. A parallel tempering method was used to execute 10 optimisation cycles, each consisting of 500000 molecular confirmations, within the refined monoclinic unit cell. All 10 cycles converged to an R_{wp} of <12%. b) shows progression of the first cycle, as well cycles 4, 7 and 10 which converged to the lowest observed R_{wp} of 11.1%. a) shows the same data on a linear x-axis.

The revised optimisation parameters iterated through 10 cycles, each consisting of 500,000 structures, ultimately yielded an R_{wp} value of 11.1 %. All 10 cycles generated structures with R_{wp} < 12 %, with cycles 4, 7 and 10 converging to the observed minima at 11.1 %. For each of these cycles, the progression of optimal R_{wp} with respect to the step number is shown in Figure 6.4. Cycle 4 was the first to reach 11.1 %. After 320 structures, the algorithm produced an R_{wp} of 14.9 %. Optimisation of the corresponding structure yielded a local minimum R_{wp} of 14.5 % after 333 iterations. It was only after the system energy was increased and reoptimised that a lower global energy minimum of 11.1 % was located. A similar behaviour was observed in cycle 7 after 7,000 iterative steps. It is this ability to simultaneously optimise for multiple minima, at varying systematic energy levels, which demonstrates the primary benefits of parallel tempering over the simulated annealing optimisation method. The outset plot (Figure 6.4) shows no cycles with any significant improvement beyond 350,000

iterations, with cycles 1, 4 and 7 reaching plateau sooner. Under the given conditions, this indicates that all cycles successfully converged within the allocated number of 500,000 steps and further improvement in R_{wp} with additional computational resources was not needed.

6.3.3. Automated Rietveld Refinement and Structure Selection

The trial structure of lowest R_{wp} was then then refined at the molecular scale using an automated Rietveld refinement process. Due to the large number of atoms and consequent degrees of molecular freedom associated with the system, an energy optimisation component was included as part of the refinement in case the powder pattern alone was insufficient for a successful structure solution. The first refinement process was executed to optimise the trial structure for the lowest potential energy with lesser regard for R_{wp}, thus resulting in the most theoretically stable structure. A second Rietveld refinement was refined with the same molecule forcefield, with a simultaneous target of maximising correlation between the experimental and simulation, thus minimising the corresponding R_{wp} (%). The resulting molecular conformations from these refinement processes, together with the *ab-initio* structure derived through density functional theory (DFT) are displayed in Figure 6.5 below.

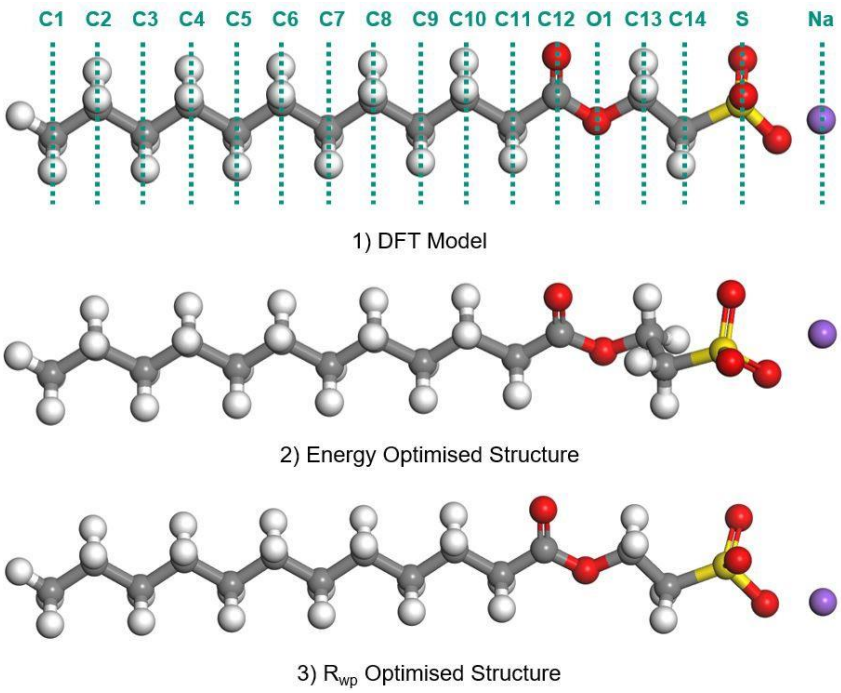

Figure 6.5: 3D representations of the molecular conformation of sodium lauroyl isethionate following an ab-initio DFT geometry optimisation (1) and Rietveld refinements of trial structures focusing on the optimisation of potential energy (2) and R_{wp} (3) respectively. Dashed lines correspond to the positional labels used in this text to reference specific atoms in the SLI skeletal backbone. Energy optimisation was executed using the COMPASS-II forcefield, whilst the DFT-derived geometry optimisation was conducted using the Def2-TZVP basis set and B3LYP-D3 functional.

A difference in molecular conformation can be discerned from the structures displayed in Figure 6.5. An analysis of the bond lengths and angles along the primary skeletal backbone revealed some quantifiable differences between the structures. The DFT model displayed a marginally shorter average C-C bond length along the alkyl chain when compared with the refined structures (1.53 Å vs 1.55Å), as well as a smaller angle at (C12-*O1*-C13) ester bond (115° vs 126°). While this contributes to the skeletal contraction observed in the DFT model, when compared with the refined structures, it fails to account for the observed visual difference in conformation between the energy and R_{wp} focused optimisations.

A torsional angle corresponds to the planar angle between any two parts of a molecule joined by a single chemical bond. The torsional angles exhibited by the different molecular forms of SLI, indicated that the energy-optimised and R_{wp}-optimised

molecules are conformational isomers. The corresponding data from all three variations of SLI are provided in Table 6.4, along with analogous measurements from the powder-derived anhydrous structure of SDS.[236]

Table 6.4: Torsional dihedral angles along the primary skeletal backbone of SLI following an ab-initio DFT geometry optimisation (1) and Rietveld refinements of trial structures focusing on the optimisation of potential energy (2) and R_{wp} (3) respectively. The labels (C1, C2, etc) in SLI correspond to specific atomic positions, as identified in Figure 6.5. For SDS, O1 corresponds to the oxygen atom bridging between the alkyl and sulfate functional groups.

Four Atom Dihedral Bond (SLI)	**(1) DFT Model Tors. (°)**	**(2) Rietveld Energy Tors. (°)**	**(3) Rietveld R_{wp} Tors. (°)**	**Four Atom Dihedral Bond (SDS)**	**Anhyd. SDS Tors. (°)**
C1-C2-C3-C4	179.999	179.511	179.997	C1-C2-C3-C4	177.875
C2-C3-C4-C5	180.000	178.404	179.952	C2-C3-C4-C5	177.956
C3-C4-C5-C6	179.999	179.163	179.994	C3-C4-C5-C6	179.761
C4-C5-C6-C7	179.999	178.830	179.906	C4-C5-C6-C7	178.197
C5-C6-C7-C8	179.995	179.534	179.983	C5-C6-C7-C8	179.465
C6-C7-C8-C9	179.938	177.717	179.864	C6-C7-C8-C9	179.371
C7-C8-C9-C10	179.986	179.551	179.982	C7-C8-C9-C10	179.469
C8-C9-C10-C11	179.954	177.266	179.849	C8-C9-C10-C11	177.571
C9-C10-C11-C12	179.996	179.810	179.806	C9-C10-C11-C12	178.705
C10-C11-C12-O1	179.957	178.759	178.140	C10-C11-C12-O1	175.521
C11-C12-O1-C13	179.905	173.560	179.058	C11-C12-O1-S	172.284
C12-O1-C13-C14	179.859	91.750	177.073	-	-
O1-C13-C14-S	179.820	177.898	179.746	-	-

The DFT model displayed an anti-coplanar conformation, with all atoms producing torsional angles of ~180°. Given that the model environment consisted of a single molecule in vacuum, this structure exhibited the least torsional and steric strain resulting in the most stable conformation. Both refined structures exhibited minimal deviation along the alkyl chain with angles close to 180°. At the centre of the ester bond, however, the energy-optimised structure displayed a syn-clinal conformation with a dihedral of 90°. In the common alkyl conformational model of butane, the 90°

eclipsed conformation results in significant torsional strain and an energy cost of ~2.5 kcal/mol when compared with the anti-coplanar conformation.[250] Figure 6.6, however, depicts the predicted energy penalties resulting from the conformational isomerism of ethyl formate, as calculated by two individual DFT simulations.[251] The C-O-C-C bond arrangement is more far representative of the C12-O1-C13-C14 ester group in SLI. The results indicate that while the anti-coplanar 180° angle is still the most stable conformation of the ester group, the syn-clinal arrangement is similar to the *gauche* conformation of butane at 60° and exists within a metastable local energy minimum with a conformational penalty of just 0.5 kcal/mol.

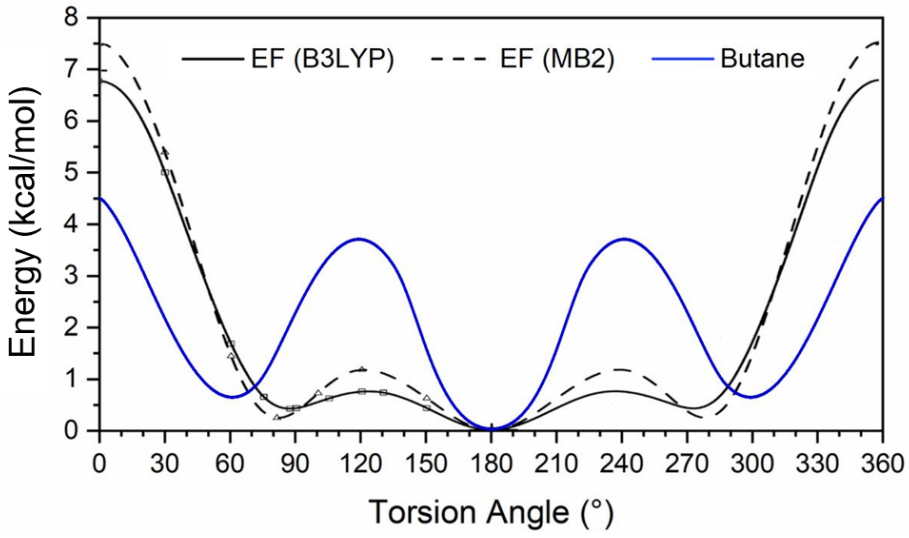

*Figure 6.6. Torsional potential energy (kcal/mol) of the C-O-C-C ester bond in ethyl formate (EF), as a function of its torsional dihedral angle. Obtained via a DFT simulation using the 6-311+G** basis set, coupled with the B3LYP and MB2 functionals respectively. Calculations were executed by Bohn and Wiberg.[251] Comparative conformational energies for the C-C-C-C bond in butane obtained from Brown et al.[250]*

A conformational analysis of the C-O-C-C ester bond in SLI confirms the stability of the 90° torsional angle conformer. Figure 6.7 shows the influence of the ester bond torsion on the total energy of the system. The minimal energy penalty resulting from torsions between 85° and 275°, compared with 180° suggests that conformations within this range could be energetically feasible in the presence of additional stabilising intermolecular interactions in the crystalline state. To assess the

implications of this conformational change on the overall lattice structure, the packing within the unit cell was considered.

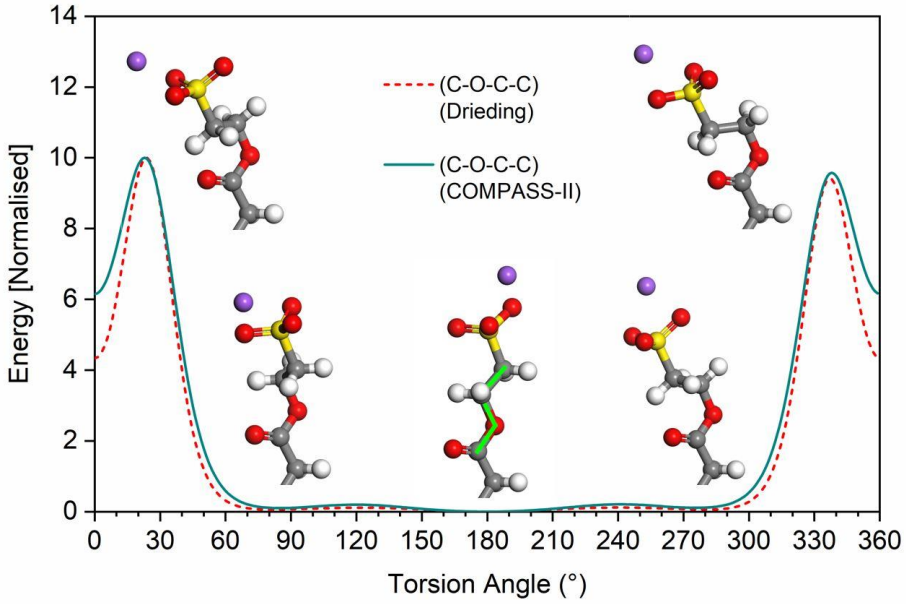

Figure 6.7: Influence of C-O-C-C ester bond torsion, on the total energy of an SLI molecule. Obtained from energy calculations using the Drieding and COMPASS-II molecular forcefields. 3D Molecular representations correspond to the conformers at local energy maxima and minima at 22°, 85°, 180°, 275°, and 338°. The C-O-C-C bond of interest is highlighted green in the 180° conformation.

Figure 6.8 shows both the energy and R_{wp} optimised structures packing with the Pawley refined unit cell from the auto-indexing process. The 90° torsion angle from the syn-clinal conformation resulted in a much tighter tilt angle, coupled with a higher lateral packing efficiency. However, given that both systems in Figure 6.8 are packed into identical unit cells, the tighter packing has resulted in a much larger gap between alkyl chains in adjacent layers for the energy optimised system. Where the R_{wp} optimised structure exhibited a planar distance of 1 Å in the *a*-axis between terminal methyl groups, the energy optimised system was significantly higher at 9.5 Å.

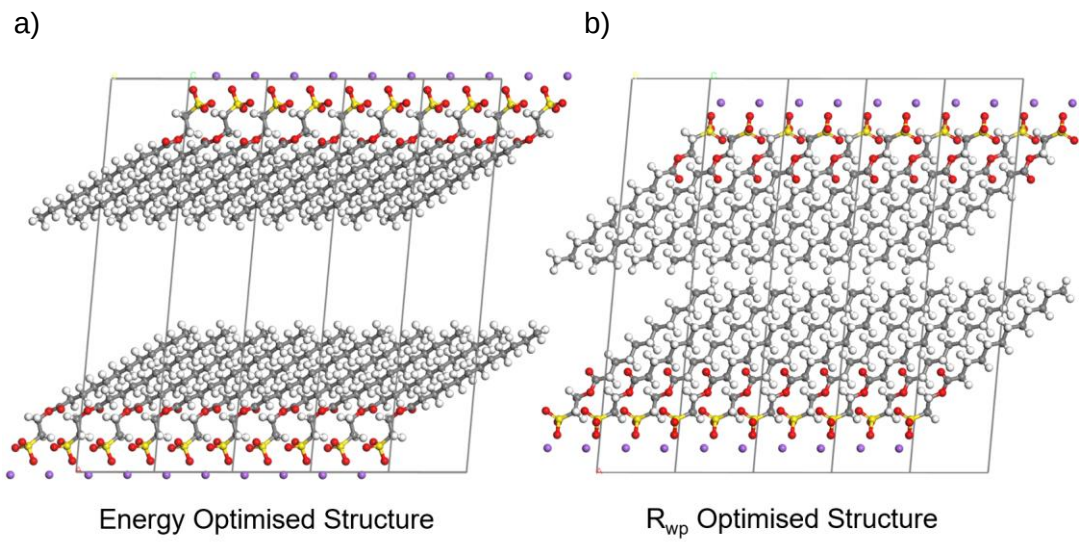

Figure 6.8: Crystalline packing of molecules produced through the Rietveld refinement of SLI through the optimisation of potential energy (left) and R_{wp} (right). R_{wp} values are 17.9% and 9.7% respectively. Both systems are constructed from identical Pawley-refined monoclinic unit cells, with a P21/c space group symmetry and 4 molecules in the asymmetric unit. Representation shows view down the b-axis, where the crystalline lamellar bilayer sheets exist in the b-plane.

Having solved the crystal structure of SDS using powder diffraction, Smith *et al.* reported a similar phenomenon where the trial structures of lowest energy also exhibited a large inter-lamellar void caused by a *gauche* molecular conformation within the alkyl chains.[236] The monohydrate form of SDS has been reported to exhibit molecules of *gauche* and co-planar conformation co-existing within a single asymmetric triclinic unit cell.[150] In the anhydrous phase, however, it was stated by Smith *et al.* that the all *gauche* conformations were deemed unstable and the final structure of anhydrous SDS was proposed to exhibit an inter-lamellar distance of ~1 Å, similar to that of the R_{wp} optimised structure. The chain packing in the energy-optimised structure also results in moderately close contacts between adjacent alkyl chains, which differs from the structure of SDS where Coiro *et al.* report that van der Waals contributions provide minimal contribution to the stability of the lattice.[150] While the energy-optimised structure in *gauche* conformation may theoretically correspond to a more stable structure of a monomeric system, the diffraction data from the current study, as well as that for anhydrous SDS, indicates that the anti-coplanar

conformation with minimal void in the unit cell is more representative of the experimental crystalline structure.

6.3.4. Lamellar Bilayer Structure of SLI

In addition to the quantitative confidence metrics utilised in the structure solution process, characteristics of the crystalline lamellar bilayer structure can be used to further rationalise the structure of SLI through comparison with similar long-chain, anionic, sulfur-based surfactants such as SDS. One of the key differences between the trial structures in the previous subsection was the angle at which alkyl chains were tilted relative to the unit cell and the resulting implications on packing within the unit cell. Trends have been identified between the size of the polar headgroup in anionic surfactants and the angle at which the surfactant is tilted within the unit cell.[149, 150, 236]

Previous studies have relied on an approximation of headgroup size based on the unit cell parameters of the crystalline.[150] In this study, the specific volume of the headgroup, based on its van der Waals radius, was measured to identify any correlation between headgroup sizes and tilt angles. Given the consistent dodecyl alkyl chains across SLI, SDS and its varying hydrates, the size of the surfactant headgroup and their corresponding tilt angles in the crystalline phase were calculated and compared in Table 6.5.

Table 6.5: Influence of headgroup size on lamellar tilt angle of various dodecyl chained sulfur-based anionic surfactants. Headgroup area was calculated from the respective unit cell parameters, as described by Coiro et al.[150] Headgroup volumes correspond to the van der Waals volume of the head group in the crystalline phase, as calculated from their respective CIF files.

Surfactant System	Head Group Area (Å^2)	Head Group Vol. (Å^3)	Lamellar Tilt Angle (°)
SDS	19.3	93.6	15
SDS.1/8H_2O	20.9	96.6	10
SDS.1/2H_2O	25.8	105.0	40
SDS.H_2O	29.5	126.2	45
SLI	35.0	156.3	48

Table 6.5 exhibits clear trends between headgroup size and lamellar tilt angle for both specific volumetric calculations of the headgroup size and the lattice-based area approximations. The data pertaining to SLI specifically also correlates with previously published structures of SDS and its varying hydrates. In addition to improving the viability of the obtained structure of SLI, this correlation reinforces the trends in surfactant packing proposed by Coiro *et al.*[150] by demonstrating their applicability to other sulfur-based dodecyl-chained surfactants.

6.3.5. Lattice Energy Calculation and Synthon Analysis

To characterise the intermolecular interactions underpinning the observed crystal structure of SLI and further provide numerical confirmation of its thermodynamic validity, the lattice energy for the proposed crystal structure was calculated using HABIT98. This energy corresponds to the electrostatic and dispersion forces constituting the crystalline lattice. The change in lattice energy with respect to the unit cell radius is shown in Figure 6.9. The optimal energy was calculated at a radius of 66.34 Å with a corresponding lattice energy of -51.42 kcal/mol.

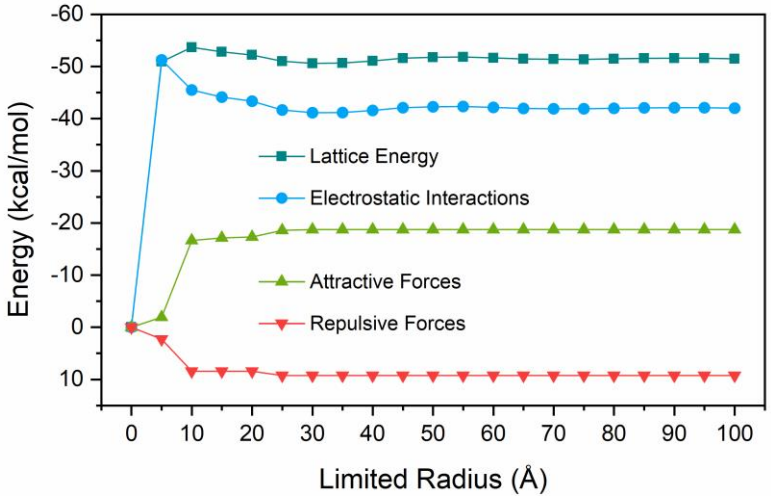

Figure 6.9: Lattice energy (kcal/mol) of SLI as a function of the limiting radius (Å). Lattice energy (grey) is a sum of the electrostatic interactions (blue), attractive forces (green) and repulsive forces (red) at the stated radius. Energies obtained via HABIT98 using the Drieding forcefield, with charges calculated independently via DFT using the Def2-TZVP basis set and B3LYP-D3 functional.

The specific intermolecular interactions contributing most to the stability of the lattice energy are listed in Table 6.6. A visual representation of the corresponding synthons (Figure 6.10) shows how the five synthons providing the largest contributions to the lattice energy are all dominated by electrostatic interactions between anionic SO_3^- groups and Na^+ ions. The attractive and repulsive energies correspond to non-coulombic intermolecular interactions such as dispersion forces, dipole interactions and hydrogen bonding. Synthon S1 corresponds to the interaction between the Na cation in closest proximity to the sulfonate group. All other synthons show how the sulfonate interacts with other Na cations in the proximity. S2 corresponds to the adjacent cation, S3 corresponds to the lateral cation in the same bilayer, S4 corresponds to the cation in an adjacent bilayer and S5 corresponds to the adjacent cation in an adjacent bilayer, as shown in Figure 6.10. The synthons S1 to S5 constitute significant proportions of the absolute lattice energy as they are offset by repulsive synthons which are dominated by positive coulombic interactions, the largest of which is +37.67 kcal/mol.

Table 6.6: Interaction energies of the intermolecular synthons exhibiting the largest absolute contributions to the lattice energy of SLI.

Synthon	Interaction Energy	Interionic Distance (Å)	Electrostatic Interactions	Attractive Forces	Repulsive Forces
S1	-50.91	2.73	-51.27	-1.93	+2.29
S2	-30.73	3.83	-30.38	-0.41	+0.06
S3	-26.50	5.45	-26.45	-0.05	-
S4	-18.03	6.40	-18.02	-0.01	-
S5	-17.34	7.02	-17.34	-0.01	-

* All energies in kcal/mol

When coulombic interactions are not considered, the remainder of the lattice energy consists of van der Waals interactions between alkyl chains. V1, V2 and V3 correspond to interactions with the adjacent molecule, adjacent bilayer and lateral interactions within the bilayer, as shown in Figure 6.11. At a limiting radius of 5Å (Figure 6.9), S1 is the only observed synthon and the lattice energy is consequently dominated by its respective electrostatic interaction. As the radius is increased, the lattice energy is offset by the introduction of synthons, V1, V2 and V3 results in a greater non-coulombic component in the overall lattice energy.

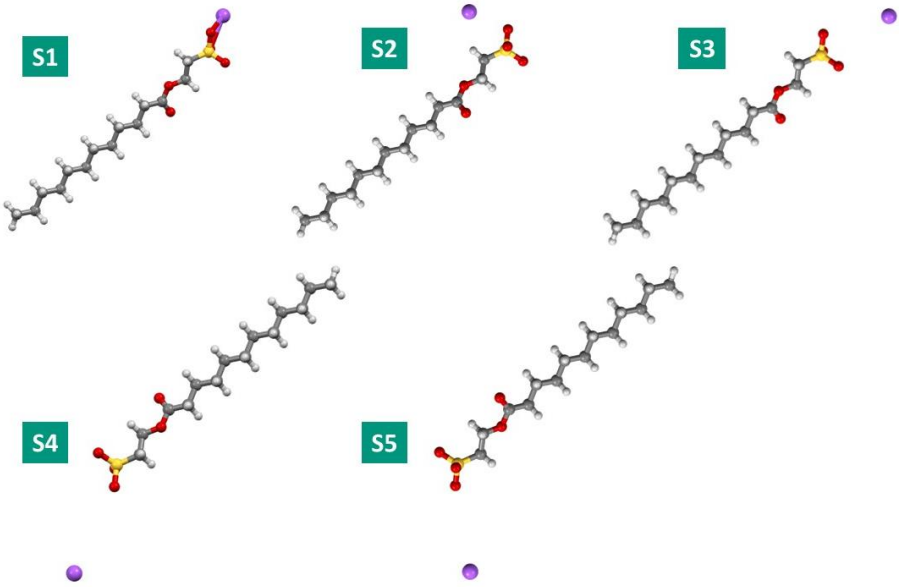

Figure 6.10: Intermolecular synthons exhibiting the largest absolute contributions to the lattice energy of SLI. Calculated via HABIT98 using the Drieding forcefield, with charges calculated independently via DFT using the Def2-TZVP basis set and B3LYP-D3 functional. The top 5 synthons consist of electrostatic interactions between anionic sulfonate groups and Na cations.

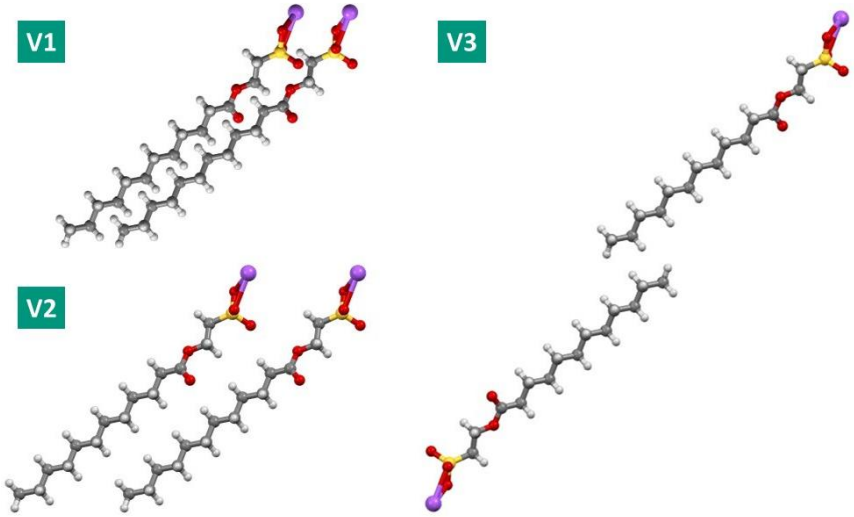

Figure 6.11: Intermolecular synthons exhibiting the largest non-coulombic contributions to the lattice energy of SLI. Calculated via HABIT98 using the Drieding forcefield, with charges calculated independently via DFT using the Def2-TZVP basis set and B3LYP-D3 functional. The top 3 non-columbic interactions consist of van der Waals interactions between alkyl carbon chains.

Table 6.7: Interaction energies of the intermolecular synthons exhibiting the largest non-coulombic contributions to the lattice energy of SLI.

Synthon	Interaction Energy	Interionic Distance (Å)	Electrostatic Interactions	Attractive Forces	Repulsive Forces
V1	-3.46	5.58	-	-4.94	+1.49
V2	-3.08	6.35	-	-4.54	+1.45
V3	-1.83	7.61	-	-5.04	+3.22

* All energies in kcal/mol

Due to the highly charged nature of the system, the lattice energy compromises of strongly attractive and repulsive components. When each atom-atom interaction is accounted for, however, the absolute contribution of each functional group to the overall lattice energy can be calculated (Table 6.8). Energy is expectedly dominated by ionic interactions between sulfonate and cationic species with additional non-coulombic stability from alkyl and oxygenated systems.

Table 6.8: Interaction energies of the intermolecular synthons exhibiting the largest non-coulombic contributions to the lattice energy of SLI.

Molecular Fragment	Electrostatic Interactions	Attractive Forces	Repulsive Forces	Total Energy	Contribution to Lattice Energy
Alkyl	+3.84	-12.88	+5.75	-3.27	**6.4%**
Ester	-1.34	-1.60	+0.67	-2.27	**4.4%**
SO_3^- Na^+	-44.87	-4.23	+2.81	-46.27	**89.3%**
Total	**-42.32**	**-18.74**	**+9.25**	**-51.81**	**100.0%**

* All energies in kcal/mol

An analysis of the van der Waals radii (vdW) arising from Synthon V1 show how the observed interdigitation between hydrogen atoms of adjacent molecules likely results from an optimisation of intermolecular interaction between alkyl chains. A comparitively larger vdW radius was observed around the Na cation, as a result of its increased electron density when compared with atoms in the hydrocarbon chain. (Figure 6.12)

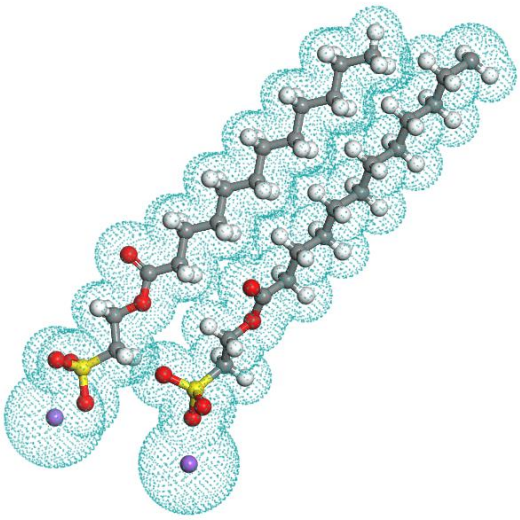

Figure 6.12. van der Waals radii arising from the strongest non-Coulombic synthon (V1) in the crystal structure of SLI. Volumes calculated via the surface tool in Materials Studio 17.0 using a vdW scale factor of 1.0.

Synthon S3 (Figure 6.10) indicates there is a coulombic attraction of -30.73 kcal/mol between the Na cation and the opposing cross-planar sulfonate anion. However, the coulombic repulsion between adjacent Na cations is larger at +34.79 kcal/mol. These electrostatic repulsions, when coupled with the larger vdW radii, could explain why the axial inter-lamellar spacing between Na cations (4.7 Å) is significantly larger than that between alkyl chains (1.0 Å), thus providing an energetic justification for the observed lamellar arrangement in the crystal structure of SLI.

6.4. Conclusion

The crystal structure of sodium lauroyl isethionate (SLI) was successfully determined through the combined application of powder X-ray diffraction and molecular simulation systems. Following an auto-indexing procedure, the lattice was found to exhibit a monoclinic unit cell with P 21/c space group, similar to the anhydrous structure of sodium dodecyl sulfate (SDS). Following Rietveld refinement and conformational energy analysis of trial structures, a molecular structure of *trans-trans* lamellar bilayer conformation was found to exhibit good agreement with the

experimental powder pattern. Through comparison with SDS and its varying hydrates, SLI was found to reflect general structural trends of an increasing lamellar tilt angle, with increasing headgroup size, as exhibited by other sulfur-based dodecyl-chained surfactants.

Synthon based lattice energy calculations revealed that the crystalline stability was dominated by coulombic interactions between anionic sulfonate groups and Na cations at varying radii. Further analysis of non-columbic interactions indicated that the observed interdigitation between alkyl chains was attributable to van der Waals interactions between adjacent molecules. The increased lamellar spacing between polar groups, when compared with non-polar groups, could explain the ready formation of a hemihydrate structure postulated in a previous study. Given the phase-dependent properties of analogous surface-active molecules, further study into the hydration of the SLI could lead to improved control with respect to critical performance-related properties in the formulation of personal care products.

Chapter 7: Temperature Resolved Small Angle X-Ray Scattering Analysis of SLI

Synoposis: *The results chapter describes the in-situ structural analysis of SLI to observe how the structure of SLI varies with temperature. Due to the propensity for thermal degradation in SLI, coupled with a decrease in structural order expected with elevated temperatures, a combined of synchrotron-sourced SAXS experiments and molecular techniques were applied for the rapid acquisition of high resolution data. The structural information from this study is intended to develop a link between process and structure to assist in future optimisations of isethionate ester manufacture.*

7.1. Introduction

SLI can be synthesised via the esterification of lauric acid with sodium isethionate, as described in Section 1.1.3. Chapter 4 describes how the starting materials were reacted at a temperature of 240°C for 4 hrs in the absence of solvent. Following completion of the reaction, the molten surfactant is typically isolated via melt crystallisation onto a flat surface under ambient conditions. It has long been proposed that the physical structure of such surfactants after this process influence performance-related properties within the resulting product such as hardness, solubility, texture and lathering performance.[78, 228, 252]

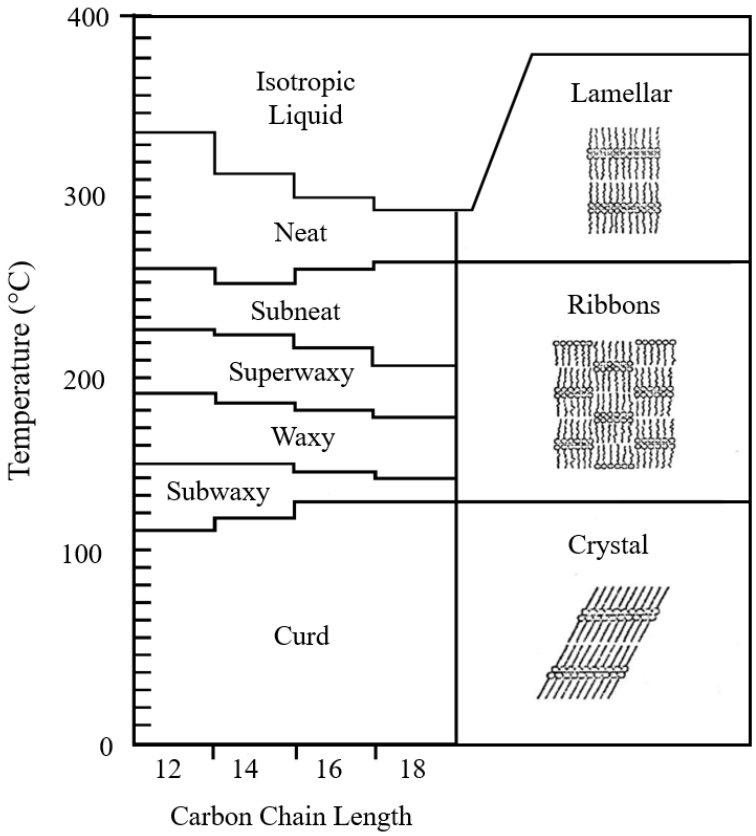

Figure 7.1. Thermotropic crystal phases exhibited by sodium carboxylate soaps of varying alkyl chain length (C12-C18) between 0 and 400°C. Right pane corresponds to the molecular structure of the surfactant at a given phase. Figure adapted from Friedman et al. [27] and Luzzati et al. [143].

Temperature-dependent studies of similar long chain organic surfactants report the presence of multiple thermotropic phases appearing between the isotropic liquid melt and the ambient crystalline form. Figure 7.1 shows how sodium carboxylate surfactants first crystallise as solid lamellar crystals, then transition into alternate layered ribbon structures, before finally reaching a crystalline, tilted lamellar bilayer structure at temperatures around 100°C.

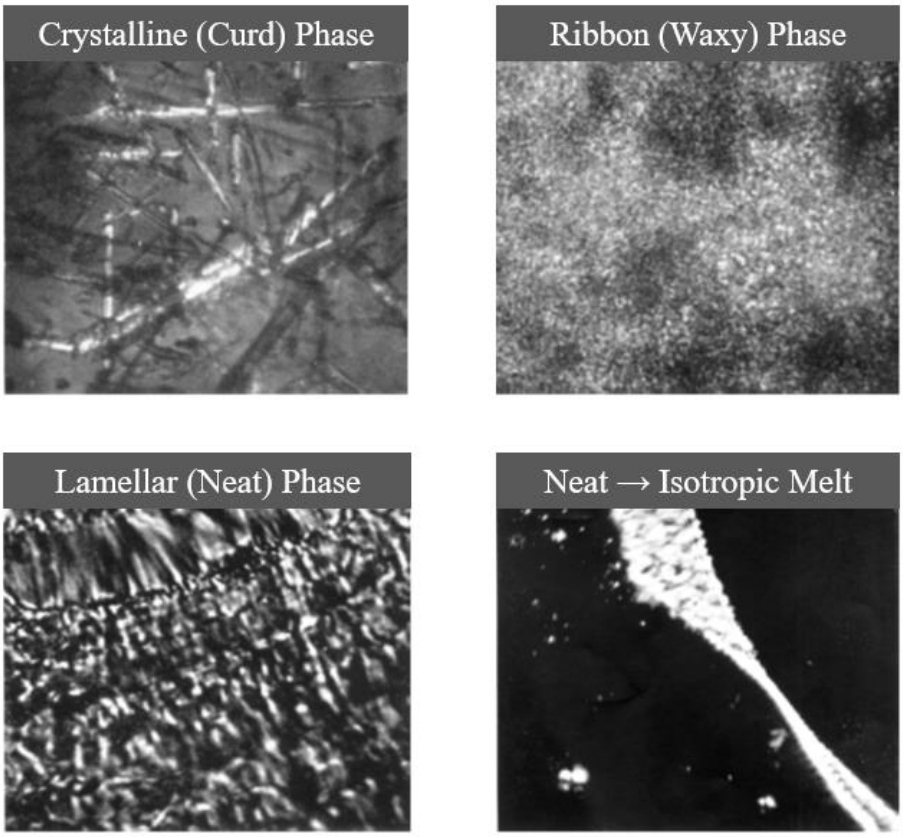

Figure 7.2: Optical microscopy images of the thermotropic phases exhibited by sodium palmitate upon heating from a solid crystalline state to an isotropic liquid melt. The final image (bottom-right) depicts remnants of the neat phase as the material transitions into the liquid state. Images were obtained via polarised light microscopy with crossed Nicols at 166x magnification, adapted from Vold et al.[253]

A physical characterisation of these temperature-dependent phases was conducted by Vold *et al.*[253] (Figure 7.2). The "curd" phase displayed fibrous microstructure coupled with a 'hard crystalline' physical form in the solid phase. The "waxy" ribbon structure displays a prominent loss in structure coupled with a reported softening of

the solid state. The transition to the "neat" phase was finally purported to occur with a gradual loss of anisotropy, coupled with a concurrent decrease in viscosity until the material existed as an isotropic melt in the liquid phase. Analogous observations pertaining to the physical form of carboxylate soaps and their phase-dependent transition temperatures were reported by Lawrence *et al.*[254] and McBain *et al.*[21]

In the more recent study of choline soaps containing a trimethyl-ethanolammonium cation, similar trends were reported in the corresponding thermotropic study of crystalline phases. Small X-ray scattering confirmed that the three phases described by Luzzati *et al.* [143] were present in their system. Despite a variation in headgroup chemistry when compared with carboxylate soaps, the previously reported succession of lamellar phases, interdigitated molecular, followed by a tilted lamellar crystalline were observed in the same sequence as previous systems. The transition temperatures, however, were lower than those observed for carboxylate soaps, as displayed in Figure 7.3.

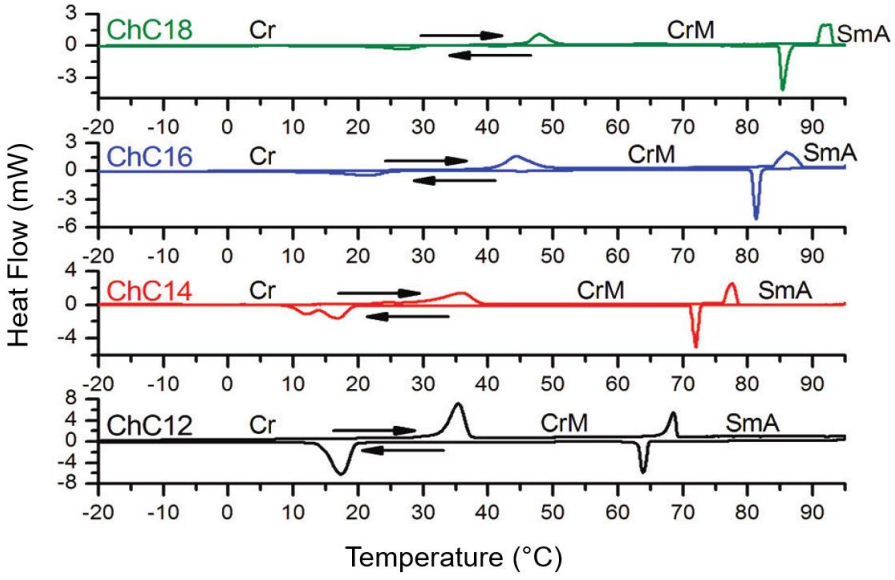

Figure 7.3: Phase transition temperatures between lamellar crystal (SmA), interdigitated ribbons (CrM) and tilted crystalline bilayer phases (Cr) in choline soaps. Data was collected via DSC with subsequent verification of phases via SAXS. Image reproduced from Klein et al.[145]

Outside of the surfactant applications, MacMillan and Roberts used a combination of existing crystallographic information and SAXS to identify changes in the temperature-dependent polymorphic phase behaviour of cocoa butter. The liquid melt at 50°C was cooled to 20°C, held at 20°C, then heated to 30°C. (Figure 7.4) Any changes in the long axis spacing were used to identify the varying polymorphs through this temperature cycle (see Figure 7.4). The plot also shows how increases in intensity correspond to the prevalence of each polymorphic phase, as an indicator of structural order within the system. Further studies into the process-controlled phase behaviour of these glyceride molecules indicates that the changes between the six identified polymorphs influence performance-dependent physical properties such as hardness, texture and stability under elevated temperatures.[255]

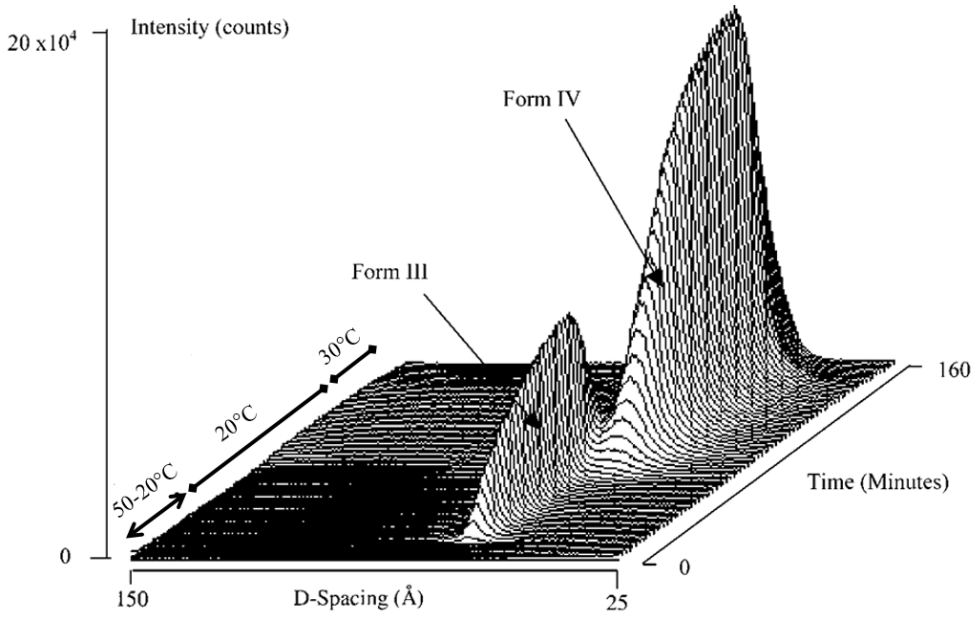

Figure 7.4. Temperature-induced changes in the structure of cocoa butter measured via synchrotron SAXS. Samples cooled from the melt at 50°C to 20°C at 8°C/min with patterns collected at 2°C increments.

In the aforementioned studies, identification of mesomorphic phases was made easier through the pre-existing data on single crystalline phases. This was predominantly collected through single crystal X-ray diffraction studies of the corresponding materials. Some examples of published lattice parameters pertaining to sodium laurate

(NaL) and sodium palmitate (NaP) are displayed in Table 7.1. A more detailed review on the single crystal phases exhibited by carboxylate has been published by Buerger *et al.* [256]. In the case of commercial surfactants, however, lower purity levels, mixtures of carbon chain lengths and less defined crystallisation conditions can lead to materials of lower crystallinity and structural order.[78, 228, 252] In the absence of high structural order, the resulting loss in high angle X-ray diffraction data renders an atomistic crystal structural analysis unachievable .[239, 242]

Table 7.1: Published lattice parameters for crystalline structures of sodium laurate (NaL) and sodium palmitate (NaP). a, b and c correspond to lengths of crystallographic axes (Å) in the unit cell, whilst α, β, and γ refer to the respective angles (°).

Soap	Form	Unit Cell	a	b	c	α	β	γ	Reference
NaL	α	Orthorh.	7.6	-	30.1	90	90	90	Thiessen et al. [257]
NaP	α	Orthorh.	8.06	9.24	47.70	90	90	90	Thiessen et al. [258]
	1/2 H_2O	Monocl.	9.13	8.01	91.85	90	94	90	Buerger et al. [256]
	1/2 H_2O	Monocl.	9.13	8.01	92.94	90	94	90	Minor *et al.* [248]

Fortunately, the data acquired at smaller X-ray diffraction angles alone can be Fourier-transformed to provide information on the electron density perpendicular to a lamellar phase. These techniques can provide valuable insight into the structural order of systems exhibiting long range structural order, in the absence of an atomistic crystalline structure. A recent study by Ladd-Parada *et al.* investigated the structure of long chain hydrocarbons using SAXS.[259] A one-dimensional electron density profile (EDP), acquired through the transformation of characteristic 00*l* scattering peaks, led to the identification of stacked, glyceride layers in a back-to-back arrangement. A similar study by Mykhaylyk *et al.* utilised changes in lamellar spacing observed through EDP analysis to estimate the tilt angle exhibited by long chain hydrocarbons. Only the 00*l* reflections were utilised in the characterisation of polymorphic phases.

In this study, SLI is analysed via temperature-dependent SAXS to identify any changes in phase behaviour, observable in the solid state, prior to isotropic melting. A

synchrotron radiation source is used in preference to a laboratory X-ray diffractometer to permit analysis times more representative of the industrial melt crystallisation process. The significantly higher flux at the synchrotron drastically improves scattering at analogous experiment times, thus increasing the likelihood of detection of 00*l* reflections at higher orders of diffraction. Electron Density Profiles (EDP) are calculated for the primary crystalline phase observed in the previous section via PXRD. The temperature-dependent EDP analysis permits changes in the lattice dimensions to be observed. Previous studies adopting EDP analyses in the characterisation of sulfur-based surfactants could not be found in the literature. The EDP data is therefore validated against a complementary quantum mechanical analysis via density functional theory (DFT) to confirm that the correct phase combination is utilised in the calculation. Any new phases measured in significant quantity are characterised via a combination of existing crystallographic and molecular mechanics based modelling techniques to determine any correlation between the phase behaviour of SLI and previous alkyl-chained anionic surfactants. Through observation of the phases exhibited by isethionate ester surfactants, valuable information related to the resulting microstructure is obtained.

7.2. Experimental

7.2.1. Preparation of SLI Samples

Sodium lauroyl isethionate (SLI) was prepared and isolated to 98% purity in accordance with the methods described in a recent study.[166] Lauric acid, 99+% (LA) was obtained from Fisher Scientific and used as received. SLI was doped with LA at concentrations between 0 and 100 wt%, at 10 wt% increments. 3-5g of SLI and LA were accurately weighed at the desired quantity to the nearest 0.1 mg using an analytical balance. Samples vials were stoppered with silicone rubber septa and purged with N_2 for 10 min. The sealed vials were then submerged in an oil bath at 240°C, with magnetic stirring in both the sample and bath fluid. Higher melting temperatures and the ingress of air was avoided to limit thermal degradation of SLI.[260] Once a homogenous melt had been obtained, samples were immediately cooled in a dewar of dry ice/acetone. A crash cool was adopted to simulate commercial crystallisation conditions and preserve any metastable phases existing within the binary system. The

resulting solid samples were ground under ambient conditions prior to instrumental analysis.

7.2.2. Small X-ray Scattering (SAXS) Analysis of SLI

SAXS experiments were executed using the 1-5 beamline at the Stanford Synchrotron Radiation Lightsource (SSRL), Menlo Park, CA, USA. Samples were exposed to X-ray radiation at an energy of 15 keV with a wavelength of 0.8265 Å. The beamline was equipped with a Rayonix SX165 2D CCD detector (2048 pixel × 2048 pixel, 79 μm pixel size) where the sample-to-detector distance was set at 432 mm. Beam centre and scattering vectors were calibrated using a silver behenate standard. Binary samples of SLI were heated from 40°C to 300°C using a heated transmission stage. X-ray patterns were collected at 10°C intervals at a Q-range between 0.03 and 1.4 A^{-1}. Upon reaching the desired temperature, a 60 s stabilization time was set prior to a 45 s acquisition time, before the sample was heated for the next measurement. Captured patterns were processed using the Nika package [261] for IGOR Pro 7 (Wavemetrics Inc.). The 2D images were azimuthally integrated into 1D plots of scattering intensity (I), as a function of scattering vector (Q). A kapton blank was also measured as a function of temperature and utilised for background subtraction. To assess the disparity between the measured temperature in the heating block and the actual temperature in the sample cell, a Type-K thermocouple was inserted into the kapton blank to provide corrected temperatures for each 10°C measurement.

7.2.3. Computational Analysis via Density Functional Theory (DFT)

A monomeric vapour phase structure of SLI was created using the Avogadro 1.2 molecular visualisation tool and preliminarily optimised using the MMF95 force field. Structures were then refined using a density functional theory (DFT) based geometry optimisation using ORCA 3.0.3 package. Calculations were executed using the def2-TZVP basis set combined with the B3LYP functional. All calculations were successfully completed within a convergence criteria of 1 x 10^{-8} au and 125 iterations.

7.2.4. Electron Density Profile Calculations

Lamellar structuring was first identified by characteristic equidistant 00*l* peaks observable at $Q < 1$ $Å^{-1}$. The corresponding signals were then fitted using Gaussian parameters due to the Type 1 crystalline thermal disorder displayed by the lamellar

system.[113, 262] Lamellar order was then verified via the fitting and zero point extrapolation of scattering vector (q) against diffraction order (h). Through this assumption of centrosymmetric planar ordering, Electron Density Profiles (EDP) depicting electron density (ρ) as a function of molecular radius (z) were produced using Eq. (24).[263, 264]

$$\rho\,(z) = \sum_{h=1}^{h\,\max} \alpha_h \cdot F_h \cdot \cos\left(\frac{2\,\pi\,h\,z}{d}\right) \tag{24}$$

F_h denotes the fitted scattering amplitude (form factor), while d is the lamellar phase periodicity in real space, corresponding to the first order diffraction peak (h = 1). The phase factor (α_h) corresponds to a value ± 1; an uncertainty which arises due to the typical convoluted intensity of interfering waves. In this instance, the electron density data obtained via DFT was used to verify the utilised phases. However, modelling approaches described in the literature,[265] as well as reconstruction of the Fourier transformed scattering pattern[266] can also be used for phase verification in the absence of a quantum mechanical simulation.

Eq. (25) shows how the Gaussian-fitted SAXS data was combined with the DFT-derived molecular model to estimate the tilt angle (θ_{tilt}) at which solid phase SLI molecules were tilted from the primary axis perpendicular to the lamellar bilayer:

$$\theta_{tilt} = arccos\left(\frac{4\pi}{Q_F \cdot d_M}\right) \tag{25}$$

Q_F corresponds to the centre (A^{-1}) of the first-order Gaussian function (001 relection) of the corresponding lamellar phase. d_M pertains to the model-derived length of a single molecule, as measured from the geometry-optimised structure of SLI. A van der Waals surface was first applied to the model using Materials Studio 17 to produce dimensions more representative of packing within the molecular crystal. Eq. (25) is based on tilt angle measurements of lipid bilayers by Sun *et al.*[267]

7.2.5. Characterisation of Phase B via Molecular Modelling

Experimental details relating to the forcefield calculations, conformational analyses, lattice energy and molecular volume calculations are presented in Section 6.3.

7.3. Results & Discussion

7.3.1. Small Angle X-ray Scattering Analysis of SLI

A 2D raw image collected via the small angle X-ray scattering analysis of SLI is displayed in Figure 7.5. Changes in intensity amplitude is indicative of a preferred orientation of crystals within the sample holder, resulting from the plate-like morphology of SLI. (See Figure 3.13 in Section 3.8).

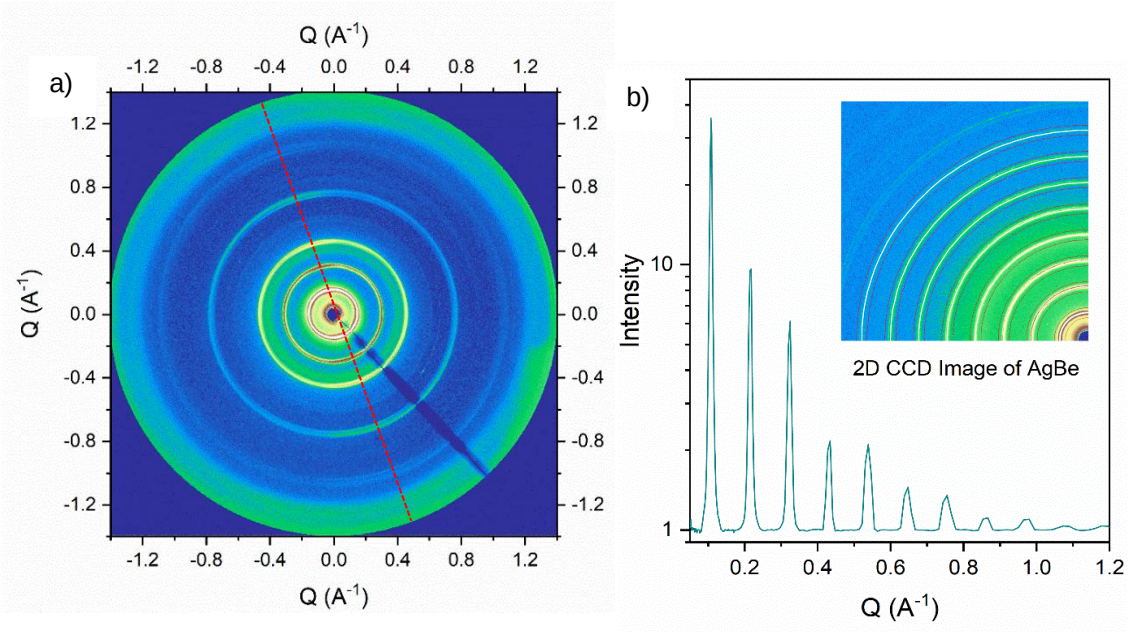

Figure 7.5: a) 2D CCD image of SLI at 38°C measured via small angle X-ray scattering. Scattering intensity measured at Q range between 0.03 and 1.4 A-1 with X-ray energy of 15 keV and wavelength (λ) of 0.8265 Å. Preferred orientation is observable via with an increased intensity of Debye rings perpendicular to the marked axis (dashed red line). b) 2D CCD image of silver behenate (AgBe) and the 1D intensity plot resulting from the calibration of its characteristic diffraction peaks at highlighted d-spacings of 58.3, 29.2, 19.5, 14.6, 11.7, 9.7, 8.3 and 7.3 Å (white/red rings in image).

To convert individual pixels to the calibrated scattering length in Q-space (A^{-1}) displayed in Figure 7.5 a reference sample of silver behenate (AgBe) was analysed using analogous SAXS parameters. The calibrant was converted to a 1D plot of scattering intensity based on the certified positions of its characteristic diffraction peaks. The 2D image and its 1D intensity plot are displayed in Figure 7.5b. All samples were analysed using an identical wavelength, energy, sample-to-detector distance and beam position to retain calibration.

Figure 7.6a shows how a minimal change in background scattering was observed over the experimental temperature range between 40 and 260°C. The characteristic bimodal distribution was modelled using OriginPro and used to subtract the background from all experimental samples, with specific care taken to retain the presence of any amorphous content. An example pattern is displayed in Figure 7.7b.

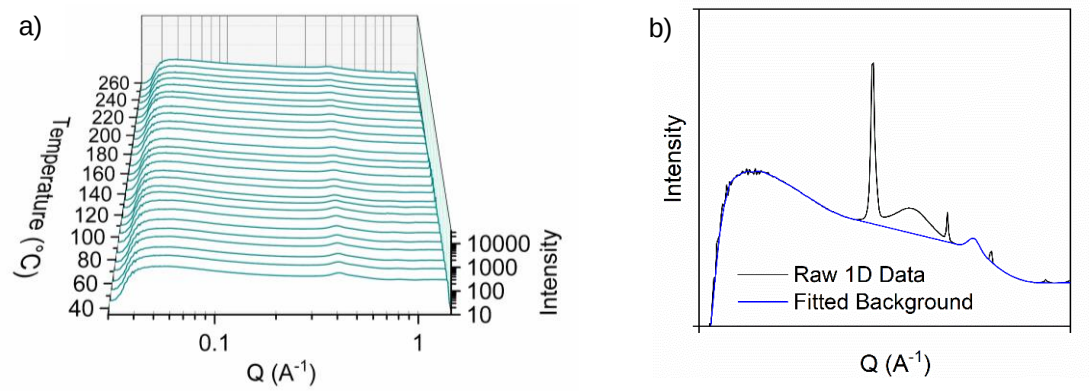

Figure 7.6. a) SAXS patterns of kapton blank measured between 40 and 260°C. Scattering intensity measured at Q range between 0.03 and 1.4 A^{-1} with X-ray energy of 15 keV and wavelength (λ) of 0.8265 Å. Radiation exposure time of 45 secs was representative of sample analysis parameters. b) Example of background subtraction procedure on the SAXS pattern of a mixed surfactant sample. The characteristic bimodal kapton signal (blue) was subtracted from all samples prior to analysis.

a

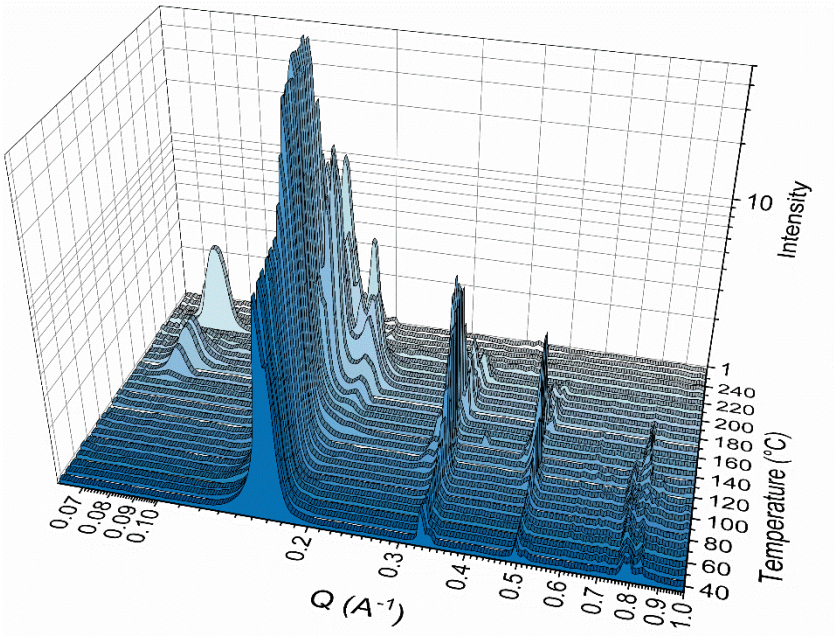

b

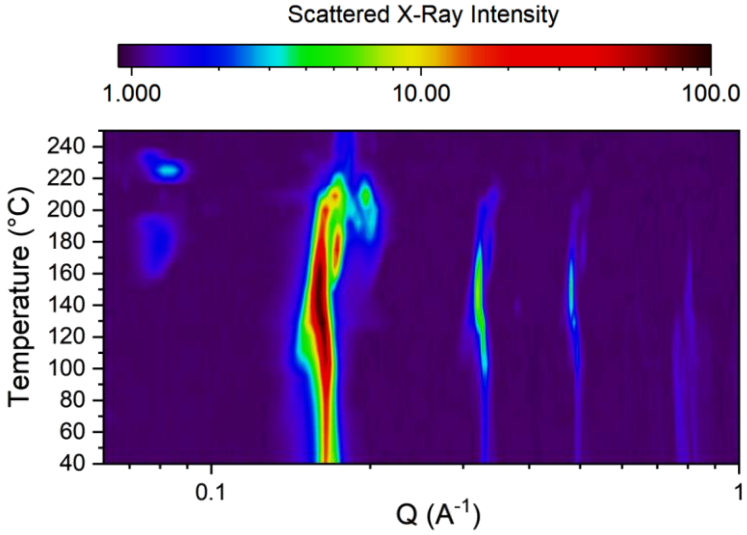

Figure 7.7: a) Temperature-resolved small angle X-ray scattering pattern of SLI (top). Sample was heated from 40°C to 260°C and exposed to 45 s of isothermal synchrotron X-ray radiation at approximately 10°C intervals. Scattering intensity measured at Q range between 0.03 and 1.4 A^{-1} with X-ray energy of 15 keV and wavelength (λ) of 0.8265 Å. b) Colormap depicting the same data on equivalent axes.

Following the data processing methodology, the temperature-dependent change in small angle X-ray scattering intensity of SLI is displayed in Figure 7.7. The plot was truncated to display data between 0.06 and 1 A^{-1} after no significant reflections were observed beyond these angles. The sustained presence of five equidistant reflections at approximately 0.16, 0.32, 0.48, 0.64 and 0.80 A^{-1} correspond to 5 orders of Bragg diffraction (h) arising from the 00*l* set of crystallographic planes. Due to the absence of existing nomenclature with respect to the structures of SLI, this phase will be termed as 'Phase A' in this study. Both the colormap and stacked plots, however, display evidence of additional co-existing phases at most temperatures. Selected SAXS plots depicting the presence of multiple phases are displayed in Figure 7.8. At lower temperatures (40°C), a shoulder peak (Phase B) is observable in all 00*l* reflections of Phase A indicating the parallel existence of two lamellar bilayer phases.

With increasing temperature, Phase A increases in structural order and overcomes the co-existing Phase B until a single set of 00*l* reflections are observed at 150°C. Beyond this temperature (175°C), an additional Phase C is detected through the appearance of a new peak at ~0.08 A^{-1}, which concurrently reduces the scattering intensity of Phase A. A more pronounced shoulder peak is also present on Phase A at 175°C. Since it cannot be confirmed if this phase differs from Phase B observed at lower temperatures due to a significant increase in structural order, it has been termed as Phase B'. Beyond 200°C, Phase B' appears to diverge into several non-distinct peaks between 0.05 and 0.5 A^{-1}. Figure 7.7b finally shows a significant drop in total scattering intensity at 225°C, which correlates with the published melting temperature of 225.3°C.[166]

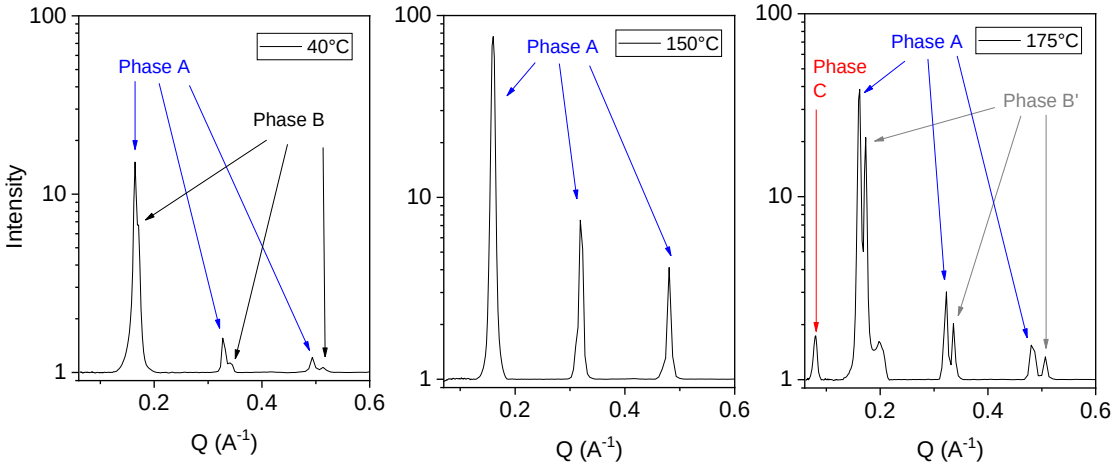

Figure 7.8: Selected SAXS plots of SLI measured at 40°C (left), 150°C (centre) and 175°C (right). Scattering intensity measured at Q range between 0.03 and 1.4 A-1 with X-ray energy of 15 keV and wavelength (λ) of 0.8265 Å.

Previous DSC and PXRD analyses of SLI have indicated a solid crystalline structure prior to melting at 225°C.[166] The thermal disorder in a system exhibiting such long-range order is resultant only from minor deviations from the three dimensional equilibrium.[268] Figure 7.8b shows how the peak width is approximately equal for all peaks corresponding to Phase A, while intensity is decreasing exponentially with diffraction order (h). These phenomena confirm thermal disorder of the 'first kind' corresponding to solid crystalline structures,[113] in which Gaussian functions are recommended for the deconvolution and characterisation of SAXS data in the characterisation of lamellar phases.[262] Figure 7.9 shows how Phases A, B and B' were identified in the multi-phasic SAXS patterns through the automated Gaussian fitting of convoluted reflections. The example shows how, even at lower diffraction orders, a bi-functional combination of Gaussian peaks (red) results in a summation (green) that closely represents the experimental SAXS pattern (blue).

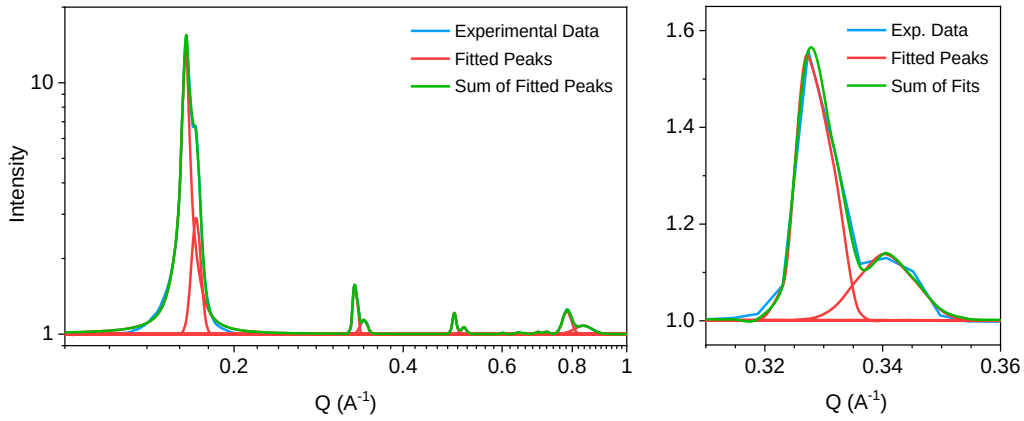

Figure 7.9. Peak fitting of Phases A and B in the temperature-dependent SAXS analyses. Example pattern depicts SLI at 40°C. Fityk was used to deconvolute incomplete and overlapping reflections using a combination of Gaussian functions.

In the absence of previous PXRD data, a crystalline lamellar structure can also be confirmed through the zero-point extrapolation of the proposed diffraction order (h) against the scattering angle (A^{-1}) at which the corresponding 00*l* reflections exhibit peak intensity. The resulting analysis is displayed in Figure 7.10. The strongly linear relationship between the two parameters, coupled with a zero intercept at all temperatures, confirms the presence of a crystalline lamellar structure corresponding to Phases A, B and B'. Due to a difference in relative intensity between Phase A and B, as well as a decaying intensity with increasing diffraction order, five orders of diffraction were consistently observed in Phase A but only three peaks were observable in Phase B/B'. This corresponds with the primary phases exhibited by other long chain organic lipidic systems, where five orders were also observed in the presence of a lamellar structure.[259, 269]. The lower scattering in Phase B/B' could be attributable to a combination of weaker structural order, as well as lower quantities when compared with Phase A. While Phase A can be characterised to greater lateral precision due to these factors, Rappolt has described how lamellar phases can be characterised with just two orders of diffraction.[270] With the deconvolution obtained through Gaussian fitting, Phase B/B' can be adequately characterised despite its poorer scattering intensity.

To assist with the characterisation of the lamellar structures corresponding to Phases A, B and B', a molecular model was created through which the equilibrium structure of SLI could be identified in the absence of a crystal structure derived from PXRD.

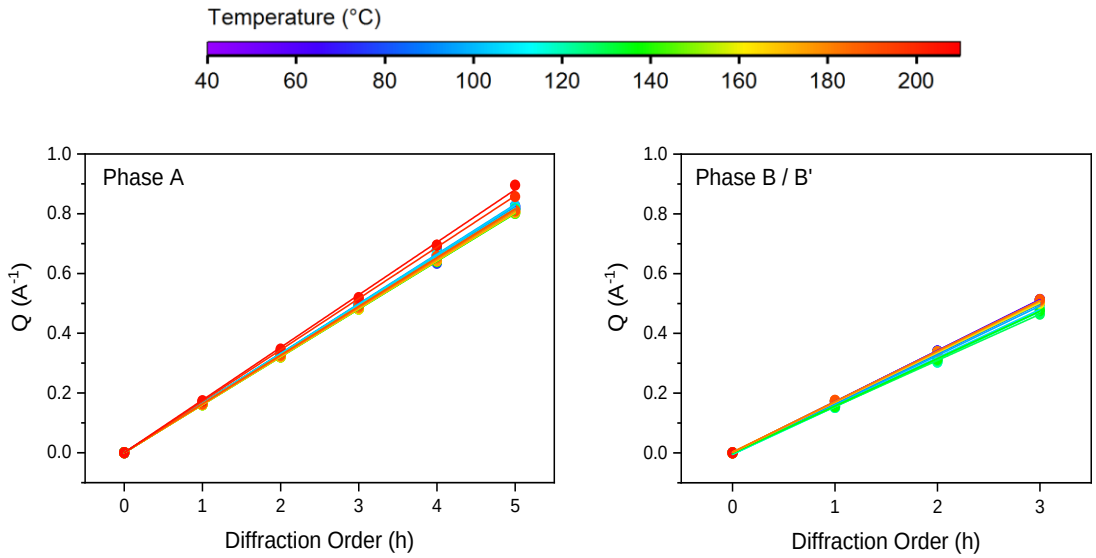

Figure 7.10: Plot of diffraction order (h) of the 00l reflections against the scattering angle (A^{-1}) of peak scattering intensity. Angle obtained from the fitted Gaussian functions corresponding to Phase A (left) and Phases B and B' (right). Zero intercept and linear relationship confirm crystalline lamellar structure in both systems. Minimum R^2 values observed for Phase A and Phase B were 0.9997 and 0.9977 respectively. Plot colours correspond to the temperature of the corresponding SAXS measurement.

7.3.2. Density Functional Theory (DFT) Analysis of SLI

A quantum mechanical simulation was executed to predict the most energetically favourable molecular orientation of a single SLI molecule in vacuum. Density functional theory (DFT) uses the Schrödinger equation to calculate the electronic structure and consequent molecular structure of a multi-atomic system. The Def2-TZVP basis set utilised in the calculation uses a combination of complex Gaussian functions to model electronic orbitals,[271] whilst the dispersion-corrected B3LYP-D3 hybrid functional [272] approximates the exchange-correlation functional that renders the Schrödinger equation otherwise insolvable. The predicted molecular geometry, electron density and atomistic electrostatic potential of SLI is displayed in Figure 7.11.

There is an expected increase in electron density around the head group with significant polarisation of charge, driven by the hetero-atomic O and Na cations. Whilst *gauche* conformations exhibit metastable structures in other dodecyl-chained sulfur-based surfactants such as SDS,[236] the energy calculations indicate that all-*trans* is the most energetically favourable and likely adopted conformation of SLI.

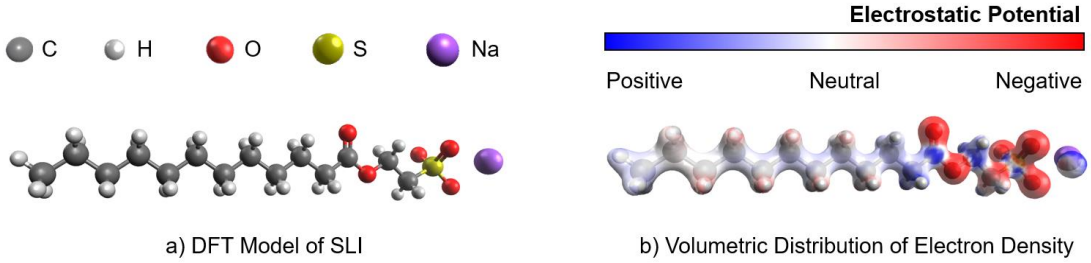

Figure 7.11: Density Functional Theory (DFT) analysis of SLI. Initial structural optimisation was executed using the COMPASS-II forcefield in Materials Studio 17. DFT-derived geometry optimisation was then conducted using the Def2-TZVP basis set and B3LYP-D3 functional using the ORCA quantum chemistry program. Surface analysis (right) displays the electron density (volume), whilst surface colourmap corresponds to electrostatic potential obtained via integrated Mullikan and Loewdin charge calculations.

Lateral measurements indicate the predicted length of the molecule in this conformation is 22.1 Å. A d-spacing measurement of the first order diffraction peak, however, indicates that the lamellar bi-layer length is 3.65 nm. Carboxylates surfactants can exist in a directly perpendicular orientation in the lamellar gel-phase form, where the length of the bilayer corresponds to twice that of a single molecule. In the crystalline form, however, both carboxylate soaps and synthetic surfactants such as SDS [236] are tilted to maximise lateral packing between alkyl chains. To determine if this is the case for SLI, an electron density profile (EDP) analysis was executed to measure the electron density along the principle lamellar axis.

7.3.3. Electron Density Profile (EDP) Analysis of Phase A

Eq. (24) shows how the EDP is dependent on the diffraction order, scattering length, scattering intensity and order-dependent phase factor. In order to determine the phase factor and simultaneously validate the experimental EDP of SLI, a model EDP was first derived from the DFT molecular model. In order to negate the electronic contribution of specific tilt angles, the model EDP was calculated assuming a perpendicular conformation, then normalised to the experimentally observed bilayer spacing of 3.65 nm. The spacing between adjacent alkyl chains was approximated from the simulated van der Waals radii of the two terminal H atoms. Due to the absence of water, no measured vacancy between polar groups was introduced.

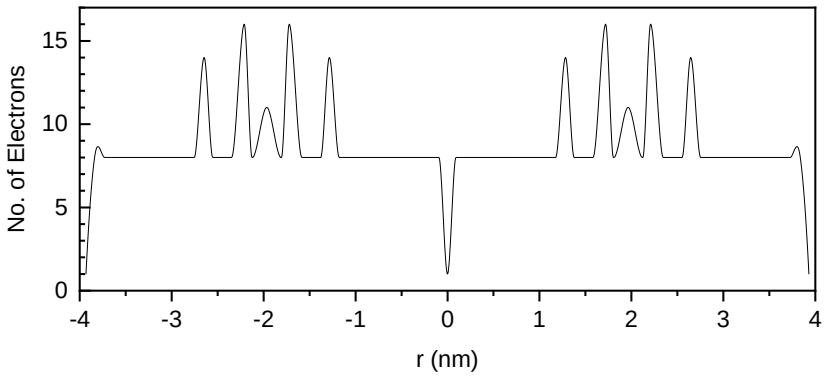

Figure 7.12. Model Electron Density Profile (EDP) for SLI, parallel to the principle molecular axis. Molecular dimensions acquired through DFT calculation of SLI obtained using the Def2-TZVP basis set and B3LYP-D3 functional.

An experimentally derived EDP was calculated for the primary Phase A of SLI at all temperatures prior to sample melting at 225°C. Whilst (2^5) 32 phase combinations were produced from the 5 orders of diffractions measured from Phase A, the total consists of two sets of 16 mathematical reflections which differ only by lattice orientation. The 16 phase combinations existing in negative space are displayed in Figure 7.13. Ladd Parada *et. al* [259], Schneider *et al.* [273] and Mykhaylyk and Hamley [269] report the -1, +1, -1, -1, -1 phase combination as most representative in their respective studies of lamellar phases of pure lipidic systems. The fourth-order peak was termed as ±1 by Ladd Parada *et. al* [259] as its amplitude was deemed too low to accurately quantify. In this study, h = 4 corresponds to the reflection at ~0.64 A^{-1} which

similarly exhibited a significantly lower scattering intensity than the order reflections exhibited by Phase A (Figure 7.7a). In Figure 7.13, Phases (1) and (3) display very similar EDPs due to this phenomenon, where the only observable differences are minor changes in intensity at r = -2, 0 and 2 nm.

Phase (8) corresponds to the – + – – – combination utilised in the aforementioned studies. Figure 7.14 shows how well this phase combination corresponds to both the one-dimensional model EDP of SLI (Figure 7.12), as well as a two-dimensional model of SLI in a tilted lamellar bilayer structure.

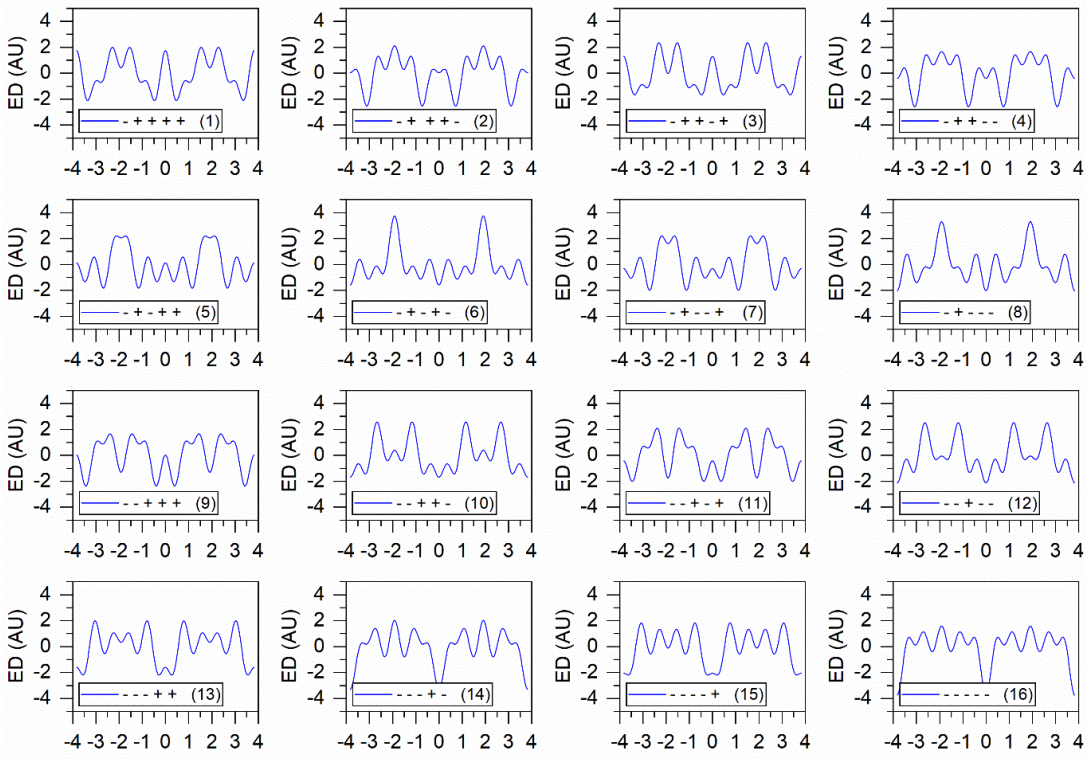

Figure 7.13: 16 negative-space phase combinations from the EDP analysis of Phase A in SLI at 40°C. EDPs calculated in accordance with Eq. (1) using the peak parameters pertaining to the Gaussian functions fitted to Phase A. Legend identifies the numbered phase combination where – – – – – pertains to -1, -1, -1, -1, -1 for diffraction orders (h) 1 to 5 respectively.

Although the experimental plot exhibits a lower lateral resolution than the model EDP, the data utilised corresponds to literature studies where five orders of diffraction were similarly utilised for the measurement of EDP.[259, 269] The most prominent electronic

features in the bilayer structure are visible in the experimental EDP, including increases pertaining to the ester, sulfonate and cationic groups, as well as the decrease around zero arising from the spacing between adjacent methyl groups. The axial distances of functional groups also correlate much better with Phases (6) and (8) than any other combination. This 'methyl trough' at 0 nm is a characteristic feature in lamellar bilayers representative of the spacing between layers. Its presence was previously utilised for the automated identification of representative phase combinations in similar systems.[274] In this study, the region was defined as the point where electron density is lowest in a lipid bilayer system. Phases (10) and (12) also exhibit a methyl trough and plausible EDP of functional groups. However, with a predicted molecular length of 22 Å, extreme tilt angles of > 60° would be required for functional groups to be observed at 10 Å. The plateau at ± 2 nm observed in Phases (10) and (12) also typically corresponds to hydration layers in bicomponent lipid-water systems.[275] Although hemi-hydration of solid SLI has been observed previously in Section 4.2.10, significant levels far beyond 10% would be required to result in the EDPs exhibited by Phases (10) and (12).

The correlation between Phase (8), the predicted EDP and the DFT derived EDP in a tilted bilayer arrangement is displayed in Figure 7.14. The largest deviation in the experimental EDP from the model derived via DFT is the absence of a flat region corresponding to the alkyl chain in the former system. Data from a previous study within the group, on the influence of the number of available diffraction peaks on the resulting EDP, is displayed in Figure 7.15. The diagram shows how Fourier inconsistencies manifested through a fewer number of diffraction peaks resulted in distortions in EDP at the alkyl chain region. In the presence of higher diffraction peaks, lateral detail emerges resulting in fewer fluctuations and a more accurate spatial representation.

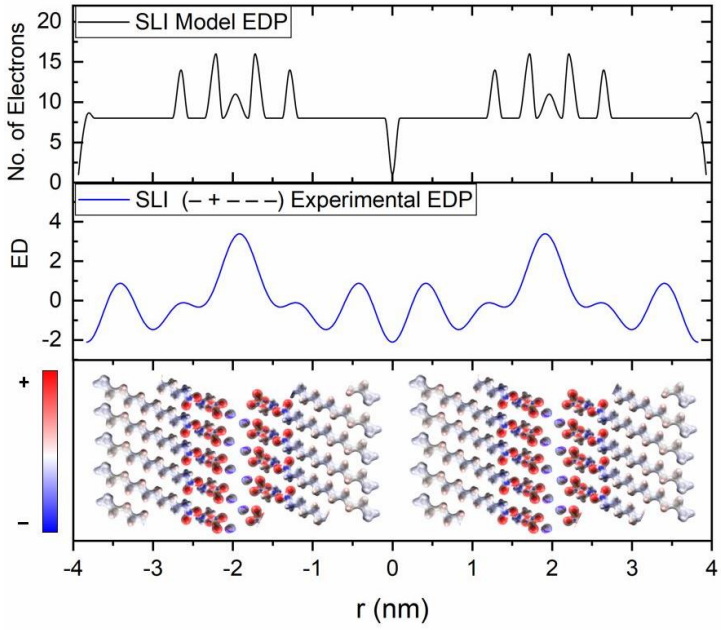

Figure 7.14: Plot of the model EDP for SLI (top), experimental EDP at 40°C derived from Phase Combination (8) (middle) and a DFT model of a tilted lamellar bilayer structure (bottom). Colourmap corresponds to the electrostatic potential ranging from negative (blue) to positive (red).

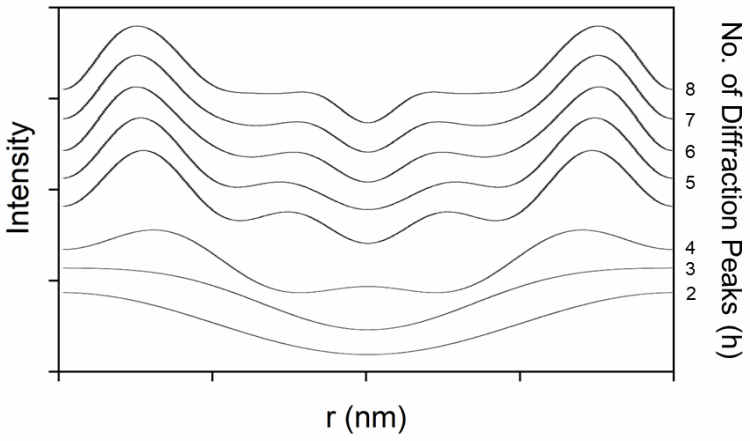

Figure 7.15. Schematic depicting the influence of an increasing number of diffraction peaks on the resulting EDP for organic DOPC lamellar bilayers. Data corresponds to a study on the lamellar bilayer structuring of long chain ethanolamine molecules.[276] Plot edited and adapted from Rappolt et al.[270]

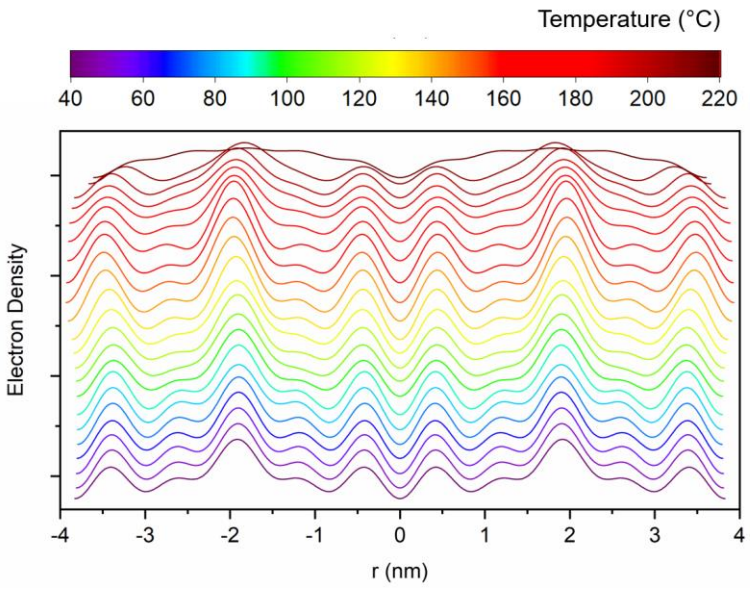

Figure 7.16. Temperature-resolved electron density profiles (EDPs) of the lamellar bilayer of Phase A in SLI. Derived from the Gaussian functions of the 00l small angle X-ray scattering reflections in a $-+---$ *phase combination.*

Figure 7.16 depicts how the experimental EDP of SLI changes as a function of temperature. As the material was heated from 40°C to 160°C, an increasing intensity in electron density was indicative of increasing structural order of the primary lamellar phase. The subsequent decrease in intensity at higher temperature was possibly resultant from the presence of additional species in the system (Phase C) which disrupted the structural order within Phase A. Through comparison with the experimental EDP and the measured lamellar bilayer spacing, a measurement of the lamellar tilt angle was obtained to characterise the temperature-dependent change structural order.

7.3.4. Lamellar Tilt Angle Measurement Angle of Phase A

The lamellar tilt angle was estimated through trigonometric treatment of lamellar spacing data using the length of a single molecule (Eq. (25)). In order to obtain an *ab-initio* estimation of molecular length in the crystalline phase without reference to PXRD data, a van der Waals surface was fitted to the DFT-derived structure of SLI. The corresponding image depicted in Figure 7.17 indicates that the molecular length representative of packing within the crystalline phase was 27.2 Å. When combined with the temperature-dependent change in lamellar bilayer spacing and EDP data, this

DFT measurement was used to calculate the change in lamellar tilt angle as a function of temperature. The corresponding data is displayed in Figure 7.18.

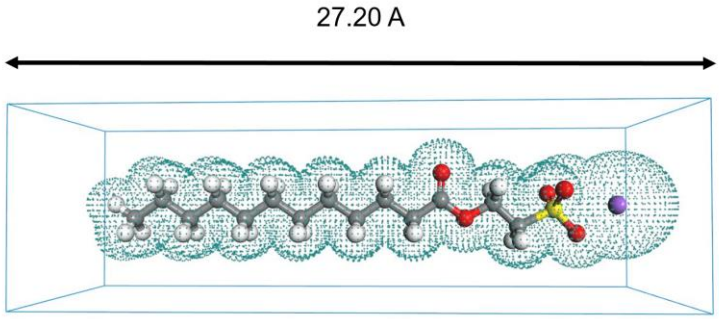

Figure 7.17: van der Waals radius of SLI calculated from its DFT-based geometry optimization using the Def2-TZVP basis set and B3LYP-D3 functional. Volumetric surface obtained via the volumetric tool in Materials Studio 17.0 using an ultra-fine grid resolution and vdW scale factor of 1.0.

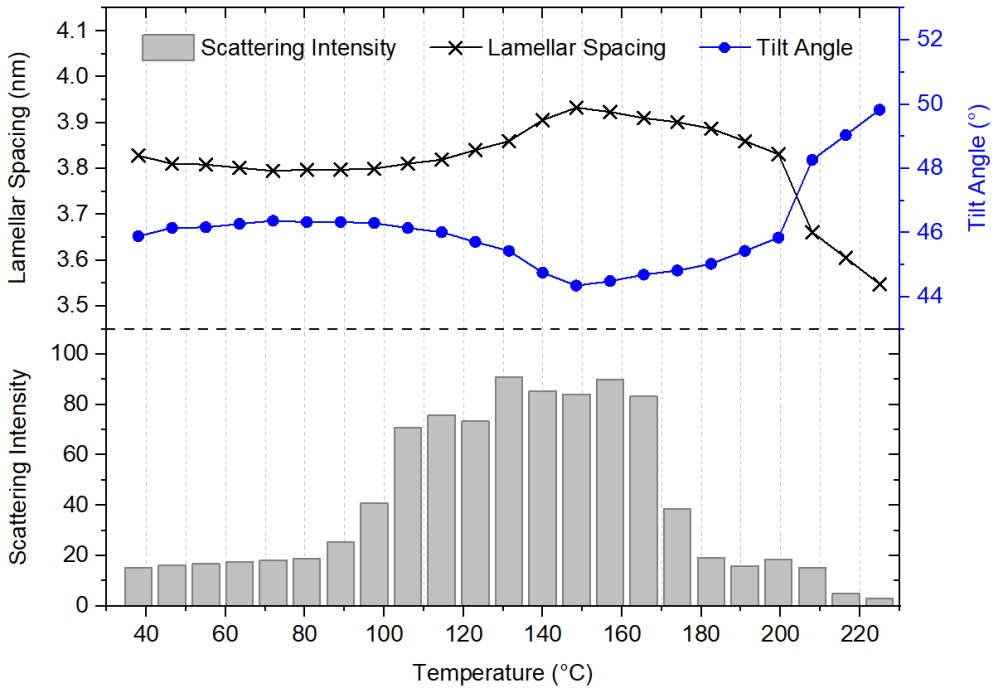

Figure 7.18: Lamellar spacing (nm) and bilayer tilt angle (°) of Phase A in SLI, as a function of temperature. Measurements obtained from the scattering angle of the fitted Gaussian function corresponding the 001 SAXS reflection at temperatures between 40 and 225°C. Column chart displays the change in peak scattering intensity over the same SAXS experiments between 40 and 225°C.

The tilt angle at 40°C correlates moderately well with the 48° measured with the atomistic crystal structure of SLI measured via PXRD. A study by Tristam-Naegle *et al.* into the measurement of lamellar tilt angles via SAXS discusses how uncertainty in the precise dimensions of the lipid molecules can lead to errors of up to 5° in the corresponding tilt angle, particularly concerning the measurement of hydrated lipid layers.[277] Although vdW forces were used to represent molecular spacing in the crystalline phase, the presence of highly charged functional groups such as the ionic Na-sulfonate interaction in SLI, may require an additional coulombic interaction to further reduce the 2° deviation measured in this experiment. In the PXRD study of SLI, the sample also exhibited some line broadening indicative of imperfect crystallinity in the solid-state. This disorder in the chain packing could have also contributed to the 1-2° difference in tilt angle between the two measurements. Nevertheless, the correlation indicates that a combination of SAXS and DFT could be useful for obtaining a representation of structural order within less ordered systems, particularly when atomistic structural data is unavailable.

There was a decrease in lamellar tilt angle with an increase in temperature between 40°C and 150°C. Whilst thermal expansion could lead to the observed increase in lattice dimensions, the reduction in tilt angle with temperature also coincides with an increase in scattering intensity. This distinct change in structure indicates an increase in order through crystalline annealing. The EDP data in Figure 7.16 shows greater fluctuation across the lamellar bilayer as temperature is increased to further support this. Figure 7.7 and Figure 7.8 also show how the sample at 40°C appears to be a mixture of Phases A and B with a respective composition of 81% and 19% respectively based on the peak area of the corresponding first-order reflections. The aforementioned increase in structural order therefore occurs as the composition of Phase B decreases from 19% at 40°C, to undetectable levels at 150°C. The highest peak scattering intensity is observed at this temperature indicating that this is the state of highest structural order within the experimental range, which suggests that the annealing process corresponds specifically to the increased prevalence and structural order of Phase A.

This annealing of a metastable phase to form a more stable structure corresponds with the phase behaviour exhibited by sodium carboxylates. Ferguson *et al.* reported the presence of metastable phase in the melt crystallisation of sodium carboxylates.[229]

This was further confirmed by Buerger *et al.* who specifically reported its presence in sodium laurate.[26] Ferguson stated that the metastable phase formed under upon melt crystallisation but transitioned into a more orthodox phase once the material had been handled during the commercial manufacturing processes. In a much later publication, Hill *et al.* suggest that the mechanical action through downstream processing may have introduced energy into the system to promote the transition to the more stable phase.[252] The SLI in this study was similarly acquired through rapid cooling of the liquid melt and the increase in temperature from the X-ray analysis may be introduced a stabilising effect similar to that described for the manufacture of carboxylate soaps. Ferguson also reported a 0.1 nm increase in *d* spacing between the two carboxylate phases. Whilst no further lattice dimensions were provided, this correlates well with the observed increase in spacing measured in the current study.

At much higher temperatures of between 150°C and 200°C, Phase A exhibits a gradual decrease in both lamellar spacing and scattering intensity. In this instance, this disorder in Phase A coincides with the appearance and increasing prevalence of the uncharacterised Phase C and return of a co-existing lamellar Phase B'. Beyond 200°C, there is a more notable increase in tilt angle. However, because this is coupled with a significant decrease in scattering intensity, the increase is likely representative of a reduction of crystalline ordering in the system rather chain specific chain tilting. Previous DSC analyses of SLI report a solid-solid phase transition commencing at ~200°C. Retention of the lamellar structure through the 001 reflection, together with a substantial reduction in subsequent diffraction suggests that this could be a rotator phase (similar to the lamellar phase in Figure 7.1) where long-range positional order of alkyl chains is lost but the three-dimensional positions of molecules within the crystalline lattice are preserved.

7.3.5. Characterisation of Phase B via Molecular Mechanics

The DVS analysis of SLI (Section 4.3.5) indicated that at humidity levels beyond 50%, the molecule is prone to hydration and a hemi-hydrated structure is plausible based on the measured changes in mass. The previous chapter also highlighted how an increase in headgroup size accompanying hydration in dodecyl chained surfactants, resulted in an increase in lamellar tilt angle and concurrent reduction in bilayer spacing (Table 6.5). Phase B, co-existing with Phase A at temperatures below 150°C, exhibits a

reduced lamellar spacing of 3.67 nm compared with the 3.82 nm corresponding to Phase A. Humidity levels at the time of measurement varied between 77% and 93% which are far beyond the levels at which molecular hydration is expected to occur. To assess the plausibility of Phase B as a hemihydrate of anhydrous SLI, a water molecule was introduced into the crystal structure of SLI and an energetic optimisation was executed. The resulting structure is displayed in Figure 7.19.

The long crystallographic axis was fixed at 3.67 nm to reflect the measured spacing of the proposed Phase B. However, no further restrictions were imposed on lattice parameters, unit cell type, symmetry or atomic positions. Despite a significant number of degrees of freedom, the optimisation retained the lamellar bilayer structure characteristic of anhydrous SLI and other long-chained organic surfactants. Figure 7.19 b shows the hemi-hydrated structure is predicted to display a hexagonal packing arrangement between adjacent lamellar bilayers. Figure 7.19 a and c further demonstrate how the water molecule stabilises bilayer stacks by bridging between head groups of alternate molecule in adjacent layers. While the *c* axis length is relatively unchanged with hydration, the *b* axes decreased from 9.7 Å in the anhydrous structure to 7.1 Å in the hemi-hydrate. This suggests the hydrogen bonding between adjacent lamellar bilayers pulls them closer together, thereby reducing the inter-lamellar spacing when compared with the anhydrous structure. Like SDS, the hemi-hydrated structure of SLI retained its monoclinic cell type with hydration. The β angle, however, was predicted to decrease from 95° to 85° to accommodate the increase in lamellar tilt angle.

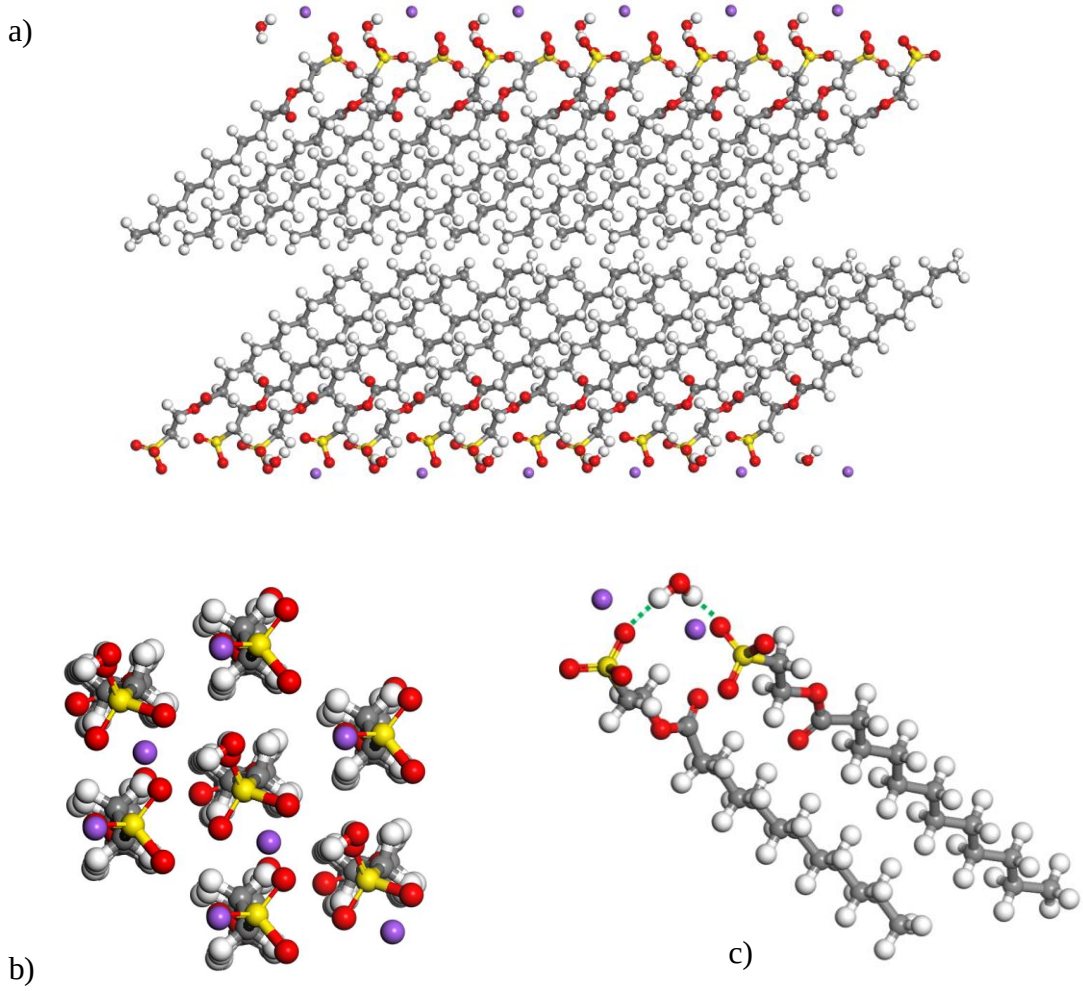

Figure 7.19: Predicted structure of the hemi-hydrated SLI.1/2H_2O generated by introducing water into the crystal structure of SLI. Figure displays a) structure of a single lamellar bilayer, b) packing of adjacent lamellar layers and c) molecular interaction between molecules in adjacent layers.

The anhydrous structure was predicted to exhibit an all-trans arrangement, where all molecules exhibit bond torsions of ~180°, analogous to that of a single molecule in vacuum. One of the molecules in the hydrated structure, however, exhibited a gauche conformation at the C12-O1-C13-C14 position, where the corresponding torsion angle is 139.4°. A conformational energy analysis of SLI was executed in the previous chapter. Figure 6.7 shows that while the energy minima for the 4-bond torsion in question exist at ~85°, 180° and 275°, the energy penalty resulting from the 139° torsion angle is < 2 kcal/mol using the COMPASS-II forcefield. Figure 7.19c further shows that in the hemihydrated structure, the gauche conformation has rotated the

sulfonate group to permit hydrogen bonding with the water molecule. This alternating *trans*/*gauche* conformation in adjacent molecules to maximise hydrogen bonding is also observed in the hydrated form of SDS.[150]

Despite the change in conformation, the total energy of the hydrated system is likely to be lower than that of the anhydrous structure as a result of these additional stabilising interactions. The lattice energy of anhydrous SLI was calculated to be -51.24 kcal/mol in the previous chapter. Through comparison of the total energy of the hemi-hydrated SLI fragments in vacuum, with the total energy of the hemi-hydrated structure in the crystalline phase, the lattice energy of SLI.1/2H_2O was similarly calculated to be -72.41 kcal/mol. The predicted hydrate structure displays analogous coulombic interactions between the Na^+ cations and SO_3^- anions present in the anhydrous form. However, the additional hydrogen bonding introduced by water molecules between adjacent surfactant layers, has further decreased the lattice energy. The synthon analysis of SLI also highlighted the van der Waals interactions between hydrocarbon chains, as a stabilising component in the crystalline lattice. The decreased spacing between lamellar layers in the hydrated state could have resulted in stronger attractive forces between adjacent layers, thus further reducing the lattice energy to the observed levels. This combination of favourable thermodynamics over the anhydrous structure, explain how the presence of water could lead to the predicted changes in the crystal structure of SLI. Table 7.2 (an extension of Table 6.5) displays the published trends between head group volume and lamellar tilt angle in various dodecyl chained sulfur-based anionic surfactants. In this regard, the structure proposed for SLI.1/2H_2O correlates with both the anhydrous structure of SLI and previously published trends in the structure of SDS, in its varying hydrated states.

Table 7.2. Influence of headgroup size on lamellar tilt angle of various dodecyl chained sulfur-based anionic surfactants. Headgroup volumes correspond to the van der Waals volume of the head group in the crystalline phase, as calculated from their respective CIF files.

Surfactant System	Head Group Vol. (Å^3)	Lamellar Tilt Angle (°)
SDS*[236]	93.6	15
SDS.1/8H_2O[238]	96.6	10
SDS.1/2H_2O[150]	105.0	40
SDS.H_2O[149]	126.2	45
SLI*	156.3	48
SLI.1/2H_2O ‡	166.5	50

* = Structure obtained via powder X-ray diffraction. ‡ = Structure generated via molecular mechanics calculation.

7.4. Conclusion

The temperature-dependent change in structure of sodium lauroyl isethionate (SLI) was measured via small angle X-ray scattering (SAXS). Characteristic 00*l* reflections confirmed the presence of multiple co-existing lamellar structures in the solid phase. Following the establishment of Type 1 thermal disorder, Gaussian functions were fitted to 00*l* peaks to determine the electron density profile (EDP) across the lamellar bilayer. An *apriori* model of expected EDP derived via DFT, indicated that the – + – – – phase combination was most representative of SLI, correlating with previous analyses of long chain hydrocarbons existing in the lamellar phase. When coupled with the molecular dimensions generated via DFT, the SAXS data indicated the primary phase existing at room temperature (Phase A) annealed with increasing temperatures of up to 150°C. A decrease in lamellar tilt angle, coupled with an increased lamellar spacing was observed. This potentially corresponds with the manufacture of sodium laurate, where a metastable phase was first observed upon melt crystallisation before more stable phases were formed, with a similar increase in lamellar spacing to that observed in this study.

The appearance of additional phases beyond this temperature are proposed to reduce the structural order in the system, due to the consequential reduction in scattering intensity and tilt angle. When compared with the phase behaviour of sodium carboxylates, SLI therefore exhibits evidence of both the 'crystal' tilted lamellar phase at lower temperatures and a perpendicular 'lamellar' phase of lower tilt angle at high temperatures. Further study incorporating higher angle diffraction may determine whether Phase C corresponds to the 'ribbon' phase exhibited by analogous systems at intermediary temperatures. Given the correlation between structure and properties identified in analogous long chain lipid systems, it is hoped that future physical characterisation of the identified phases could help develop a fundamental understanding of the influence of process conditions on the performance of isethionate ester surfactants.

The secondary phase co-existing at lower temperatures was proposed to be the hemi-hydrated form of SLI following correlation with previous DVS data. In a manner similar to the hydration of SDS, the hemi-hydrated structure retains its monoclinic lattice type, whilst exhibiting a reduced spacing in the principle axis. Hydrogen bonding between water molecules and alternate surfactants in adjacent lamellar layers were found to contract the spacing between layers, whilst simultaneously introducing a gauche conformation in alternate molecules to optimise hydrogen bonding. When compared with the existing structural trends correlating head group volume with lamellar tilt angle, both the anhydrous and predicted hemihydrate structure of SLI conform to the previous structures of dodecyl chained sulfur-based anionic surfactants, in varying states of hydration.

Existing high resolution powder diffraction from the previous chapter was utilised for the atomistic postulation of a hemi-hydrated structure of Phase B. The novel combination of DFT and SAXS utilised for the characterisation of Phase A, however, demonstrates how a molecular scale structural analysis of solid lamellar phases can be achieved in the absence of high-quality wide-angle diffraction data beyond $Q = 1\ A^{-1}$. In this study, the electron density profiles (EDP) generated via SAXS and DFT yielded structures of a tilt angle similar to that measured via PXRD in the previous chapter. The observed internal correlation between the SAXS-derived and DFT-derived EDPs could increase confidence in the proposed combined approach had this data not been available. In commercial surfactants, the presence of impurities, unreacted reagents

and varying chain lengths typically render the challenging atomistic instrumental analyses presented in the previous chapter almost impossible to achieve due to the resulting loss in critical high angle diffraction data. The techniques presented in this study are therefore extremely valuable for improving the identification and characterisation of phases in complex, multi-component surfactant systems.

Chapter 8: Conclusion

Synopsis: *This chapter draws together the outcomes of the preceding chapters for a holistic assessment of their contributions to the aims and objectives of the project. The section is concluded with suggestions on how the research could progress in the future to maximise impact on the optimisation of isethionate ester surfactant manufacture.*

8.1. Conclusion

An absence of fundamental research into the chemistry, structure and properties of isethionate ester surfactants has resulted in notable shortcomings in the manufacture of modern personal care products. The structures of traditional sodium carboxylate soaps were extensively studied throughout the 20th century. The resulting research on their complex phase behaviour and consequential influence of process conditions was used to create structure-property models to optimise manufacturing processes for the production of personal care products with desirable performance characteristics.

Olsen's three link chain rule was identified as a means of developing a similar level of knowledge with respect to the isethionate ester manufacturing process. Through a detailed characterisation of molecular structure under both ambient and dynamic process conditions, this research aimed to develop the foundations upon which a holistic understanding of the system could be achieved.

Due to the compositional complexity of industrial isethionate surfactants, a chromatographic analysis was first conducted on a commercial blend of isethionate reagents to identify a species upon which a model surfactant system could be developed. The resulting chain length analysis indicated that the dodecyl chain length was the most abundant constituent. The isethionate derivate, sodium lauroyl isethionate (SLI) was therefore selected as a model detergent for the study.

As a result of the limited commercial availability of pure isethionate derivatives, a review of the patent literature pertaining to isethionate esters was conducted to assist in the development of a synthesis procedure. Key aspects of the commercial manufacturing process were identified and integrated into a laboratory scale reactor. SLI was subsequently synthesised at the laboratory scale without the use of ancillary solvent, chlorinated species or catalysts. The reaction time of 4-6 hrs, reaction temperature of ~240°C and obtained purity levels of 83% were in line with previous synthesis processes. Three consecutive recrystallisations of SLI in methanol resulted in purity levels of 98%.

A subsequent polythermal solubility analysis of SLI in methanol generated temperatures and concentrations through which the material could be purified via cooling crystallisation. Whilst these parameters could be scaled-up for commercial

purification of isethionate esters, the data provided a means through which a reproducible surfactant could be obtained for further structural analysis.

A physicochemical analysis of SLI confirmed degradation onset temperatures of 300°C under dynamic heating. A more comprehensive kinetic analysis of the thermal degradation process confirmed mass loss to be 28 times higher in air than N_2. In addition to recommendations for stringently inert process conditions, the validated predictive models from this analysis suggest that reaction temperatures could be increased to 250°C for an increased reaction rate, before significant increases in degradation would be observed. Given that changes in performance-critical characteristics such as activity levels, colour, and odour have been linked with isethionate degradation, the limits to which the product is chemically stable under varying temperatures can be valuable data for the optimisation of isethionate ester surfactants manufacturing processes.

The ensuing study of evolved gases revealed production of carbon dioxide, carbon disulfide, sulfur dioxide, water vapour and organic fragments at elevated temperatures. The temperature-dependent data had the benefit of providing information on the potential hazards associated with thermal degradation, whilst simultaneously providing chemical insight of the degradation process that could be used for performance modelling. The correlation between observed and predicted levels of thermal degradation provided reliable models through which the reproducible temperature-dependent structure of isethionate esters could be measured without risking unexpected changes in chemical composition.

Due to the lack of structural data on solid isethionate ester surfactants, a detailed characterisation of pure SLI under ambient conditions was conducted before a temperature-dependent analysis of SLI. While single crystal X-ray diffraction is the most common technique for acquiring atomistic crystal structures, a microscopic analysis of the crystals following purification of SLI revealed a plate-like morphology, where a restricted z-axis encumbered the acquisition of single crystal data of suitable quality. Following a literature review on crystal structures of sodium carboxylate soaps and other dodedyl-chained sulfur-based surfactants, the crystal structure of SLI was determined through combined powder X-ray diffraction and molecular simulation. The crystal lattice was found to exhibit a monoclinic unit cell with P 21/c space group, similar to the anhydrous structure of sodium dodecyl sulfate (SDS).

A molecular-mechanics based global optimisation of potential structures yielded a *trans-trans* tilted lamellar bilayer conformation. This structure was found to exhibit good agreement with the experimental X-ray diffraction data, the known structure of SDS, as well as the crystal structures exhibited by pure sodium carboxylate soaps under ambient conditions. SLI was found to reflect general structural trends of increasing lamellar tilt angle with increasing headgroup size, as exhibited by other sulfur-based dodecyl-chained surfactants. In addition to increasing the credibility of these trends, the correlation raises confidence in the observed atomistic crystal structure.

A detailed characterisation of the intermolecular interactions constituting the structure of SLI provided insight into the thermodynamics governing the stability of the tilted lamellar bilayer conformation ubiquitous to anionic surfactants. Crystalline stability was found to be dominated by coulombic interactions between anionic sulfonate groups and Na cations. A non-coulombic component of 35%, however, indicated that the observed atomic interdigitation between alkyl chains was also attributable for the observed solid-state stability. The specific combination of molecular mechanics and PXRD used for the crystal structure analysis of SLI is novel in the study of anionic surfactants. Due to the pervasiveness of plate-like morphologies in such surfactant systems, the methodologies described here for the solution of crystal structures also provide an invaluable workflow for the study of other surfactant systems when single crystal analysis are precluded due to particle morphology.

The atomistic crystal structure analysis provided a wealth of physical data on highly ordered crystalline phases. In commercial surfactants systems, however, lower purity levels, mixtures of carbon chain lengths and non-ideal crystallisation conditions lead to materials of lower structural order. A review of traditional soaps confirmed decreasing structural order with temperature, where poor levels of X-ray diffraction were likely to obfuscate the data required for such analyses. The temperature-dependent structural analysis of SLI employed a combination of small angle X-ray scattering and molecular modelling techniques to permit an *in-situ* analysis of the material during typical manufacturing conditions. As with sodium carboxylate soaps, pure SLI was found to exhibit a rich, combination of phases when exposed to varying temperatures. A representation of the primary crystalline phase under ambient conditions could be observed and characterised using an electron density profile (EDP) produced from a combination of SAXS and DFT. Between 40 and 150°C, an

increase in scattering intensity and structural order was observed, where the measured increase in lamellar spacing (0.1 nm) correlated with the structural change associated with the annealing of sodium laurate. Above 150°C, the appearance of additional phases decreased the scattering intensity in the primary phase until isotropic melting was observed at >220°C, as confirmed by DSC. When compared with the thermotropic phases of traditional soaps published by Luzatti *et al.*, clear evidence of the low-temperature crystalline phases and high-temperature lamellar phases was found. A powder diffraction analysis of the uncharacterised phase would confirm whether the ribbon structure is also present between the two phases.

The physicochemical analysis of SLI indicated the possibility of hemi-hydration in the crystal structure of SLI. Evidence of this phase was observed at temperatures below 150°C, and using a combination of SAXS and molecular mechanics the crystal structure constrained to the measured lattice spacing was determined. The resulting tilted bilayer structure conformed to the structural trends of observed in Chapter 6. The molecular conformation resulting from favourable hydrogen bonding interactions provided a thermodynamic explanation for the increases in tilt angle with hydration of general sulfur-based anionic surfactants. In general, the phase behaviour of SLI displayed strong correlation with the thermotropic phase behaviour of traditional soaps with atomistic structures corresponding to those previously determined for dodecyl-chain, sulfur-based anionic surfactants. This confirms that the wealth of structural-performance data pertaining for the optimisation traditional soaps are highly relevant for the design of future manufacturing processes pertaining to isethionate ester synthesis.

The structural characterisation of amphiphilic molecules exhibiting a rich, thermotropic phase behaviour can be challenging due to significant changes in structural order exhibited with temperature. The synergistic combinations of laboratory diffraction techniques, synchrotron radiation, molecular mechanics and quantum mechanical methods demonstrated, provide a template through which future structural characterisation of surfactant systems could be conducted, irrespective of the structural order. Prior to further study, the data pertaining to the physical properties of SLI, synthesis in the absence of catalysts, kinetic models of thermal stability, degradation chemistry, purification via crystallisation, and performance in aqueous environments can also be utilised to optimise and improve the current isethionate manufacturing processes.

8.2. Further Work

Beginning with the uncharacterised phase observed in the temperature-dependent analysis of SLI, a combined SAXS-WAXS study would help confirm whether this uncharacterised phase corresponds to the ribbon phase exhibited by sodium carboxylate system. Scattering at wider angles will help determine if the packing of alkyl chains is consistent with the expected spacings between ribbon chains, while the sub-structures developed from independent regions of ribbon structuring can be measured via SAXS.[143, 273] Given that Phase C was not be observed in isolation in this study, computational modelling will be needed in conjunction with experimental techniques to deconvolute the scattering with respect to the desired phase.

The complex array of hydrates exhibited by SDS,[149, 150, 238] coupled with the hemi-hydration suspected in SLI, indicates that further effort should be dedicated to studying the hydration of SLI and the resulting impact on its physical properties. Follow-up research should consider varying matrices of temperatures and humidity levels to ascertain whether additional phases are observable within a wider experimental space. One possibility would be to crystallise the material in solvent environments of varying aqueous content to determine the feasibility of high levels of hydration.

The introduction of water may lead to a multi-component study on the influence of process parameters on structure in isethionate ester surfactants. While a benefit of performance-focused process design is that process conditions can be used to develop desirable performance characteristics from fewer constituent materials, additional components are often required to meet manufacturing and market demands. In the formulation of SLI-based solid formulations, residual fatty acid from the surfactant synthesis is the second most abundant ingredient.[10] It has the functional benefit of improving hardness and lathering ability, whilst simultaneously reducing material cost.[33] In the case of sodium palmitate soap, the presence of palmitic acid content on the structure exhibited by the binary system has been studied. In addition to the expected mixtures of various polymorphic phases, there are compositions in which the fatty acid molecule acid is incorporated into the crystalline lattice at the molecular level. A detailed characterisation of SLI and lauric acid, using both XRD and DSC, would be useful to determine whether similar structures can be formed in the binary acid-soap system of isethionate ester surfactants.

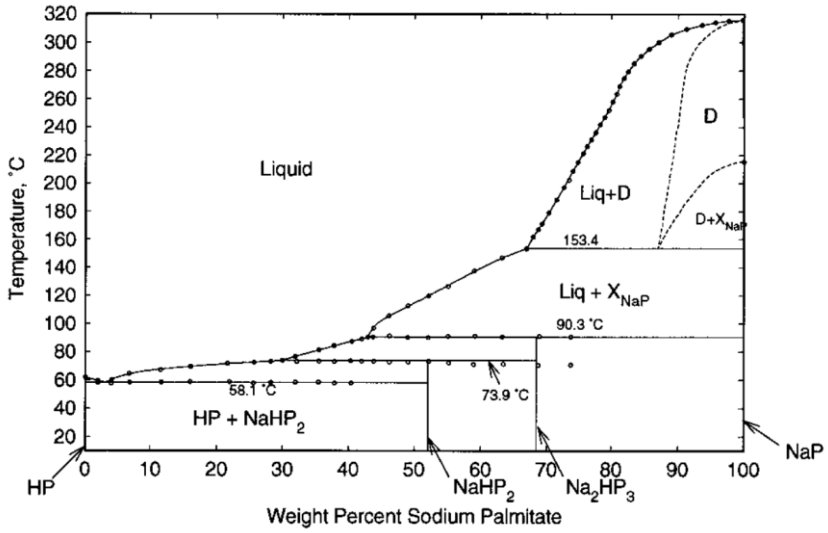

Figure 8.1. Binary phase diagram displaying the complex phase behaviour of palmitate acid (HP) and sodium palmitate (NaP) [sodium hexadecanoate]. NaH_xP_2 correspond to acid-soap structures where palmitic acid has incorporated itself into the crystalline lattice of sodium palmitate in varying stoichiometries. D = anistropic liquid soap. X = crystalline sodium palmitate.

If structure-performance models for isethionate ester surfactants are indeed desired, then the final step of the process would be to isolate observed phase combinations and measure the physical properties underpinning desirable performance characteristics. Since traditional testing methods for solid soap formulations consist predominantly of subjective consumer-based testing methodologies,[27] the key performance criteria of such products could be improved via quantification through more reproducible scientific methods. Beyond visual assessment, the physical appearance and 'whiteness' of formulations could be measured via colorimetric techniques.[278] Intrinsic properties such as the hardness of the finished product could be measured via atomic force microscopy or indentation techniques.[279] 'Washdowns', which typically consist on consumer testing, could then be supplanted by tribological studies involved varying degrees of aqueous content to quantitively characterise bar feel and wet usage.[280] The dynamic structure of such systems, with respect to varying aqueous content is an established field which utilises a range of methods including small angle X-ray scattering, calorimetry, light scattering and optical microscopy.[281] Through a combination of data derived from solid and aqueous studies, a holistic representation of structure and performance of solid soap formulations could be achieved.

Bibliography

1. J. W. McCutcheon, 'Soap by saponification', *Journal of the American Oil Chemists' Society*, 1952, **29**, 500-505.
2. J. Davidsohn, *Soap Manufacture*, Interscience Publishers, 1953.
3. J. McBain and W. Sierichs, 'The solubility of sodium and potassium soaps and the phase diagrams of aqueous potassium soaps', *Journal of the American Oil Chemists' Society*, 1948, **25**, 221-225.
4. N. Hall, 'Implications of Soap Structure for Formulation and User Properties' in Soap Manufacturing Technology, L. Spitz, AOCS, 2010, 83-114.
5. P. Khuwijitjaru, S. Adachi and R. Matsuno, 'Solubility of Saturated Fatty Acids in Water at Elevated Temperatures', *Bioscience, Biotechnology, and Biochemistry*, 2002, **66**, 1723-1726.
6. F. D. Snell, 'Soap and Syndets', *Industrial & Engineering Chemistry*, 1957, **49**, 50A-52A.
7. L. Spitz, *Soap Manufacturing Technology*, AOCS Press, 2010.
8. B. E. Davies, 'The UK geochemical environment and cardiovascular diseases: magnesium in food and water', *Environmental Geochemistry and Health*, 2015, **37**, 411-427.
9. P. J. Petter, 'Fatty acid sulphoalkyl amides and esters as cosmetic surfactants', *International Journal of Cosmetic Science*, 1984, **6**, 249-260.
10. M. I. Hill and A. J. Post, 'Design of the Dove® Beauty Bar' in Computer Aided Chemical Engineering, K. M. Ng, R. Gani and K. Dam-Johansen, Elsevier, 2007, 275-287.
11. J. Rosenburg, *Soap, Bath and Shower Products - US (Market Intelligence Report)*, Mintel, 2014.
12. United States Patent, 1,932,180, 'Sulphuric acid derivatives of amides', *Ig Farbenindustrie Ag*, 1933.
13. United States Patent, 3,029,264, 'Preparation of a mixture of fattyacyl-oxyalkane sulphonates', *Lever Brothers Company*, 1962.
14. L. G. Wade, *Organic Chemistry*, Pearson Prentice Hall, 2006.
15. Clariant, *SCI - GPS Product Safety Summary*, Clariant.
16. United States Patent, 3,420,857, 'Process for the continuous production of fatty acid esters of hydroxy sulfonates', *Lever Brothers Company*, 1969.
17. United States Patent, 3,333,385, 'Preparation of surface-active agents using a dissolved zirconium catalyst', *Lever Brothers Company*, 1968.
18. United States Patent, 3,429,136, 'Process for preparing hydroxy sulfonate esters', *Lever Brothers Company*, 1968.
19. A. Skoulios and V. Luzzati, 'Structure of Anhydrous Sodium Soaps at High Temperatures', *Nature*, 1959, **183**, 1310-1312.
20. O. E. A. Bolduan, J. W. McBain and S. Ross, 'Diffraction of X-rays by Sodium Laurate and Sodium Palmitate at Higher Temperatures', *The Journal of Physical Chemistry*, 1943, **47**, 528-535.

21. J. W. McBain and M. C. Field, 'Phase Rule Equilibria of Acid Soaps. I. Anhydrous Acid Potassium Laurate', *The Journal of Physical Chemistry*, 1932, **37**, 675-684.

22. J. W. McBain and M. C. Field, 'Phase Rule Equilibria of Acid Soaps. IV. The Three-Component System Potassium Laurate—Lauric Acid—Water1', *Journal of the American Chemical Society*, 1933, **55**, 4776-4793.

23. R. Klein, D. Touraud and W. Kunz, 'Choline carboxylate surfactants: biocompatible and highly soluble in water', *Green Chemistry*, 2008, **10**, 433-435.

24. F. D. Gunstone, J. L. Harwood and F. B. Padley, *The Lipid Handbook*, Taylor & Francis, 1994.

25. N. Hall, 'Implications of Soap Structure for Formulation and User Properties' in Soap Manufacturing Technology, L. Spitz, AOCS Press, 2016, 1-33.

26. M. J. Buerger, L. B. Smith, F. V. Ryer and J. E. Spike, 'The Crystalline Phases of Soap', 1945, **31**, 226-233.

27. L. Spitz, *Soap Manufacturing Technology*, AOCS Press, 2016.

28. M. Hollstein and L. Spitz, 'Manufacture and properties of synthetic toilet soaps', *Journal of the American Oil Chemists' Society*, 1982, **59**, 442-448.

29. United Kingdom Patent, GB853590, 'Improvements in the Manufacture of Surface-Active Acylated Hydroxysulphonates', *Lever Brothers Company*, 1961.

30. United States Patent, 5,656,579, 'Toilet soap bars', *Lever Brothers Company*, 1997.

31. United States Patent, 5,284,598, 'Process for making mild, detergent-soap, toilet bars and the bar resulting therefrom', *Colgate-Palmolive Company*, 1994.

32. United States Patent, 7,579,311, 'No-strip process for producing bars comprising acyl-isethionate and free fatty acid, and having consumer desirable properties', *Unilever*, 2009.

33. M. Friedman, 'Chemistry, Formulation, and Performance of Syndet and Combo Bars' in Soap Manufacturing Technology, L. Spitz, AOCS Press, 2016.

34. G. B. Olson, 'Computational Design of Hierarchically Structured Materials', *Science*, 1997, **277**, 1237-1242.

35. S. Allen and E. L. Thomas, *The Structure of Materials*, Wiley, 1999.

36. United States Patent, 6,069,262, 'Fatty acid esters of hydroxyalkyl sulfonate salts and process for producing same', *Finetex Inc.*, 2000.

37. A. S. Myerson, *Handbook of Industrial Crystallization*, Butterworth-Heinemann, 2002.

38. J. Mullin, *Crystallization*, Butterworth-Heinemann, 2001.

39. W. Clegg, *Crystal Structure Determination*, Oxford University Press, 1998.

40. A. Bravais, *Etudes Cristallographiques*, Gauthier Villars, 1866.

41. R. J. D. Tilley, *Crystals and Crystal Structures*, Wiley, 2006.

42. W. Beckmann, *Crystallization: Basic Concepts and Industrial Applications*, Wiley, 2013.

43. J. Bauer, S. Spanton, R. Henry, J. Quick, W. Dziki, W. Porter and J. Morris, 'Ritonavir: An Extraordinary Example of Conformational Polymorphism', *Pharmaceutical Research*, 2001, **18**, 859-866.

44. P. Atkins and J. de Paula, *Physical Chemistry*, Oxford University Press, 2014.

45. M. E. Glicksman, 'Crystals and Melts' in Principles of Solidification: An Introduction to Modern Casting and Crystal Growth Concepts, Springer, 2011, 3-25.

46. J. Ulrich and H. C. Bülau, 'Melt Crystallization' in Handbook of Industrial Crystallization, Butterworth-Heinemann, 2002, 161-179.

47. G. J. Sloan and A. R. McGhie, *Techniques of Melt Crystallization*, Wiley, 1988.

48. J. Ulrich and J. Bierwirth, 'Melt Layer Crystallization' in Science and Technology of Crystal Growth, J. P. van der Eerden, Springer, 1995, 245-258.

49. M. Zief and W. R. Wilcox, *Fractional Solidification*, Edward Arnold, 1967.

50. C. J. Adkins, *Equilibrium Thermodynamics*, Cambridge University Press, 1983.

51. J. W. Gibbs, 'Equilibrium of Heterogeneous Substances', *Transactions of the Connecticut Academy of Arts and Sciences*, 1876, **3**, 108-520.

52. W. Koch and M. C. Holthausen, *A Chemist's Guide to Density Functional Theory*, Wiley, 2001.

53. D. M. Hanson, E. Harvey, R. Sweeney and T. J. Zielinski, *Quantum States of Atoms and Molecules*, JCE, 2005.

54. K. A. Baseden and J. W. Tye, 'Introduction to Density Functional Theory: Calculations by Hand on the Helium Atom', *Journal of Chemical Education*, 2014, **91**, 2116-2123.

55. J. M. Thijssen, *Computational Physics*, Cambridge University Press, 2007.

56. P. W. Atkins and R. S. Friedman, *Molecular Quantum Mechanics*, Oxford University Press, 1997.

57. E. Schrödinger, 'An Undulatory Theory of the Mechanics of Atoms and Molecules', *Physical Review*, 1926, **28**, 1049-1070.

58. M. Born, 'Zur Quantenmechanik der Stoßvorgänge', *Zeitschrift für Physik*, 1926, **37**, 863-867.

59. D. R. Hartree, 'The Wave Mechanics of an Atom with a Non-Coulomb Central Field. Part I. Theory and Methods', *Mathematical Proceedings of the Cambridge Philosophical Society*, 1928, **24**, 89-110.

60. V. Fock, 'Näherungsmethode zur Lösung des quantenmechanischen Mehrkörperproblems', *Zeitschrift für Physik*, 1930, **61**, 126-148.

61. J. C. Slater, 'The Theory of Complex Spectra', *Physical Review*, 1929, **34**, 1293-1322.

62. R. Hartree Douglas and W. Hartree, 'Self-consistent field, with exchange, for beryllium', *Proceedings of the Royal Society of London. Series A - Mathematical and Physical Sciences*, 1935, **150**, 9-33.

63. W. Pauli, 'Über den Zusammenhang des Abschlusses der Elektronengruppen im Atom mit der Komplexstruktur der Spektren', *Zeitschrift für Physik*, 1925, **31**, 765-783.

64. L. H. Thomas, 'The calculation of atomic fields', *Mathematical Proceedings of the Cambridge Philosophical Society*, 1927, **23**, 542-548.

65. E. Fermi, 'Eine statistische Methode zur Bestimmung einiger Eigenschaften des Atoms und ihre Anwendung auf die Theorie des periodischen Systems der Elemente', *Zeitschrift für Physik*, 1928, **48**, 73-79.

66. P. Hohenberg and W. Kohn, 'Inhomogeneous Electron Gas', *Physical Review*, 1964, **136**, B864-B871.

67. W. Kohn and L. J. Sham, 'Self-Consistent Equations Including Exchange and Correlation Effects', *Physical Review*, 1965, **140**, A1133-A1138.

68. A. D. Becke, 'Density-functional thermochemistry. I. The effect of the exchange-only gradient correction', *The Journal of Chemical Physics*, 1992, **96**, 2155-2160.

69. K. I. Ramachandran, G. Deepa and K. Namboori, *Computational Chemistry and Molecular Modeling: Principles and Applications*, Springer Berlin Heidelberg, 2008.

70. R. Ditchfield, W. J. Hehre and J. A. Pople, 'Self-Consistent Molecular-Orbital Methods. IX. An Extended Gaussian-Type Basis for Molecular-Orbital Studies of Organic Molecules', *The Journal of Chemical Physics*, 1971, **54**, 724-728.

71. K. Machida, *Principles of Molecular Mechanics*, Wiley, 1999.

72. A. K. Rappé and C. J. Casewit, *Molecular Mechanics Across Chemistry*, University Science, 1997.

73. C. F. Kettering, L. W. Shutts and D. H. Andrews, 'A Representation of the Dynamic Properties of Molecules by Mechanical Models', *Physical Review*, 1930, **36**, 531-543.

74. K. B. Wiberg, 'A Scheme for Strain Energy Minimization. Application to the Cycloalkanes', *Journal of the American Chemical Society*, 1965, **87**, 1070-1078.

75. S. L. Price, 'Computational prediction of organic crystal structures and polymorphism', *International Reviews in Physical Chemistry*, 2008, **27**, 541-568.

76. G. Clydesdale, K. J. Roberts and R. Docherty, 'HABIT95 — a program for predicting the morphology of molecular crystals as a function of the growth environment', *Journal of Crystal Growth*, 1996, **166**, 78-83.

77. J. F. Malone, C. M. Murray, G. M. Dolan, R. Docherty and A. J. Lavery, 'Intermolecular Interactions in the Crystal Chemistry of N,N‘-Diphenylisophthalamide, Pyridine-2,6-dicarboxylic Acid Bisphenylamide, and Related Compounds', *Chemistry of Materials*, 1997, **9**, 2983-2989.

78. F. D. Gunstone, *Fatty Acid and Lipid Chemistry*, Chapman & Hall, 1996.

79. C. Poole, *Gas Chromatography*, Elsevier, 2012.

80. D. C. Harris, *Quantitative Chemical Analysis*, W. H. Freeman, 2010.

81. A. B. Littlewood, *Gas Chromatography: Principles, Techniques, and Applications*, Elsevier Science, 2013.

82. O. D. Sparkman, Z. Penton and F. G. Kitson, *Gas Chromatography and Mass Spectrometry: A Practical Guide*, Elsevier, 2011.

83. A. T. James and A. J. P. Martin, 'Gas-liquid partition chromatography: the separation and micro-estimation of volatile fatty acids from formic acid to dodecanoic acid', *Biochemical Journal*, 1952, **50**, 679-690.

84. J. G. Nikelly, 'Gas chromatography of free fatty acids', *Analytical Chemistry*, 1964, **36**, 2244-2248.

85. J. Vičanová, E. Tvrzická and K. Štulík, 'Capillary gas chromatography of underivatized fatty acids with a free fatty acid phase column and a programmed temperature vaporizer injector', *Journal of Chromatography B: Biomedical Sciences and Applications*, 1994, **656**, 45-50.

86. W. W. Christie, *Gas Chromatography and Lipids*, The Oily Press, 1989.

87. United States Patent, 3,320,292 'Preparation of sulfonated fatty acid ester surface-active agents', *Lever Brothers Company*, 1967.

88. G. S. Hartley and D. F. Runnicles, 'The Determination of the Size of Paraffin-Chain Salt Micelles from Diffusion Measurements', *Proceedings of the Royal Society of London A: Mathematical, Physical and Engineering Sciences*, 1938, **168**, 420-440.

89. G. F. Longman, *The Analysis of Detergents and Detergent Products*, John Wiley & Sons, 1976.

90. S. R. Epton, 'A rapid method of analysis for certain surface-active agents', *Nature*, 1947, **160**, 795.

91. M. Rieger and L. D. Rhein, *Surfactants in Cosmetics*, Marcel Dekker, 1997.

92. M. E. Turney and D. W. Cannell, 'Alkaline methylene blue method for determination of anionic surfactants and for amine oxides in detergents', *Journal of the American Oil Chemists' Society*, 1965, **42**, 544-546.

93. E. Chiavaro, *Differential Scanning Calorimetry: Applications in Fat and Oil Technology*, Taylor & Francis, 2014.

94. G. Höhne, W. Hemminger and H. J. Flammersheim, *Differential Scanning Calorimetry*, Springer, 2003.

95. H. Lorenz, 'Solubility and Solution Equilibria' in Crystallization, Wiley, 2013, 35-74.

96. M. E. Brown, *Introduction to Thermal Analysis: Techniques and Applications*, Springer Netherlands, 2001.

97. M. P. Sepe, *Thermal Analysis of Polymers*, Smithers Publishing, 1997.

98. S. Materazzi and S. Vecchio, 'Evolved Gas Analysis by Mass Spectrometry', *Applied Spectroscopy Reviews*, 2011, **46**, 261-340.

99. C. A. Wilkie, 'TGA/FTIR: An extremely useful technique for studying polymer degradation', *Polymer Degradation and Stability*, 1999, **66**, 301-306.

100. S. H. Hansen, S. Pedersen-Bjergaard and K. Rasmussen, *Introduction to Pharmaceutical Chemical Analysis*, Wiley, 2011.

101. J. L. McHale, *Molecular Spectroscopy*, CRC Press, 2017.

102. D. C. Harris and M. D. Bertolucci, *Symmetry and Spectroscopy: An Introduction to Vibrational and Electronic Spectroscopy*, Dover Publications, 1989.

103. G. Socrates, *Infrared and Raman Characteristic Group Frequencies: Tables and Charts*, Wiley, 2004.

104. B. C. Smith, *Fundamentals of Fourier Transform Infrared Spectroscopy*, CRC Press, 2011.

105. P. R. Griffiths, J. A. De Haseth and J. D. Winefordner, *Fourier Transform Infrared Spectrometry*, Wiley, 2007.

106. B. C. Smith, *Infrared Spectral Interpretation: A Systematic Approach*, CRC Press, 1998.

107. D. Welti, *Infrared Vapour Spectra*, Heyden & Son, 1970.

108. C. E. Housecroft and A. G. Sharpe, *Inorganic Chemistry*, Pearson, 2012.

109. S. R. Byrn, G. Zografi and X. Chen, 'X-ray Powder Diffraction' in Solid State Properties of Pharmaceutical Materials, 107-123.

110. R. E. Dinnebier, S. J. L. Billinge, A. L. Bail, L. M. D. Cranswick and I. Madsen, *Powder Diffraction: Theory and Practice*, Royal Society of Chemistry, 2008.

111. W. H. Zachariasen, *Theory of X-Ray Diffraction in Crystals*, Dover Publications, 2004.

112. A. G. Marangoni and L. H. Wesdorp, *Structure and Properties of Fat Crystal Networks*, CRC Press, 2012.

113. M. Rappolt, P. Laggner and G. Pabst, 'Structure and elasticity of phospholipid bilayers in the Lα phase: A comparison of phosphatidylcholine and phosphatidylethanolamine membranes', *Recent Research Developments in Biophysics*, 2004, **3**, 363-394.

114. H. Schnablegger and Y. Singh, *The SAXS Guide (3rd Edition)*, Anton Parr, 2013.

115. O. M. Londoño, P. Tancredi, P. Rivas, D. Muraca, L. M. Socolovsky and M. Knobel, 'Small-Angle X-Ray Scattering to Analyze the Morphological Properties of Nanoparticulated Systems' in Handbook of Materials Characterization, S. K. Sharma, Springer International Publishing, 2018, 37-75.

116. L. A. Feigin and D. I. Svergun, *Structure Analysis by Small-Angle X-Ray and Neutron Scattering*, Springer, 2013.

117. C. L. Froebe, F. A. Simion, L. D. Rhein, R. H. Cagan and A. Kligman, 'Stratum corneum Lipid Removal by Surfactants: Relation to in vivo Irritation', *Dermatology*, 1990, **181**, 277-283.

118. G. Imokawa, S. Akasaki, Y. Minematsu and M. Kawai, 'Importance of intercellular lipids in water-retention properties of the stratum corneum: induction and recovery study of surfactant dry skin', *Archives of Dermatological Research*, 1989, **281**, 45-51.

119. M. Kawai and G. Imokawa, 'The induction of skin tightness by surfactants', *Journal of the Society of Cosmetic Chemists*, 1984, **35**, 147-156.

120. J. Faucher and E. Goddard, 'Interaction of keratinous substrates with sodium lauryl sulfate: I. Sorption', *Journal of the Society of Cosmetic Chemists*, 1978, **29**, 323-337.

121. C. Prottey and T. Ferguson, 'Factors which determine the skin irritation potential of soaps and detergents', *Journal of the Society of Cosmetic Chemists*, 1975, **26**, 29-46.

122. G. Sauermann, A. Doerschner, U. Hoppe and P. Wittern, 'Comparative-Study of Skin Care Efficacy and In-Use Properties of Soap and Surfactant Bars', *Journal of the Society of Cosmetic Chemists*, 1986, **37**, 309-327.

123. D. D. Strube and G. Nicoll, 'The irritancy of soaps and syndets', *Cutis*, 1987, **39**, 544-545.

124. K. Ananthapadmanabhan, L. Yang, C. Vincent, L. Tsaur, K. M. Vetro, V. Foy, S. Zhang, A. Ashkenazi, E. Pashkovski and V. Subramanian, 'A Novel Technology in Mild and Moisturizing Cleansing Liquids', *Cosmetic Dermatology*, 2009, **22**, 307-316.

125. E. Bárány, M. Lindberg and M. Lodén, 'Biophysical characterization of skin damage and recovery after exposure to different surfactants', *Contact Dermatitis*, 1999, **40**, 98-103.

126. D. Wilson, E. Berardesca and H. I. Maibach, 'In vivo transepidermal water loss and skin surface hydration in assessment of moisturization and soap effects', *International Journal of Cosmetic Science*, 1988, **10**, 201-211.

127. K. P. Ananthapadmanabhan, K. K. Yu, C. L. Meyers and M. P. Aronson, 'Binding of surfactants to stratum corneum', *Journal of the Society of Cosmetic Chemists*, 1996, **47**, 185-200.

128. M. Friedman and R. Wolf, 'Chemistry of soaps and detergents: Various types of commercial products and their ingredients', *Clinics in Dermatology*, 1996, **14**, 7-13.

129. S. Soontravanich, H. E. Lopez, J. F. Scamehorn, D. A. Sabatini and D. R. Scheuing, 'Dissolution Study of Salt of Long Chain Fatty Acids (Soap Scum) in Surfactant

Solutions. Part I: Equilibrium Dissolution', *Journal of Surfactants and Detergents*, 2010, **13**, 367-372.

130. K. A. Western, D. R. Perera and M. G. Schultz, 'Pentamidine isethionate in the treatment of pneumocystis carinii pneumonia', *Annals of Internal Medicine*, 1970, **73**, 695-702.

131. H. J. Barber and R. Slack, 'The search for chemotherapeutic amidines. Part IV. Two polyamidines', *Journal of the Chemical Society*, 1947, 82-84.

132. J. Orsavova, L. Misurcova, J. V. Ambrozova, R. Vicha and J. Mlcek, 'Fatty acids composition of vegetable oils and its contribution to dietary energy intake and dependence of cardiovascular mortality on dietary intake of fatty acids', *International Journal of Molecular Sciences*, 2015, **16**, 12871-12890.

133. R. G. Bistline, Jr., E. S. Rothman, S. Serota, A. J. Stirton and A. N. Wrigley, 'Surface active agents from isopropenyl esters: Acylation of isethionic acid and N-methyltaurine', *Journal of the American Oil Chemists' Society*, 1971, **48**, 657-660.

134. T. Hikota, 'Studies of Ester-Containing Surfactants. Preparation and Properties of Sodium Sulfoalkyl Alkanoates', *Bulletin of the Chemical Society of Japan*, 1970, **43**, 2236-2240.

135. J. M. Prausnitz, R. N. Lichtenthaler and E. G. de Azevedo, *Molecular Thermodynamics of Fluid-Phase Equilibria*, Prentice Hall, 1998.

136. D. M. Camacho Corzo, A. Borissova, R. B. Hammond, D. Kashchiev, K. J. Roberts, K. Lewtas and I. More, 'Nucleation mechanism and kinetics from the analysis of polythermal crystallisation data: methyl stearate from kerosene solutions', *CrystEngComm*, 2014, **16**, 974-991.

137. T. D. Turner, D. M. C. Corzo, D. Toroz, A. Curtis, M. M. Dos Santos, R. B. Hammond, X. Lai and K. J. Roberts, 'The influence of solution environment on the nucleation kinetics and crystallisability of para-aminobenzoic acid', *Physical Chemistry Chemical Physics*, 2016, **18**, 27507-27520.

138. United States Patent, 2,857,370, 'Process of preparing ester and amide type anionic surface active agents', *General Aniline & Film Corporation*, 1958.

139. T. M. Schmitt, *Analysis of Surfactants*, Marcel Dekker, 2001.

140. L. Cui, M. Puerto, J. L. López-Salinas, S. L. Biswal and G. J. Hirasaki, 'Improved Methylene Blue Two-Phase Titration Method for Determining Cationic Surfactant Concentration in High-Salinity Brine', *Analytical Chemistry*, 2014, **86**, 11055-11061.

141. E. Pretsch, P. Bühlmann and C. Affolter, *Structure Determination of Organic Compounds: Tables of Spectral Data*, Springer Berlin Heidelberg, 2000.

142. NIST, *Atomic Weights and Isotopic Compositions for All Elements*, http://physics.nist.gov/cgi-bin/Compositions/stand_alone.pl?ele=&all=all, 2016.

143. A. E. Skoulios and V. Luzzati, '(FR) La structure des colloïdes d'association. III. Description des phases mésomorphes des savons de sodium purs, rencontrées au-dessus de 100°C', *Acta Crystallographica*, 1961, **14**, 278-286.

144. K. Binnemans, 'Ionic Liquid Crystals', *Chemical Reviews*, 2005, **105**, 4148-4204.

145. R. Klein, H. Dutton, O. Diat, G. J. T. Tiddy and W. Kunz, 'Thermotropic Phase Behavior of Choline Soaps', *The Journal of Physical Chemistry B*, 2011, **115**, 3838-3847.

146. C. Gustavsson and L. Piculell, 'Isotherms and Kinetics of Water Vapor Sorption/Desorption for Surface Films of Polyion–Surfactant Ion Complex Salts', *The Journal of Physical Chemistry B*, 2016, **120**, 6778-6790.

147. J. Ouyang, J. Wang, Y. Wang, Q. Yin and H. Hao, 'Thermodynamic study on dynamic water and organic vapor sorption on amorphous valnemulin hydrochloride', *Frontiers of Chemical Science and Engineering*, 2015, **9**, 94-104.

148. S. S. Dell, 'The Crystal Structure of Sodium Dodecylsulfate', *Acta Chemica Scandinavica Series A: Physical and Inorganic Chemistry*, 1977, **31**.

149. V. M. Coiro, F. Mazza and G. Pochetti, 'Crystal phases obtained from aqueous solutions of sodium dodecyl sulfate. The structure of a monoclinic phase of sodium dodecyl sulfate hemihydrate', *Acta Crystallographica Section C*, 1986, **42**, 991-995.

150. V. M. Coiro, M. Manigrasso, F. Mazza and G. Pochetti, 'Structure of a triclinic phase of sodium dodecyl sulfate monohydrate. A comparison with other sodium dodecyl sulfate crystal phases', *Acta Crystallographica Section C*, 1987, **43**, 850-854.

151. J. C. Callahan, G. W. Cleary, M. Elefant, G. Kaplan, T. Kensler and R. A. Nash, 'Equilibrium Moisture Content of Pharmaceutical Excipients', *Drug Development and Industrial Pharmacy*, 1982, **8**, 355-369.

152. Council-of-Europe, *European Pharmacopoeia, 5th Edition*, Council of Europe, 2004.

153. A. W. Newman, S. M. Reutzel-Edens and G. Zografi, 'Characterization of the "hygroscopic" properties of active pharmaceutical ingredients', *Journal of Pharmaceutical Sciences*, 2008, **97**, 1047-1059.

154. W. P. Bryan, 'Sorption hysteresis and the laws of thermodynamics', *Journal of Chemical Education*, 1987, **64**, 209.

155. D. H. Everett, 'The Solid-Gas Interface Vol. 2', E. A. Flood, Marcel Dekker, 1967.

156. A. W. Ralston and C. W. Hoerr, 'The Solubilities of the Normal Saturated Fatty Acids', *The Journal of Organic Chemistry*, 1942, **07**, 546-555.

157. C. W. Hoerr and A. W. Balston, 'The Solubilities of the Normal Saturated Fatty Acids II', *The Journal of Organic Chemistry*, 1944, **09**, 329-337.

158. D. Kashchiev and G. M. van Rosmalen, 'Review: Nucleation in solutions revisited', *Crystal Research and Technology*, 2003, **38**, 555-574.

159. S. Khan, C. Y. Ma, T. Mahmud, R. Y. Penchev, K. J. Roberts, J. Morris, L. Özkan, G. White, B. Grieve, A. Hall, P. Buser, N. Gibson, P. Keller, P. Shuttleworth and C. J. Price, 'In-Process Monitoring and Control of Supersaturation in Seeded Batch Cooling Crystallisation of l-Glutamic Acid: From Laboratory to Industrial Pilot Plant', *Organic Process Research & Development*, 2011, **15**, 540-555.

160. I. Miyata, A. Takada, M. Yonese and H. Kishimoto, 'Solution Behavior of Sodium Dodecyl Sulfate in Methanol', *Bulletin of the Chemical Society of Japan*, 1990, **63**, 3502-3507.

161. K. J. Mysels, 'Surface tension of solutions of pure sodium dodecyl sulfate', *Langmuir*, 1986, **2**, 423-428.

162. A. Chatterjee, S. P. Moulik, S. K. Sanyal, B. K. Mishra and P. M. Puri, 'Thermodynamics of Micelle Formation of Ionic Surfactants: A Critical Assessment for Sodium Dodecyl Sulfate, Cetyl Pyridinium Chloride and Dioctyl Sulfosuccinate (Na Salt) by Microcalorimetric, Conductometric, and Tensiometric Measurements', *The Journal of Physical Chemistry B*, 2001, **105**, 12823-12831.

163. F. Hernáinz and A. Caro, 'Variation of surface tension in aqueous solutions of sodium dodecyl sulfate in the flotation bath', *Colloids and Surfaces A: Physicochemical and Engineering Aspects*, 2002, **196**, 19-24.

164. R. Yonekura and M. W. Grinstaff, 'The effects of counterion composition on the rheological and conductive properties of mono- and diphosphonium ionic liquids', *Physical Chemistry Chemical Physics*, 2014, **16**, 20608-20617.

165. Z. K. Nagy, J. W. Chew, M. Fujiwara and R. D. Braatz, 'Comparative performance of concentration and temperature controlled batch crystallizations', *Journal of Process Control*, 2008, **18**, 399-407.

166. M. I. Jeraal, K. J. Roberts, I. McRobbie and D. Harbottle, 'Process-Focused Synthesis, Crystallization, and Physicochemical Characterization of Sodium Lauroyl Isethionate', *ACS Sustainable Chemistry & Engineering*, 2018, **6**, 2667-2675.

167. United States Patent, 3,420,858, 'Process for the production of fatty acid esters of hydroxy sulfonates', *Lever Brothers Company*, 1969.

168. United States Patent, 4,515,721, 'Process for the production of fatty acid esters of hydroxyalkyl sulfonate salts', *Jordan Chemical Company*, 1985.

169. United States Patent, 4,405,526, 'Process for producing directly esterified fatty acyl isethionate by a mixed zinc oxide-sulfonic acid catalyst', *Lever Brothers Company*, 1983.

170. O. I. Chernikov, R. V. Glagolev and T. I. Zvyagina, 'Thermostability of surfactants having various chemical structures', *Journal of Applied Chemistry of the USSR*, 1983, **56**, 1347-1349.

171. T. H. Liddicoet and L. H. Smithson, 'Analysis of surfactants using pyrolysis-gas chromatography', *Journal of the American Oil Chemists' Society*, 1965, **42**, 1097-1102.

172. S. Vyazovkin, *Isoconversional Kinetics of Thermally Stimulated Processes*, Springer International Publishing, 2016.

173. J. H. Flynn, 'A critique of lifetime prediction of polymers by thermal analysis', *Journal of Thermal Analysis*, 1995, **44**, 499-512.

174. S. Vyazovkin and C. A. Wight, 'Isothermal and non-isothermal kinetics of thermally stimulated reactions of solids', *International Reviews in Physical Chemistry*, 1998, **17**, 407-433.

175. S. Vyazovkin, A. K. Burnham, J. M. Criado, L. A. Pérez-Maqueda, C. Popescu and N. Sbirrazzuoli, 'ICTAC Kinetics Committee recommendations for performing kinetic computations on thermal analysis data', *Thermochimica Acta*, 2011, **520**, 1-19.

176. S. Vyazovkin, K. Chrissafis, M. L. Di Lorenzo, N. Koga, M. Pijolat, B. Roduit, N. Sbirrazzuoli and J. J. Suñol, 'ICTAC Kinetics Committee recommendations for collecting experimental thermal analysis data for kinetic computations', *Thermochimica Acta*, 2014, **590**, 1-23.

177. D. R. White and R. L. White, 'Isoconversion Effective Activation Energy Profiles by Variable Temperature Diffuse Reflection Infrared Spectroscopy', *Applied Spectroscopy*, 2008, **62**, 116-120.

178. E. Bonnet and R. L. White, 'Species-specific isoconversion effective activation energies derived by thermogravimetry–mass spectrometry', *Thermochimica Acta*, 1998, **311**, 81-86.

179. S. A. Madbouly and J. U. Otaigbe, 'Kinetic Analysis of Fractal Gel Formation in Waterborne Polyurethane Dispersions Undergoing High Deformation Flows', *Macromolecules*, 2006, **39**, 4144-4151.

180. J. Farjas and P. Roura, 'Isoconversional analysis of solid state transformations (Part II. Complex transformations)', *Journal of Thermal Analysis and Calorimetry*, 2011, **105**, 767-773.

181. J. M. Criado, A. Ortega and F. Gotor, 'Correlation between the shape of controlled-rate thermal analysis curves and the kinetics of solid-state reactions', *Thermochimica Acta*, 1990, **157**, 171-179.

182. S. Vyazovkin, 'Modern Isoconversional Kinetics: From Misconceptions to Advances' in Handbook of Thermal Analysis and Calorimetry, S. Vyazovkin, N. Koga and C. Schick, Elsevier Science, 2018, 131-172.

183. S. Vyazovkin and C. A. Wight, 'Estimating Realistic Confidence Intervals for the Activation Energy Determined from Thermoanalytical Measurements', *Analytical Chemistry*, 2000, **72**, 3171-3175.

184. H. L. Friedman, 'Kinetics of thermal degradation of char-forming plastics from thermogravimetry. Application to a phenolic plastic', *Journal of Polymer Science Part C: Polymer Symposia*, 1964, **6**, 183-195.

185. A. K. Burnham and L. N. Dinh, 'A comparison of isoconversional and model-fitting approaches to kinetic parameter estimation and application predictions', *Journal of Thermal Analysis and Calorimetry*, 2007, **89**, 479-490.

186. G. Berčič, 'The universality of Friedman's isoconversional analysis results in a model-less prediction of thermodegradation profiles', *Thermochimica Acta*, 2017, **650**, 1-7.

187. P. M. Madhusudanan, K. Krishnan and K. N. Ninan, 'New approximation for the p(x) function in the evaluation of non-isothermal kinetic data', *Thermochimica Acta*, 1986, **97**, 189-201.

188. C. D. Doyle, 'Series Approximations to the Equation of Thermogravimetric Data', *Nature*, 1965, **207**, 290.

189. J. H. Flynn, 'The 'Temperature Integral' — Its use and abuse', *Thermochimica Acta*, 1997, **300**, 83-92.

190. J. H. Flynn and L. A. Wall, 'A quick, direct method for the determination of activation energy from thermogravimetric data', *Journal of Polymer Science Part B: Polymer Letters*, 1966, **4**, 323-328.

191. T. Akahira and T. Sunose, 'Method of determining activation deterioration constant of electrical insulating materials', *Research Report of Chiba Institute of Technology*, 1971, **16**, 22-31.

192. H. E. Kissinger, 'Reaction Kinetics in Differential Thermal Analysis', *Analytical Chemistry*, 1957, **29**, 1702-1706.

193. A. W. Coats and J. P. Redfern, 'Kinetic Parameters from Thermogravimetric Data', *Nature*, 1964, **201**, 68.

194. P. Murray and J. White, 'Kinetics of the thermal dehydration of clays. (Part IV: Interpretation of the differential thermal analysis of the clay minerals)', *Transactions and Journal of the British Ceramic Society*, 1955, **54**, 204-238.

195. M. J. Starink, 'A new method for the derivation of activation energies from experiments performed at constant heating rate', *Thermochimica Acta*, 1996, **288**, 97-104.

196. R. E. Lyon, 'An integral method of nonisothermal kinetic analysis', *Thermochimica Acta*, 1997, **297**, 117-124.

197. S. Vyazovkin and D. Dollimore, 'Linear and Nonlinear Procedures in Isoconversional Computations of the Activation Energy of Nonisothermal Reactions in Solids', *Journal of Chemical Information and Computer Sciences*, 1996, **36**, 42-45.

198. S. Vyazovkin, 'Evaluation of activation energy of thermally stimulated solid-state reactions under arbitrary variation of temperature', *Journal of Computational Chemistry*, 1997, **18**, 393-402.

199. J. Wang, M.-P. G. Laborie and M. P. Wolcott, 'Comparison of model-free kinetic methods for modeling the cure kinetics of commercial phenol–formaldehyde resins', *Thermochimica Acta*, 2005, **439**, 68-73.

200. H. Li, S. Niu, C. Lu and Y. Wang, 'Comprehensive Investigation of the Thermal Degradation Characteristics of Biodiesel and Its Feedstock Oil through TGA–FTIR', *Energy & Fuels*, 2015, **29**, 5145-5153.

201. H. Li, S. Niu, C. Lu and S. Cheng, 'Comparative evaluation of thermal degradation for biodiesels derived from various feedstocks through transesterification', *Energy Conversion and Management*, 2015, **98**, 81-88.

202. J. M. Patterson, Z. Kortylewicz and W. T. Smith, 'Thermal degradation of sodium dodecyl sulfate', *Journal of Agricultural and Food Chemistry*, 1984, **32**, 782-784.

203. S. Vyazovkin, 'Thermal Analysis', *Analytical Chemistry*, 2008, **80**, 4301-4316.

204. E. L. Charsley, P. G. Laye, V. Palakollu, J. J. Rooney and B. Joseph, 'DSC studies on organic melting point temperature standards', *Thermochimica Acta*, 2006, **446**, 29-32.

205. S. Vyazovkin and N. Sbirrazzuoli, 'Isoconversional Kinetic Analysis of Thermally Stimulated Processes in Polymers', *Macromolecular Rapid Communications*, 2006, **27**, 1515-1532.

206. A. S. Reshad, P. Tiwari and V. V. Goud, 'Thermal Degradation Kinetic Study of Rubber Seed Oil and Its Methyl Esters under Inert Atmosphere', *Energy & Fuels*, 2017, **31**, 9642-9651.

207. S. Vyazovkin, 'Model-free kinetics', *Journal of Thermal Analysis and Calorimetry*, 2006, **83**, 45-51.

208. J. Sestsk and M. Stulikova, *Thermophysical Properties of Solids: Their Measurements and Theoretical Thermal Analysis*, Elsevier, 1984.

209. K. Pielichowski, 'Kinetic analysis of the thermal decomposition of polyaniline', *Solid State Ionics*, 1997, **104**, 123-132.

210. S. Vyazovkin and N. Sbirrazzuoli, 'Isoconversional Kinetic Analysis of Thermally Stimulated Processes in Polymers', *Macromol. Rapid Commun.*, 2006, **27**, 1515-1532.

211. J. Farjas and P. Roura, 'Isoconversional analysis of solid state transformations (Part II. Complex transformations)', *J. Therm. Anal. Calorim.*, 2011, **105**, 767-773.

212. G. Berčič, 'The universality of Friedman's isoconversional analysis results in a model-less prediction of thermodegradation profiles', *Thermochim. Acta*, 2017, **650**, 1-7.

213. M. I. Jeraal, K. J. Roberts, I. McRobbie and D. Harbottle, 'Process-Focused Synthesis, Crystallization, and Physicochemical Characterization of Sodium Lauroyl Isethionate', *ACS Sus. Chem. Eng.*, 2018, **6**, 2667-2675.

214. J. F. d. S. Petruci, A. Wilk, A. A. Cardoso and B. Mizaikoff, 'Online Analysis of H2S and SO2 via Advanced Mid-Infrared Gas Sensors', *Analytical Chemistry*, 2015, **87**, 9605-9611.

215. S. Bhagavantam, 'The Infrared and Raman Spectra of CS2', *Physical Review*, 1932, **39**, 1020-1020.

216. H. N. Ritland, *Technical Report: The Infrared Absorption Spectrum of Water Vapor and Carbon Dioxide*, Lockheed Information Systems Laboratory, 1962.

217. I. R. Hill and I. W. Levin, 'Vibrational spectra and carbon–hydrogen stretching mode assignments for a series of n-alkyl carboxylic acids', *The Journal of Chemical Physics*, 1979, **70**, 842-851.

218. R. Alexander, P. G. Kralert and R. I. Kagi, 'Kinetics and mechanism of the thermal decomposition of esters in sediments', *Organic Geochemistry*, 1992, **19**, 133-140.

219. S. F. Lu, M. Chen and C. H. Chen, 'Mechanisms and kinetics of thermal degradation of poly(butylene succinate-co-propylene succinate)s', *Journal of Applied Polymer Science*, 2011, **123**, 3610-3619.

220. S. E. Stein, *NIST Standard Reference Database Number 69 - Infrared Spectra*, National Institute of Standards and Technology, 2018.

221. Z. Ma, J. Wang, Y. Yang, Y. Zhang, C. Zhao, Y. Yu and S. Wang, 'Comparison of the thermal degradation behaviors and kinetics of palm oil waste under nitrogen and air atmosphere in TGA-FTIR with a complementary use of model-free and model-fitting approaches', *Journal of Analytical and Applied Pyrolysis*, 2018, **134**, 12-24.

222. D. J. Hautman, F. L. Dryer, K. P. Schug and I. Glassman, 'A Multiple-step Overall Kinetic Mechanism for the Oxidation of Hydrocarbons', *Combustion Science and Technology*, 1981, **25**, 219-235.

223. Z. Ma, D. Chen, J. Gu, B. Bao and Q. Zhang, 'Determination of pyrolysis characteristics and kinetics of palm kernel shell using TGA–FTIR and model-free integral methods', *Energy Conversion and Management*, 2015, **89**, 251-259.

224. K. Lazdovica, L. Liepina and V. Kampars, 'Catalytic pyrolysis of wheat bran for hydrocarbons production in the presence of zeolites and noble-metals by using TGA-FTIR method', *Bioresource Technology*, 2016, **207**, 126-133.

225. J. O. Morley and D. W. Roberts, 'Molecular Modeling Studies on Aromatic Sulfonation. 1. Intermediates Formed in the Sulfonation of Toluene', *The Journal of Organic Chemistry*, 1997, **62**, 7358-7363.

226. N. Gao, A. Li, C. Quan, L. Du and Y. Duan, 'TG–FTIR and Py–GC/MS analysis on pyrolysis and combustion of pine sawdust', *Journal of Analytical and Applied Pyrolysis*, 2013, **100**, 26-32.

227. S. E. Manahan, *Toxicological Chemistry*, Lewis Publishers, 1992.

228. F. Shahidi, *Bailey's Industrial Oil and Fat Products*, Wiley, 2005.

229. R. H. Ferguson, F. B. Rosevear and R. C. Stillman, 'Solid Soap Phases', *Industrial & Engineering Chemistry*, 1943, **35**, 1005-1012.

230. A. D. Bond, 'On the crystal structures and melting point alternation of the n-alkyl carboxylic acids', *New Journal of Chemistry*, 2004, **28**, 104-114.

231. E. Moreno-Calvo, G. Gbabode, R. Cordobilla, T. Calvet, M. À. Cuevas-Diarte, P. Negrier and D. Mondieig, 'Competing Intermolecular Interactions in the High-Temperature Solid Phases of Even Saturated Carboxylic Acids ($C_{10}H_{19}O_2H$ to $C_{20}H_{39}O_2H$)', 2009, **15**, 13141-13149.

232. E. von Sydow, 'On the Structure of Crystal Form A of Lauric Acid', *Acta Chemica Scandinavica*, 1956, **10**, 1-8.

233. T. Lomer, 'The crystal and molecular structure of lauric acid (form A)', *Acta Crystallographica*, 1963, **16**, 984-988.

234. M. Goto and E. Asada, 'The Crystal Structure of the A-super Form of Lauric Acid', *Bulletin of the Chemical Society of Japan*, 1978, **51**, 70-74.

235. E. Moreno, R. Cordobilla, T. Calvet, M. A. Cuevas-Diarte, G. Gbabode, P. Negrier, D. Mondieig and H. A. J. Oonk, 'Polymorphism of even saturated carboxylic acids from n-decanoic to n-eicosanoic acid', *New Journal of Chemistry*, 2007, **31**, 947-957.

236. L. A. Smith, R. B. Hammond, K. J. Roberts, D. Machin and G. McLeod, 'Determination of the crystal structure of anhydrous sodium dodecyl sulphate using a combination of synchrotron radiation powder diffraction and molecular modelling techniques', *Journal of Molecular Structure*, 2000, **554**, 173-182.

237. J. M. Vincent and A. Skoulios, '`Gel' et `coagel'. I. Indentification. Localisation dans un diagramme de phases et détermination de la structure du `gel' dans le cas du stéarate de potassium', 1966, **20**, 432-440.

238. S. Sundell, 'Crystal Structure of Sodium Dodecylsulfate', *Acta Chemica Scandinavica Series A: Physical and Inorganic Chemistry*, 1977, **31**, 799-807.

239. K. D. M. Harris and M. Tremayne, 'Crystal Structure Determination from Powder Diffraction Data', *Chemistry of Materials*, 1996, **8**, 2554-2570.

240. K. D. M. Harris, 'Powder Diffraction Crystallography of Molecular Solids' in Advanced X-Ray Crystallography, K. Rissanen, Springer Berlin Heidelberg, 2012, 133-177.

241. M. Tremayne, Engineering of Crystalline Materials Properties, Dordrecht, 2008.

242. W. I. F. David, K. Shankland, C. Baerlocher, L. McCusker and L. Baerlocher, *Structure Determination from Powder Diffraction Data*, Oxford University Press, 2002.

243. K. D. M. Harris, M. Tremayne and B. M. Kariuki, 'Contemporary Advances in the Use of Powder X-Ray Diffraction for Structure Determination', *Angewandte Chemie International Edition*, 2001, **40**, 1626-1651.

244. K. J. Roberts, R. B. Hammond, V. Ramachandran and R. Docherty, 'Synthonic Engineering' in Computational Pharmaceutical Solid State Chemistry, Y. A. Abramov, Wiley, 2016, 175-210.

245. I. Rosbottom, K. J. Roberts and R. Docherty, 'The solid state, surface and morphological properties of p-aminobenzoic acid in terms of the strength and directionality of its intermolecular synthons', *CrystEngComm*, 2015, **17**, 5768-5788.

246. T. T. H. Nguyen, I. Rosbottom, I. Marziano, R. B. Hammond and K. J. Roberts, 'Crystal Morphology and Interfacial Stability of RS-Ibuprofen in Relation to Its Molecular and Synthonic Structure', *Crystal Growth & Design*, 2017, **17**, 3088-3099.

247. A. A. Moldovan, I. Rosbottom, V. Ramachandran, C. M. Pask, O. Olomukhoro and K. J. Roberts, 'Crystallographic Structure, Intermolecular Packing Energetics, Crystal Morphology and Surface Chemistry of Salmeterol Xinafoate (Form I)', *Journal of Pharmaceutical Sciences*, 2017, **106**, 882-891.

248. J. E. Minor and E. C. Lingafelter, 'A Comparison of the Long Spacings of Some Soap Hemihydrates', *Journal of the American Chemical Society*, 1949, **71**, 1145-1146.

249. S. Speakman, *Profile Fitting for Analysis of XRPD Data*, Massachusetts Institute of Technology.

250. W. H. Brown, B. L. Iverson, E. Anslyn and C. S. Foote, *Organic Chemistry*, Wadsworth Cengage, 2013.

251. R. K. Bohn and K. B. Wiberg, 'Conformations of ethyl esters versus thiolesters', *Theoretical Chemistry Accounts*, 1999, **102**, 272-278.

252. M. Hill and T. Moaddel, 'Soap Structure and Phase Behavior' in Soap Manufacturing Technology, L. Spitz, AOCS Press, 2016, 35-54.

253. R. D. Vold and M. J. Vold, 'Successive Phases in the Transformation of Anhydrous Sodium Palmitate from Crystal to Liquid', *Journal of the American Chemical Society*, 1939, **61**, 808-816.

254. A. S. C. Lawrence, 'Liquid Crystals and Anisotropic Solutions', *Journal of the Royal Microscopical Society*, 1938, **58**, 30-48.

255. S. T. Beckett, *Industrial Chocolate Manufacture and Use*, Wiley, 2011.

256. M. J. Buerger, 'Soap Crystals', *American Mineralogist*, 1945, **30**, 551-571.

257. P. A. Thiessen and R. Spychalski, 'Anordnung der Moleküle in Seifenmicelen', *Zeitschrift für Physikalische Chemie*, 1931, **156**, 435-456.

258. A. Thiessen Peter and J. Stauff, in *Zeitschrift für Physikalische Chemie*, Editon edn., 1936, vol. 176A, pp. 397-429.

259. M. Ladd Parada, A. Sadeghpour, J. Vieira, M. Povey and M. Rappolt, 'Global Small-Angle X-ray Scattering Data Analysis of Triacylglycerols in the α-Phase (Part II)', *The Journal of Physical Chemistry B*, 2018, **122**, 10330-10336.

260. M. I. Jeraal, K. J. Roberts, I. McRobbie and D. Harbottle, 'Assessment of the Thermal Degradation of Sodium Lauroyl Isethionate Using Predictive Isoconversional Kinetics and a Temperature-Resolved Analysis of Evolved Gases', *Industrial & Engineering Chemistry Research*, 2019.

261. J. Ilavsky, 'Nika: software for two-dimensional data reduction', *Journal of Applied Crystallography*, 2012, **45**, 324-328.

262. N. Li, S. Perutkova, A. Iglic and M. Rappolt, 'My first electron density map: A beginner's guide to small angle X-ray diffraction', *Elektrotehniski Vestnik*, 2017, **84**, 69-75.

263. A. E. Blaurock and C. R. Worthington, 'Treatment of Low Angle X-Ray Data from Planar and Concentric Multilayered Structures', *Biophysical Journal*, 1966, **6**, 305-312.

264. G. Pabst, M. Rappolt, H. Amenitsch and P. Laggner, 'Structural information from multilamellar liposomes at full hydration: Full q-range fitting with high quality x-ray data', *Physical Review E*, 2000, **62**, 4000-4009.

265. C. R. Worthington, G. I. King and T. J. McIntosh, 'Direct Structure Determination of Multilayered Membrane-Type Systems Which Contain Fluid Layers', *Biophysical Journal*, 1973, **13**, 480-494.

266. A. E. Blaurock and G. I. King, 'Asymmetric structure of the purple membrane', *Science*, 1977, **196**, 1101-1104.

267. W. J. Sun, S. Tristram-Nagle, R. M. Suter and J. F. Nagle, 'Structure of gel phase saturated lecithin bilayers: temperature and chain length dependence', *Biophysical Journal*, 1996, **71**, 885-891.

268. A. E. Blaurock, 'Evidence of bilayer structure and of membrane interactions from X-ray diffraction analysis', *Biochimica et Biophysica Acta (BBA) - Reviews on Biomembranes*, 1982, **650**, 167-207.

269. O. O. Mykhaylyk and I. W. Hamley, 'The Packing of Triacylglycerols from SAXS Measurements: Application to the Structure of 1,3-Distearoyl-2-oleoyl-sn-glycerol Crystal Phases', *The Journal of Physical Chemistry B*, 2004, **108**, 8069-8083.

270. M. Rappolt, 'Bilayer thickness estimations with “poor” diffraction data', *Journal of Applied Physics*, 2010, **107**, 084701.

271. F. Weigend and R. Ahlrichs, 'Balanced basis sets of split valence, triple zeta valence and quadruple zeta valence quality for H to Rn: Design and assessment of accuracy', *Physical Chemistry Chemical Physics*, 2005, **7**, 3297-3305.

272. A. D. Becke, 'Density-functional thermochemistry. III. The role of exact exchange', *The Journal of Chemical Physics*, 1993, **98**, 5648-5652.

273. M. F. Schneider, R. Zantl, C. Gege, R. R. Schmidt, M. Rappolt and M. Tanaka, 'Hydrophilic/Hydrophobic Balance Determines Morphology of Glycolipids with Oligolactose Headgroups', *Biophysical Journal*, 2003, **84**, 306-313.

274. P. E. Harper, S. M. Gruner, R. N. A. H. Lewis and R. N. McElhaney, 'Electron density modeling and reconstruction of infinite periodic minimal surfaces (IPMS) based phases in lipid-water systems. II. Reconstruction of D surface based phases', *The European Physical Journal E*, 2000, **2**, 229-245.

275. M. Rappolt, A. Hickel, F. Bringezu and K. Lohner, 'Mechanism of the Lamellar/Inverse Hexagonal Phase Transition Examined by High Resolution X-Ray Diffraction', *Biophysical Journal*, 2003, **84**, 3111-3122.

276. J. Katsaras, K. R. Jeffrey, D. S. C. Yang and R. M. Epand, 'Direct evidence for the partial dehydration of phosphatidylethanolamine bilayers on approaching the hexagonal phase', *Biochemistry*, 1993, **32**, 10700-10707.

277. S. Tristram-Nagle, R. Zhang, R. M. Suter, C. R. Worthington, W. J. Sun and J. F. Nagle, 'Measurement of chain tilt angle in fully hydrated bilayers of gel phase lecithins', *Biophysical Journal*, 1993, **64**, 1097-1109.

278. G. Lukács, 'Whiteness — a feasible method for its evaluation', *Measurement*, 1989, **7**, 77-84.

279. B. Bhushan and V. N. Koinkar, 'Nanoindentation hardness measurements using atomic force microscopy', *Applied Physics Letters*, 1994, **64**, 1653-1655.

280. K. D. Bogie, 'Nonlinear Response of Soap and Synthetic Base Greases', *Journal of Tribology*, 1968, **90**, 592-602.

281. R. G. Laughlin, *The Aqueous Phase Behavior of Surfactants*, Elsevier, 1996.

Appendix

Table A.1. Friedman-derived activation energies for the degradation of SLI in N_2.

α	Intercept	Error	Gradient	Error	Ea (kJ/mol)	Error (kJ/mol)	Adj. R-Square
0.01	19.70	0.87	-18425	514	**153.19**	**4.27**	0.9977
0.02	21.07	1.41	-17370	839	**144.42**	**6.98**	0.9930
0.03	20.82	1.07	-16963	644	**141.04**	**5.36**	0.9957
0.04	20.76	1.03	-16792	619	**139.61**	**5.14**	0.9959
0.05	21.37	0.75	-17091	452	**142.10**	**3.76**	0.9979
0.06	21.05	0.67	-16849	406	**140.09**	**3.38**	0.9983
0.07	21.36	0.44	-17006	268	**141.39**	**2.23**	0.9993
0.08	21.78	0.59	-17239	360	**143.33**	**2.99**	0.9987
0.09	21.93	0.71	-17319	434	**144.00**	**3.61**	0.9981
0.10	21.56	0.59	-17077	363	**141.99**	**3.02**	0.9986
0.11	22.63	0.38	-17724	236	**147.37**	**1.96**	0.9995
0.12	21.86	0.60	-17256	371	**143.48**	**3.09**	0.9986
0.13	23.02	0.41	-17960	254	**149.33**	**2.11**	0.9994
0.14	22.61	0.50	-17707	312	**147.23**	**2.59**	0.9991
0.15	22.81	0.55	-17839	338	**148.33**	**2.81**	0.9989
0.16	23.03	0.48	-17973	295	**149.43**	**2.45**	0.9992
0.17	24.21	0.61	-18710	376	**155.56**	**3.13**	0.9988
0.18	23.90	0.73	-18526	451	**154.03**	**3.75**	0.9982
0.19	24.29	0.61	-18772	377	**156.08**	**3.13**	0.9988
0.20	24.68	0.66	-19022	410	**158.16**	**3.41**	0.9986
0.21	24.53	0.83	-18934	517	**157.42**	**4.30**	0.9978
0.22	24.45	0.57	-18899	359	**157.13**	**2.98**	0.9989
0.23	24.32	0.63	-18831	397	**156.57**	**3.30**	0.9987
0.24	24.53	0.67	-18977	420	**157.78**	**3.49**	0.9985
0.25	25.04	0.75	-19302	472	**160.48**	**3.93**	0.9982
0.26	24.73	0.84	-19123	525	**159.00**	**4.37**	0.9977
0.27	24.87	0.75	-19234	469	**159.92**	**3.90**	0.9982
0.28	24.60	0.74	-19078	465	**158.62**	**3.87**	0.9982
0.29	24.82	0.67	-19231	420	**159.89**	**3.49**	0.9986
0.30	25.14	0.64	-19454	402	**161.75**	**3.34**	0.9987
0.31	24.86	0.87	-19297	550	**160.45**	**4.57**	0.9976
0.32	24.70	1.10	-19221	694	**159.82**	**5.77**	0.9961
0.33	24.90	1.07	-19372	678	**161.07**	**5.64**	0.9963
0.34	24.49	1.18	-19138	750	**159.13**	**6.24**	0.9954
0.35	24.75	1.05	-19334	664	**160.75**	**5.52**	0.9965
0.36	24.70	1.22	-19339	776	**160.79**	**6.45**	0.9952
0.37	24.73	1.26	-19400	801	**161.30**	**6.66**	0.9949
0.38	24.33	1.18	-19183	753	**159.50**	**6.26**	0.9954
0.39	24.47	1.34	-19317	854	**160.61**	**7.10**	0.9942
0.40	25.18	1.09	-19812	696	**164.72**	**5.78**	0.9963
0.41	25.41	0.96	-19993	615	**166.23**	**5.11**	0.9972
0.42	25.83	0.85	-20305	545	**168.83**	**4.53**	0.9978
0.43	26.08	0.69	-20502	446	**170.47**	**3.70**	0.9986
0.44	26.79	0.76	-20980	490	**174.44**	**4.08**	0.9984
0.45	26.75	0.72	-20971	463	**174.36**	**3.85**	0.9985
0.46	27.15	0.93	-21239	601	**176.59**	**5.00**	0.9976
0.47	26.92	1.09	-21081	702	**175.28**	**5.84**	0.9967
0.48	26.97	1.16	-21095	749	**175.39**	**6.23**	0.9962
0.49	27.37	1.13	-21326	732	**177.32**	**6.08**	0.9965
0.50	26.20	1.29	-20547	836	**170.83**	**6.95**	0.9951

α	Intercept	Error	Gradient	Error	Ea (kJ/mol)	Error (kJ/mol)	Adj. R-Square
0.51	27.07	1.11	-21073	719	**175.21**	**5.98**	0.9965
0.52	26.98	1.04	-20978	675	**174.42**	**5.61**	0.9969
0.53	26.23	1.11	-20459	718	**170.11**	**5.97**	0.9963
0.54	26.03	1.17	-20294	761	**168.74**	**6.32**	0.9958
0.55	25.83	0.98	-20146	636	**167.51**	**5.29**	0.9970
0.56	25.31	1.16	-19783	753	**164.48**	**6.26**	0.9957
0.57	24.88	1.18	-19477	768	**161.94**	**6.39**	0.9953
0.58	25.28	0.74	-19709	484	**163.87**	**4.03**	0.9982
0.59	25.23	0.76	-19663	497	**163.48**	**4.13**	0.9981
0.60	24.93	0.91	-19455	596	**161.76**	**4.95**	0.9972
0.61	24.82	1.26	-19371	819	**161.06**	**6.81**	0.9947
0.62	24.34	1.38	-19054	901	**158.42**	**7.49**	0.9933
0.63	23.85	1.62	-18737	1058	**155.79**	**8.79**	0.9905
0.64	23.60	1.96	-18565	1281	**154.36**	**10.65**	0.9859
0.65	23.55	2.03	-18533	1327	**154.09**	**11.03**	0.9848
0.66	23.20	1.91	-18310	1250	**152.24**	**10.39**	0.9861
0.67	22.59	2.12	-17928	1385	**149.06**	**11.52**	0.9823
0.68	22.43	2.22	-17829	1453	**148.24**	**12.08**	0.9803
0.69	22.23	2.36	-17713	1543	**147.27**	**12.83**	0.9776
0.70	22.13	2.30	-17661	1506	**146.84**	**12.52**	0.9785
0.71	21.49	2.58	-17265	1689	**143.55**	**14.04**	0.9718
0.72	21.03	2.89	-16984	1895	**141.22**	**15.76**	0.9635
0.73	20.71	2.62	-16814	1717	**139.80**	**14.28**	0.9693
0.74	20.61	1.72	-16798	1129	**139.67**	**9.39**	0.9866
0.75	19.63	2.12	-16224	1393	**134.90**	**11.58**	0.9782
0.76	19.96	1.88	-16511	1232	**137.28**	**10.24**	0.9835
0.77	20.28	0.93	-16820	608	**139.85**	**5.06**	0.9961
0.78	21.14	1.99	-17512	1310	**145.60**	**10.89**	0.9834
0.79	24.61	1.55	-19937	1022	**165.76**	**8.50**	0.9922
0.80	28.08	2.27	-22348	1494	**185.81**	**12.42**	0.9867
0.81	27.73	2.79	-22180	1843	**184.41**	**15.32**	0.9796
0.82	25.03	3.27	-20425	2163	**169.82**	**17.99**	0.9671
0.83	21.76	3.40	-18283	2249	**152.02**	**18.70**	0.9559
0.84	17.11	4.41	-15262	2925	**126.89**	**24.32**	0.8973
0.85	13.19	4.95	-12725	3289	**105.80**	**27.34**	0.8232
0.86	7.68	5.94	-9184	3947	**76.36**	**32.82**	0.5954
0.87	3.11	7.46	-6284	4973	**52.25**	**41.35**	0.1659
0.88	-1.01	7.87	-3678	5262	**30.58**	**43.75**	-0.2055
0.89	-3.11	6.53	-2443	4382	**20.31**	**36.43**	-0.2982
0.90	-1.69	3.63	-3634	2448	**30.21**	**20.35**	0.2864
0.91	3.55	2.08	-7518	1412	**62.51**	**11.74**	0.9012
0.92	9.83	1.45	-12144	994	**100.97**	**8.26**	0.9802
0.93	15.25	1.39	-16174	965	**134.47**	**8.02**	0.9894
0.94	19.45	1.07	-19327	752	**160.69**	**6.25**	0.9955
0.95	21.24	1.38	-20779	976	**172.77**	**8.12**	0.9934
0.96	20.95	2.53	-20737	1813	**172.42**	**15.07**	0.9774
0.97	19.99	2.89	-20252	2094	**168.38**	**17.41**	0.9686
0.98	19.70	1.30	-20353	951	**169.22**	**7.90**	0.9935
0.99	20.70	0.86	-21542	641	**179.11**	**5.33**	0.9974
1.00	22.24	2.49	-23851	1901	**198.31**	**15.80**	0.9812

Table A.2. KAS-derived activation energies for the thermal degradation of SLI in N_2.

α	Intercept	Error	Gradient	Error	Ea (kJ/mol)	Error (kJ/mol)	Adj. R-Square
0.01	20.53	1.14	-18011	673	**149.75**	**5.60**	0.9958
0.02	19.58	1.17	-17691	697	**147.09**	**5.79**	0.9954
0.03	19.03	1.10	-17490	663	**145.42**	**5.51**	0.9957
0.04	18.66	1.06	-17354	638	**144.29**	**5.30**	0.9960
0.05	18.43	1.02	-17289	616	**143.75**	**5.12**	0.9962
0.06	18.23	0.98	-17224	594	**143.21**	**4.94**	0.9964
0.07	18.07	0.92	-17181	561	**142.85**	**4.66**	0.9968
0.08	17.97	0.89	-17167	542	**142.74**	**4.51**	0.9970
0.09	17.89	0.84	-17157	514	**142.65**	**4.28**	0.9973
0.10	17.80	0.81	-17139	497	**142.50**	**4.13**	0.9975
0.11	17.77	0.77	-17158	476	**142.66**	**3.96**	0.9977
0.12	17.70	0.75	-17151	459	**142.60**	**3.82**	0.9979
0.13	17.69	0.71	-17178	438	**142.82**	**3.65**	0.9981
0.14	17.65	0.69	-17186	424	**142.89**	**3.53**	0.9982
0.15	17.64	0.67	-17205	417	**143.05**	**3.47**	0.9982
0.16	17.62	0.65	-17224	405	**143.21**	**3.37**	0.9983
0.17	17.66	0.63	-17275	391	**143.63**	**3.25**	0.9985
0.18	17.68	0.61	-17314	380	**143.96**	**3.16**	0.9986
0.19	17.71	0.59	-17360	369	**144.34**	**3.07**	0.9987
0.20	17.76	0.57	-17414	358	**144.79**	**2.98**	0.9987
0.21	17.79	0.55	-17456	344	**145.14**	**2.86**	0.9988
0.22	17.82	0.54	-17497	339	**145.48**	**2.82**	0.9989
0.23	17.84	0.53	-17536	334	**145.80**	**2.78**	0.9989
0.24	17.87	0.54	-17576	335	**146.13**	**2.79**	0.9989
0.25	17.91	0.53	-17627	332	**146.56**	**2.76**	0.9989
0.26	17.94	0.53	-17666	330	**146.89**	**2.75**	0.9990
0.27	17.98	0.54	-17714	337	**147.28**	**2.80**	0.9989
0.28	18.00	0.54	-17751	337	**147.59**	**2.80**	0.9989
0.29	18.04	0.54	-17796	340	**147.97**	**2.83**	0.9989
0.30	18.08	0.54	-17843	341	**148.35**	**2.84**	0.9989
0.31	18.11	0.55	-17884	348	**148.69**	**2.89**	0.9989
0.32	18.13	0.57	-17923	360	**149.02**	**2.99**	0.9988
0.33	18.17	0.58	-17965	370	**149.37**	**3.08**	0.9987
0.34	18.18	0.61	-17997	385	**149.63**	**3.20**	0.9986
0.35	18.21	0.63	-18038	397	**149.97**	**3.30**	0.9986
0.36	18.24	0.65	-18078	410	**150.31**	**3.41**	0.9985
0.37	18.26	0.67	-18119	424	**150.65**	**3.53**	0.9984
0.38	18.28	0.69	-18152	437	**150.92**	**3.63**	0.9983
0.39	18.30	0.71	-18190	455	**151.24**	**3.78**	0.9981
0.40	18.35	0.73	-18249	465	**151.73**	**3.87**	0.9981
0.41	18.41	0.74	-18316	471	**152.28**	**3.91**	0.9980
0.42	18.49	0.74	-18396	476	**152.95**	**3.95**	0.9980
0.43	18.59	0.74	-18483	474	**153.68**	**3.94**	0.9980
0.44	18.70	0.73	-18584	470	**154.51**	**3.91**	0.9981
0.45	18.81	0.72	-18680	464	**155.31**	**3.86**	0.9982
0.46	18.92	0.71	-18776	459	**156.12**	**3.82**	0.9982
0.47	19.02	0.70	-18863	450	**156.84**	**3.74**	0.9983
0.48	19.10	0.69	-18938	444	**157.46**	**3.69**	0.9984
0.49	19.18	0.68	-19012	437	**158.07**	**3.63**	0.9984
0.50	19.21	0.68	-19052	437	**158.41**	**3.63**	0.9984

α	Intercept	Error	Gradient	Error	Ea (kJ/mol)	Error (kJ/mol)	Adj. R-Square
0.51	19.26	0.66	-19103	430	**158.83**	**3.58**	0.9985
0.52	19.30	0.67	-19147	431	**159.20**	**3.58**	0.9985
0.53	19.32	0.64	-19177	415	**159.45**	**3.45**	0.9986
0.54	19.34	0.64	-19201	415	**159.65**	**3.45**	0.9986
0.55	19.34	0.63	-19219	412	**159.79**	**3.42**	0.9986
0.56	19.34	0.62	-19228	404	**159.87**	**3.36**	0.9987
0.57	19.33	0.62	-19235	406	**159.93**	**3.38**	0.9987
0.58	19.33	0.62	-19245	403	**160.01**	**3.35**	0.9987
0.59	19.31	0.61	-19249	395	**160.04**	**3.28**	0.9987
0.60	19.30	0.60	-19251	391	**160.06**	**3.25**	0.9988
0.61	19.29	0.60	-19252	394	**160.07**	**3.27**	0.9988
0.62	19.27	0.61	-19251	399	**160.06**	**3.32**	0.9987
0.63	19.23	0.62	-19239	405	**159.96**	**3.36**	0.9987
0.64	19.20	0.63	-19228	414	**159.87**	**3.44**	0.9986
0.65	19.17	0.66	-19217	428	**159.78**	**3.56**	0.9985
0.66	19.13	0.67	-19202	440	**159.66**	**3.66**	0.9984
0.67	19.08	0.69	-19180	452	**159.47**	**3.76**	0.9983
0.68	19.04	0.72	-19161	470	**159.32**	**3.91**	0.9982
0.69	18.99	0.75	-19138	488	**159.12**	**4.06**	0.9981
0.70	18.93	0.77	-19112	504	**158.91**	**4.19**	0.9979
0.71	18.87	0.80	-19083	523	**158.66**	**4.35**	0.9978
0.72	18.81	0.84	-19052	548	**158.41**	**4.55**	0.9975
0.73	18.73	0.87	-19011	568	**158.06**	**4.72**	0.9973
0.74	18.65	0.89	-18971	581	**157.74**	**4.83**	0.9972
0.75	18.54	0.92	-18912	602	**157.24**	**5.01**	0.9970
0.76	18.45	0.94	-18862	618	**156.83**	**5.14**	0.9968
0.77	18.35	0.92	-18814	604	**156.43**	**5.02**	0.9969
0.78	18.27	0.90	-18775	589	**156.11**	**4.90**	0.9971
0.79	18.27	0.87	-18803	574	**156.33**	**4.77**	0.9972
0.80	18.42	0.93	-18925	616	**157.35**	**5.12**	0.9968
0.81	18.56	1.01	-19043	666	**158.33**	**5.54**	0.9963
0.82	18.59	1.10	-19091	727	**158.73**	**6.04**	0.9957
0.83	18.48	1.18	-19042	783	**158.33**	**6.51**	0.9950
0.84	18.14	1.32	-18850	874	**156.73**	**7.27**	0.9936
0.85	17.60	1.49	-18522	991	**154.00**	**8.24**	0.9915
0.86	16.63	1.75	-17912	1166	**148.93**	**9.69**	0.9874
0.87	15.11	2.16	-16949	1442	**140.92**	**11.99**	0.9786
0.88	13.01	2.63	-15603	1758	**129.73**	**14.62**	0.9629
0.89	10.67	2.97	-14095	1996	**117.19**	**16.60**	0.9422
0.90	8.70	3.01	-12845	2033	**106.80**	**16.91**	0.9284
0.91	7.58	2.78	-12182	1887	**101.29**	**15.69**	0.9313
0.92	7.46	2.44	-12235	1675	**101.73**	**13.93**	0.9458
0.93	8.25	2.11	-12936	1463	**107.55**	**12.16**	0.9626
0.94	9.62	2.04	-14068	1429	**116.97**	**11.88**	0.9697
0.95	11.08	2.09	-15278	1485	**127.03**	**12.34**	0.9722
0.96	12.26	2.31	-16290	1656	**135.44**	**13.77**	0.9696
0.97	13.08	2.51	-17060	1815	**141.85**	**15.09**	0.9668
0.98	13.80	2.29	-17791	1675	**147.92**	**13.93**	0.9739
0.99	14.79	1.77	-18793	1317	**156.26**	**10.95**	0.9854
1.00	16.88	1.22	-20945	931	**174.15**	**7.74**	0.9941

Table A.3. Friedman-derived activation energies for the degradation of SLI in Air.

α	Intercept	Error	Gradient	Error	Ea (kJ/mol)	Error (kJ/mol)	Adj. R-Square
0.01	-5.68	2.16	-962	1075	**7.99**	**8.94**	-0.0716
0.02	-3.73	2.02	-1990	1020	**16.55**	**8.48**	0.4838
0.03	-0.87	2.05	-3480	1047	**28.93**	**8.71**	0.7700
0.04	1.35	1.36	-4654	701	**38.70**	**5.83**	0.9350
0.05	2.86	1.10	-5482	575	**45.58**	**4.78**	0.9677
0.06	4.11	0.83	-6178	437	**51.36**	**3.63**	0.9851
0.07	5.30	0.79	-6869	419	**57.12**	**3.48**	0.9889
0.08	6.46	0.56	-7540	300	**62.69**	**2.50**	0.9953
0.09	7.37	0.86	-8096	465	**67.32**	**3.87**	0.9902
0.10	8.81	1.08	-8947	589	**74.39**	**4.90**	0.9871
0.11	11.13	0.70	-10300	385	**85.64**	**3.20**	0.9958
0.12	13.25	0.81	-11548	450	**96.02**	**3.74**	0.9955
0.13	14.90	0.79	-12526	442	**104.14**	**3.68**	0.9963
0.14	16.85	0.95	-13686	537	**113.79**	**4.47**	0.9954
0.15	18.37	0.78	-14586	443	**121.28**	**3.69**	0.9972
0.16	20.03	0.50	-15566	283	**129.42**	**2.36**	0.9990
0.17	20.53	0.66	-15875	380	**131.99**	**3.16**	0.9983
0.18	21.41	0.86	-16389	496	**136.27**	**4.13**	0.9973
0.19	21.78	0.64	-16615	372	**138.15**	**3.09**	0.9985
0.20	22.71	0.63	-17155	369	**142.63**	**3.07**	0.9986
0.21	22.51	0.93	-17043	542	**141.70**	**4.51**	0.9970
0.22	22.97	1.03	-17307	601	**143.90**	**5.00**	0.9964
0.23	23.21	1.38	-17453	808	**145.11**	**6.72**	0.9936
0.24	23.06	1.75	-17362	1029	**144.36**	**8.56**	0.9895
0.25	23.57	1.66	-17654	982	**146.78**	**8.17**	0.9908
0.26	23.30	1.95	-17499	1158	**145.50**	**9.62**	0.9870
0.27	23.18	2.24	-17433	1327	**144.94**	**11.03**	0.9828
0.28	23.61	2.33	-17682	1385	**147.02**	**11.51**	0.9818
0.29	23.38	2.37	-17546	1409	**145.89**	**11.71**	0.9809
0.30	23.05	2.53	-17353	1510	**144.28**	**12.55**	0.9776
0.31	22.95	2.76	-17292	1650	**143.77**	**13.72**	0.9732
0.32	23.34	2.42	-17514	1450	**145.62**	**12.05**	0.9797
0.33	22.83	2.55	-17218	1530	**143.16**	**12.72**	0.9767
0.34	22.64	2.68	-17110	1609	**142.26**	**13.38**	0.9739
0.35	22.39	2.65	-16963	1595	**141.04**	**13.26**	0.9739
0.36	22.72	2.35	-17155	1417	**142.63**	**11.78**	0.9798
0.37	22.46	2.37	-17001	1426	**141.36**	**11.86**	0.9792
0.38	22.28	2.45	-16905	1479	**140.56**	**12.30**	0.9774
0.39	21.87	2.29	-16659	1381	**138.51**	**11.49**	0.9797
0.40	21.82	2.18	-16633	1322	**138.29**	**10.99**	0.9813
0.41	22.26	1.95	-16895	1179	**140.47**	**9.80**	0.9855
0.42	21.81	1.96	-16638	1187	**138.34**	**9.87**	0.9849
0.43	21.55	1.89	-16485	1149	**137.06**	**9.56**	0.9856
0.44	21.63	1.97	-16544	1198	**137.55**	**9.96**	0.9844
0.45	21.45	1.94	-16442	1183	**136.70**	**9.84**	0.9846
0.46	22.05	1.65	-16808	1006	**139.75**	**8.36**	0.9893
0.47	21.85	1.82	-16694	1108	**138.80**	**9.21**	0.9869
0.48	21.69	1.89	-16606	1153	**138.07**	**9.58**	0.9857
0.49	21.75	2.09	-16654	1280	**138.47**	**10.64**	0.9825
0.50	21.68	2.18	-16614	1335	**138.14**	**11.10**	0.9809

α	Intercept	Error	Gradient	Error	Ea (kJ/mol)	Error (kJ/mol)	Adj. R-Square
0.51	22.01	2.31	-16831	1414	**139.94**	**11.75**	0.9791
0.52	22.07	2.32	-16868	1420	**140.25**	**11.80**	0.9790
0.53	21.72	2.41	-16671	1478	**138.61**	**12.29**	0.9768
0.54	21.81	2.72	-16739	1669	**139.17**	**13.88**	0.9708
0.55	21.80	2.81	-16748	1727	**139.25**	**14.36**	0.9688
0.56	21.59	2.75	-16630	1691	**138.27**	**14.06**	0.9696
0.57	21.32	2.77	-16485	1708	**137.06**	**14.20**	0.9685
0.58	21.27	2.78	-16472	1714	**136.95**	**14.25**	0.9682
0.59	21.24	2.67	-16472	1647	**136.95**	**13.69**	0.9706
0.60	21.42	2.77	-16606	1709	**138.07**	**14.21**	0.9689
0.61	21.11	2.64	-16437	1633	**136.67**	**13.58**	0.9710
0.62	20.63	2.67	-16167	1649	**134.42**	**13.71**	0.9694
0.63	20.02	2.99	-15820	1852	**131.54**	**15.40**	0.9600
0.64	19.94	2.67	-15791	1657	**131.29**	**13.77**	0.9677
0.65	19.78	2.82	-15726	1752	**130.75**	**14.56**	0.9637
0.66	19.78	2.73	-15759	1695	**131.03**	**14.09**	0.9661
0.67	18.72	2.93	-15130	1820	**125.80**	**15.13**	0.9578
0.68	18.46	2.93	-15011	1824	**124.81**	**15.16**	0.9570
0.69	18.29	3.02	-14936	1882	**124.19**	**15.65**	0.9539
0.70	17.53	2.89	-14506	1806	**120.61**	**15.02**	0.9549
0.71	16.79	3.13	-14088	1959	**117.13**	**16.28**	0.9442
0.72	16.94	2.55	-14218	1598	**118.22**	**13.28**	0.9631
0.73	16.99	2.63	-14300	1644	**118.90**	**13.67**	0.9614
0.74	15.89	2.69	-13673	1685	**113.68**	**14.01**	0.9558
0.75	16.05	2.15	-13831	1350	**115.00**	**11.22**	0.9720
0.76	16.48	1.67	-14161	1052	**117.74**	**8.75**	0.9836
0.77	16.79	1.41	-14443	891	**120.08**	**7.41**	0.9887
0.78	17.90	0.49	-15219	312	**126.54**	**2.59**	0.9987
0.79	19.50	0.32	-16321	201	**135.70**	**1.68**	0.9995
0.80	21.58	1.19	-17733	757	**147.44**	**6.29**	0.9946
0.81	23.75	1.97	-19201	1251	**159.65**	**10.40**	0.9874
0.82	26.52	2.43	-21057	1548	**175.08**	**12.87**	0.9840
0.83	31.56	2.97	-24324	1898	**202.24**	**15.78**	0.9820
0.84	34.92	2.62	-26540	1677	**220.67**	**13.94**	0.9881
0.85	39.04	2.53	-29217	1627	**242.93**	**13.53**	0.9908
0.86	40.69	2.32	-30291	1495	**251.86**	**12.43**	0.9927
0.87	41.72	1.98	-30924	1276	**257.12**	**10.61**	0.9949
0.88	40.34	2.41	-29975	1556	**249.23**	**12.93**	0.9920
0.89	37.26	2.24	-27919	1447	**232.13**	**12.03**	0.9920
0.90	32.92	2.07	-25020	1344	**208.03**	**11.18**	0.9914
0.91	29.20	1.11	-22550	717	**187.49**	**5.96**	0.9970
0.92	26.54	1.06	-20772	687	**172.71**	**5.71**	0.9967
0.93	23.97	0.88	-19110	573	**158.89**	**4.76**	0.9973
0.94	23.13	0.71	-18581	465	**154.49**	**3.86**	0.9981
0.95	22.67	0.68	-18330	441	**152.40**	**3.67**	0.9983
0.96	21.44	0.83	-17617	541	**146.48**	**4.50**	0.9972
0.97	20.94	0.78	-17393	510	**144.61**	**4.24**	0.9974
0.98	18.71	0.24	-16135	158	**134.15**	**1.31**	0.9997
0.99	18.71	0.32	-16382	212	**136.21**	**1.76**	0.9995
1.00	24.06	1.08	-20400	708	**169.62**	**5.89**	0.9964

Table A.4. KAS-derived activation energies for the thermal degradation of SLI in Air.

α	Intercept	Error	Gradient	Error	Ea (kJ/mol)	Error (kJ/mol)	Adj. R-Square
0.01	16.31	5.58	-12993	2783	**108.03**	**23.14**	0.8740
0.02	10.67	3.38	-10330	1708	**85.89**	**14.20**	0.9222
0.03	7.99	2.18	-9094	1117	**75.61**	**9.29**	0.9561
0.04	6.42	1.53	-8395	791	**69.80**	**6.58**	0.9738
0.05	5.44	1.12	-7981	585	**66.36**	**4.87**	0.9840
0.06	4.82	0.89	-7741	467	**64.36**	**3.88**	0.9892
0.07	4.45	0.72	-7627	384	**63.41**	**3.19**	0.9924
0.08	4.27	0.57	-7607	308	**63.25**	**2.56**	0.9951
0.09	4.22	0.47	-7657	255	**63.67**	**2.12**	0.9967
0.10	4.34	0.42	-7795	228	**64.81**	**1.90**	0.9974
0.11	4.70	0.42	-8074	230	**67.13**	**1.91**	0.9976
0.12	5.25	0.44	-8458	247	**70.32**	**2.06**	0.9974
0.13	5.86	0.44	-8874	248	**73.79**	**2.06**	0.9977
0.14	6.58	0.48	-9357	271	**77.80**	**2.25**	0.9975
0.15	7.35	0.51	-9864	291	**82.01**	**2.42**	0.9974
0.16	8.15	0.55	-10389	312	**86.38**	**2.60**	0.9973
0.17	8.87	0.60	-10861	343	**90.30**	**2.85**	0.9970
0.18	9.52	0.65	-11292	374	**93.89**	**3.11**	0.9967
0.19	10.11	0.70	-11690	404	**97.20**	**3.36**	0.9964
0.20	10.66	0.74	-12062	434	**100.29**	**3.61**	0.9961
0.21	11.13	0.80	-12380	465	**102.93**	**3.87**	0.9958
0.22	11.56	0.85	-12672	497	**105.36**	**4.13**	0.9954
0.23	11.95	0.91	-12939	532	**107.58**	**4.43**	0.9949
0.24	12.28	0.98	-13173	576	**109.53**	**4.79**	0.9943
0.25	12.59	1.03	-13391	609	**111.34**	**5.06**	0.9938
0.26	12.86	1.09	-13581	648	**112.92**	**5.39**	0.9932
0.27	13.09	1.16	-13751	688	**114.33**	**5.72**	0.9925
0.28	13.32	1.22	-13916	726	**115.70**	**6.03**	0.9919
0.29	13.52	1.28	-14061	763	**116.91**	**6.34**	0.9912
0.30	13.68	1.34	-14184	798	**117.93**	**6.64**	0.9906
0.31	13.82	1.40	-14297	836	**118.88**	**6.95**	0.9898
0.32	13.97	1.45	-14407	866	**119.79**	**7.20**	0.9893
0.33	14.08	1.49	-14499	892	**120.55**	**7.42**	0.9887
0.34	14.18	1.54	-14582	924	**121.24**	**7.68**	0.9880
0.35	14.26	1.58	-14652	951	**121.82**	**7.91**	0.9875
0.36	14.34	1.61	-14722	969	**122.41**	**8.06**	0.9871
0.37	14.41	1.64	-14785	987	**122.93**	**8.21**	0.9867
0.38	14.47	1.66	-14844	1005	**123.42**	**8.36**	0.9864
0.39	14.52	1.68	-14891	1018	**123.81**	**8.46**	0.9861
0.40	14.55	1.70	-14931	1030	**124.15**	**8.56**	0.9859
0.41	14.60	1.71	-14977	1038	**124.53**	**8.63**	0.9857
0.42	14.63	1.72	-15014	1046	**124.83**	**8.69**	0.9856
0.43	14.64	1.73	-15041	1049	**125.06**	**8.72**	0.9855
0.44	14.66	1.73	-15069	1054	**125.29**	**8.76**	0.9855
0.45	14.67	1.74	-15096	1059	**125.51**	**8.80**	0.9854
0.46	14.70	1.74	-15132	1058	**125.81**	**8.80**	0.9855
0.47	14.73	1.74	-15164	1061	**126.08**	**8.82**	0.9855
0.48	14.75	1.74	-15192	1065	**126.31**	**8.85**	0.9854
0.49	14.77	1.75	-15222	1070	**126.57**	**8.90**	0.9853
0.50	14.79	1.76	-15254	1077	**126.83**	**8.96**	0.9852

α	Intercept	Error	Gradient	Error	Ea (kJ/mol)	Error (kJ/mol)	Adj. R-Square
0.51	14.83	1.77	-15290	1083	**127.13**	**9.00**	0.9851
0.52	14.86	1.78	-15323	1091	**127.41**	**9.07**	0.9849
0.53	14.87	1.79	-15351	1101	**127.64**	**9.15**	0.9847
0.54	14.89	1.81	-15379	1113	**127.87**	**9.25**	0.9845
0.55	14.92	1.84	-15408	1128	**128.11**	**9.38**	0.9841
0.56	14.93	1.86	-15433	1144	**128.32**	**9.51**	0.9837
0.57	14.94	1.88	-15454	1157	**128.49**	**9.62**	0.9834
0.58	14.95	1.90	-15476	1172	**128.67**	**9.74**	0.9830
0.59	14.96	1.92	-15496	1186	**128.84**	**9.86**	0.9826
0.60	14.97	1.94	-15520	1200	**129.04**	**9.97**	0.9823
0.61	14.98	1.96	-15541	1211	**129.21**	**10.07**	0.9820
0.62	14.97	1.98	-15554	1224	**129.32**	**10.17**	0.9817
0.63	14.95	2.00	-15554	1237	**129.32**	**10.29**	0.9813
0.64	14.93	2.02	-15560	1250	**129.37**	**10.39**	0.9809
0.65	14.90	2.03	-15558	1261	**129.36**	**10.48**	0.9806
0.66	14.88	2.05	-15562	1273	**129.39**	**10.58**	0.9802
0.67	14.82	2.07	-15547	1288	**129.27**	**10.71**	0.9797
0.68	14.77	2.09	-15530	1302	**129.13**	**10.83**	0.9792
0.69	14.70	2.11	-15508	1316	**128.94**	**10.94**	0.9787
0.70	14.62	2.13	-15476	1332	**128.68**	**11.07**	0.9781
0.71	14.50	2.16	-15421	1350	**128.22**	**11.23**	0.9774
0.72	14.40	2.17	-15382	1359	**127.89**	**11.30**	0.9769
0.73	14.29	2.18	-15333	1369	**127.49**	**11.38**	0.9765
0.74	14.15	2.20	-15266	1383	**126.93**	**11.50**	0.9758
0.75	14.01	2.21	-15208	1387	**126.45**	**11.53**	0.9755
0.76	13.89	2.19	-15158	1380	**126.03**	**11.48**	0.9755
0.77	13.79	2.17	-15118	1366	**125.70**	**11.36**	0.9759
0.78	13.73	2.11	-15113	1329	**125.65**	**11.05**	0.9772
0.79	13.76	2.01	-15163	1272	**126.07**	**10.57**	0.9792
0.80	13.89	1.87	-15285	1186	**127.08**	**9.86**	0.9821
0.81	14.14	1.69	-15484	1076	**128.74**	**8.95**	0.9856
0.82	14.56	1.53	-15794	977	**131.32**	**8.12**	0.9886
0.83	15.22	1.40	-16260	893	**135.19**	**7.42**	0.9910
0.84	16.04	1.35	-16835	863	**139.98**	**7.18**	0.9922
0.85	17.03	1.40	-17518	897	**145.65**	**7.46**	0.9922
0.86	18.01	1.50	-18195	968	**151.28**	**8.05**	0.9916
0.87	18.92	1.63	-18818	1054	**156.46**	**8.77**	0.9906
0.88	19.60	1.75	-19294	1133	**160.42**	**9.42**	0.9897
0.89	20.05	1.84	-19613	1190	**163.07**	**9.89**	0.9890
0.90	20.28	1.88	-19781	1220	**164.47**	**10.14**	0.9887
0.91	20.36	1.88	-19853	1220	**165.07**	**10.15**	0.9888
0.92	20.37	1.86	-19880	1209	**165.29**	**10.05**	0.9890
0.93	20.31	1.83	-19857	1189	**165.10**	**9.89**	0.9893
0.94	20.23	1.79	-19826	1166	**164.84**	**9.69**	0.9897
0.95	20.15	1.75	-19788	1138	**164.52**	**9.46**	0.9901
0.96	20.02	1.68	-19727	1094	**164.02**	**9.10**	0.9908
0.97	19.87	1.62	-19652	1055	**163.39**	**8.77**	0.9914
0.98	19.60	1.56	-19503	1016	**162.15**	**8.44**	0.9919
0.99	19.26	1.45	-19326	950	**160.68**	**7.90**	0.9928
1.00	19.35	1.35	-19470	888	**161.88**	**7.38**	0.9938